THE·UNIVERSITY·OF

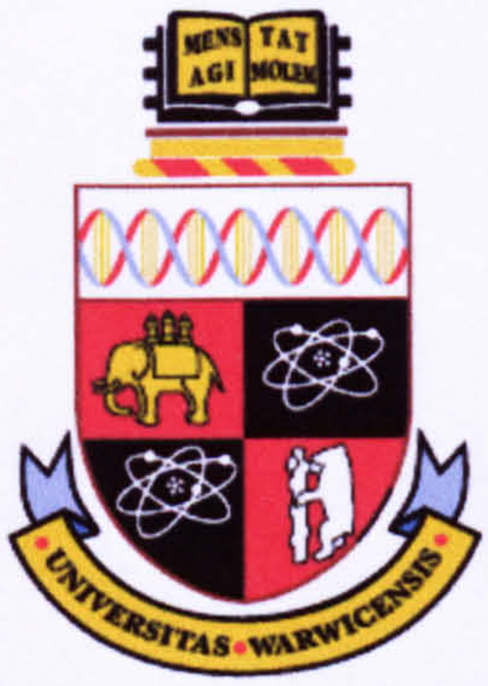

WARWICK

Ultrasonic Air-Coupled Capacitive Arrays

By

Adrian Neild B.Eng. (Hons)

Submitted for the degree of

Ph.D. in Engineering

to the

University of Warwick

Describing research conducted in the

School of Engineering

Submitted January 2003

THE UNIVERSITY OF

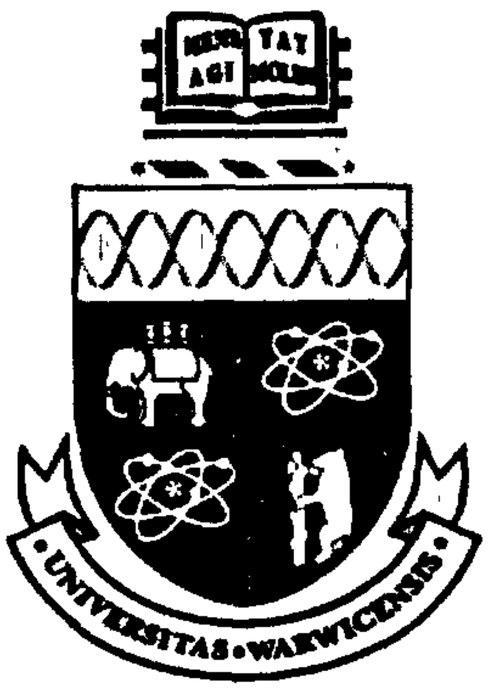

WARWICK

Ultrasonic Air-Coupled Capacitive Arrays

By

Adrian Neild B.Eng. (Hons)

Submitted for the degree of

Ph.D. in Engineering

to the

University of Warwick

Describing research conducted in the

School of Engineering

Submitted January 2003

Table of contents

Table of contents	i
List of figures	v
List of tables	xi
Acknowledgements	xii
Declaration	xiii
Summary	xiv
Chapter 1: Introduction	1
1.1 Introduction	1
1.2 Basic properties of sound	1
1.3 Propagation of sound across an interface	3
1.4 Attenuation	4
1.5 Diffraction due to a finite sized source	5
1.5.1 Farfield Approximation	6
1.5.2 Impulse Response model	7
1.6 Nearfield and farfield	12
1.7 Thesis outline	14
1.8 References	15
Chapter 2: Review of air-coupled technology	17
2.1 Introduction	17
2.2 Coupling	17
2.3 Drive signals	18
2.4 Piezoelectric transducers for use in air	20
2.5 Capacitive devices	23
2.5.1 Construction of polymer-membrane devices	23
2.5.2 Principles of operation	24
2.5.3 Transducer response	25
a) Roughened backplate	25
b) Grooved backplate	26
c) Micromachined backplate	27
d) Fully micromachined device	27
2.6 Other non-contact methods	29
2.7 Conclusions	30
2.8 References	30
Chapter 3: Theoretical predictions for phased arrays	35
3.1 Introduction	35
3.2 Calculating phasing for arrays	35
3.3 Farfield directivity model applied to arrays	39
3.4 Impulse response method applied to arrays	41
3.4.1 Predicted fields from a single source	42
3.4.2 Modelling the fields of arrays in air	45
3.4.3 Designing arrays for focussing	52
a) Interference fields	53

b) Side lobes 57
c) Effect of element size on array characteristics 58
d) Summary of factors, which affect the focused field 61
3.5 Conclusions 62
3.6 References 63

Chapter 4: Phased capacitance air-coupled arrays 65

4.1 Introduction 65
4.2 Construction 65
4.3 Phasing Electronics 67
4.4 Apodisation of elements 69
4.5 Focussed source 71
4.5.1 Focussed field scans 71
4.5.2 Full width half maximum 78
4.6 Beam-steering 81
4.7 Conclusions 87
4.8 References 88

Chapter 5: A theoretical model for the effect of a finite-size receiver 89

5.1 Introduction 89
5.2 Overview 90
5.3 A new geometrical approach to the convolution integral 92
5.4 General solutions 98
5.4.1 Corner limited integration 98
5.4.2 Edge limited Integral 103
5.4.3 Planar Integral 105
5.4.4 General solution to integration over active area 106
5.5 Regions 108
5. 6 Reconstruction of the source 112
5.6.1 An example of source reconstruction in Region 2 113
5.6.2 An example of source reconstruction in Region 3 115
5.6.3 An example of source reconstruction in Region 4 117
5.6.4 All Regions 120
5.7 Algorithm 123
5.8 Finite receiver model predictions 125
5.9 Comparison to an alternative modelling approach 129
5.10 Some predictions of the effect of changing the receiver size 132
5.11 Comparison of model predictions to experimental measurements 135
5.12 Conclusions 141
5.13 References 141

Chapter 6: Focussing in air using a parabolic mirror 143

6.1 Introduction 143
6.2 The Impulse Response model for a circular piston 143
6.3 Reflection and mirror geometry 145
6.4 Comparison of theoretical and experimental results 152
6.5 The effect of changing the mirror parameters 159

6.6 Conclusions 166
6.7 References 167

Chapter 7: Imaging with ultrasonic capacitive arrays 168

7.1 Introduction 168
7.2 Cross Coupling 168
7.3 Through-thickness imaging of solids using a 2-D array receiver 172
7.4 A combined receiver and phased source array for surface imaging 177
7.5 Synthetic aperture focussing technique and ellipse crossing for volumetric imaging in air 183
7.6 Conclusions 191
7.7 References 192

Chapter 8: Conclusions and further work 194

8.1 General conclusions 194
8.2 Further work 196

Publications 198

Appendix A: Phasing for 2-D array beam-steering 199

Appendix B: Matlab programs 201

B.1 Pressure field model of an array 201
B.2 Interference fields 204
B.3 Comparative interference fields 204
B.4 Half pressure fields 204
B.5 Full width half maximum 205
B.6 Finite receiver program 205
B.7 Parabolic mirror model 205
B.8 SAFT and ellipse crossing programs 210
B.8.1 Main program 210
B.8.2 Filtering 211
B.8.3 Time windowing 211
B.8.4 SAFT image calculation 213
B.8.5 Ellipse crossing image calculation 215

Appendix C: Equipment specifications 217

C.1 Panametrics 5055PR 217
C.2 Second wave NCA1000 Chirp generator 217
C.3 Cooknell CA6/C charge amplifier 218
C.4 Scanning Stage 218

Appendix D: Calculation of Finite receiver model integrals 219

D.1 Integral A 219
D.2 Integral B 219

List of figures

Chapter 1: Introduction

Figure 1.1: Snell's law
Figure 1.2: Approximate directivity
Figure 1.3: Arbitrary shaped source in an infinite baffle
Figure 1.4: Geometry within the plane of the Piston
Figure 1.5: Plane and edge waves, (i), (iii), and (v) show the impulse response at different radial distances from the axis, at 0, 0.6 and 1.2 of the radius, respectively. Whilst (ii), (iv), and (vi) show the time derivative of the impulse response over each time step, for the same positions in the field
Figure 1.6: Axial plot of normalised pressure amplitude, for a circular source of diameter (i) 4 wavelengths, (ii) 8 wavelengths, and (iii) 16 wavelengths
Figure 1.7: Nearfield-farfield boundary for (i) a square piston and (ii) a circular piston

Chapter 2: Review of air-coupled technology

Figure 2.1: Toneburst signal in (i) time, and (ii) frequency domains
Figure 2.2: Broadband signal in (i) time, and (ii) frequency domains
Figure 2.3: Chirp signal in (i) time, and (ii) frequency domains
Figure 2.4: Structure of 1-3 connectivity piezoelectric composite transducer
Figure 2.5: Capacitive transducer
Figure 2.6: Manufacture of a micromachined transducer

Chapter 3: Theoretical predictions for phased arrays

Figure 3.1: Array geometry
Figure 3.2: Array in beam-steering mode of operation
Figure 3.3: Directivity plot, of (i) a single line element, (ii) an array of points, and (iii) an array of line elements
Figure 3.4: Directivity plot, of (i) an array of points steered to 20° and (ii) an array of line elements steered to the same angle
Figure 3.5: Predicted pressure field from a single 3.94 mm diameter circular source in air, in (i) the *xz* plane, and in (ii) and (iii) the *xy* plane at $z = 14$ mm and 7 mm respectively
Figure 3.6: Predicted pressure field in air from a single 3.5 by 3.5 mm square source, in (i) the *xz* plane, and in (ii) and (iii) the *xy* plane at $z = 14$ mm and 7 mm respectively
Figure 3.7: Predicted pressure field in air from a single 3.5 by 3.5 mm square source, in the *xz* plane, using a (i) broadband and (ii) a chirp drive signal
Figure 3.8: Predicted pressure field from a single 0.8 by 10 mm rectangular source, in (i) the *xz* plane, and in (ii) *yz* plane
Figure 3.9: Simplifying (i) an array of elements with a field point to (ii) an element with an array of points
Figure 3.10: Demonstrating the affect of phasing at the focal point. (i) The unfocussed impulse response from each element of an 8 element array, and these are summed in (ii). (iii) The effect of phasing when located at the focal point,

and these are summed in (iv). The resultant pressure waveform can then be seen for the unphased case (v), and the phased case (vi)

Figure 3.11: Demonstrating the affect of phasing at a point displaced from the focal point by 1.5 mm, (i) shows the unfocussed impulse response from each element of an 8 element array and these are summed in (ii), (iii) shows the effect of phasing, and these are summed in (iv). The resultant pressure waveform can then be seen for the unphased case (v), and the phased case (vi)

Figure 3.12: Predicted peak-to-peak pressure field in air from an 8 element array, driven by a 500kHz toneburst, for (i) all elements in phase, with (ii) and (iii) phased with the phases calculated such that they are focussed at (ii) x = 0 mm, y = 0 mm and z = 20 mm and (iii) x = 5 mm, y = 0 mm and z = 20

Figure 3.13: Peak-to-peak pressure field from an 8 element array, focussed on 0 mm, 0 mm, 20 mm driven by (i) a broadband signal, and (ii) a chirp signal both centred at 500 kHz

Figure 3.14: Demonstration of the fact that accurate focussing can be achieved, for (i) an eight element array focussed at x = 0 mm, y = 0 mm and z = 12 mm, and for (ii) a sixteen element array focussed at x = 0 mm, y = 0 mm, and z = 20 mm in air

Figure 3.15: The interference fields from an array of conceptual sources on a pitch of 1 mm driven by a phased 500 KHz waveform, in (i) 8 sources are focussed at z = 20mm, in (ii) 8 sources are focussed at 12 mm, and in (iii) 16 sources are focussed at z = 20 mm

Figure 3.16 The location of four points around the focal point

Figure 3.17: Predicting the focussing ability using the interference method for (i) 8 elements on a pitch of 1mm, and (ii) for 16 elements, using in both cases a frequency of 500 kHz

Figure 3.18: An array of 8 conceptual sources on a pitch of 1mm focussing at z = 20 mm using a drive frequency of (i) 300, (ii) 500, (iii) 700, and (iv) 1000 kHz

Figure 3.19: Elimination of side lobes

Figure 3.20: The pressure field of a single 0.8 by 10 mm element drive by toneburst signal centred at (i) 500 kHz and (ii) 1 MHz

Figure 3.21: Half axial pressure fields for a single element 0.8 by 10 mm, for (i) a drive frequency of 500 kHz, and (ii) 1 MHz

Figure 3.22: Number of contributing elements from an 8 element array on a 1mm pitch, with each element measuring 0.8 by 10 mm, for (i) a drive frequency of 500 kHz, and (ii) 1 MHz

Figure 3.23: The application of the techniques derived in this chapter to a specific array geometry. (i) shows the comparative interference field, (ii) shows the half pressure field of a single element, (iii) shows the number of contributing elements

Chapter 4: Phased capacitance air-coupled arrays

Figure 4.1: Photographs of a capacitive array, (i) the backplate of a 32 element array, and (ii) finished array complete with membrane

Figure 4.2: Block diagram for phasing circuitry

Figure 4.3: The miniature micromachined probe tip, (i) a scanning electron micrograph (SEM) of a single element, and (ii) a photograph showing two such elements with the one on the left connected as a receiver
Figure 4.4: Experimental apparatus used to assess the apodisation of the elements of an array
Figure 4.5: The maximum peak-to-peak voltage received in front of each element of a 32 element array
Figure 4.6: A comparison of the measured waveform and that used for the simulation, (i) shows the measured signal, (ii) the windowed waveform and simulated version, and (iii) the Fourier transform of each
Figure 4.7: Theoretical and experimental maximum peak-to-peak pressure field plots when focussing at (i) z = 12 mm, x = 0 mm, and (ii) z = 20 mm, x = 0 mm
Figure 4.8: Theoretical and experimental maximum peak-to-peak pressure field plots when focussing at (i) z = 30 mm, x = 0 mm, and (ii) z = 40 mm, x = 0 mm
Figure 4.9: Theoretical and experimental maximum peak-to-peak pressure field plots when focussing at (i) z = 20 mm, x = 5 mm, and (ii) z = 20 mm, x = 8 mm
Figure 4.10: An example of (i) a measured waveform and (ii) the frequency spectrum at the focal point, in this case at z = 20 mm, and x = 0 mm
Figure 4.11: The measured peak-to-peak pressure along a line at a constant distance of z = 20 mm from the array
Figure 4.12: A comparison of the theoretical and experimentally FWHM achieved using a phased array at various focal points in the field
Figure 4.13: A comparison of the theoretical and experimentally normalised maximum pressure achieved using a phased array at various focal points in the field
Figure 4.14: A comparison of theoretical and experimental field plots, for (i) an unphased source, and (ii) phasing through as angle of 15°
Figure 4.15: The apparatus used to perform a rotational scan
Figure 4.16: A comparison of the theoretical and experimental directivity of an array steered by (i) 0°, (ii) 10°, and (iii) –10°
Figure 4.17: A comparison of the theoretical and experimental directivity of an array steered by (i) 20°, (ii) 30°, (iii) 40° and (iv) 50°
Figure 4.18: A comparison of the theoretical and experimental directivity of a single element

Chapter 5: A theoretical model for the effect of a finite-size receiver

Figure 5.1: Arc subtended at the projection of point P onto the plane of the piston
Figure 5.2: Definition of angles in the z = 0 plane
Figure 5.3: Region Segmentation, Whole Piston Approach
Figure 5.4: Region Segmentation for edge AB
Figure 5.5: Angle constant along line parallel to edge
Figure 5.6: Corner limited integration, when the receiver is crossed by both A`, and B`
Figure 5.7: Corner limited integration split into two parts for edge AB
Figure 5.8: Dimensions used in deriving corner limited integral
Figure 5.9: Receiver at various time intervals

Figure 5.10: Demonstrating the need to define an edge limited integral
Figure 5.11: Active area for an edge limited integral
Figure 5.12: Edge limited integral
Figure 5.13: Regions and Sectors
Figure 5.14: An example of segmentation, the whole receiver (i), is divided into four parts: (ii), (iii), (iv) and (v)
Figure 5.15: Labelling of the source
Figure 5.16: An example in Region 2 for Edge 1
Figure 5.17: Example in Region 3, for Edge 4
Figure 5.18: Edge 4, point 1 and point 2
Figure 5.19: Two Points within Region 4 for (i) point P, and (ii) point Q
Figure 5.20: Amending the Plane contribution
Figure 5.21: The pressure field from a single element, for (i) a point receiver, and for (ii) a 0.5 mm, (iii) a 1 mm and (iv) a 2mm square receiver
Figure 5.22: The pressure field from a 16 element array focussed at $z = 20$ mm, for (i) a point receiver, and for (ii) a 0.5 mm, (iii) a 1 mm and (iv) a 2mm square receiver
Figure 5.23: A cross-section through the pressure field at z = 20 mm, for (i) a single element, and (ii) a 16 element array focussed at z = 20 mm, for in both cases a point receiver, and receivers measuring 0.5, 1, and 2 mm square
Figure 5.24: Field scan coordinate system
Figure 5.25: A comparison of predictions from the Finite Receiver model with those from a grid of points approach, using a 5mm square source and a 5mm square receiver: V is the velocity waveform at the source surface, (i) shows the impulse response, and (ii) the pressure waveform
Figure 5.26: A comparison of the Finite Receiver model with a grid of points approximation, at three field points
Figure 5.27: Reversing transducers
Figure 5.28: Increasing x from 0 to 28mm in 4mm steps, for (i) a finite receiver, and (ii) a point receiver
Figure 5.29: The effect on pressure amplitude of a finite receiver
Figure 5.30: Comparison of receiver sizes, with varying z on axis
Figure 5.31: The effect on the maximum pressure amplitude of varying the shape of the receiver
Figure 5.32: Experimental Apparatus
Figure 5.33: 5 mm square source and 0.5 mm square receiver, (i) experimental, (ii) theoretical for finite receiver
Figure 5.34: 5 mm square source and 4mm square receiver, (i) experimental and (ii) theoretical
Figure 5.35: Theoretical field for a 5 mm square source and a point receiver
Figure 5.36: 6mm × 4 mm source and 1 mm × 8 mm receiver (x,y), (i) experimental and (ii) theoretical field plots
Figure 5.37: 6 mm × 4mm source and 8mm × 1mm receiver (x,y), (i) experimental and (ii) theoretical
Figure 5.38: Theoretical field for a point receiver from a 6×4 mm source

Chapter 6: Focussing in air using a parabolic mirror

Figure 6.1: Variables used to model a circular source
Figure 6.2: (i) Schematic and (ii) photograph of the device used in this work

Figure 6.3: Definition of terms used to define the reflecting mirror

Figure 6.4: The impulse response at eleven points on the mirror, and the resulting total scalar response and pressure waveforms at two points in the field, the first being the focal point, and the second displaced by 1mm. (i) shows the eleven points, (ii) the scalar impulse response at each of the points, (iii) shows the total impulse response at the focal point, and (iv) shows the resulting waveform, (v) shows the total impulse response at 1 mm from the focal point, and (vi) the corresponding pressure waveform

Figure 6.5: The velocity waveform of the piston used in the simulation of a 500kHz toneburst

Figure 6.6: Experimental apparatus

Figure 6.7: Comparison of (i) experimental and (ii) theoretical results with 500 kHz toneburst drive signal

Figure 6.8: Comparison of (i) experimental and (ii) theoretical results with 1 MHz toneburst drive signal

Figure 6.9: Comparison of (i) experimental and (ii) theoretical results with a broadband drive signal centred at 625 kHz

Figure 6.10: Comparison of (i) experimental and (ii) theoretical results with a 500kHz toneburst, in the *uw* plane passing through the focal point.

Figure 6.11 Mirror shape used to simulate the experimental device, (i) wireframe, (ii) cross section through the x =0 plane, (iii) contour plot.

Figure 6.12: Through transmission scan of a composite plate (axes in mm)

Figure 6.13: The experimental apparatus used for a through transmission scan

Figure 6.14: A comparison of the predicted pressure field of three different mirror diameters, displayed as wireframe and image plots

Figure 6.15: The cross section of the larger and smaller mirrors

Figure 6.16: A comparison of the predicted pressure field from three mirror with focal points located at different y_f values, displayed as wireframe and image plots

Figure 6.17: The cross section of two mirror with a different y_f value

Figure 6.18: A comparison of the predicted pressure field from three mirrors with focal points located at different z_f values, displayed as wireframe and image plots

Figure 6.19: The cross section of two mirrors with a different z_f value

Figure 6.20: Contour plots of the focal point for five mirrors defined by different focal points

Chapter 7: Imaging with ultrasonic capacitive arrays

Figure 7.1: Experimental apparatus used to establish that each element acts independently

Figure 7.2: The received waveform from each element, numbered from 1 to 16

Figure 7.3: Schematic of a large source fired at an array receiver

Figure 7.4: Analysing the origin of the secondary waveform

Figure 7.5: The peak-to-peak amplitude measured by each element, (i) for the case described above, and (ii) when the array is rotated about the axis by 180°

Figure 7.6: The backplate of a 2-D array

Figure 7.7: The apparatus used to create a through-thickness image using a 2-D array

Figure 7.8: Image of a defect in a composite plate obtained using a static 2-D array, taken using (i) time of flight and (ii) amplitude
Figure 7.9: Simulating a larger 2-D array by stepping a small receiver
Figure 7.10: A 25 mm square defect imaged using a simulated 2-D array, of 23× 23 elements each measuring 2 mm square on a pitch of 2.2 mm, taken using (i) time of flight and (ii) the maximum amplitude using a tight time window
Figure 7.11: A 25 mm square defect imaged using a simulated 2-D array, of 41× 41 elements each measuring 1 mm square on a pitch of 1.5 mm, taken using (i) time of flight and (ii) the maximum amplitude using a tight time window
Figure 7.12: A (i) photograph and (ii) schematic of a combined phased source and receiver transducer
Figure 7.13: A simulation of the pressure field emerging from the split source
Figure 7.14: Apparatus used to line scan the phased source
Figure 7.15: A theoretical and experimental line scan through the focal point of the phased source
Figure 7.16: Experimental apparatus used for scanning reflecting surfaces
Figure 7.17: A theoretical and experimental line scan of the reflection of a 0.5 mm diameter wire
Figure 7.18: A line scan of a 1 mm step in a aluminium sample
Figure 7.19: The paths travelled between source and receiver via a field point
Figure 7.20: Experimental apparatus used to image a 3 mm bar
Figure 7.21: An image of a 3 mm bar using a source located at 90° to the receiver array, using both a (i) SAFT and (ii) ellipse crossing method using a broadband drive signal
Figure 7.22: The waveforms reflected by a 3 mm diameter bar, when a source at 90° to the receiver array is used with a broadband drive signal
Figure 7.23: An image of a 3 mm bar using a source located at 90° to the receiver array, using both a (i) SAFT and (ii) ellipse crossing method using with a chirp drive signal
Figure 7.24: The cross-correlated waveforms reflected by a 3 mm diameter bar, when a source at 90° to the receiver array is used with a chirp drive signal
Figure 7.25: An image of two wires using a source located at 90° to the receiver array, using both a (i) SAFT and (ii) ellipse crossing method using with a chirp drive signal
Figure 7.26: The cross-correlated waveforms reflected by two wires, when a source at 90° to the receiver array is used with a chirp drive signal
Figure 7.27: Experimental apparatus used to image a 3 mm bar using a combined source and receiver device
Figure 7.28: An image of a 3 mm bar obtained using a combined source and receiver transducer, using (i) SAFT, and (ii) ellipse crossing
Figure 7.29: The waveforms reflected by a 3mm bar, when a source parallel to the receiver array is used with a broadband drive signal

Appendix A: Phasing for 2-D array beam-steering

Figure A.1: The geometry of 2-D array beam-steering

List of tables

Chapter 2: Review of air-coupled technology

Table 2.1: Acoustical properties of some piezoelectric materials

Chapter 3: Theoretical predictions for phased arrays

Table 3.1: Location of four points surrounding the focal point

Chapter 5: A theoretical model for the effect of a finite-size receiver

Table 5.1: Overview of finite receiver model
Table 5.2: Piston considered as a whole
Table 5.3: Piston considered as series of edges
Table 5.4: Dimensions within each time period
Table 5.5: Segmentation of receiver
Table 5.6: Subdivision of the receiver within Region 4
Table 5.7: Angles subtended at Point P and Q
Table 5.8: Location and Size constants
Table 5.9: C_a and C_b
Table 5.10: C_c and C_d
Table 5.11: Exceptions for t_p^{end}
Table 5.12: A schematic table of the steps required for an algorithm
Table 5.13: Comparison of running time

Acknowledgements

I would like to thank Professor D. A. Hutchins for his excellent supervision, and support throughout. I would also like to thank Dr D. R. Billson, and my collegues J. S. McIntosh, D. W. Choi, T. J. Robertson and T. H. Gan for their help and encouragement. I am also grateful to F. Courtney for his willingness to bond CMUT probe tips at short notice.

I would like to thank Beate for her endless support and encouragement throughout the course of this work, and our daughter, Juliana, for making the final four months much more enjoyable and providing plenty of distractions.

Adrian Neild, January 2003

Declaration

The work presented in this thesis has been carried out by the author, except where otherwise stated. It has been performed in the School of Engineering, at the University of Warwick. No part of this work has previously been submitted to the University of Warwick, or any other academic institution for consideration for a higher degree. All publications to date arising from this work are listed prior to the appendices.

Adrian Neild, January 2003

Summary

The work described in this thesis is based on an investigation into ultrasonic air-coupled capacitive arrays. Much of the work has involved the theoretical modelling of pressure fields, which has been achieved by taking the Impulse Response method, and utilising it in novel ways. In addition, polymer-membrane capacitive ultrasonic arrays have been constructed, and have been used experimentally in both beam-steering and focussing modes of operation. In both cases, the resulting pressure field was measured. It is shown that the theory accurately predicts the experimental observations.

A model is developed which is capable of predicting the pressure field of a rectangular source, as measured by a finite-sized receiver. This novel method treats the problem in a new way, which allows an integration to be performed over the area of the receiver. Previously it has only been possible to model two circular transducers coaxially aligned. The model is used to identify a receiver, which can be used to measure the highly focussed pressure field from a phased array, with only a negligible effect due to the receiver size. Predictions from the model are compared to experimental data, and show a good correlation.

A parabolic mirror used to focus the field from a circular device in air has been studied, and a model developed to predict the pressure field produced by this device. This is done by an approximation of the mirror surface to a grid of finely spaced points. The model correlates well with measured results. In addition, an image of a defect in a solid sample was produced.

Arrays are then used to image solid samples in air. This is done using three techniques. The first is a combined phased source and receiver, which is shown to locate a wire accurately and to measure a step in the surface of a sample. A 2-D array is shown to image a defect in a composite plate, and the potential for a fast through-transmission air-coupled system is indicated. In addition, two post-processing techniques are used on data recorded using an array receiver, to locate an object in air. Of these two techniques, ellipse crossing is shown to have better results for large signal to noise ratios, and SAFT for lower ratios.

The combination of theoretical modelling and experimental observations has indicated that the transducers and arrays constructed for use in air are well-understood, and that their characteristics can be predicted.

Chapter 1: Introduction

1.1 Introduction

Sound arises from the oscillation of particles, and the resultant propagation of a wave through the medium concerned. Sound waves can have a periodicity, and hence be classified by their frequency, f, which is related to the speed of sound, c, and the wavelength, λ, by

$$f = c/\lambda . \tag{1.1}$$

When a sound wave has a frequency above 20 kHz it is termed ultrasound, as it is outside the human auditory range.

Ultrasound has a wide range of applications, including medical diagnostics, echolocation such as used by bats whilst in flight, and in SONAR (SOund Navigation And Ranging) where submerged vessels or shoals of fish can be detected. In addition, it can be used to test many mechanical properties, such as position, thickness, surface profile and material properties, and can be used in non-destructive testing (NDT) to detect flaws within materials.

1.2 Basic properties of sound

As the sound passes through a medium, variations in acoustic pressure occur, and these are related to the acoustic particle velocity, v and the acoustic impedance of the medium, Z, according to

$$p = Zv \tag{1.2}$$

This is analogous to Ohm's law, $V = IR$, where V corresponds to p, I to v, and the resistance, R, to Z. The acoustic impedance of a medium is expressed as

$$Z = \rho c, \tag{1.3}$$

where ρ is the density and c is the propagation speed of sound through the medium.

Sound waves can propagate in several different ways, although not all types of medium, whether gaseous, liquid or solid, can support all wave types. When the motion of the particles is parallel to the direction of propagation the wave is termed a longitudinal wave, the movement of the particles causes areas of rarefaction and

compression along the length of the wave. This type of wave can occur in any propagation medium.

In solid substances, where each particle is constrained to a position of rest by elastic forces, other wave types can be present. When the direction of oscillation of the particles is perpendicular to the propagation direction, a transverse wave exists, and the sound wave is sometimes termed a shear wave.

The speed of a longitudinal wave is related to the medium properties through which it travels by

$$c_L = \sqrt{\frac{E}{\rho}.\frac{1-\mu}{(1+\mu)(1-2\mu)}}, \tag{1.4}$$

and the speed of a shear wave is given by

$$c_T = \sqrt{\frac{G_s}{\rho}} = \sqrt{\frac{E}{\rho}.\frac{1}{2(1+\mu)}}, \tag{1.5}$$

where in both cases E is the Young's modulus, ρ the density, μ the Poisson's ratio, and G_s the shear modulus [1].

The speed of sound in air has been the topic of much work. It is effected by parameters such as frequency, humidity, temperature and pressure [2]. The relationship with temperature, can be expressed as

$$c = c_0 + \gamma\theta, \tag{1.6}$$

where c_0 is the speed of sound in air at atmospheric pressure at 273° K (331.0 ms^{-1}), γ is the temperature coefficient (0.61 for air), and θ is the temperature difference from 273° K [1]. This yields a result of $c = 343.2\ ms^{-1}$ at room temperature and pressure. An equation which relates speed of sound in gaseous air to temperature and pressure, and which has been fitted to measured data [3, 4], yields a result of $c = 342.8\ ms^{-1}$. For this work a value of $c = 343\ ms^{-1}$ will be used.

Other types of waves occur at interfaces between two media. At the free boundary of a solid a Rayleigh wave can occur [5], in which the particles move in an elliptical trajectory, which attenuates with depth. A Rayleigh wave has components of both transverse and longitudinal motion [6]. Lamb waves can occur in plates, where motion of the two surfaces is coupled together. Again, displacements occur both perpendicular and parallel to the direction of propagation. There are two types of Lamb wave, asymmetric and symmetric, and they can occur in numerous modes depending on

the plate thickness in relation to the wavelength [7]. As this thesis concentrates on the propagation of sound through air, a more detailed knowledge of these waves is not presented, but can be found in the references cited.

1.3 Propagation of sound across an interface

When a planar sound wave, (a wave in which the phase of oscillation is the same at any point in a plane), crosses an interface between two materials of different acoustic impedance, some of the energy of the wave is reflected and some is transmitted. When the incidence of the wave is normal to the interface, the intensity of the two waves can be expressed in terms of the acoustic impedances of the initial medium of propagation, Z_1, and that of the medium which the sound wave meets, Z_2. A coefficient can be expressed for the ratio of intensity in the second medium to the intensity in the first medium. The transmission coefficient is

$$T = \frac{4Z_1Z_2}{(Z_1+Z_2)^2} \tag{1.7}$$

and the coefficient of reflection is

$$R = \left(\frac{Z_1 - Z_2}{Z_1 + Z_2}\right)^2. \tag{1.8}$$

If the two materials have the same acoustical impedance, then it can be seen that the transmission coefficient is 1 and the reflection coefficient is 0, and so the wave passes unaltered through the interface.

When a planar wave meets an interface at an angle α, some part of the wave will be reflected and some part refracted. If the angle of incidence is measured from the normal to the interface, the part of the wave that is transmitted into the second medium will be refracted at a different angle and this angle can be found using Snell's law:

$$\frac{\sin\alpha}{\sin\beta} = \frac{c_1}{c_2} \tag{1.9}$$

where α is the angle of incidence, β is the angle of emergence, and c_1 and c_2 are the speeds of sound in the first and second materials respectively, as shown in Figure 1.1 for the case of $c_2 > c_1$.

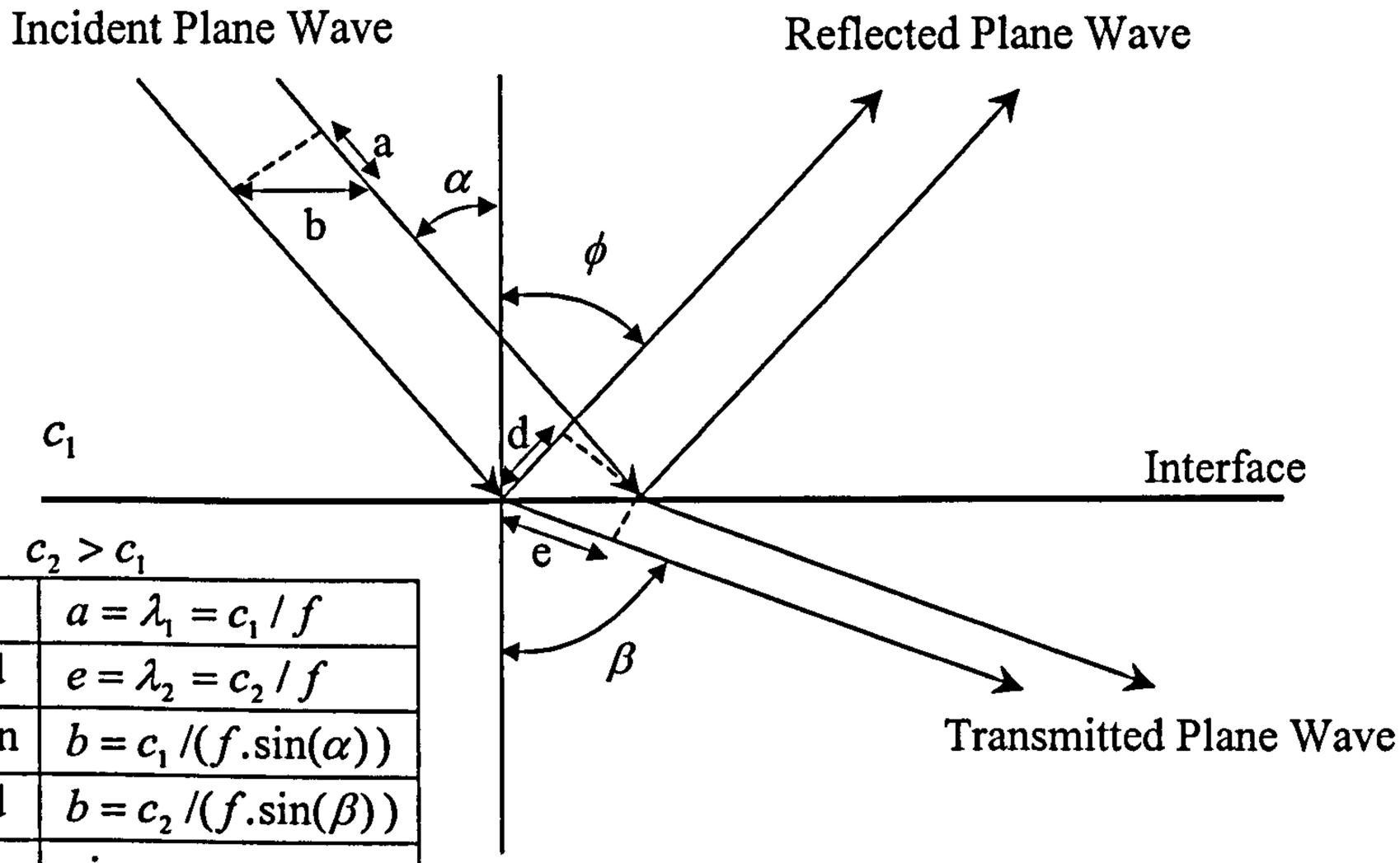

$c_2 > c_1$

If	$a = \lambda_1 = c_1 / f$
and	$e = \lambda_2 = c_2 / f$
then	$b = c_1 /(f.\sin(\alpha))$
and	$b = c_2 /(f.\sin(\beta))$
∴	$\frac{\sin\alpha}{\sin\beta} = \frac{c_1}{c_2}$

Figure 1.1: Snell's law

At an interface, where one or both of the media support shear wave propagation, mode conversion can also occur, where a longitudinal wave can be converted to a shear wave, or vice versa. As the longitudinal wave has a different speed to a shear wave, the angle of refraction for each will differ, as will the angle of reflection. If no mode conversion takes place then φ in Figure 1.1 will equal α. The longitudinal wave has a higher speed than that of the shear wave, and so is refracted at the greater angle from the normal.

1.4 Attenuation

As the sound wave propagates through the medium there will be energy dissipation, termed attenuation. In the case of ultrasonic systems attenuation can be divided into three main types. These are absorption by the medium of propagation, diffraction and scattering. Of these, diffraction will be considered in more detail in the next section.

Scattering occurs within materials which are not homogeneous, because in the bulk of this type of material different acoustic impedances are present. As explained in the previous Section, such mismatches of impedance can cause reflection, and hence signal loss.

The mechanisms of absorption losses are numerous, but they can be broadly classified as classical losses which occur due to the conversion of kinetic energy into heat due to viscous and thermal losses, and relaxation losses where the kinetic energy is converted into internal energy within the particles constituting the medium [8]. The relaxation losses for air can be divided into a rotational loss and vibrational relaxation losses in nitrogen, and oxygen (the principle gasses constituting air). At frequencies between 500 kHz and 20 MHz, however, the absorption is dominated by a combination of classical and rotational losses and hence other factors can be ignored. This approximation worsens as the frequency drops below 500 kHz. An empirical expression for the absorption due to classical and rotational losses, α_{cr} has been found to be:

$$\alpha_{cr} = \frac{15.895\times10^{-11}\left(\frac{T}{T_0}\right)^{1/2} f^2}{\left(\frac{P}{P_0}\right)} \text{ dB/m} \qquad (1.10)$$

where f is the frequency, T and P are the measured temperature and pressure respectively, T_0 is the reference temperature of 293.15^0 K, and P_0 is the reference pressure of 101.325 kPa. This expression is true for a temperature range of 0 to 40 ^0C, and for pressures below 200 kPa [9].

In the modelling of pressure fields done in this work, this equation has been used to compensate for absorption in certain measurements.

1.5 Diffraction due to a finite sized source

Huygens' principle states that every point on a primary wavefront, (i.e. a wavefront over which the phase is constant) is the source of a secondary spherical wavelet, such that at a later time point the primary wavefront is the envelope of these wavelets. This means that an oscillating point source causes a spherical wave to propagate in a homogeneous medium [10]. Two models of the pressure field from a finite sized source are presented in this Section, and this is the underlying principle used in both of them.

1.5.1 Farfield approximation

If two point sources, which are driven in-phase by the same waveform are considered, then at any position in the radiating field the signal present will be the sum of the waves emitted by the two sources. In some places, the difference in path lengths from the two sources will be such that the waves will add constructively, resulting in a larger amplitude than from a single point, and at others the waves will add destructively so the amplitude will be reduced. At large distances from a line source, the directivity can be found using the differences in path length to a point in the field [11]. As the restriction has been imposed that the distance from the source must be large, it can be assumed to be approximately the same for all points on the source, so the dispersive nature of each point source along the line with distance can be ignored. The directivity of the line source is usually expressed as the pressure against angle, which is displayed as a polar plot. The variables, which are necessary to find the directivity of a line source are shown in Figure 1.2.

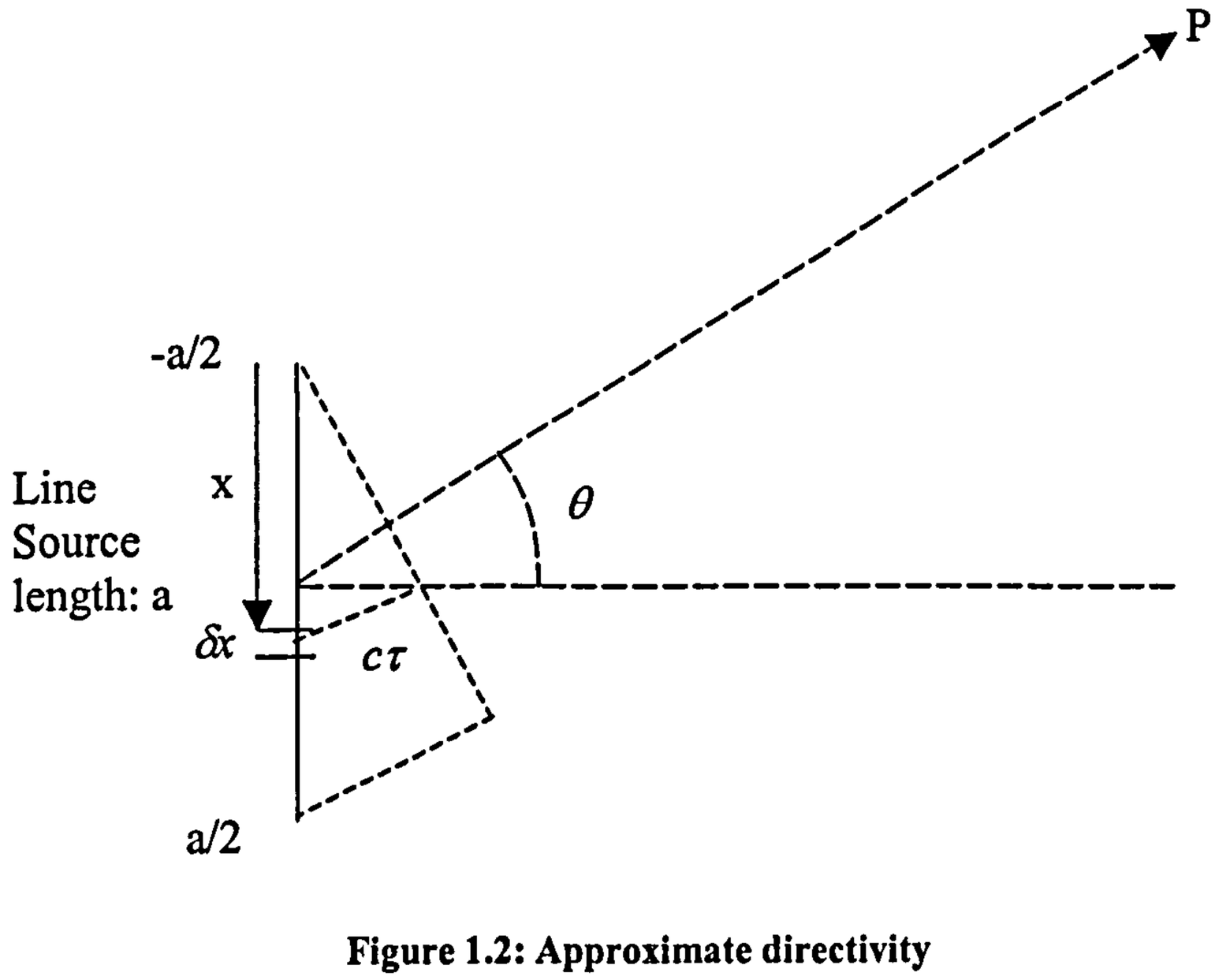

Figure 1.2: Approximate directivity

When the line source emits a sinusoidal signal, then the pressure arriving at point P, per unit length of source, is found by,

$$P = \frac{1}{a}\int_{-a/2}^{a/2} \sin(2\pi.f(t-\tau))dx \tag{1.11}$$

where τ is the relative time difference, found by,

$$\tau = \frac{x\sin\theta}{c} \tag{1.12}$$

Performing this definite integral and manipulating using trigonometric identities gives the result

$$P = \frac{\lambda.\sin(2\pi.ft)}{\pi.a\sin\theta}.\sin(\pi.a\sin\theta/\lambda). \tag{1.13}$$

When expressed as a normalized peak-to-peak pressure, the directivity becomes:

$$D(\theta) = \left|\frac{\sin(\pi.a\sin\theta/\lambda)}{\pi.a\sin\theta/\lambda}\right|, \tag{1.14}$$

which is the same result as obtained by Wooh [12].

1.5.2 Impulse Response method

In order to predict the pressure for all areas of the field from a finite-sized source, a different method needs to be used. A finite source of sound can be considered as an area consisting of points, all emitting sound in the way described by Huygens' principle. In this way, the pressure field can be modelled using a surface integral over the area of the source. There are several ways this problem can be tackled [13]. In this work a convolution method, based on the Rayleigh surface integral, will be used, an approach sometimes called the Impulse Response method. The approach used assumes that the source acts as a planar piston, meaning that across the face of the source the movement is uniform, and that the rest of the plane (to infinity) within which the face of the source lies, termed the baffle, is rigid. In addition, the medium is assumed to be nondissipative, isotropic and homogeneous, so that the only attenuation mechanism considered is diffractive. Rayleigh stated that the time-dependent velocity potential, $\phi(\bar{r},t)$ is

$$\phi(\bar{r},t) = \int_s \frac{v(t-R/c)}{2\pi R}dS, \tag{1.15}$$

where $v(t-R/c)$ is the normal velocity across the area of the source within the plane it moves, $\bar{r}$ is the vector which defines the point at which ϕ occurs at time, t, and R is

the distance from the point to the surface element, dS, of the source under consideration, as can be seen in Figure 1.3 [5].

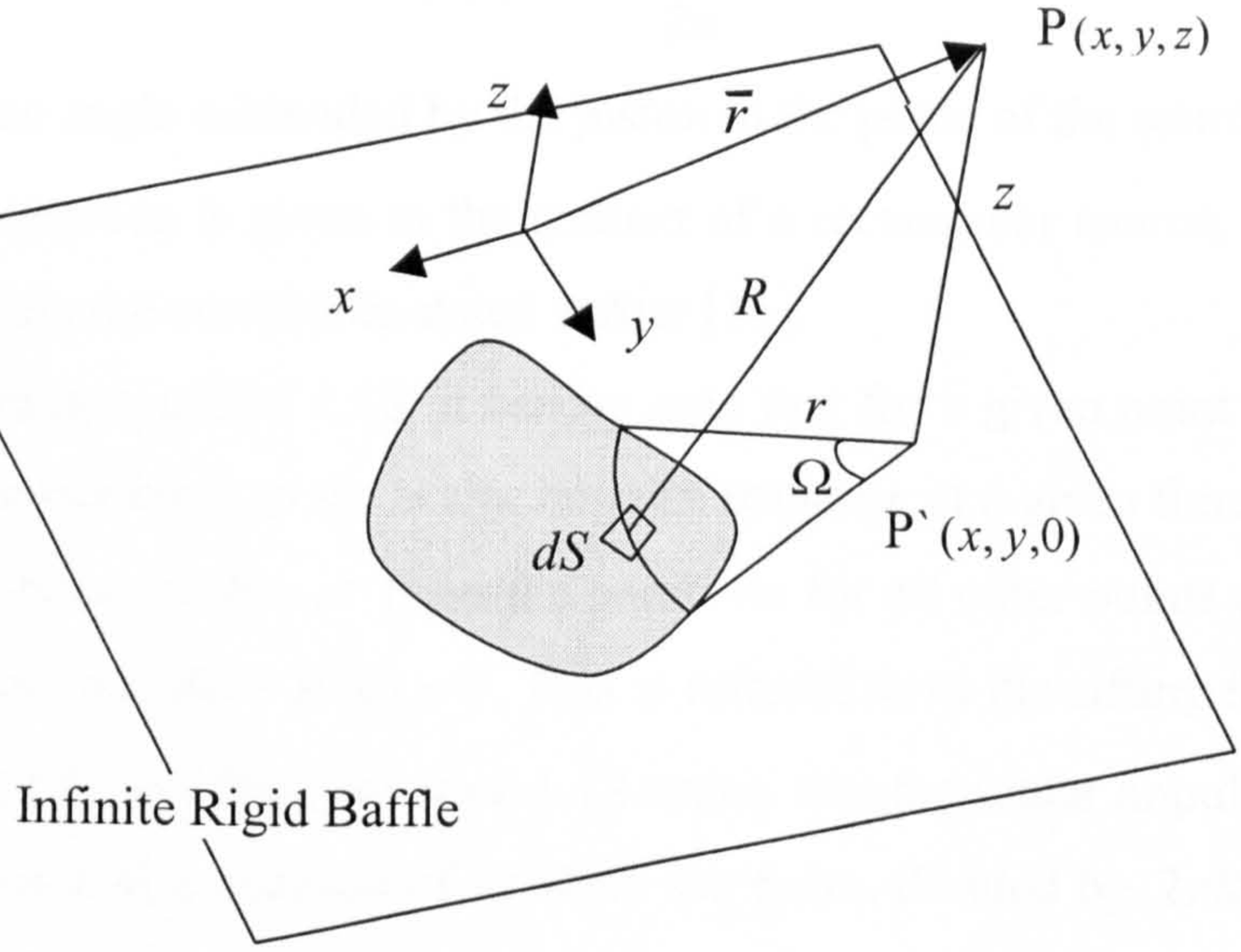

Figure 1.3: Arbitrary shaped source in an infinite baffle

The velocity potential is related to the pressure by

$$p(\bar{r},t) = \rho \frac{\partial \phi(\bar{r},t)}{\partial t} \tag{1.16}$$

It should be noted that although the work in this thesis assumes that the velocity of the source is planar, the Rayleigh integral can be used for non-uniform source velocities profiles [14].

By the use of the Dirac delta function and convolution operator, the problem can be expressed in any of three ways,

$$\begin{aligned} p(\bar{r},t) &= \rho \frac{\partial [v(t) * h(\bar{r},t)]}{\partial t} \\ &= \rho \frac{\partial [v(t)]}{\partial t} * h(\bar{r},t) \\ &= \rho . v(t) * \frac{\partial [h(\bar{r},t)]}{\partial t} \end{aligned} \tag{1.17}$$

where $v(t)$ is the velocity of the source, and $h(\bar{r},t)$ is the scalar impulse response generated by a movement of the source which follows a Dirac delta function, and so is given by,

$$h(\bar{r},t) = \int_S \frac{\delta(t - R/c)}{2\pi R} dS \,. \tag{1.18}$$

San Emeterio [15] stated that this yields the result,

$$h(\bar{r},t) = c.\frac{\Omega(\bar{r},t)}{2\pi} \tag{1.19}$$

where $\Omega(\bar{r},t)$ is the angle subtended by the piston in the plane of the source as shown in Figure 1.3. This equation is given in the context of a rectangular source, but applies to any source satisfying the conditions stated earlier [16].

By examining equation 1.18, it can be seen that for a given point P, the area of the source which contributes to the scalar impulse response at a given time, t, is the area which lies at a distance of $R = ct$ from the point. As for all other points on the source, the Dirac delta function, $\delta(t - R/c) = 0$. This is referred to as the sifting function of the Dirac delta pulse [17]. In effect, equation 1.18 states, that the scalar impulse response is the area of the source at a distance of ct from the point, divided by $2\pi R$. To simplify equation 1.18 to that given as 1.19 the small area in the plane of the piston as R is increased to $R + \delta R$, as shown in Figure 1.4. This area can be found by considering the sphere centred at the point P. The plane of the piston will intersect this sphere, and the line of intersection will be a circle centred at P`. If the coordinate system is set up as shown in Figure 1.3, then if the distance to point P is R then the radius of this circle is $r = \left(R^2 - z^2\right)^{1/2}$, and similarly if the distance to point P is $R + \delta R$ then $r + \delta r = [(R + \delta R)^2 - z^2]^{1/2}$, which means that $r\delta r = R\delta R$.

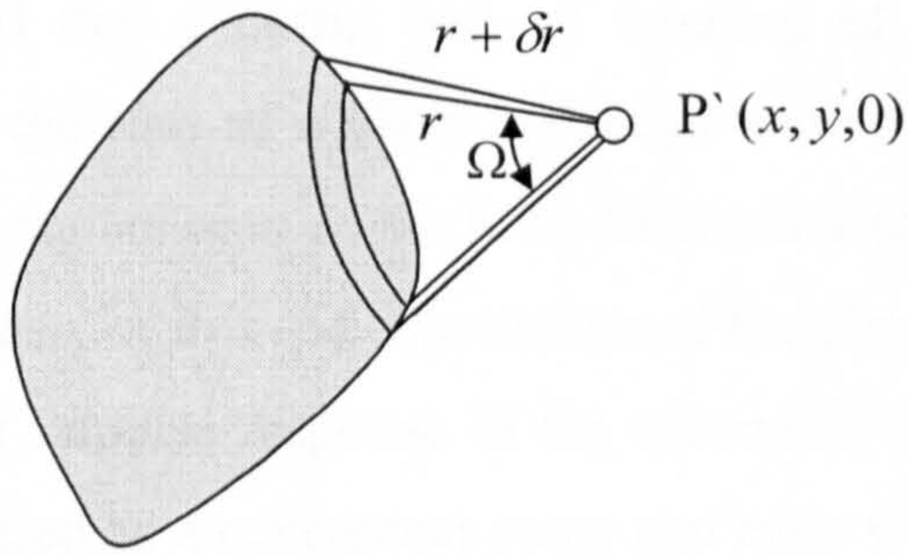

Figure 1.4: Geometry within the plane of the Piston

The small area, δs, considered in Figure 1.4 can be expressed as $\Omega.r.\delta r$ or $\Omega.R.\delta R$. Hence, the surface integral expressed in equation 1.18 can be expressed as an integral with respect to δR over the infinite range of R,

$$h(\bar{r},t) = \int_0^\infty \frac{\delta(t - R/c)\Omega(\bar{r},R).R}{2\pi R} dR \tag{1.20}$$

if $\tau = R/c$ then,

$$h(\bar{r},t) = \int_0^\infty \frac{\delta(t - \tau)\Omega(\bar{r},t).c}{2\pi} d\tau \tag{1.21}$$

As discussed earlier the sifting function of the Dirac delta is such that this integral can be simplified to equation 1.19, where the angle $\Omega(\bar{r},t)$ refers to the angle in the plane of the piston, from the point defined by $\bar{r}$ at radius of $R = ct$, a result which lends itself well to numerical modelling in which subsequent time steps are considered. In this way, the problem is reduced to one of geometry. The result is a time-limited function, where the limits are the shortest and longest path lengths from the point to the source. Some attempts have been made to speed up the computation of the scalar impulse response by the use of linear [18] and quadratic approximations [19], as the time sampling frequency must be quite high, however such approximations have not been found to be necessary in this work.

The Rayleigh integral and convolution approach has been used to produce a numerical model for circular sources [17, 20] and for rectangular sources [15, 20, 21]. In later Chapters, the model for a circular source offered by Stepanishen [17] has been used to model a parabolic mirror used to focus a circular source. The model of a square source offered by San Emeterio [15] has been used to model an array of elements, and the basis of this model has been deconstructed and used to model a finite receiver.

It has been suggested that a useful way of thinking of the scalar impulse response is to consider it as the sum of a plane and edge wave [22]. Equation 1.17 states that the pressure is the convolution of the time differential of the piston velocity with the scalar impulse response, or it is the convolution of the piston velocity with the time differential of the scalar impulse response. If the second of these are considered then the result can be considered as a conceptual plane and edge wave. In Figure 1.5 a circular source has been modelled using the equations given by Stepanishen [17], based on the theory described above. Figures 1.5 (i), (iii), and (v) show the scalar impulse response at a fixed distance (twice the radius of the source) from the plane of the source

and at different radial distances from the axis, being on-axis, 0.6 of the radius, and 1.2 of the radius, respectively. Figures 1.5 (ii), (iv), and (vi) show the difference of the scalar impulse potential over each time step, for the same positions in the field. In Figure 1.5 (ii) the plane and edge wave have been labelled, p and e. In Figure 1.5 (i) it can be seen that the scalar impulse response on axis, is constant at *c*. This is because the time at which the sphere of radius *R* centred at the point on axis first crosses the plane of the source, until the time when the sphere crosses the edge of the source, the subtended arc is 2π. Consequently, the time differential of the scalar impulse response can be considered as a conceptual plane wave and an edge wave. When a point, which is not on axis, is considered the edge wave occurs over a finite period of time as can be seen from Figure 1.5 (iv).

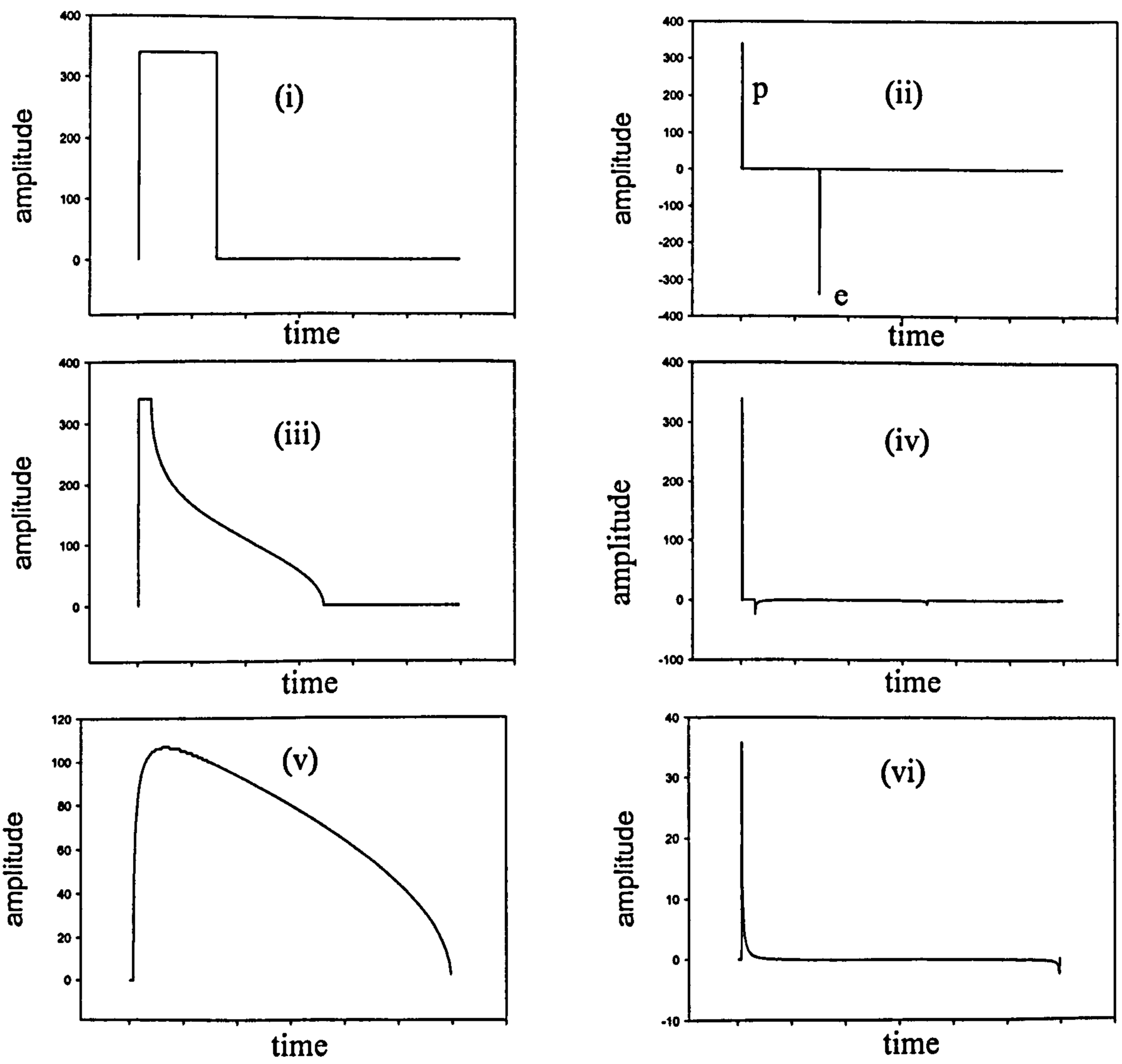

Figure 1.5: Plane and edge waves, (i), (iii), and (v) show the impulse response at different radial distances from the axis, at 0, 0.6 and 1.2 of the radius, respectively. Whilst (ii), (iv), and (vi) show the time derivative of the impulse response over each time step, for the same positions in the field

When the point lies outside the source, the scalar impulse response will rise slowly as the subtended arc rises, reach a maximum and then fall off to zero, as shown in Figure 1.5 (v), (note the vertical scale change). This is considered as an edge wave with no plane wave, as the conceptual plane wave emerging from the source will not pass through a point at a distance off-axis greater than the radius (Figure 1.5 (vi)).

Plane and edge waves have been used as an alternative modelling method to that of finding the angle subtended by the arc which falls on the source face, as it is suggested that it lends itself better to the modelling of more complex polygons [23].

1.6 Nearfield and farfield

The nearfield-farfield boundary is defined as the axial distance from the face of the source at which the last maximum occurs. As a point in the field is moved further from the source whilst remaining on-axis, the effect is that the impulse scalar potential is of the same magnitude and shape but lasts a shorter time period, as the difference between the time from the face and the time to the furthest extremity falls. When thought of in terms of plane and edge waves, the time difference between the two decreases. As shown by equation 1.17, the plane and edge waves must be convolved with the velocity of the piston. By inspection of Figure 1.5 (ii) this convolution, for a circular transducer when on-axis, is reduced to the summation of the piston velocity, to the negative piston velocity offset by a phase lag. The resultant amplitude will vary as this phase lag changes. When the distance is small, the phase lag changes rapidly with incremental steps along the axis, but as the distance from the source becomes larger the phase lag changes less for the same incremental step, until at a certain distance the last maximum occurs. Figure 1.6 shows the axial peak-to-peak for three circular transducers, in each case the distance from the source is measured as a factor of the wavelength of the continuous harmonic drive signal. The diameters of the three sources are 4, 8 and 16 wavelengths. In Figure 1.6 (ii) and (iii) it appears that the pressure does not drop down to 0 at the first few minima this is due to the finite step size used, rather than a real effect.

If the piston velocity is harmonic, with wavelength λ, then at the nearfield-farfield boundary the phase lag is $\lambda/2$. This distance, z_{crit}, can be found for a circular transducer, and similarly for other shaped transducers, as shown in Figure 1.7. Using the

equation given for a circular transducer in Figure 1.7, the nearfield-farfield boundary occurs at a distance of 3.75, 15.75, and 63.75 times the wavelength for transducers of 4, 8 and 16 wavelengths diameter respectively. This can be seen to agree with the location of the final maximum in each case in Figure 1.6.

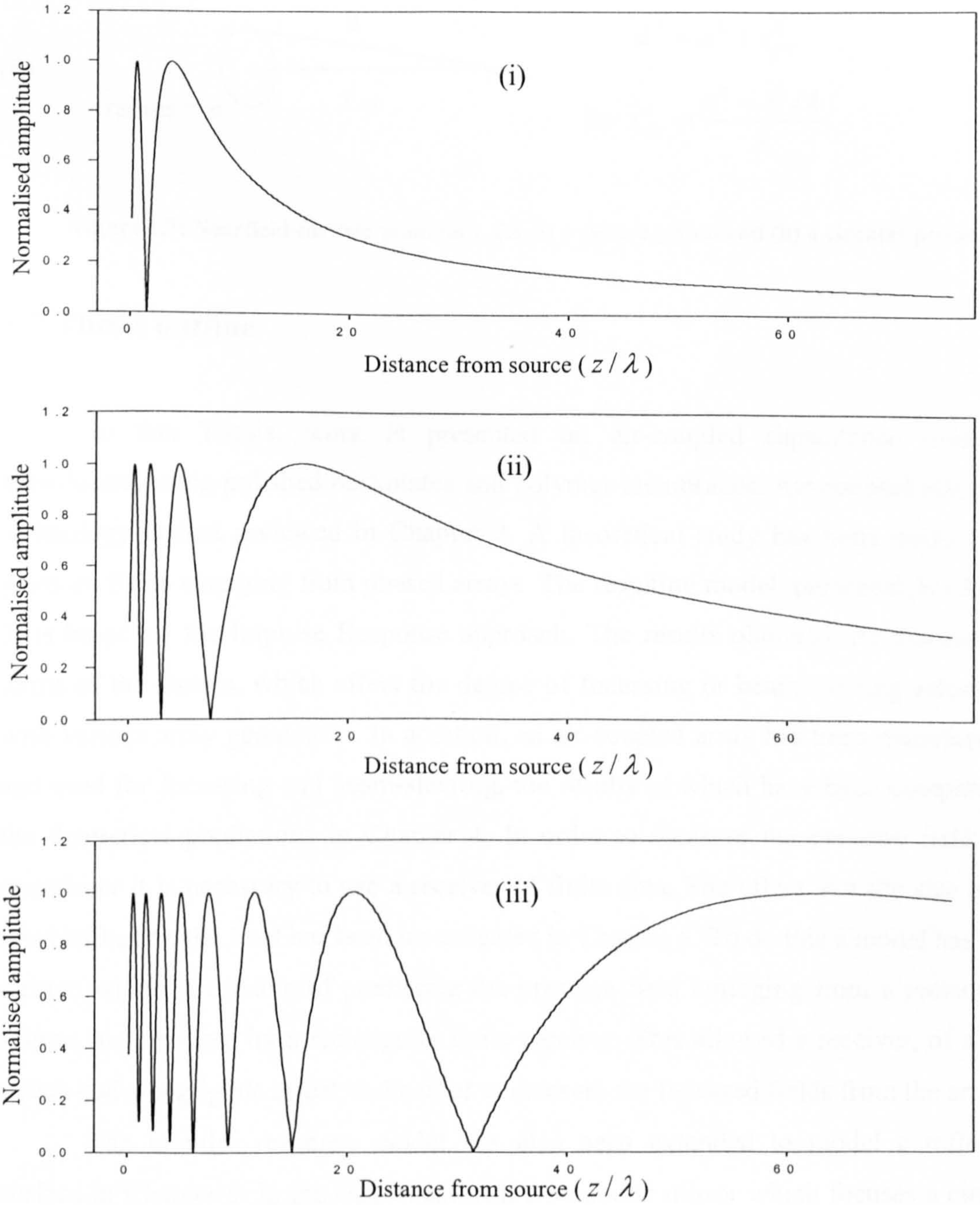

Figure 1.6: Axial plot of normalised pressure amplitude, for a circular source of diameter (i) 4 wavelengths, (ii) 8 wavelengths, and (iii) 16 wavelengths

(i)

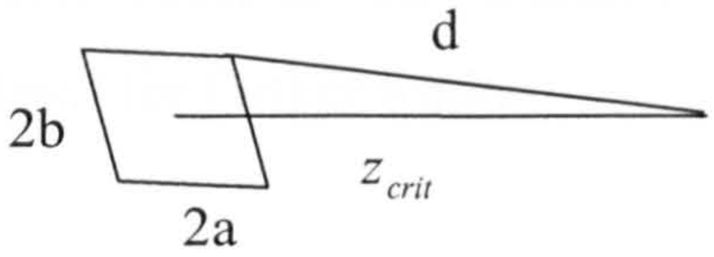

At the nearfield-farfield boundary d= $z_{crit} + \lambda/2$

$$d^2 = a^2 + b^2 + z_{crit}^2$$

So $z_{crit} = \dfrac{a^2 + b^2 - \lambda^2/4}{\lambda}$

(ii)

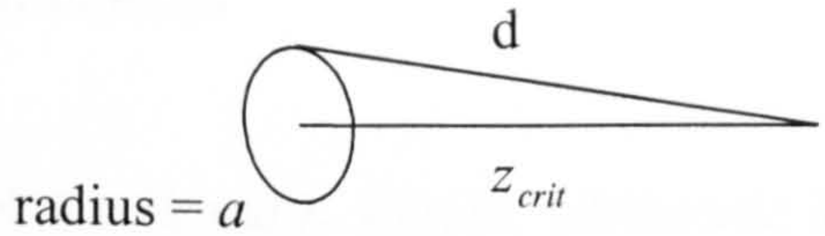

$$d^2 = a^2 + z_{crit}^2$$

So $z_{crit} = \dfrac{a^2 - \lambda^2/4}{\lambda}$

Figure 1.7: Nearfield-farfield boundary, for (i) a square piston and (ii) a circular piston

1.7 Thesis outline

In this Thesis, work is presented on air-coupled capacitance ultrasonic transducers, using polished backplates and polymer-membranes. Air-coupled ultrasonic technology is first reviewed in Chapter 2. A theoretical study has been made of the pressure fields emerging from phased arrays. The resulting model, presented in Chapter 3, is based on the Impulse Response approach. The results obtained are discussed in terms of the factors, which affect the degree of focussing or beam-steering achievable with various array geometries. In addition, an air-coupled array has been manufactured and used for focussing and beam-steering, the results of which have been compared to the theoretical predictions in Chapter 4. In order to measure the pressure field of a transducer it is necessary to use a receiver of finite area. The effect that the size of the receiver has on the field has been investigated in Chapter 5. To do this a model has been written which is capable of predicting the pressure field emerging from a rectangular source, as measured by a rectangular finite receiver. This allowed a receiver, of a size, which had a negligible affect, to be used to measure the focussed fields from the arrays.

The impulse response model has also been extended to model a reflecting surface in Chapter 6. In the case examined, a parabolic mirror which focuses a circular transducer, has been modelled. This allows an investigation of the affect that changing the parameters of the mirror has on the focal point.

Images have been obtained non-destructively, using fabricated polymer membrane arrays. This has been achieved using an array with a large central element,

which acts as a receiver, a 2-D array used for through transmission imaging, and an array used in combination with a large source and post-processing techniques used for object location. These are all described in Chapter 7. This is followed by Conclusions and suggestions for further work.

1.8 References

[1] S. Kociš and Z. Figura, *Ultrasonic Measurements and Technologies*, 1st ed. London: Chapman & Hall, 1996.

[2] R. C. Hart, R. J. Balla, and G. C. Herring, "Optical measurement of the speed of sound in air over the temperature range 300-650 K," *Journal of the Acoustical Society of America*, vol. 108, pp. 1946-1948, 2000.

[3] B. A. Younglove and R. D. McCarty, "Speed-of-sound measurements for nitrogen gas at temperatures from 80 to 350K and pressures to 1.5 MPa," *J. Chem. Thermodyn*, vol. 12, pp. 1121-1128, 1980.

[4] G. S. K. Wong, L. X. Wu, and K. Leung, "Variation of measured sound speeds in gaseous and liquid air with temperature and pressure," *Journal of the Acoustical Society of America*, vol. 108, pp. 662-663, 2000.

[5] J. W. S. Rayleigh, *The Theory of Sound*, vol. 1. New York: Dover Publications Inc., 1945.

[6] I. A. Viktorov, *Rayleigh and Lamb waves - Physical Theory and Applications*: Plenum Press, 1967.

[7] H. Lamb, *The Dynamical Theory of Sound.*, 2nd ed. New York: Dover Publications Inc., 1960.

[8] H. E. Bass, L. C. Sutherland, J. E. Piercy, and L. B. Evans, *Absorption of Sound by the Atmosphere*, vol. XVII,Physical Acoustics, pp145-233. New York: Academic Press, 1984.

[9] L. J. Bond, C. H. Chiang, and C. M. Fortunko, "Absorption of ultrasonic waves in air at high frequencies (10-20 Mhz)," *Journal of the Acoustical Sociey of America*, vol. 92, pp. 2006-2015, 1992.

[10] E. Hecht, *Optics*, 2nd ed: Addison-Wesley Publishing Company, 1987.

[11] R. A. Monzingo and T. W. Miller, *Introduction to Adaptive Arrays*, 1st ed. New York: Wiley, 1980.

[12] S. Wooh and Y. Shi, "Influence of phased array element size on beam steering behaviour," *Ultrasonics*, vol. 36, pp. 737-749, 1998.

[13] G. R. Harris, "Review of Transient Field-Theory for a Baffled Planar Piston," *Journal of the Acoustical Society of America*, vol. 70, pp. 10-20, 1981.

[14] G. R. Harris, "Transient Field of a Baffled Planar Piston Having an Arbitrary Vibration Amplitude Distribution," *Journal of the Acoustical Society of America*, vol. 70, pp. 186-204, 1981.

[15] J. L. San Emeterio and L. G. Ullate, "Diffraction Impulse-Response of Rectangular Transducers," *Journal of the Acoustical Society of America*, vol. 92, pp. 651-662, 1992.

[16] J. Krautkrämer and H. Krautkrämer, *Ultrasonic Testing of Materials*, 4th ed: Springer-Verlag, 1990.

[17] P. R. Stepanishen, "Transient Radiation from Pistons in an Infinite Planar Baffle," *Journal of the Acoustical Society of America*, vol. 49, pp. 1629-1638, 1971.

[18] T. J. Teo, "An improved approximation for the spatial impulse response of a rectangular transducer," *IEEE Transactions on Ultrasonics Ferroelectrics and Frequency Control*, vol. 45, pp. 76-83, 1998.

[19] H. Masuyama, K. Nagai, and K. Mizutani, "Quadratic-curve approximation of impulse responses to calculate radiated fields from rectangular transducers," *Japanese Journal of Applied Physics Part 1-Regular Papers Short Notes & Review Papers*, vol. 39, pp. 3144-3149, 2000.

[20] J. C. Lockwood and J. G. Willette, "High-Speed method for computing the exact solution for the pressure variations in the nearfield of a baffled piston," *Journal of the Acoustical Society of America*, vol. 53, pp. 735-741, 1973.

[21] A. Freedman, "Sound Field of a Rectangular Piston," *Journal of the Acoustical Society of America*, vol. 32, pp. 197-209, 1960.

[22] D. A. Hutchins and G. Hayward, "Radiated Fields of Ultrasonic Transducers," in *Physical Acoustics*, vol. XIX, R. N. Thurston and A. D. Pierce, Eds. London: Academic Press Inc., 1990.

[23] U. P. Svensson, K. Sakagami, and M. Morimoto, "Line integral model of transient radiation from planar pistons in baffles," *Acustica*, vol. 87, pp. 307-315, 2001.

Chapter 2: Review of air-coupled technology

2.1 Introduction

This Chapter outlines the transducers and drive waveforms commonly used in air-coupled ultrasound and some of the applications of this field of study. Particular attention is paid to the development and construction of capacitive devices, as these are used throughout the work contained in this thesis.

2.2 Coupling

The transfer of acoustical energy from the transducer to the surrounding medium is essential for ultrasonic imaging. At each material boundary the efficiency of the energy transfer is dictated by the acoustic impedances of the two materials either side of this boundary (see Chapter 1).

A common method used for contact ultrasonic inspection is to coat a piezoelectric transducer with a couplant material and place it on the test specimen. This couplant reduces problems arising from surface irregularities and contamination of the transducer from dust and dirt. The couplant layer need only have a thickness of one tenth of a wavelength to affect the acoustic properties of the load as seen by the transducer [1]. It is therefore important to choose the couplant on the basis of acoustic impedance as well as taking into considerations such variables as the viscosity, lower viscosity being better for surfaces of high surface roughness, the ease of removal of the couplant from the specimen post-testing, the temperature of the surface and contamination of the surface [2]. Using the contact method has drawbacks such as the need to maintain a good degree of coupling, and although the couplant protects the transducer to a certain degree there is a problem of wear especially when large areas need to be scanned [3].

Another common method of coupling is to use water, either by use of an immersion tank or by ensuring there is a constant flow of water around the transducer. This method allows for automated scanning without wear on the transducer [4, 5]. There are however many materials and industrial manufacture processes where the presence of water will cause damage or inconvenience. In addition the presence of water decreases

the possibility of detecting surface flaws in polymer-matrices and internal flaws in porous materials [6]. Materials such as foam, wood, paper products, many reinforced plastics, propellants, pieces of art and many materials intended for the aerospace industry are not compatible with water [7].

Air-coupled ultrasound allows for rapid scanning without damage to the specimen material [8]. The relatively short wavelengths in air provide the potential for high-resolution imaging as the transducer is more directional [9]. It is a minimally-invasive technique requiring no more contact than the natural environment. This advantage of air-coupled ultrasound has been sufficient to invoke investigation despite considerable drawbacks, primarily the difference in acoustic impedance of air and solid test specimens. At the interface between water and steel, approximately 35% of the signal will be transmitted, however between air and steel this figure drops to approximately 0.5%. In addition, it is necessary to consider the transmission of acoustical energy from the transducer to the air, and the design of suitable transducers will be discussed later in this Chapter. These devices can also be used for gas-flow and spatial measurements.

2.3 Drive signals

Source transducers are driven by an applied voltage, the shape of which is one determinate of the ultrasonic output waveform (another being the frequency response of the device). Three output waveforms will be discussed here, all of which are used in this work.

A toneburst signal is a narrowband signal lasting for several cycles (see Figure 2.1). It can be generated by a voltage input of the same centre frequency. The amplitude is greatly increased if the frequency falls within the natural response of the device. This type of signal is termed narrowband, as it consists of energy distributed over a small frequency range, and is therefore well suited to a highly resonant device. An example of this method being used, is the air-coupled scans reported by Buckley on wood, structural foams and laminate specimens using a resonant piezoelectric transducer [10].

A broadband signal is one in which acoustic energy occurs over a wide range of frequencies. It can be invoked by driving a broadband transducer with a voltage spike, although the output wave shape would then be dependent on the frequency response of

the transducer. A broadband signal and accompanying Fourier transform are shown in Figure 2.2. Both this waveform and that shown in Figure 2.1 have been numerically generated using a formula for the velocity of the piston, used by San Emeterio, which can be written as

$$v(t) = t^3 e^{-Kft} \cos(2\pi ft), \tag{2.1}$$

with values of K being 0.4 and 3.5 respectively [11]. The value of K will be used to describe waveform shapes used for simulations throughout the thesis. A broadband signal of this type has several advantages over a toneburst signal. These include higher resolution capability, better results from some post-processing techniques such as SAFT (see Chapter 7), reduction of the "dead zone" when used in pulse-echo mode, less sidelobes, and a more uniform nearfield [12, 13].

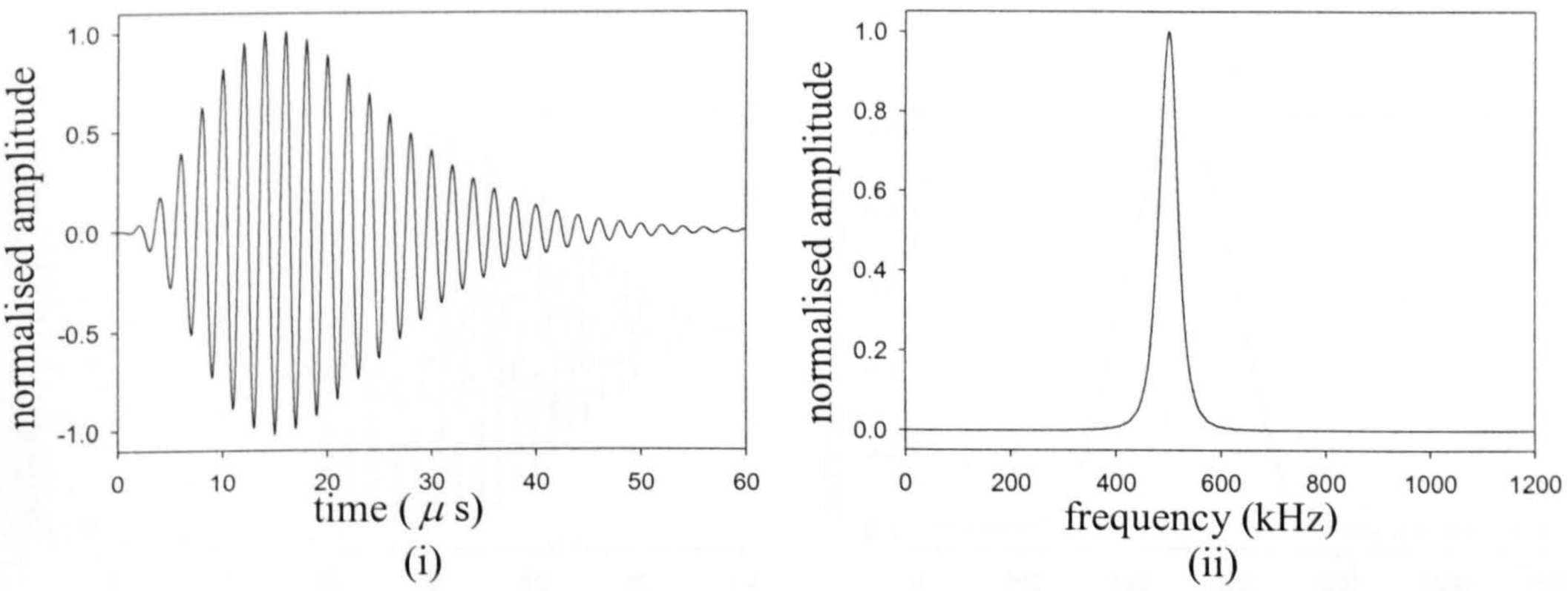

Figure 2.1: Toneburst signal in (i) time, and (ii) frequency domains

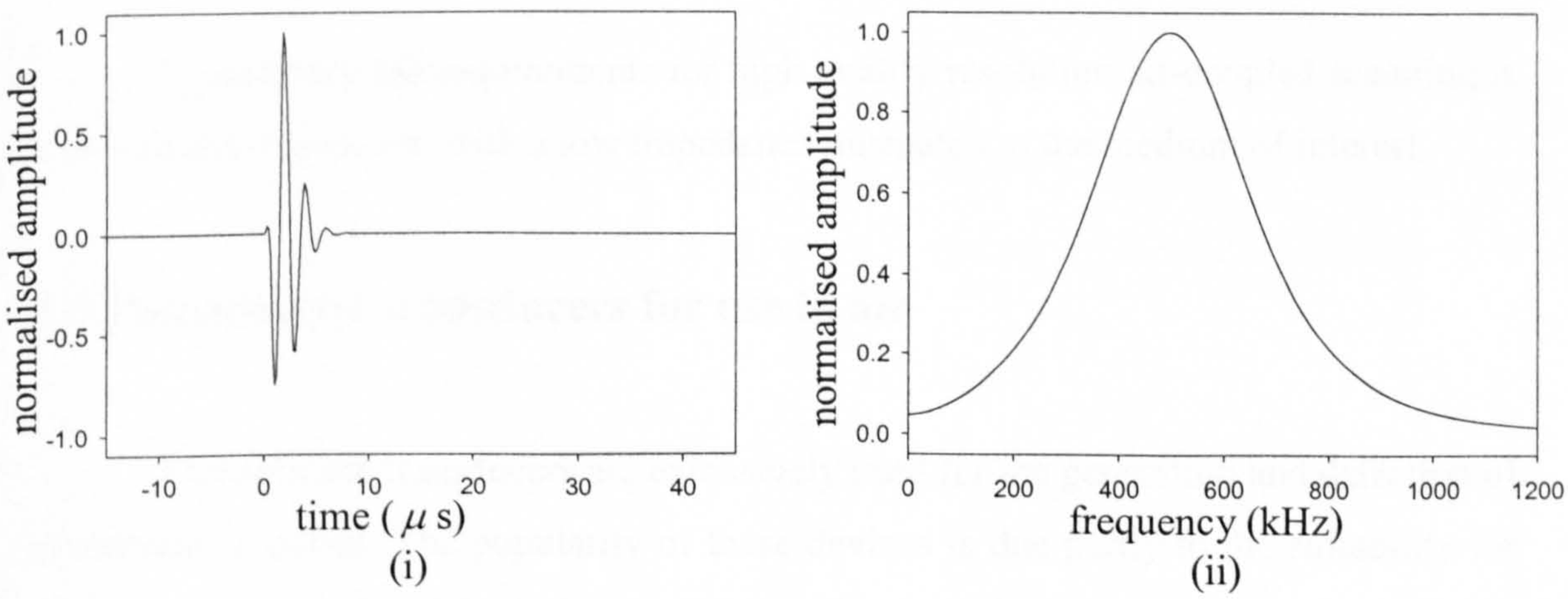

Figure 2.2: Broadband signal in (i) time, and (ii) frequency domains

A chirp signal is one in which the frequency is changed as a function of time. Figure 2.3 shows a chirp signal with a frequency range of between 250 and 750 kHz, and duration of 50 μs, multiplied by a Hanning envelope. This signal requires a broadband transducer as can be seen in the accompanying Fourier transform. The waveform has been numerically generated using

$$P(t) = \frac{1}{2}\left[1 - \cos\left(\frac{2\pi t}{T}\right)\right]\sin\left(2\pi f_s t + \frac{\pi B}{T}t^2\right), \tag{2.2}$$

where, f_s is the lowest frequency, B is the bandwidth and T is the signal duration [14]. By performing the post-processing technique of pulse compression, in which cross correlation of the received signal is performed in the time domain, a large signal-to-noise enhancement is possible [15, 16]. This has allowed the air-coupled testing of materials with a high acoustic impedance such as brass [17], and steel [18].

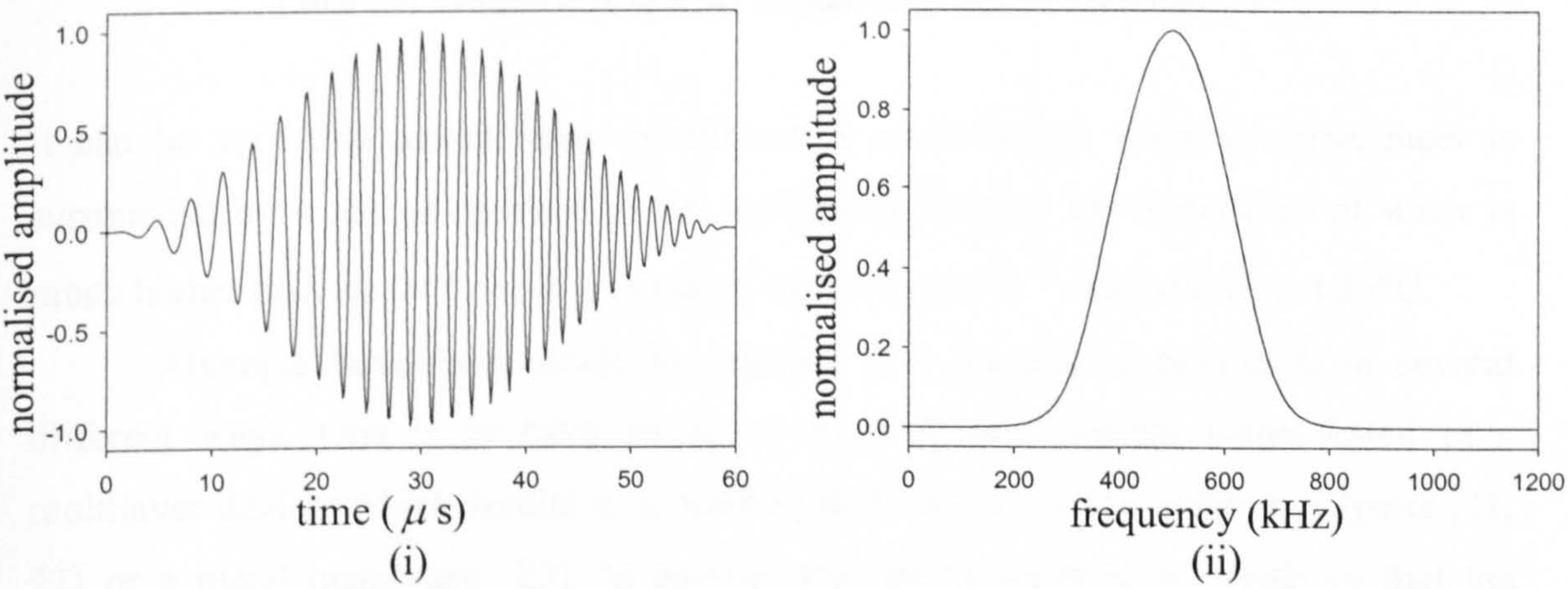

Figure 2.3: Chirp signal in (i) time, and (ii) frequency domains

In summary the requirements for high quality resolution air-coupled scanning is a broadband transducer, with a low impedance mismatch to the medium of interest.

2.4 Piezoelectric transducers for use in air

Piezoelectric transducers are extensively used for the generation and detection of ultrasound in solids. The popularity of these devices is due partly to the suitability for routine use in industrial environments, as the transducers are typically compact, ruggedly designed, efficient and capable of operation in a wide range of temperatures

[19]. However, standard piezoelectric transducers are inefficient when operated in air, due to the high impedance mismatch, which occurs at the boundary between transducer and air. The acoustic impedances (Z) and transmission coefficients (T), calculated using equation 1.7, with water and air are given in Table 2.1.

Material	Density ρ ($kg.m^{-3}$)	Propagation Velocity c_L ($m.s^{-1}$)	Acoustic Impedance Z ($kg.m^{-3}s^{-1}$)	T_{water}	T_{air}
Quartz SiO_2	2650	5760	$15.3x10^6$	0.325	$10.8x10^{-5}$
Zirconate piezoceramic PZT-5A	7750	3880	$30x10^6$	0.181	$5.5x10^{-5}$
Lead-niobate Piezoceramic $PbNb_2 0_6$	5800	2800	$16x10^6$	0.313	$10.3x10^{-5}$
Piezopolymer PVDF	1780	2260	$4.6x10^6$	0.742	$35.9x10^{-5}$

Table 2.1: Acoustical properties of some piezoelectric materials [20]

It can be seen that transmission coefficient is much higher when the transducer is surrounded by water as opposed to air, and this is because the impedance of water is much higher than air, at $1.5x10^6$ compared to 414 $kg.m^{-3}s^{-1}$ respectively, at 20°C.

Attempts have been made to improve this impedance mismatch in several different ways. One is to have an active piezoelectric element incorporated in a multilayer device, which results in a bending motion [12], using either a polymer [21, 22] or a metal membrane [23]. In another attempt to combine materials so that the matching problems are reduced, a conical shell is attached to a piezoelectric ring which when driven causes flexural motion in the cone wall, and this lamb wave leaks energy into the air [24].

A common approach has been to bond a matching layer to the front of the device. This layer has an acoustical impedance between that of air and the piezoelectric, the optimum value, Z_L, is given by,

$$Z_L = \sqrt{Z_1.Z_2} \tag{2.3}$$

where Z_1 and Z_2 are the impedances of air and the piezoelectric material respectively. This is derived by considering the transfer coefficients, equation (1.7), of the two boundaries, that between the piezoelectric and the matching layer, and then that between

the matching layer and air, and multiplying them. This product is then differentiated and equated to zero in the normal way to find a maximum. The attempt to find a suitable material has been the source of much work. Materials that have been tried include: silicon rubber [25], epoxy [26], balsa wood [27], cork [28] and silica aerogel (a substance with a porosity of between 80 and 99.8%) [29]. This however reduces the bandwidth of the device, as for maximum energy transfer to occur, a matching layer of thickness equal to a quarter wavelength at the centre frequency of interest is required, this dictates the frequency at which the transducer operates most effectively. Multiple matching layers, or a back damping layer have been proposed, these can be used to broaden the bandwidth at the expense of signal intensity [30].

Another approach to reducing the impedance mismatch between air and the transducer is to use a composite piezoceramic. This composite has a lower density and speed of sound, and hence, a lower acoustical impedance. There are many geometrical configurations possible, termed connectivity patterns [31]. A popular pattern for this application is 1-3 connectivity, which is a series of piezoceramic pillars embedded in an epoxy filler covered on both sides with a thin metallic electrode [32, 33] as depicted in Figure 2.4.

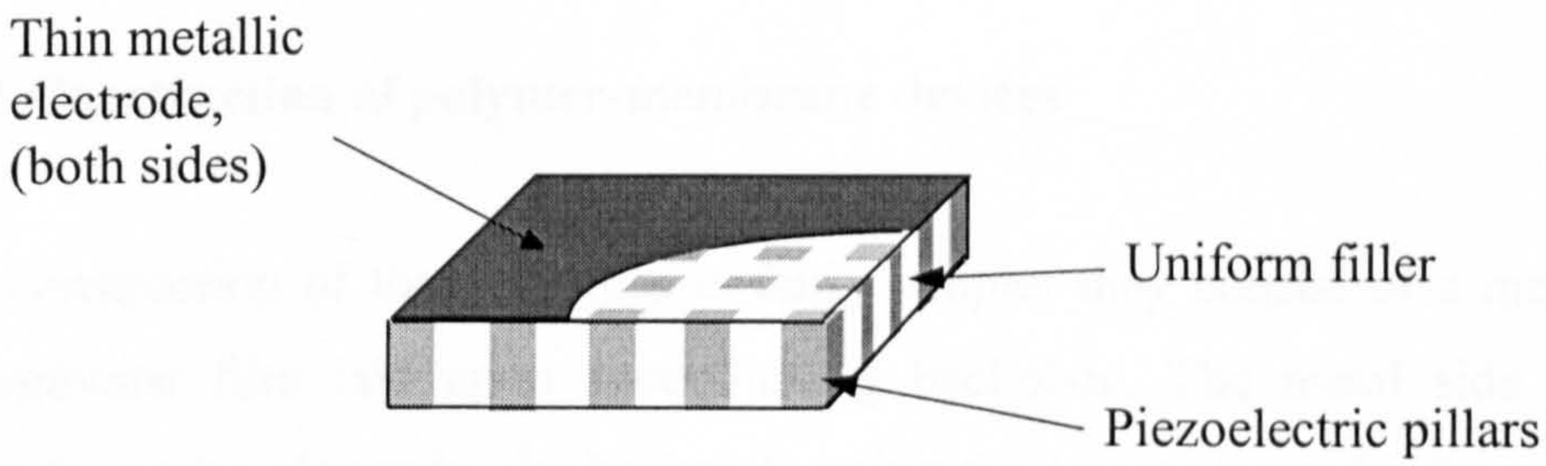

Figure 2.4: Structure of 1-3 connectivity piezoelectric composite transducer

This can be manufactured relatively easily by cutting a piece of piezoceramic, which is temporarily mounted on a plate, with a high-speed saw before filling the gaps with a low viscosity epoxy [34]. A drawback in the design process of such composites is the complexity of the resonance modes for a single phase material it is dependent on geometry and dimensions, whilst for a composite it is necessary to consider planar,

thickness and lateral modes of vibration [35, 36]. The different modes of vibration have been turned into an advantage, by bringing the different resonant frequencies close together to broaden the bandwidth of the device. However, when tested this device had a poorer sensitivity to received signals than a capacitive device [37].

In all the designs of piezoelectric devices discussed a compromise is required between bandwidth and sensitivity when used in air-coupled ultrasound. These devices have been used to scan an aircraft brake disc [10] and a specimen of carbon fibre reinforced plastic [38], in both cases a narrowband device was used.

2.5 Capacitive devices

The capacitive transducer consists of two metal electrodes separated by a small distance, and has been described in the context of sound generation as early as 1917 [39]. This transducer, termed a condenser transmitter, consists of a thin metal film stretched across a fixed metal backplate, and has a resonant frequency of 17 kHz. The use of a metalised polymer membrane and the study of the backplate design have allowed the frequency response of these transducers to be broadened, and increased well into the ultrasonic region. It is the improved impedance matching to air of the capacitive transducer when compared with the piezoelectric transducer, and the high bandwidth, which makes this type of transducer highly suitable for air-coupled applications.

2.5.1 Construction of polymer-membrane devices

The construction of these devices is fairly simple; they consist of a metalised polymer membrane film laid upon a conducting backplate. The metal side of the membrane is the upper electrode, the backplate being the lower electrode, the polymer side of the membrane and air gaps provide the insulation between electrodes, as shown in Figure 2.5. The membrane is typically 2-15 μm, usually metalised Mylar or Kapton is used.

Between the metalised polymer membrane and the backplate there are trapped pockets of air, and it is in this trapped air that pressure fluctuations occur during the reception or generation of sound. Consequently the device is intrinsically well suited to

air-coupling [40]. The conducting layer of the membrane is usually connected to a metal body surrounding the transducer, which is earthed to reduce r.f. noise.

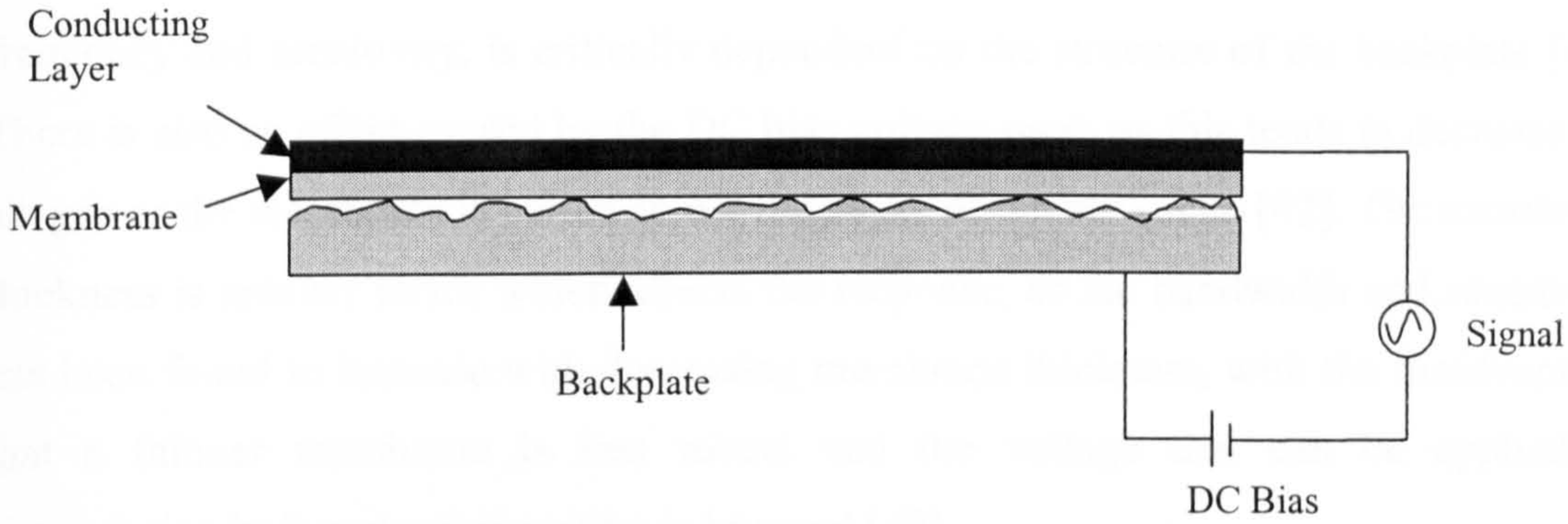

Figure 2.5: Capacitive transducer

2.5.2 Principles of operation

The capacitance of two parallel plates separated by an air gap is given by,

$$C = \frac{\varepsilon_o A}{d} \tag{2.4}$$

where A is the surface area, d is the thickness of the air gap, and ε_o the permittivity of free space. In reception the membrane will be moved by the fluctuations of air pressure, this causes a change in the separation of the parallel plates, Δx, and consequently a change in the capacitance, ΔC, which can be found by differentiation to be,

$$\Delta C = -\frac{\varepsilon_o A.\Delta x}{d^2}. \tag{2.5}$$

When a DC bias voltage is applied across the two plates then there is a charge change of

$$\Delta Q = -\frac{\varepsilon_o A.\Delta x}{d^2}.V_{DC}. \tag{2.6}$$

So it can be seen from this equation that in reception the size of the charge change is proportional to the surface area, and DC bias, and inversely proportional to the square of the initial electrode separation distance. In transmission the application of a changing voltage causes the charge difference between the plates to alter, which in turn causes a change in the electrostatic forces and so membrane movement. It must be noted that this is a simplistic method of modelling the situation, which assumes ideal parallel plates.

2.5.3 Transducer response

The behaviour of a capacitance transducer, in terms of bandwidth, centre frequency and sensitivity, is critically dependent on the structure of the backplate [41]. There is also an effect caused by the DC bias voltage used, as this tends to decrease the air-gap as the membrane is pulled across the peaks of the backplate [42]. The membrane thickness is another factor which affects the response, as the bandwidth and sensitivity has been found to increase with decreasing membrane thickness, with the disadvantage that a thinner membrane is less robust and the voltage that can be applied in transmission before short-circuiting is lowered [40].

The type of backplate used in the design of an air-coupled transducer can be broadly split into three groups, those using a roughened surface, grooves or a micromachined surface.

a) Roughened backplate

When a roughened backplate is used it has been found that the frequency at which peak amplitude occurs is increased as roughness is decreased [41, 43]. (It should be noted that the description of a transducer as having a roughened backplate can mean that the surface is highly polished, the term indicates that the dominate feature of the surface profile is the roughness). It has been suggested that this situation can be modelled as a frictionless piston. Using this approach, the membrane is treated as a piston, which is constrained by a spring, the air gap. This yields a predicted resonant frequency of

$$f_0 = \frac{1}{2\pi}\sqrt{\frac{\gamma P_a}{\rho d_m d_a}}, \tag{2.7}$$

where γ is the adiabatic constant of air, P_a is the atmospheric pressure, ρ is the membrane density, and d_m and d_a are the thicknesses of the membrane and air-gap respectively. This provides reasonably accurate predictions despite the approach's shortcomings. For whilst it is straightforward to establish the membrane thickness, the air gap will vary greatly at different points, as the membrane is pulled over the surface profile. In addition there is no allowance for the tension in the membrane or the separation of the ridge points on which it is in contact with the backplate [40]. In the

case of the roughened backplate the sensitivity has been found to increases with DC bias until a point when the air layer is too much reduced by the electrostatic force, thus restricting movement [44].

b) Grooved backplate

The use of V-grooved backplates has been extensively studied, because the groove pattern divides the backplate into many individual resonate elements which can be modelled, and is more predictable than a roughened backplate where the surface finish can vary even when using a consistent manufacturing technique [45]. If the wavelength is longer than all the different dimensions of the resonator, the Helmholtz model can be applied to predict the frequency of peak amplitude,

$$f_0 = \frac{c}{\pi}\sqrt{\frac{\rho_0}{2\sigma h}}, \tag{2.8}$$

where c is the speed of sound in air, ρ_0 is the density of air, σ is the mass per unit area of the membrane, and h is the depth of the groove. This equation which ignores groove width, is shown to have good correlation with measured results and it is confirmed experimentally that the membrane tension has little effect on the resonant frequency [46]. As this type of backplate is periodic in nature the effect is to reduce the bandwidth, and consequently an attempt has been made to use varying sizes of grooves across the backplate. The best performance occurred when just two sizes of grooves where used, and the difference in the two groove sizes is not great so as to avoid a frequency response spectrum with two peaks [47]. The sensitivity of devices made of this type of backplate is best when the membrane is thin and light, and when the grooves are highly regular. The second of these factors has the disadvantage of a narrower bandwidth [48, 49].

Transducers have also been made using flat-bottomed grooves and these have been compared to rough surface backplates. The nature of these devices means that between each ridge, there is a flat peak, the membrane lies on this peak and in these areas the behaviour is effectively like a roughened backplate. It was found that above the grooves resonance could be observed, whilst over the peaks the bandwidth was significantly wider but the signal amplitude lower [50].

c) Micromachined backplate

Micromachined backplates have also been used in an attempt to make highly sensitive and well-characterised devices capable of operating at MHz frequencies, a combination of characteristics not achieved by other backplates. The grooved back plates typically operate at less than 200kHz, whilst the higher frequency roughened backplates are not well characterised. Micromachined backplates have been manufactured from a polished silicon wafer, in which 40 μm diameter pits were etched to a depth of 35 μm on a pitch of 80 μm. As with grooved backplates these pits trap air under the membrane, acting as air-springs, and having the effect of reducing the membranes rigidity. These devices were found to be of wide bandwidth, and this bandwidth can be altered by applying different DC bias voltages, due to a similar mechanism as described for the grooved backplate [51-53].

d) Fully micromachined device

In addition to making a micromachined backplate, a further step is to make a fully micromachined device, so no additional metalised membrane is required. Such a device is usually fabricated using a surface micromachining technique based on that used for the processing of microelectronics, allowing the possibility of the integration of the device and electronics [54]. This process involves deposition and removal of thin layers on a substrate. Typically a conducting substrate acting as lower electrode is covered by a layer which will become the membrane of the device, an intermediate sacrificial layer separates the two, where the sacrificial layer is removed airgaps are left causing the membrane to be suspended above the substrate, the membrane is then coated with a metalised layer so acting as the upper electrode. Capacitive micromachined ultrasonic transducers (CMUTs) have been studied by several groups, and although the techniques of manufacture vary, the geometry of the devices produced allow these groups to be divided into two categories, the first make cells on the micrometer scale, many of which are combined in a matrix to make a single element, the second makes an element from a single cell on the millimetre scale.

Hexagonal cells of between 20 and 100 μm diameter have been fabricated with membranes in a thickness range of 0.5 to 4 μm [55-57]. It has been stated that these

diameters are the maximum possible for an operating frequency of between 1 and 2 MHz in air [55]. This is based on modelling each small cell as an oscillating disk, the restorative force of the gas within the cavity behind the membrane is ignored as it is said to be two orders of magnitude smaller than the forces within the membrane. Consequently the resonant frequency is given by,

$$f_0 = \frac{2.405}{\pi D}\left(\frac{T}{\rho}\right)^{1/2}, \tag{2.9}$$

where D is the membrane diameter, T is the tension within the static membrane, and ρ is the membrane density. This approach has been applied to micromachined cells by two groups [58, 59], and is the same approach used when modelling the first capacitive devices in which a metal film is stretched across the backplate with an airgap between them [39, 42]. However a more elaborate method of modelling claims to have shown that the compression of the air does have a significant effect [60].

The small cells that have been described tend to operate in a way defined by the cell geometry, and consequently they have a centre frequency of operation, and tend not to have a very broad bandwidth. As stated earlier, micromachined transducers up to a size of 5mm have also been fabricated as a whole, rather than a matrix of small cells [61]. As this type of transducer has been used in the work described in this thesis, these transducers will be described in more detail. A layer of thermally grown oxide insulates a silicon substrate. A sputtering operation is then performed to form the bottom electrode on this insulating layer; this layer is defined in shape by optical lithography. A 1 μm (typically) sacrificial layer is spun coated on the insulating layer; again optical lithography was used to define islands. A PECVD (Plasma-Enhanced Chemical Vapour Deposition) process is used to form the membrane layer over the whole substrate, the thickness of this layer as with the sacrificial layer will be a critical factor in the performance of the device, as will the intrinsic stress of the membrane. The final layer is the top electrode, which is formed by sputtering. Etch holes, typically 3 μm in diameter, are then formed in the uppermost two layers, using optical lithography, allowing the removal of the sacrificial layer in an oxygen plasma, and so turning the layered structure, shown in Figure 2.6 (i), into a capacitive ultrasonic transducer, as shown in Figure 2.6 (ii) [62].

This device made by QinetiQ, Malvern, has been found to behave reasonably closely to the air spring model, with centre frequencies at approximately 1.2MHz. The

application of increasing DC bias has been found to increase the amplitude and centre frequency of received signals [61, 63].

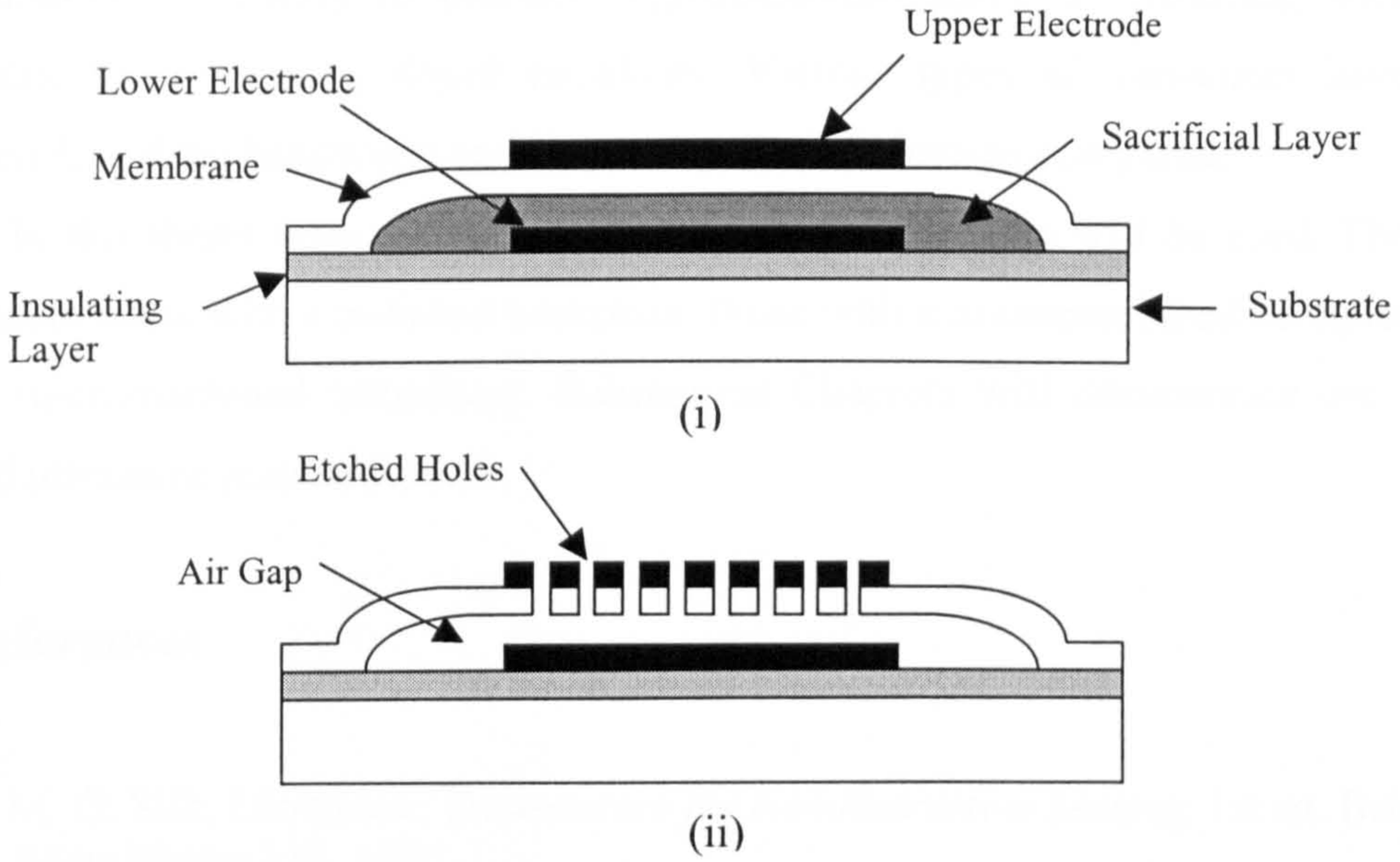

Figure 2.6: Manufacture of a micromachined transducer [61]

2.6 Other non-contact methods

There are other possibilities for the generation and detection of ultrasound without the need for contact with the test specimen. They include electromagnetic acoustic transducers (EMATs) and the use of lasers. As with all other methods both have advantages and disadvantages. EMATs allow the generation of longitudinal or shear waves depending on the design of the transducer, but must be kept very close to the material surface, and because the ultrasound occurs due to the production of eddy currents only conducting specimens can be tested. Lasers can also generate both longitudinal and shear waves depending on the mode of operation, and can be positioned at a long distance from the specimen, however for large signals a small amount of ablation will occur, and for the detection of ultrasound interferometry is used which requires a reflective surface [1].

2.7 Conclusions

The advantages of broadband air-coupled ultrasound have been discussed. They are primarily the ability to produce high-resolution scans of materials, which are vulnerable to damage by liquid couplants. Various types of transducer have been considered, and the bandwidth and sensitivity of such devices compared.

In this thesis three different types of capacitive device will be used. These are transducers made with a polished backplate, those with a micromachined backplate, and a fully micromachined transducer. Subsequent Chapters will demonstrate use in air-coupled ultrasonic measurement.

2.8 References

[1] M. G. Silk, *Ultrasonic Transducers for Nondestructive Testing*, 1st ed. Bristol: Adam Hilger Ltd, 1984.

[2] R. Halmshaw, *Non-Destructive Testing*, 2 ed. London: Arnold, 1991.

[3] J. Krautkrämer and H. Krautkrämer, *Ultrasonic Testing of Materials*, 4th ed: Springer-Verlag, 1990.

[4] L. K. English, "Non-Destructive Testing for Composite Quality," *Materials Engineering*, vol. 104, pp. 75-77, 1987.

[5] M. D. Enderby, A. R. Clarke, M. Patel, P. Ogden, and A. A. Johnson, "An automated ultrasonic immersion technique for the determination of three-dimensional elastic constants of polymer composites," *Ultrasonics*, vol. 36, pp. 245-249, 1998.

[6] W. A. Grandia and C. M. Fortunko, "NDE Applications of Air-coupled Ultrasonic Transducers," presented at IEEE Ultrasonics Symposium, 1995.

[7] J. Buckley, "Priciples and application of air-coupled ultrasonics," *Insight*, vol. 40, pp. 755-759, 1998.

[8] J. O. Strycek and H. P. Loertscher, "High Speed Large Area Scanning using air-coupled ultrasound," presented at 15th WCNDT (published by ndt.net), Roma, 2000.

[9] D. W. Schindel and D. A. Hutchins, "Applications of Micromachined Capacitance Transducers in Air-coupled Ultrasonics and Nondestructive Evaluaton," *IEEE Transactions on Ultrasonics Ferroelectrics and Frequency Control*, vol. 42, pp. 51-57, 1995.

[10] J. Buckley, "Air-coupled Ultrasound- A Millennial Review," presented at 15th WCNDT (published on ndt.net), Roma, 2000.

[11] J. L. San Emeterio and L. G. Ullate, "Diffraction Impulse-Response of Rectangular Transducers," *Journal of the Acoustical Society of America*, vol. 92, pp. 651-662, 1992.

[12] W. Manthey, N. Kroemer, and V. Mágori, "Ultrasonic transducers and transducer arrays for applications in air," *Measurement Science and Technology*, vol. 3, pp. 249-261, 1992.

[13] G. Rizzatto, "Ultrasound Transducers," *European Journal of radiology*, vol. 27, pp. 188-195, 1998.
[14] Rao N. A. H. K., Mehra S., Bridges J., and Venkatraman S., "Experimental Point Spread Function of FM Pulse Imaging Scheme," *Ultrasonic Imaging*, vol. 17, pp. 114-141, 1995.
[15] N. Rao and S. Mehra, "Medical Ultrasound Imaging Using Pulse-Compression," *Electronics Letters*, vol. 29, pp. 649-651, 1993.
[16] N. Rao, "Investigation of a Pulse-Compression Technique for Medical Ultrasound - a Simulation Study," *Medical & Biological Engineering & Computing*, vol. 32, pp. 181-188, 1994.
[17] T. H. Gan, D. A. Hutchins, and D. R. Billson, "Preliminary studies of a novel air-coupled ultrasonic inspection system for food containers," *Journal of Food Engineering*, vol. 53, pp. 315-323, 2002.
[18] E. Blomme, D. Bulcaen, and F. Declercq, "Air-coupled ultrasonic NDE: experiments in the frequency range 750 kHz-2MHz," *NDT&E International*, 2002.
[19] W. Sachse and N. N. Hsu, "Ultrasonic Transducers for Materials Testing and Their Characterization," in *Physical Acoustics*, vol. XIV, R. N. Thurston, Ed. London: Academic Press, 1979, pp. 277-407.
[20] S. Kociš and Z. Figura, *Ultrasonic Measurements and Technologies*, 1st ed. London: Chapman & Hall, 1996.
[21] V. Magori and H. Walker, "Ultrasonic Presence Sensors with Wide-Range and High Local Resolution," *IEEE Transactions on Ultrasonics Ferroelectrics and Frequency Control*, vol. 34, pp. 202-211, 1987.
[22] L. Durris, L. Goujon, A. Pelourson, P. Gonnard, M. Brissaud, and C. Richard, "Airborne ultrasonic transducer," *Ultrasonics*, vol. 34, pp. 153-158, 1996.
[23] M. Babic, "A 200-kHz Ultrasonic Transducer Coupled to the Air with a Radiating Membrane," *IEEE Transactions on Ultrasonics Ferroelectrics and Frequency Control*, vol. 38, pp. 252-255, 1991.
[24] H. Dabirikhah and C. W. Turner, "Leaky Plate Wave Airborne Ultrasonic Transducer," *Electronics Letters*, vol. 30, pp. 1549-1550, 1994.
[25] J. D. Fox, B. T. Khuri-Yakub, and G. S. Kino, "High-frequency acoustic wave measurements inair," presented at IEEE Ultrasonics Symposium, 1983.
[26] J. D. Fox, B. T. Khuri-Yakub, and G. S. Kino, "Acoustic resonator transducer for operation in air," *Electronics Letters*, vol. 21, pp. 694-696, 1985.
[27] J. Stor-Pellinen, M. Oksanen, R. Vuohelainen, J. Rantala, J. Hartkainen, and M. Luukkala, "Photoacoustic inspection of matching layers of ultrasonic air-coupled transducers," presented at IEEE Ultrasonics Symposium, 1989.
[28] S. Schiller, C.-K. Hsieh, C.-H. Chou, and B. T. Khuri-Yakub, "Novel high frequency air transducers," *Rev. Prog. Quant. NonDestr. Eval.*, vol. 9, pp. 795-798, 1990.
[29] O. Krauss, R. Gerlach, and J. Fricke, "Experimental and Theoretical Investigations of SiO2-Aerogel Matched Piezo-Transducers," *Ultrasonics*, vol. 32, pp. 217-222, 1994.
[30] T. Gudra and K. J. Opielinski, "Influence of acoustic impedance of multilayer acoustice systems on the transfer function of ultrasonic airborne transducers," *Ultrasonics*, vol. 40, pp. 457-463, 2002.
[31] R. E. Newnham, D. P. Skinner, and L. E. Cross, "Connectivity and piezoelectric-pyroelectric composites," *Material Research Bulletin*, vol. 13, pp. 525-536, 1978.

[32] T. R. Gururaja, W. A. Schulze, L. E. Cross, and R. E. Newnham, "Piezoelectric Composite Materials for Ultrasonic Transducer Applications. Part 2: Evaluation of Ultrasonic Medical Applications," *IEEE Transactions on Sonics and Ultrasonics*, vol. 32, pp. 499-513, 1985.

[33] M. I. Haller and B. T. Khuri-Yakub, "Micromachined 1-3 composites for ultrasonic air transducers," *Review Scientific Instruments*, vol. 65, pp. 2095-2098, 1994.

[34] H. P. Savakus, K. A. Klicker, and R. E. Newnham, "PZT-epoxy piezoelectric transducer: a simplified fabrication procedure," *Material Research Bulletin*, vol. 16, pp. 677-680, 1981.

[35] J. A. Hossack and G. Hayward, "Finite-Element Analysis of 1-3 Composite Transducers," *IEEE Transactions on Ultrasonics Ferroelectrics and Frequency Control*, vol. 38, pp. 618-629, 1991.

[36] T. R. Gururaja, W. A. Schulze, L. E. Cross, R. E. Newnham, B. A. Auld, and Y. J. Wang, "Piezoelectric Composite Materials for Ultrasonic Transducer Applications. Part 1: Resonant Modes of Vibration of PZT Rod-Polymer Composites," *IEEE Transactions on Sonics and Ultrasonics*, vol. 32, pp. 481-498, 1985.

[37] A. Gachagan and G. Hayward, "Improving th bandwidth of 1-3 connectivity composite receivers using mode coupling," *Journal of the Acoustical Society of America*, vol. 103, pp. 3344-3352, 1998.

[38] R. Stoessel, N. Krohn, K. Pfleiderer, and G. Busse, "Air-coupled ultrasound inspection of various materials," *Ultrasonics*, vol. 40, pp. 159-163, 2002.

[39] E. C. Wente, "A condenser transmitter as a uniformly sensitive instrument for the absolute measurement of sound intensity," *Physical Review*, vol. 10, pp. 39-63, 1917.

[40] C. Wykes, "Advances in Air-Coupled Ultrasonic Transducers," *Nondestr. Test. Eval.*, vol. 12, pp. 155-180, 1995.

[41] H. Carr and C. Wykes, "Diagnostic measurments in capacitive transducers," *Ultrasonics*, vol. 31, pp. 13-20, 1993.

[42] W. Kuhl, G. R. Schodder, and F.-K. Schroeder, "Condenser Transmitter and Microphones with solid Dielectric for Airborne Ultrasound," *Acustica*, vol. 4, pp. 519-532, 1954.

[43] A. G. Bashford, D. A. Hutchins, and D. W. Schindel, "The Response of an Air-Coupled Ultrasonic Transducer for Various Backplates and Apertures," in *Review of Progress in Quantitative Nondestructive Evaluation*, vol. 15, D. E. Chimenti, Ed. New York: Plenum Press, 1996, pp. 1043-1050.

[44] L. Pizarro, D. Certon, M. Lethiecq, and B. Hosten, "Airborne ultrasonic electrostatic transducers with conductive grooved backplates: tailoring their centre frequency, sensitivity and bandwidth," *Ultrasonics*, vol. 37, pp. 493-503, 1999.

[45] M. Rafiq and C. Wykes, "The performance of capacitive ultrasonic transducers using v-grooved backplates," *Measurement Science and Technology*, vol. 2, pp. 168-174, 1991.

[46] J. Hietanen, J. Stor-Pellinen, and M. Luukkala, "A Helmholtz resonator model for an electrostatic ultrasonic air transducer with V-grooved backplate," *Sensors and Actuators A: Physical*, vol. 39, pp. 129-132, 1993.

[47] M. Mattila and J. Hietanen, "Bandwidth control of an electrostatic transducer," *Sensors and Actuators A: Physical*, vol. 45, pp. 203-208, 1994.

[48] J. Hietanen, "Closed-form formulation for sensitivity of capacitive ultrasonic transducers using V-grooved backplates," *Sensors and Actuators A: Physical*, vol. 69, pp. 139-142, 1998.

[49] J. Hietanen, M. Mattila, J. Stor-Pellinen, F. Tsuzuki, H. Väätäjä, K. Sasaki, and M. Luukkala, "Factors effecting the sensitivity of electrostatic ultrasonic transducers," *Measurement Science and Technology*, vol. 4, pp. 1138-1142, 1993.

[50] L. Pizarro, D. Certon, M. Lethiecq, O. Boumatar, and B. Hosten, "Experimental Investigation of Electrostatic Ultrasonic Transducers with Grooved Backplates," presented at IEEE International Ultrasonics Symposium, Toronto, Canada, 1997.

[51] D. W. Schindel, D. A. Hutchins, L. Zou, and M. Sayer, "The Design and Characterization of Micromachined Air-Coupled Capacitance Transducers," *IEEE Transactions on Ultrasonics Ferroelectrics and Frequency Control*, vol. 42, pp. 42-50, 1995.

[52] D. A. Hutchins, D. W. Schindel, A. G. Bashford, and W. M. D. Wright, "Advances in ultrasonic electrostatic transduction," *Ultrasonics*, vol. 36, pp. 1-6, 1998.

[53] D. W. Schindel, D. A. Hutchins, and W. A. Grandia, "Capacitive and piezoelectric air-coupled transducers for resonant ultrasonic inspection," *Ultrasonics*, vol. 34, pp. 621-627, 1996.

[54] P. Eccardt, K. Niederer, and B. Fischer, "Micromachined transducers for ultrasound applications," presented at Ultrasonics Symposium, Toronto, Canada, 1997.

[55] J. Xuecheng, I. Ladabaum, and B. T. Khuri-Yakub, "The Microfabrication of Capacitive Ultrasonic Transducers," *Journal of Microelectromechanical Systems*, vol. 7, pp. 295-302, 1998.

[56] P. C. Eccardt and K. Niederer, "Micromachined ultrasound transducers with improved coupling factors from a CMOS compatible process," *Ultrasonics*, vol. 38, pp. 774-780, 2000.

[57] E. Cianci, V. Foglietti, G. Caliano, and M. Pappalardo, "Micromachined capacitive ultrasonic transducers fabricated using silicon on insulator wafers," *Microelectronic Engineering*, vol. 61-62, pp. 1025-1029, 2002.

[58] P. C. Eccardt, K. Nieder, and B. Fischer, "Micromachined Transducers for Ultrasound Applications," presented at 1997 IEEE Ultrasonics Symposium, 1997.

[59] M. I. Haller and B. T. Khuri-Yakub, "A Surface Micromachined Electrostatic Ultrasonic Air Transducer," *IEEE Transactions on Ultrasonics Ferroelectrics and Frequency Control*, vol. 43, pp. 1-6, 1996.

[60] A. Caronti, G. Caliano, A. Iula, and M. Pappalardo, "An accurate Model for Capacitive Micromachined Ultrasonic Transducers," *IEEE Transactions on Ultrasonics Ferroelectrics and Frequency Control*, vol. 49, pp. 159-168, 2002.

[61] J. S. McIntosh, D. A. Hutchins, D. R. Billson, T. J. Robertson, R. A. Noble, and A. D. R. Jones, "The characterization of capacitive micromachined ultrasonic transducers in air," *Ultrasonics*, vol. 40, pp. 477-483, 2002.

[62] R. A. Noble, A. D. R. Jones, T. J. Robertson, D. A. Hutchins, and D. R. Billson, "Novel, wide bandwidth, micromachined ultrasonic transducers," *IEEE Transactions on Ultrasonics Ferroelectrics and Frequency Control*, vol. 48, pp. 1495-1507, 2001.

[63] M. J. Anderson, J. A. Hill, C. M. Fortunko, N. S. Dogan, and R. D. Moore, "Broadband electrostatic transducers: Modeling and experiments," *Journal of the Acoustical Society of America*, vol. 97, pp. 262-271, 1995.

Chapter 3: Theoretical predictions for phased arrays

3.1 Introduction

A number of previous studies have been reported into the various techniques for focusing ultrasound in air. These include the use of a Fresnel zone-plate in front of a circular transducer driven by a tone burst signal [1, 2], the use of curved backplates [3], and the use of a parabolic mirror [4]. Another approach to focussing on which there has been little air-coupled work is the use of phased arrays, and this is the subject of this and the following Chapter. The previous work which has been done on the use of air-coupled arrays, concentrates on the use of the array as a phased receiver, using post-processing techniques, rather than as a phased source [5, 6].

In this chapter two different approaches to modelling phased arrays will be discussed. Both models are applicable to earlier air and water coupled work. One uses an approximation to find the directivity in the farfield and the other uses the Impulse Response method. Both of these modelling methods will be used to discuss the effect certain parameters of the array have on performance. In this Chapter some simulated fields found using these models will be presented, the following Chapter will contain experimental results to compare to the theoretical results found using the more suitable of these modelling techniques, the Impulse Response model. The Impulse Response model builds on the predictions made by San Emeterio [7], for a pressure field from a rectangular source, this model is extended for a phased array. The modelling of phased arrays seems to be concentrated on beam-steering a farfield effect, there appears to be a lack of work on focussing using phased arrays. For air coupled work focussing appears to be a potentially useful effect, as if a sample needs to be examined it would be possible to focus at various locations on the front surface, maximising energy coupled into the solid.

3.2 Calculating phasing for arrays

In order to create a pressure field which exhibits focussing it is necessary that, at the focal point, the pressure waves interfere constructively. For this to be the case the

ultrasound wavelets arriving from the device and interfering at the focal point must be in phase. Consequently, the common feature to all of the unphased focussing methods described in the introduction is that the path length from any part of the source to the focal point is constant across the face of the source, ensuring that pressure waveforms emitted from any part of the source arrive at the focal point in phase with pressure emitted from any other part of the source.

The path length from a particular element to a focal point is not constant for an array. However, by applying a phase difference to each element the time of arrival at the focal point can be made equal. At the time of the last element being fired then, the remaining path length of a waveform emitted from any element to the focal point is equal.

In order to calculate the phasing necessary to create a focal point, it is necessary to define the terms, which describe the geometry of the array; these can be seen in Figure 3.1. The array itself lies in the $z = 0$ plane, with the origin of the *xyz* coordinate system at the centre of the array. The width of an element is termed w, the height, h, the pitch of the elements p and the total width of the array is termed W. The focal point is at x_f, 0, z_f, and the array considered is linear as opposed to 2-D as the array is just one element wide in the y direction.

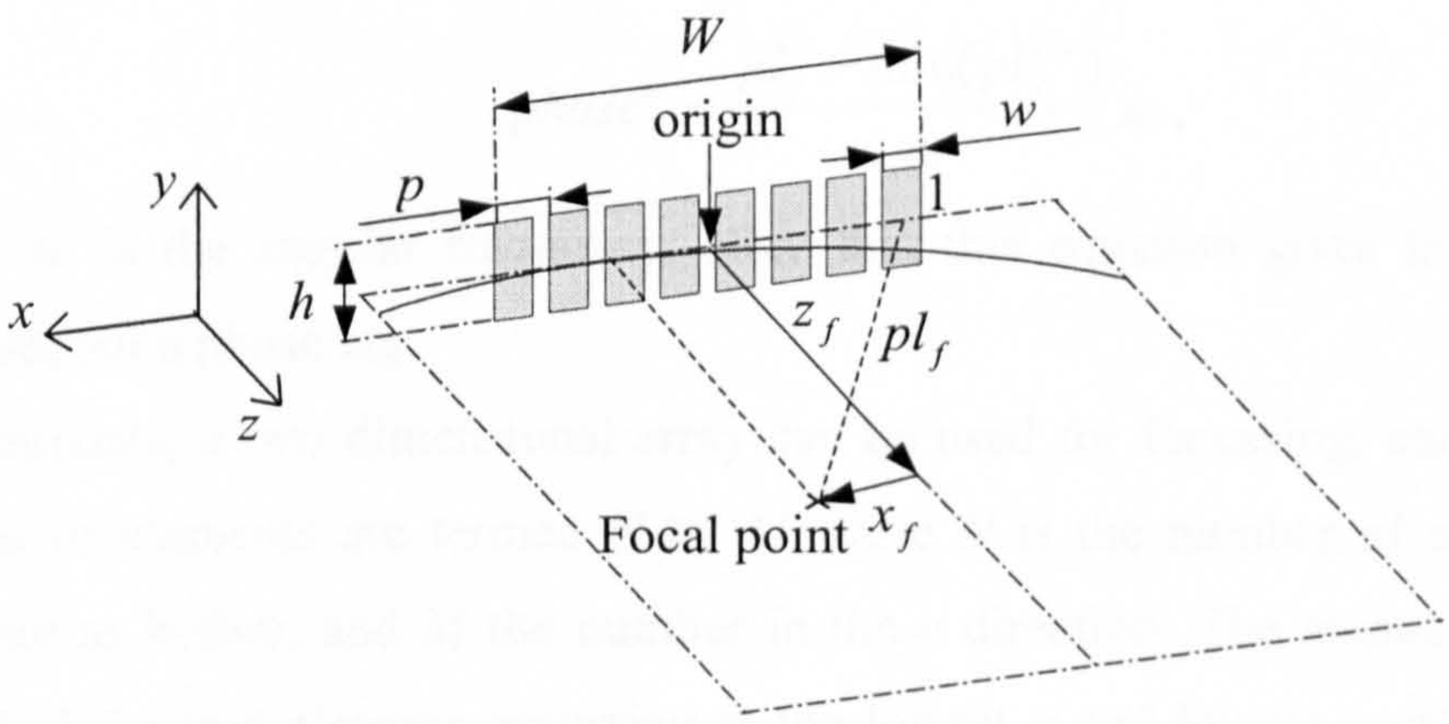

Figure 3.1: Array geometry

In order to calculate the phasing of each element, it is necessary first to find the location of the centre of each element. Assuming that the elements are numbered from the one that occurs at the lowest x value to the one at the highest, (i.e. from right to left in Figure 3.1), then the location of the centre of the element is given by:

$$x^n_{centre} = \left(n - \frac{N+1}{2}\right).p \ , \tag{3.1}$$

where n is the element number, and N is the number of elements in the x direction. The length pl_f is shown in Figure 3.1 as the distance from the centre of the element to the focal point. In the case depicted element 1, to the focal point, this distance can be calculated as,

$$pl^n_f = \sqrt{(x_f - x^n_{centre})^2 + {z_f}^2} \ . \tag{3.2}$$

It can be seen that this distance is different for each element, but the criterion for a focus is that the time of arrival of pressure waveforms emerging from an element should be the same as that for all other elements at the focal point. So the differences in pl_f, must be compensated for in the phase difference. At the time of the last element being driven the wavefronts from all the other elements should form an arc around the focal point, as shown in Figure 3.1, so that the remaining path length is constant for all elements. When the focal point is directly in front of the array, i.e. $-\frac{W}{2} \le x_f \le \frac{W}{2}$, then the radius of the arc centred at the focal point is z, as this is the shortest path length to the focal point; otherwise, the shortest distance can be expressed simply as $\min(pl^n_f)$ for $n = 1{:}N$. Consequently the phased difference is given by

$$phase^n = \frac{pl^n_f - \min(pl^{1:N}_f)}{c}.\omega \ , \tag{3.3}$$

where ω is the angular frequency. Note that this equation gives the phase advance required, not a phase lag.

Similarly, a two dimensional array can be used for focussing, and in this case the number of elements are termed N by M, were N is the number of elements in the x direction as before, and M the number in the y direction. The elements are numbered from 1, 1 for that element occurring at the lowest x and lowest y value to N, M. The location of the centre of an element in the x direction is as in equation 3.1. The location in the y direction is given by

$$y^m_{centre} = \left(m - \frac{M+1}{2}\right).p \ . \tag{3.4}$$

where m is the element number. The total path length to the focal point can be worked out for any element, n, m, as

$$pl_f^{n,m} = \sqrt{(x_f - x_{centre}^n)^2 + z_f{}^2 + (y_f - y_{centre}^m)^2} \,. \tag{3.5}$$

where the focal point is defined as being located at x_f, y_f, z_f. The wavefront at the time of the last element being driven, in the case of a linear array, is a segment of the circle centre at the focal point radius z_f, here the wavefront lies on a segment of a sphere, of the same radius and location. The phase differences are given by

$$phase^{n,m} = \frac{pl_f^{n,m} - \min(pl_f^{1:N,1:M})}{c}.\omega \,. \tag{3.6}$$

Arrays can also be phased to cause beam-steering. This is where the wavefront at the time of the last element being driven is a straight line at an angle of α to the z axis, as shown in Figure 3.2.

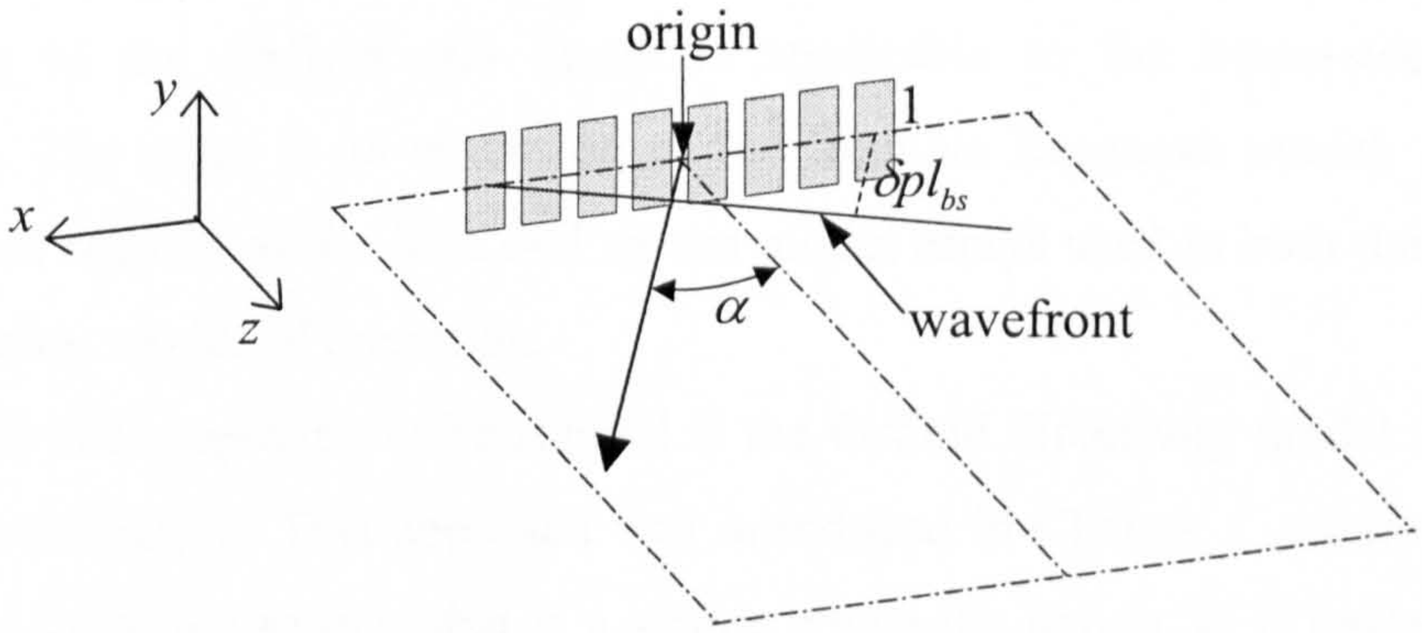

Figure 3.2: Array in beam-steering mode of operation

It can be seen that the difference in path length, which is compensated for by phasing is δpl_{bs}^n, as labelled in Figure 3.2 for element 1. The phase advance for each element is this distance divided by c. This can be found by

$$phase^n = \left\{ \left(\frac{N-1}{2} \right).p - x_{centre}^n \right\} \frac{\sin\alpha}{c}.\omega \,. \tag{3.7}$$

for a linear array. An expression for a 2-D array can be found in Appendix A.

Beam-steering is a mode of operation used to create sector views, such as those commonly used in medical imaging. The distance objects are from the array can be found using time of flight. In the nearfield of an unphased source, there are many ripples in the pressure field which lessen as the distance from the transducer increases, this is also the case for a steered beam and consequently this technique is not well suited to imaging in close proximity to the source.

An advantage of the focussing mode of operation is that there is a high intensity of pressure at the focal point. It is possible to move the focal point around, though the tightness of focussing reduces as the distance away form the source increases. If a specimen requires imaging using air or water coupled ultrasound it would be possible to move the focal point around on the front surface of the sample, so that high resolution imaging can be performed and the largest signal possible is coupled into the sample at the point of interest.

3.3 Farfield directivity model applied to arrays

Two different approaches of modelling arrays will be examined in this and the following Section. One is the plane wave approximation, which is suitable for modelling in the farfield and hence is applicable to the beam-steering mode of operation. The other is an extension of the Impulse Response model, and as such is valid for all regions of the field and so can model arrays used in both the beam-steering and focussing modes of operation.

The first approach to be studied is the farfield directivity model using the plane wave approximation. This approach was introduced in Chapter 1, where the directivity was found for a line source, that is a source where the height, h, is neglected. This was found by integrating the path length differences along the length of the source and yielded a directivity described by

$$D(\theta) = \left| \frac{\sin(\pi . w \sin\theta / \lambda)}{\pi . w \sin\theta / \lambda} \right|, \tag{3.8}$$

where θ is the angle from the normal to the source, and w is the width. It is assumed that the source is driven by a continuous sinusoidal wave, of wavelength λ.

A similar approach to that used to derive an expression for the directivity of a single line source, can be used to find the directivity of a beam-steered array. The directivity of a phased array is given by

$$D(\theta) = \left| \frac{\sin(\pi . w \sin\theta / \lambda)}{\pi . w \sin\theta / \lambda} \frac{\sin(N\pi . p(\sin\alpha - \sin\theta)/\lambda)}{N \sin(\pi . p(\sin\alpha - \sin\theta)/\lambda)} \right| \tag{3.9}$$

where p is the pitch, N is the number of elements in the line array, and α is the angle through which the beam is steered [8]. As can be seen the first expression in equation 3.9 is the same as equation 3.8, so the directivity of a line array is the directivity of a

single line source multiplied by a directivity dictated by N and p so relating to the array spacing and size. This is termed the product theorem for transducers [9], expressed as

$$D(\theta) = D_{element}(\theta) D_{array}(\theta) \tag{3.10}$$

where $D_{element}(\theta)$ is given by equation 3.8, and $D_{array}(\theta)$ is

$$D_{array}(\theta) = \left| \frac{\sin(N\pi.p(\sin\alpha - \sin\theta)/\lambda)}{N\sin(\pi.p(\sin\alpha - \sin\theta)/\lambda)} \right|. \tag{3.11}$$

This approach has been used in many different contexts in which arrays are used such as sonar [9], radiotelescopes [10] and radar [11].

An example of the results this approach predicts is shown in Figure 3.3. The directivity is plotted as a function of θ (the angle in degrees from the normal) for a single 0.5mm wide element and a wavelength of 0.68mm (approximately corresponding to 500kHz in air) is shown in Figure 3.3 (i). The directivity of a series of 16 points distributed at a pitch of 0.6mm, driven in phase by a 500kHz signal in air, is shown in Figure 3.3 (ii). This is $D_{array}(\theta)$ calculated from equation 3.11. It can be seen that there is a main lobe, with either side of it a series of grating lobes symmetrically distributed, arising from the N term in equation 3.11. The directivity $D(\theta)$ of an array of 16 line elements all 0.5mm wide, and on a pitch of 0.6mm, driven by a frequency of 500kHz, is then the product of these previous two directivities, and this is shown in Figure 3.3 (iii).

Figure 3.4 (i) shows the directivity of the same array of points used for Figure 3.3 (ii), but for a steering angle, α, of 20°. It can be seen that the main lobe now occurs at 20^0 from the normal. However, a second large peak also occurs, and this is usually termed a side lobe in the context of ultrasound termed, with the smaller peaks between termed grating lobes. When the array of points becomes an array of line elements of width 0.5mm (the directivity of which is in Figure 3.3 (i)), as shown in Figure 3.4 (ii) it can be seen that the directivity of the line source causes the amplitude of the side lobe to reduce. This model is limited to the farfield, and a continuous wave excitation, and also only considers a line source, so that h is ignored.

This method of modelling the pressure patterns emerging from phased arrays has been used to investigate the design of arrays for beam-steering, in a series of papers by Wooh and Shi [8, 12-14]. However as this approach is only suitable for use in the farfield, it is not possible to use it for the study of focussing. There appears to be no similar discussion in the literature using a different model for the design of arrays for focussing; consequently, the next section will discuss this topic.

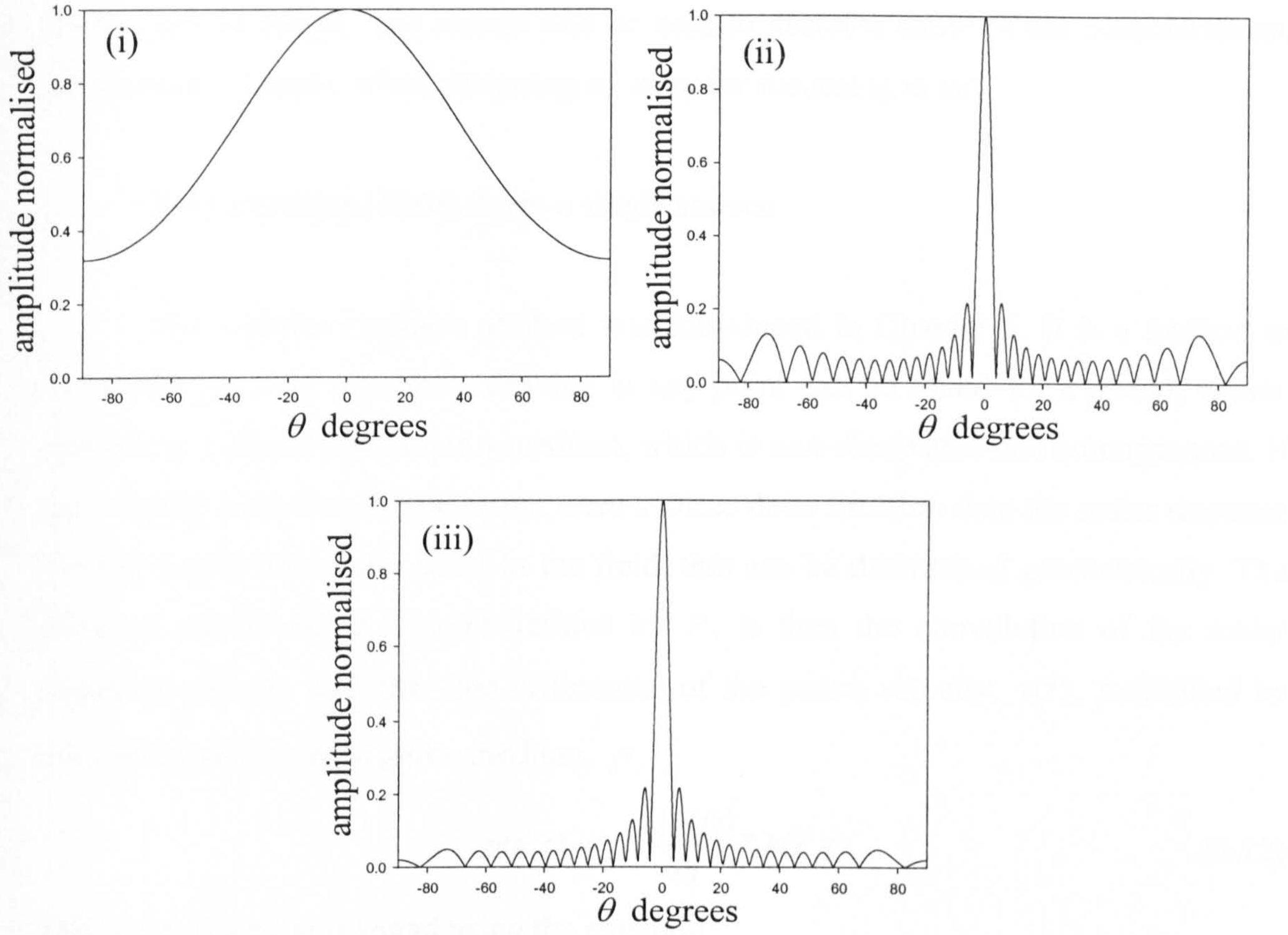

Figure 3.3: Directivity plot, of (i) a single line element, (ii) an array of points, and (iii) an array of line elements

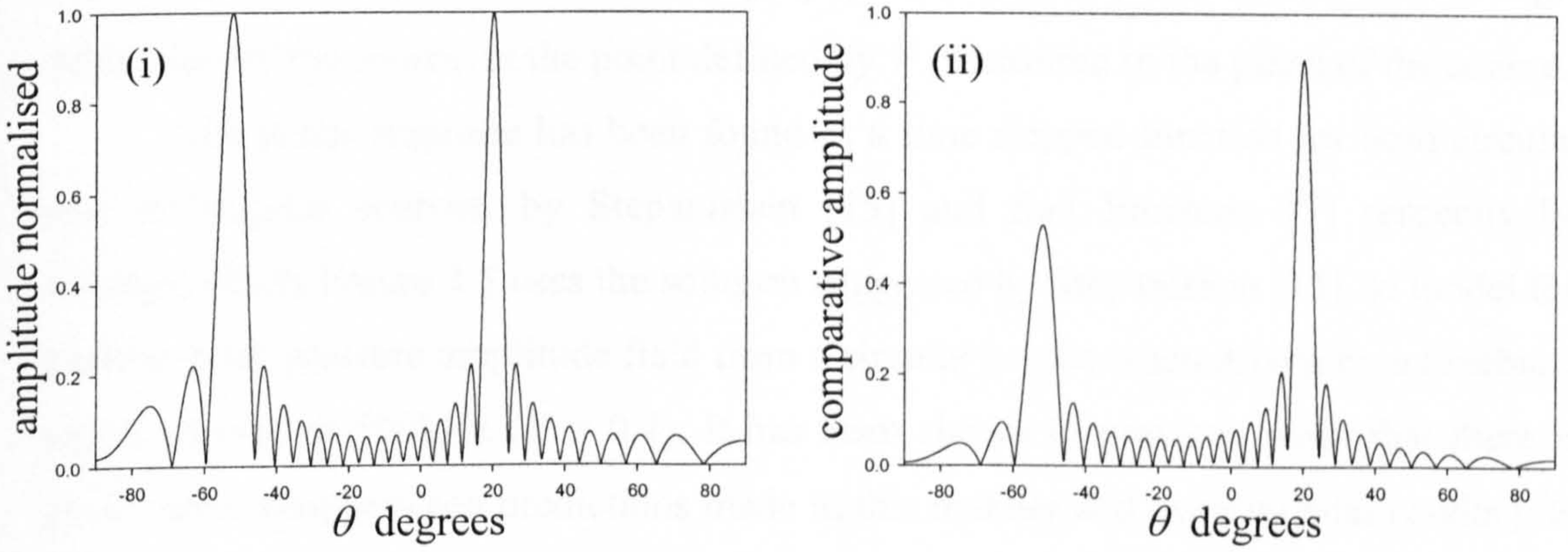

Figure 3.4: Directivity plot, of (i) an array of points steered to 20° and (ii) an array of line elements steered to the same angle

3.4 Impulse response method applied to arrays

In this Section, the Impulse Response model first described in Chapter 1 will be briefly reviewed. This approach will be used to predict pressure fields from single

sources of different geometries, before developing the method to model arrays and finally phased arrays. The results will be used to describe some of the considerations, which must be made, when designing an array for focussing in air.

3.4.1 Predicted fields from a single source

The impulse response method was introduced in Chapter 1. It is a method in which the pressure waveform arriving at any point can be found for a piston, which, vibrates in a planar manner, in a medium, which is non-dissipative and homogeneous. If the velocity waveform of the piston were a Dirac delta function then the scalar response is what would arrive at a point in the field, this can be determined geometrically. The pressure waveform, at a point defined by $\bar{r}$, is then the convolution of the scalar response, $h(\bar{r},t)$, with the time differential of the piston velocity, $v(t)$, multiplied by the density of the propagation medium, ρ.

$$p(\bar{r},t) = \rho.\frac{\partial[v(t)]}{\partial t} * h(\bar{r},t) \tag{3.12}$$

The scalar response is found using the equation

$$h(\bar{r},t) = c.\frac{\Omega(\bar{r},t)}{2\pi} \tag{3.13}$$

where c is the speed of sound in the propagation medium, and $\Omega(\bar{r},t)$ is the angle subtended by the source, at the point defined by $\bar{r}$, measured in the plane of the source.

The scalar response has been found as a time stepped function for both circular and rectangular sources, by Stepanishen [15] and San Emeterio [7] respectively, amongst others.Figure 3.5 uses the solution suggested by Stepanishen [15], to model the peak-to-peak pressure amplitude field from a circular source when driven by a toneburst signal centred at 500kHz (K = 0.4). It has been shown in previous work that there is good correlation between predictions made in this manner and experimental results [16, 17].

Figure 3.6 uses the solution suggested by San Emeterio [7], to model the peak-to-peak pressure amplitude field from a square source when driven by a toneburst signal centred at 500kHz (K = 0.4). The area of the square source is equal to that of the circular source used in simulations displayed in Figure 3.5. It can be seen by comparing the simulation, in the xz plane of the square and circular sources, that the sidelobes are produced at similar angles. It can also be seen that the peaks and troughs on axis occur

at the same distance form the source. In the *xy* plane, at both $z = 7$ mm and 14 mm the sidelobes have a rotational symmetry around the axis for the circular source, whilst for the square source there is symmetry in the $x = 0$, and $y = 0$ planes. The symmetry displayed by both sets of the pressure field is the same as that of the source shape used.

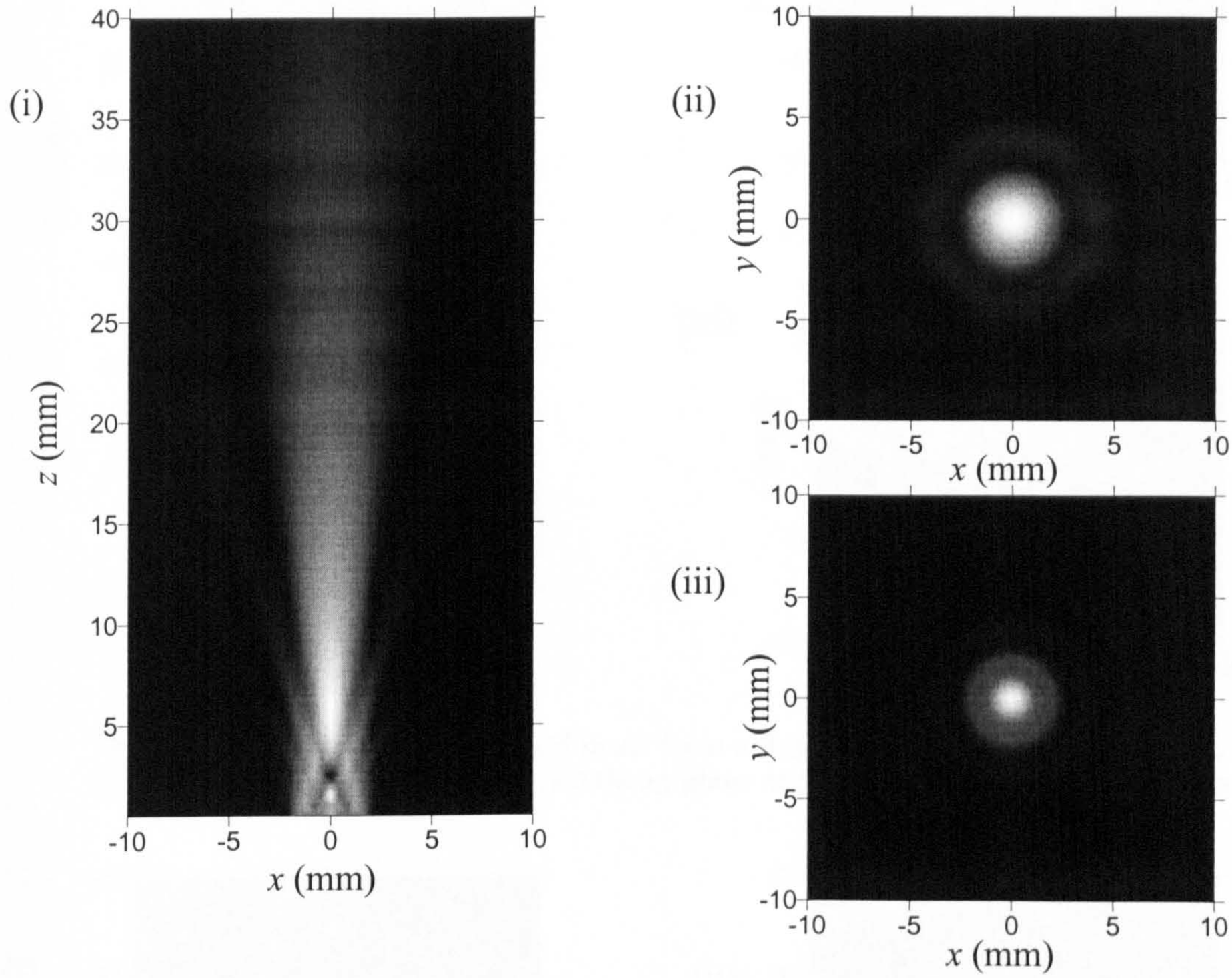

Figure 3.5: Predicted pressure field from a single 3.94 mm diameter circular source in air, in (i) the *xz* plane, and in (ii) and (iii) the *xy* plane at $z = 14$ mm and 7 mm respectively

In Figures 3.5 and 3.6 the predicted pressure field from a square and circular source, respectively, has been shown when a toneburst drive signal is used. In order to compare the effect of changing to a different type of drive signal, Figure 3.7 shows the pressure field in the *xz* plane for a square device, for comparison to Figure 3.6 (i). The drive signals used are a broadband signal centred at 500 kHz (K=3.5), and a chirp centred also at 500 kHz, with a 500 KHz bandwidth, and 0.5 ms long and enveloped by a Hanning window. It can be seen that due to the shorter length of the broadband signal, the interference that causes the sidelobes and nearfield ripples cannot occur and the affect is to smooth the pressure field. The use of a chirp drive signal can be seen to yield a similar field pattern to the toneburst.

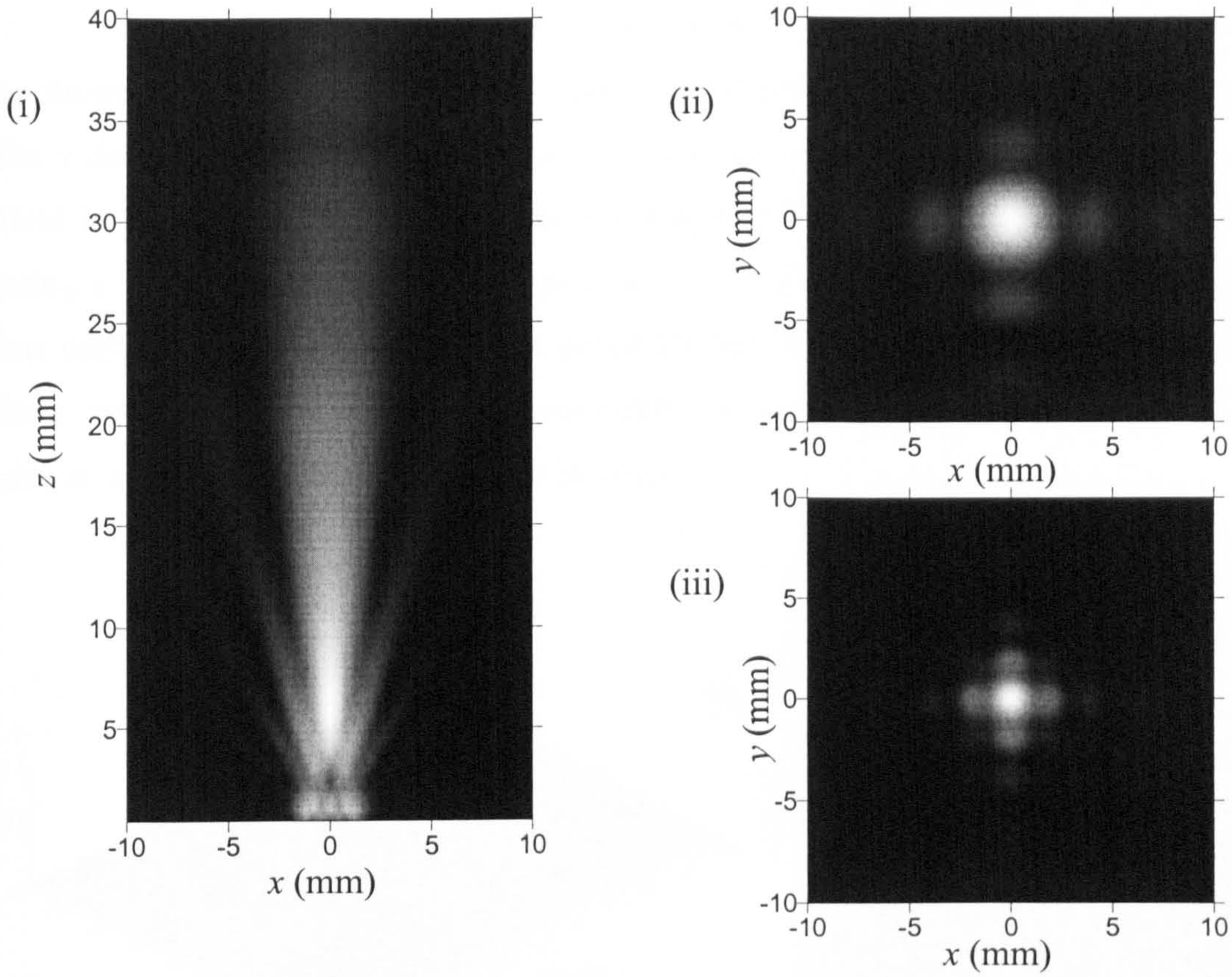

Figure 3.6: Predicted pressure field in air from a single 3.5 by 3.5 mm square source, in (i) the *xz* plane, and in (ii) and (iii) the *xy* plane at z = 14 mm and 7 mm respectively

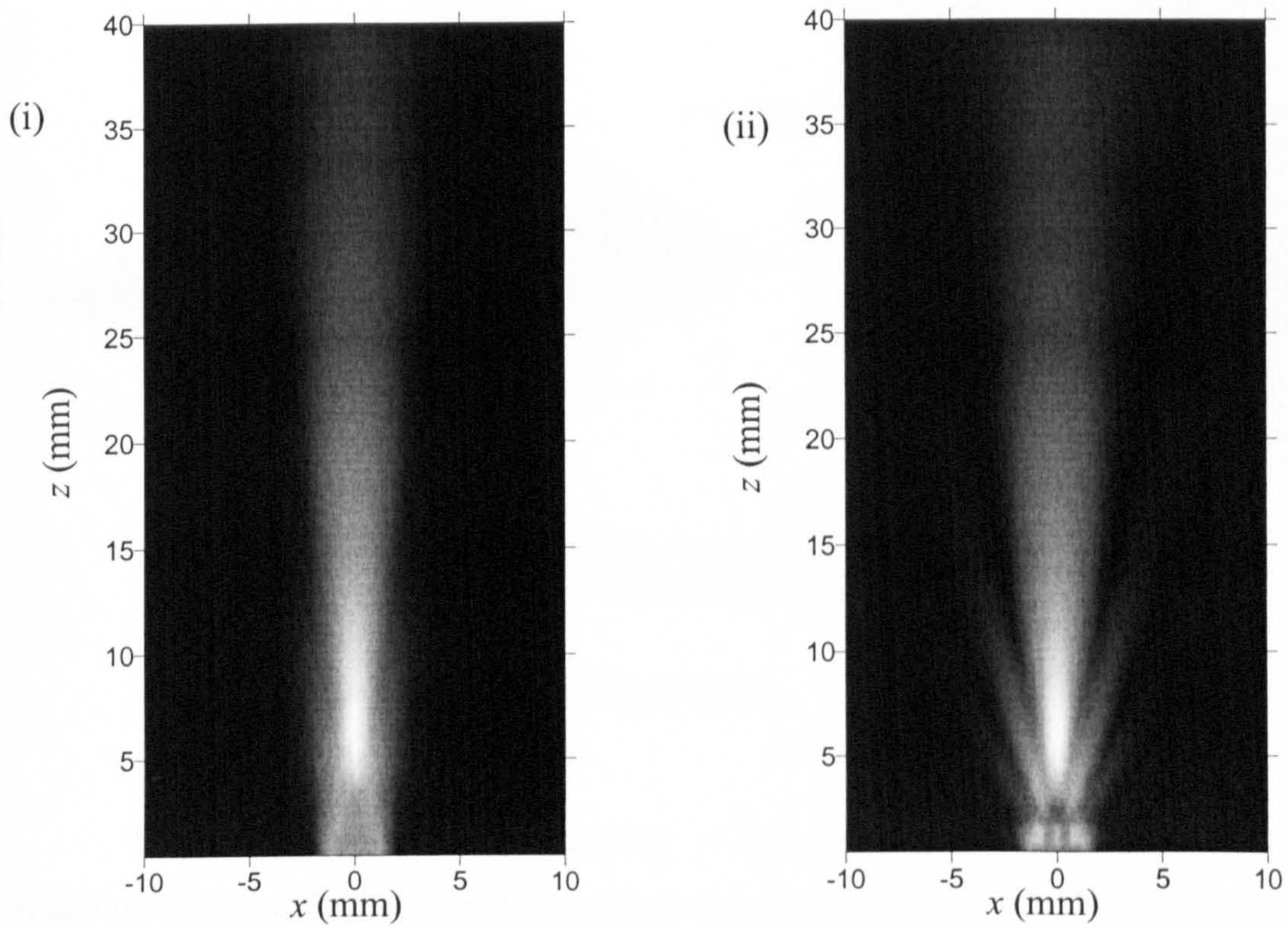

Figure 3.7: Predicted pressure field in air from a single 3.5 by 3.5 mm square source, in the *xz* plane, using a (i) broadband and (ii) a chirp drive signal

The single elements in a line array will be larger in one direction than the other as shown in Figure 3.1. So pressure fields from a rectangular device, which is 10 mm in the *y* direction, and 0.8 mm in the *x* direction, are shown in Figure 3.8. The pressure field in the *xz* plane, and the *yz* plane are shown in Figure 3.8 (i) and (ii), respectively, using a 500 kHz toneburst drive signal (K = 0.4). For clarity the form of presentation has been altered to a wireframe and greyscale plot in each case, the field size has also been increased to that required for modelling an array constructed of elements of this size so a more direct comparison can be made.

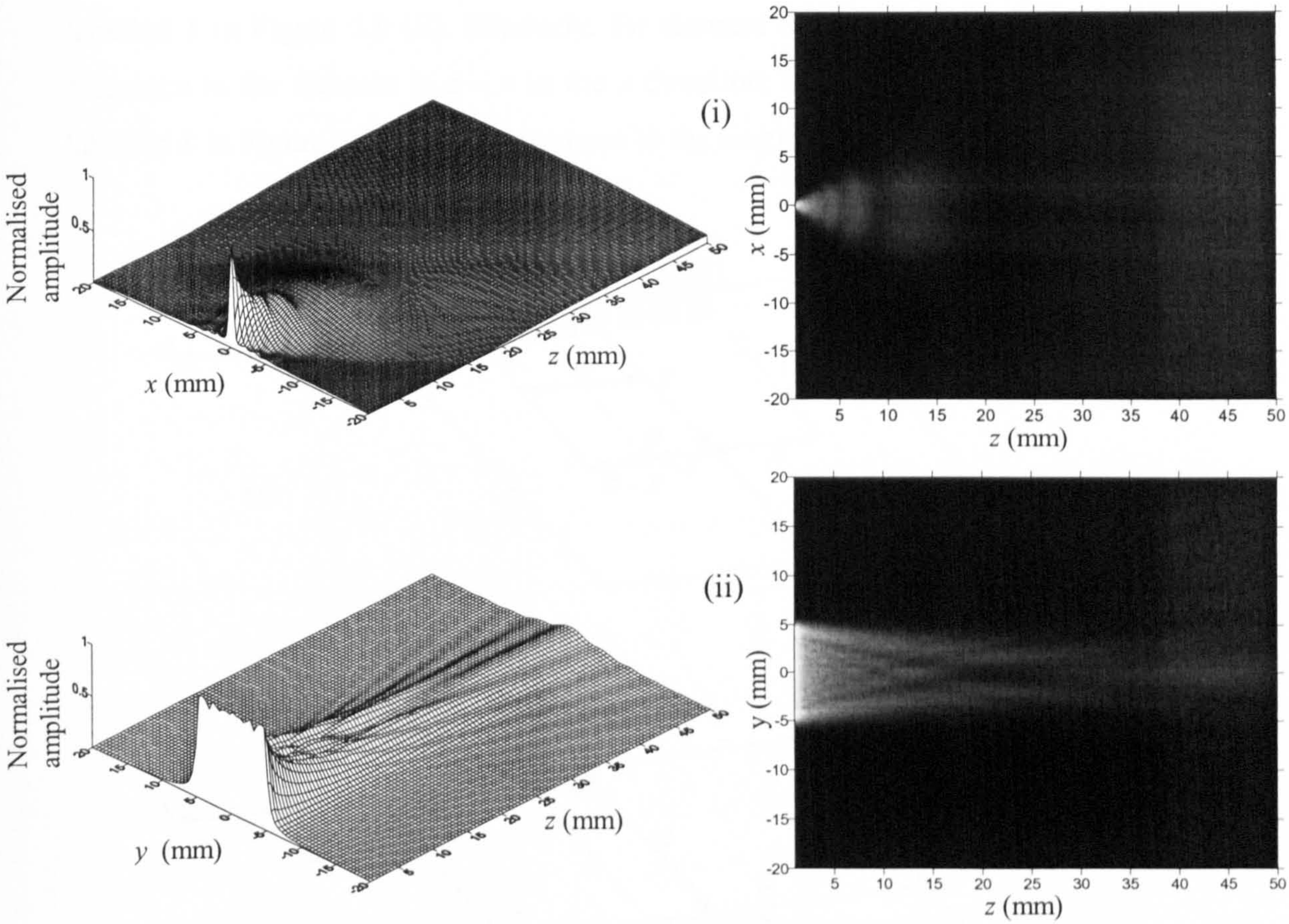

Figure 3.8 Predicted pressure field in air from a single 0.8 by 10 mm rectangular source, in (i) the *xz* plane, and in (ii) *yz* plane

3.4.2 Modelling the field of arrays in air

The pressure waveform at a point in the field can be found for a rectangular element, as was described and demonstrated in the previous subsection. This modelling technique will be adapted to the modelling of arrays. A simplification to the rectangular source Impulse Response model has been suggested by Ullate [18] for use in the

modelling of beam-steering in arrays, but there appears to be very little work in the literature on focussing using arrays. In Figure 3.9 (i) an array is shown. Consider a point in the field, P (x, 0, z), at this point the total pressure wave arriving from the array, is the same as the sum of the pressure arriving from each individual element. This means that instead of considering an array of elements this can be simplified to an array of points with a single element source as shown in Figure 3.9 (ii). The pitch of the points in the field will be the same as the pitch of the array. An illustration of this is given for elements 1 and 8. When considering an array of elements, the field point P is located at $x + a$, z with respect to element 1, where $a = 3.5 \times p$, and this is equivalent to the point labelled 1 in Figure 3.9 (ii). Similarly, for element 8, the position of the point P with reference to the element is $d - x$ in the x direction, so this is the position of the point labelled 8 in Figure 3.9 (ii) with reference to the single element, where $d = 3.5 \times p$.

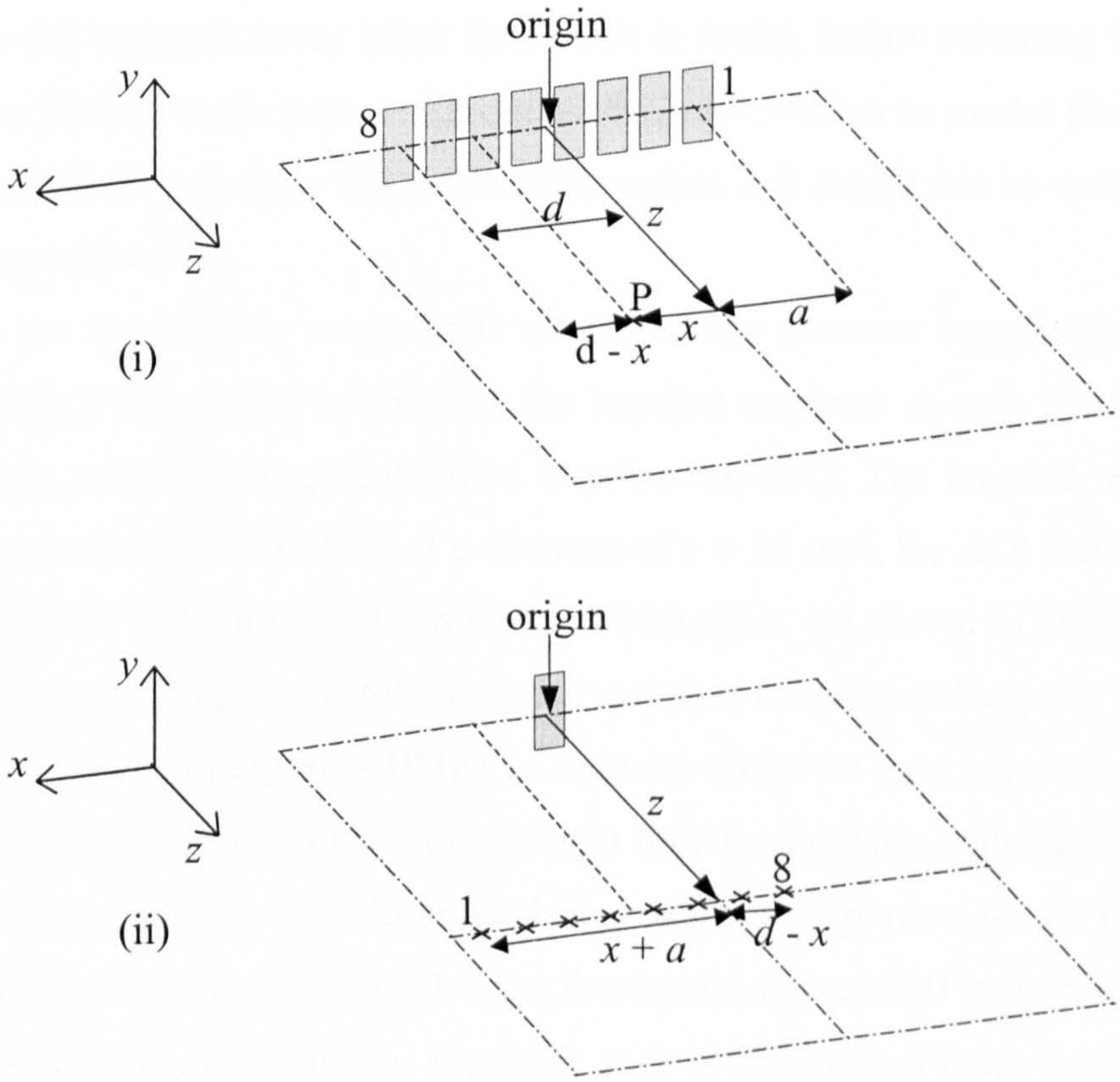

Figure 3.9: Simplifying (i) an array of elements with a field point to (ii) an element with an array of points

It is worth noting that because of the symmetry of the pressure field emerging from the single element as shown in Figure 3.9 (ii) in the $x = 0$ plane, the points relating to elements 7 and 8 which have a negative x coordinate can be reflected into the area of

positive x by taking the absolute of the x coordinate. The location of each point to be considered in place of each element (n), can then be expressed as

$$x^n_{point} = \left| x - x^n_{centre} \right|, \tag{3.14}$$

where x^n_{centre} is given by equation 3.1.

To find the total pressure at P it has been necessary to find the pressure due to a single element at 8 points as previously described, each of these points are on a pitch of p, the same as the array pitch. If the next point to be considered by a program finding the pressure field is point Q located at a displacement in x direction of a distance p from point P, then many of the calculated waveforms will be the same. In fact the number of common waveforms will be N-1, albeit with a different set of phase values. By utilising this fact it is possible to greatly reduce the computer processing time. Consequently the restriction that the step size in the x direction must be related to p is used, for example $p/2$. In this example every other field point is found, before returning to the start of the loop and filling in the holes. A program has been written to model phased arrays using this method in both the x and y direction, so that 2-D arrays can be modelled efficiently, (see Appendix B.1).

As the impulse response is related to the pressure by equation 3.12 (a linear equation), it is possible to consider the impulse response at each point, rather than the pressures, summing to give the total impulse response. The impulse responses arriving at a point on-axis in the field at a distance of $z = 20$ mm, for an 8 element array, where each element is 0.8 mm by 10 mm on a 1 mm pitch, are shown in Figure 3.10 (i). These can be summed to give the total impulse response arriving at that point from that source, and this is given in Figure 3.10 (ii). In order to achieve a focussing effect, it is necessary to shift each of these impulse responses in time by applying a phase to each element, as found using equation 3.3. The time shifted impulse responses are shown in Figure 3.10 (iii), where they are phased so that the focal point is at $z = 20$ mm on axis. The resultant total impulse response in the focussed case is shown in Figure 3.10 (iv). The total impulse response is convolved with the time differential of the piston velocity waveform and multiplied by the medium density to give a pressure waveform. In this case a toneburst velocity waveform centred at 500 kHz is used ($K = 0.4$). This is done for each case, the pressure for the unfocussed case is shown in Figure 3.10 (v) displayed as a comparative amplitude to the focussed case, which has been normalised and is shown in Figure 3.10 (vi).

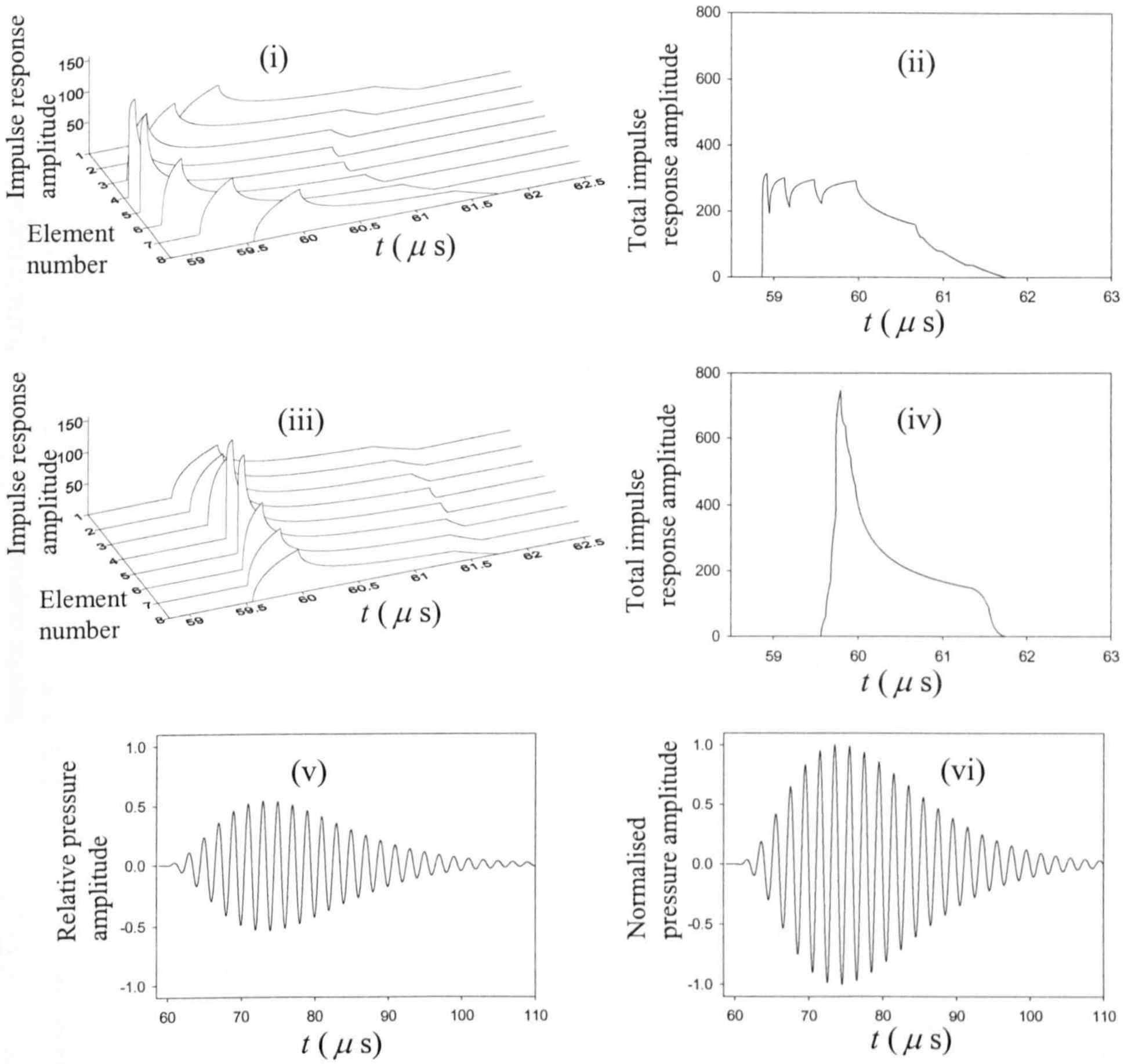

Figure 3.10: Demonstrating the affect of phasing at the focal point. (i) The unfocussed impulse response from each element of an 8 element array, and these are summed in (ii). (iii) The effect of phasing when located at the focal point, and these are summed in (iv). The resultant pressure waveform can then be seen for the unphased case (v), and the phased case (vi)

It can be seen from Figure 3.10 (v) and (vi) that the focussed pressure amplitude is double that of the unfocussed case. However, larger changes occur, at points displaced a small distance from the focal point. In Figure 3.11 the relative pressure (that is relative to Figure 3.10 (vi)) arriving at a point at position, $x = 1.5$ mm, $y = 0$ mm, and $z = 20$ mm, is given for the unphased case and the case where the phasing causes a focal point at $x = 0$ mm, $y = 0$ mm, and $z = 20$ mm. In Figures 3.11 (i) and (iii) the impulse responses due to each element are given in firstly the unphased and then the phased scenario. Again these are summed to give the total impulse response for (ii) the unphased case and (iv) the phased case. These summed impulse responses are used to

find the pressure waveform, which are shown relative to the pressure arriving at the focal point in Figures 3.11 (v) and (vi) for the unphased and phased case.

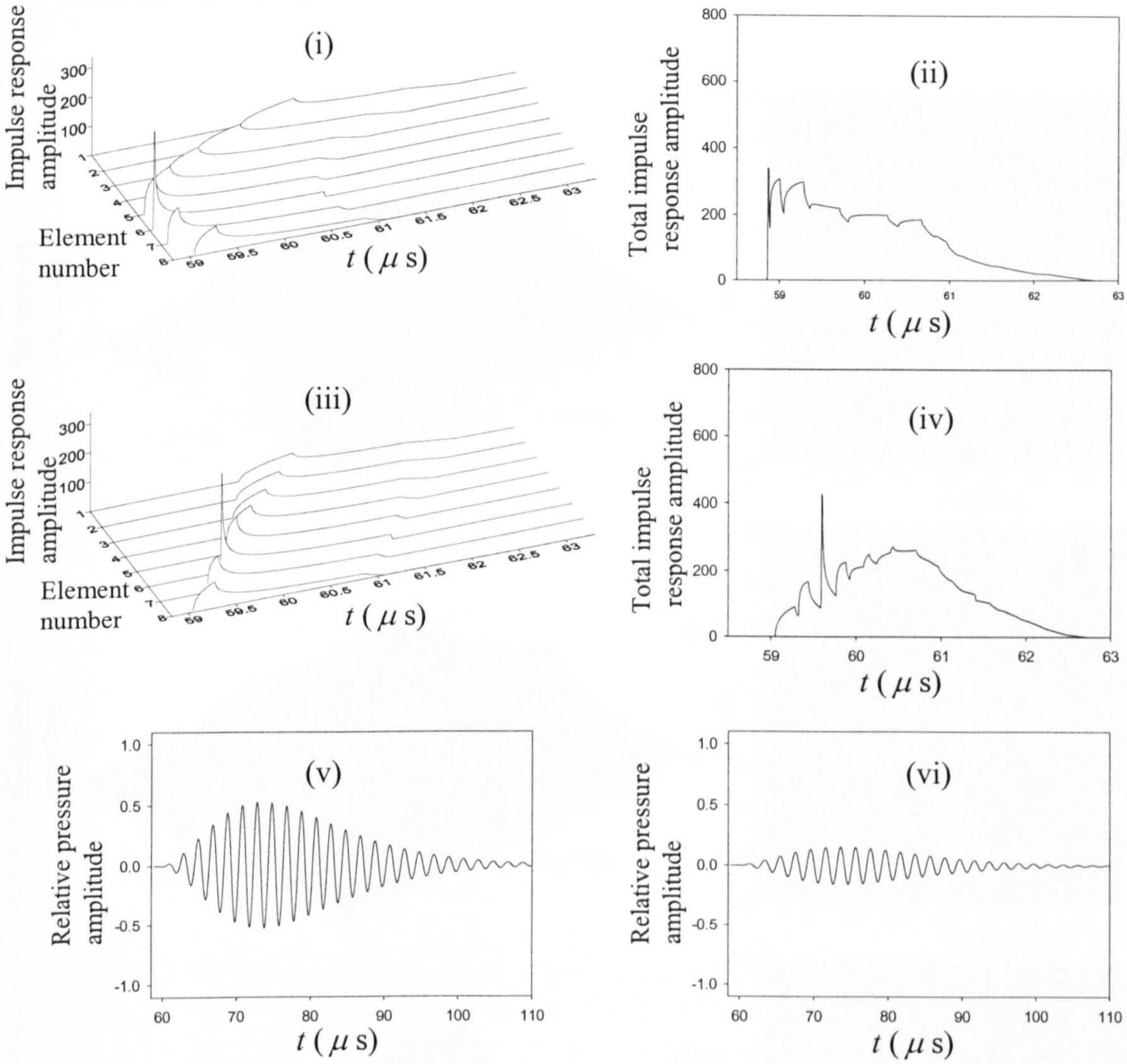

Figure 3.11: Demonstrating the affect of phasing at a point displaced from the focal point by 1.5 mm, (i) shows the unfocussed impulse response from each element of an 8 element array and these are summed in (ii), (iii) shows the effect of phasing, and these are summed in (iv). The resultant pressure waveform can then be seen for the unphased case (v), and the phased case (vi)

It can be seen that in the focussed case the ratio of the pressure amplitudes at the focal point at 0, 0, 20 mm, and the point 1.5, 0, 20 mm is 6:1, whilst for the unfocussed case the ratio is approximately 1:1. Hence a focussing effect is observed.

Using the method described above of finding the impulse response at 8 points (for an 8 element array), and applying the phasing to each in turn prior to summing, the pressure field emerging from a phased array can be found. This has been done by way of an example for an 8 element array of 0.8 mm by 10 mm elements on a 1 mm pitch.

The normalised pressure fields from such an array when driven by a 500 kHz toneburst ($K = 0.4$), in the case of no phasing, focussed at x = 0 mm, y = 0 mm, and z = 20 mm, and focussed at x = 5 mm, y = 0 mm, and z = 20 mm, are shown in Figures 3.12 (i), (ii) and (iii) respectively.

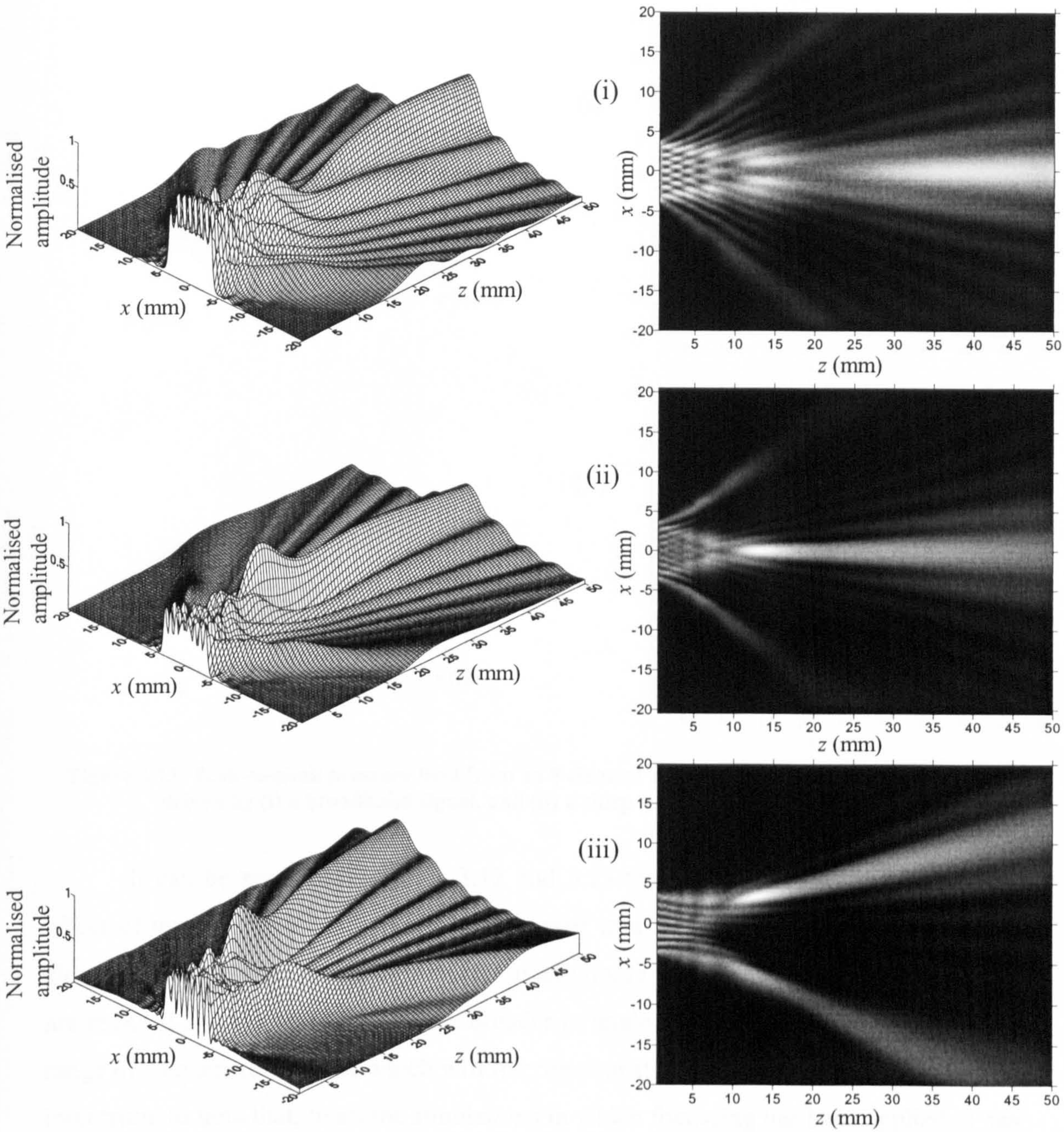

Figure 3.12: Predicted peak-to-peak pressure field in air from an 8 element array, driven by a 500kHz toneburst, for (i) all elements in phase, with (ii) and (iii) phased with the phases calculated such that they are focussed at (ii) $x = 0$ mm, $y = 0$ mm and $z = 20$ mm and (iii) $x = 5$ mm, $y = 0$ mm and $z = 20$ mm

Figure 3.13 (i) shows the peak-to-peak pressure field when phasing is applied to each element calculated to give a focal point at $x = 0$ mm, $y = 0$ mm, and $z = 20$ mm,

with each element driven with a broadband signal centred at 500 kHz (K = 3.5). The array used is the same as that described for Figure 3.12. In the case of Figure 3.13 (ii) the same phasing is applied but the drive signal on each element is changed to a chirp centred at 500 kHz, with a 500 kHz bandwidth and a duration length of 500 μ s.

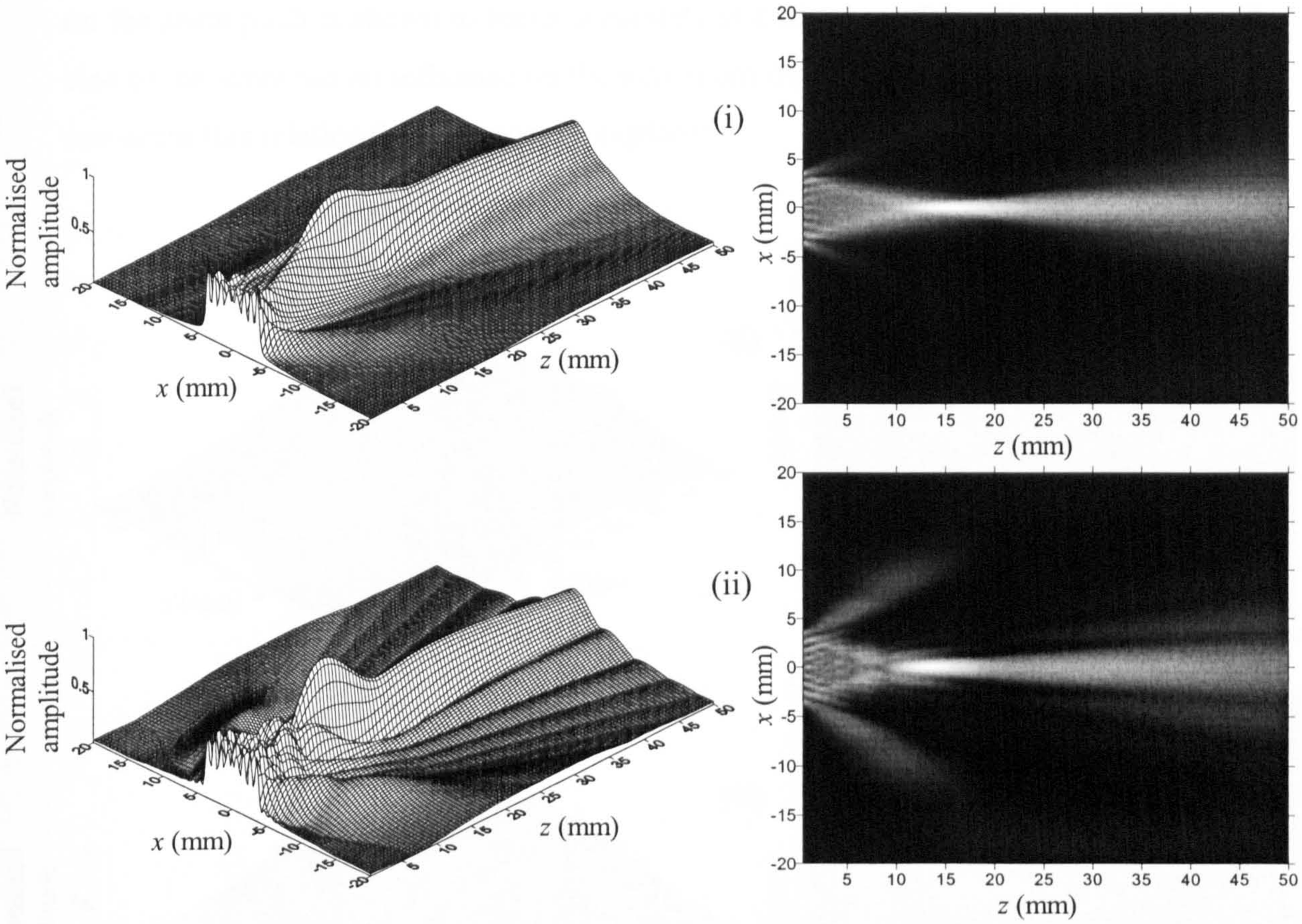

Figure 3.13: Peak-to-peak pressure field from an 8 element array, focussed on 0 mm, 0 mm, 20 mm driven by (i) a broadband signal, and (ii) a chirp signal both centred at 500 kHz

It can be seen from Figures 3.12 and 3.13 that as with the single element the effect of using a broadband signal as compared to a toneburst drive signal is that the side and grating lobes are much reduced in amplitude. For a chirp signal the side lobes are reduced and the grating lobes are broader in angle. This is due to the presence of a range of frequencies each of which will interfere constructively at a different angle. It is interesting to note that, in all the simulations in which focussing has been applied, it can be seen that the focal point is not where it would be expected to be. For the case of focussing at x = 0 mm, y = 0 mm, and z = 20 mm, the peak amplitude occurs at approximately z = 15 mm, whilst for the case of focussing off axis in Figure 3.12 (iii) the peak amplitude occurs at approximately x = 4 mm, y = 0 mm, and z = 15 mm, rather

than the position of $x = 5$ mm, $y = 0$ mm and $z = 20$ mm which was used to calculate the phase differences. This shows a limitation of the ability of this array to focus at these points, not an error in the simulation. This can be seen from Figures 3.14 (i) where the 8-element array is seen to focus accurately at $x = 0$ mm, $y = 0$ mm and $z = 12$ mm. In Figures 3.14 (ii) a sixteen element array of the same sized elements as used previously on the same pitch is shown to focus accurately at a distance of $z = 20$ mm. The overall size of the array has an influence on the maximum distance at which accurate focussing can occur this relationship will now be explored.

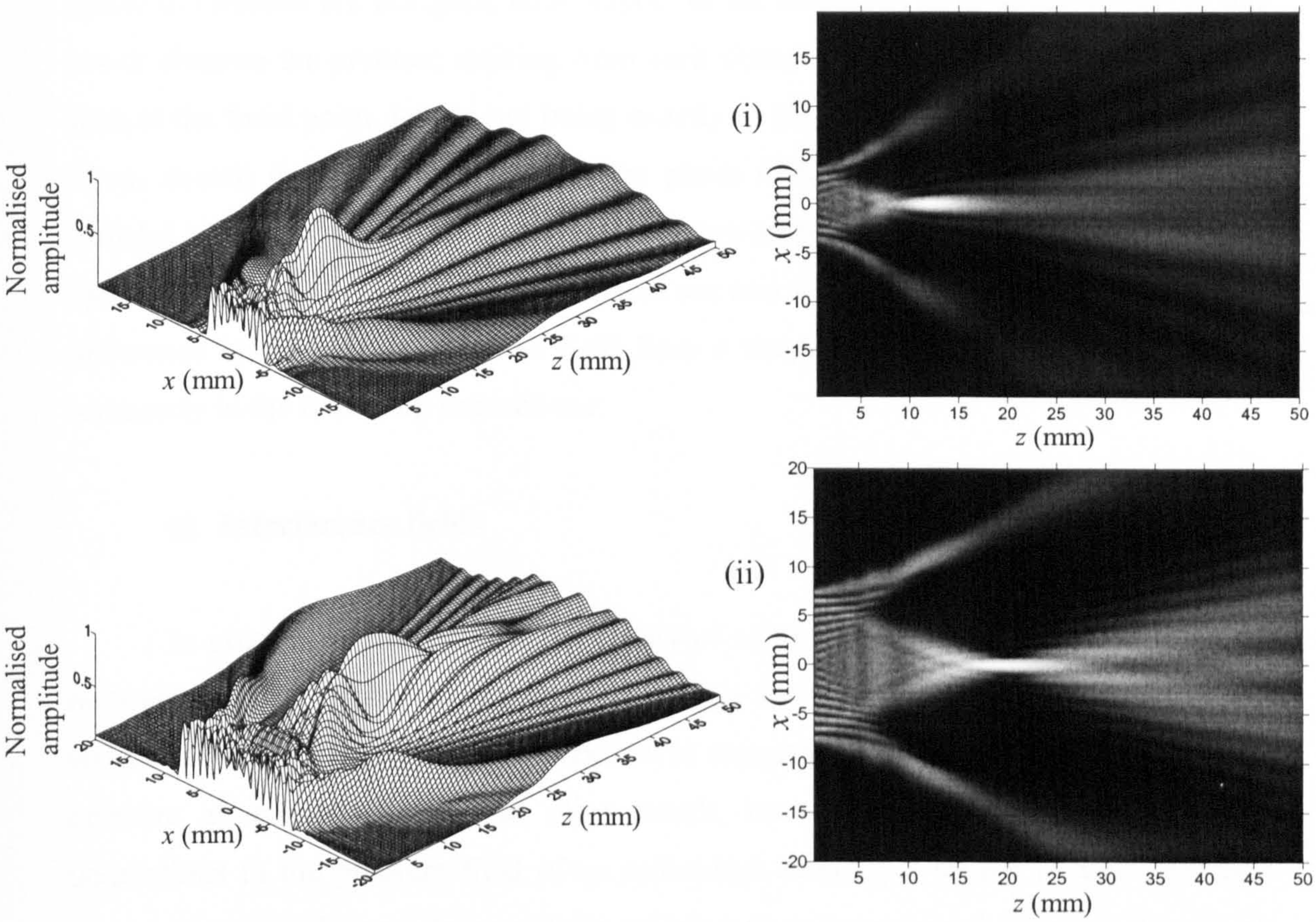

Figure 3.14: Demonstration of the fact that accurate focussing can be achieved, for (i) an eight element array focussed at x = 0 mm, y = 0 mm and z = 12 mm, and for (ii) a sixteen element array focussed at x = 0 mm, y = 0 mm, and z = 20 mm in air

3.4.3 Designing arrays for focussing

It is important firstly to understand why the point of maximum pressure amplitude is not at the focal point for the cases shown in Figures 3.12 and 3.13. The phase difference applied to each element is calculated to cause the pressure waveform arriving from each individual element to arrive in time. The difference in the phase

applied to each element will become less the further from the array the focal point is located. This can be seen from equation 3.2, as the z_f term is increased in size the variation in pl_f for each element will decrease. It is this difference in the phase, which is applied to each element, which causes the focussing. Hence, when the amount of phasing is decreased the focussing will be less pronounced. The calculated pressure field is shown in Figure 3.8 for a single element measuring 0.8 ×10 mm, driven by a 500 kHz toneburst. It can be seen in Figure 3.8 (ii) that, at a distance of z = 15 mm from the element that the pressure amplitude is greater than at z = 20 mm. If then the phase differences are not great with respect to the frequency, it is possible that at this lower distance the pressure arriving from each element will add to give a greater value than at the focal point despite not being exactly in phase. In the case of the 16 element array, shown in Figure 3.14 (iii, iv) the phase differences applied to each element differed enough to ensure the maximum pressure amplitude occurs at the focal point. It can be seen from this explanation that there are two key factors involved: the degree of difference in the phasing, and the field from a single element. These will be studied separately in the following subsections.

a) Interference fields

In order to explore further the ability of an array to focus correctly, an array of notional sources has been considered, in which the pressure field of each individual source is flat, i.e. the maximum pressure at any point is the same as the maximum pressure at any other point. In other words, because part of the problem is the undulations in the pressure field of an individual element, a source is used in which there are no undulations, these will be referred to as "conceptual sources". It will be assumed that each of these conceptual sources is driven with a continuous sinusoidal waveform, for the case of a broadband signal it has already been seen that the major effect is a lessening of the grating lobes. The pathlength to a point in the field is found from each of the elements, and phasing is then used in conjunction with the pathlength to find the relative phase of the sine wave arriving from each element. The maximum peak-to-peak value is then calculated. This will be termed the "interference value", as it is the degree to which the interference is constructive or destructive, and will be plotted as part of an "interference field". Figure 3.15 shows the interference field from an 8

element array of point sources on a pitch of 1 mm, when focussed (i) at $z = 20$ mm, and (ii) focussed at $z = 12$ mm. Figure 3.15 (iii) shows the interference field from a 16 element array focussed on axis at $z = 20$ mm. In all three cases a 500 kHz drive signal is used. It can be seen in Figure 3.15 that, for an increased number of elements, and a focal point closer to the array, a better focussing effect is achieved, (the Matlab program written to generate these images can be seen in Appendix B.2).

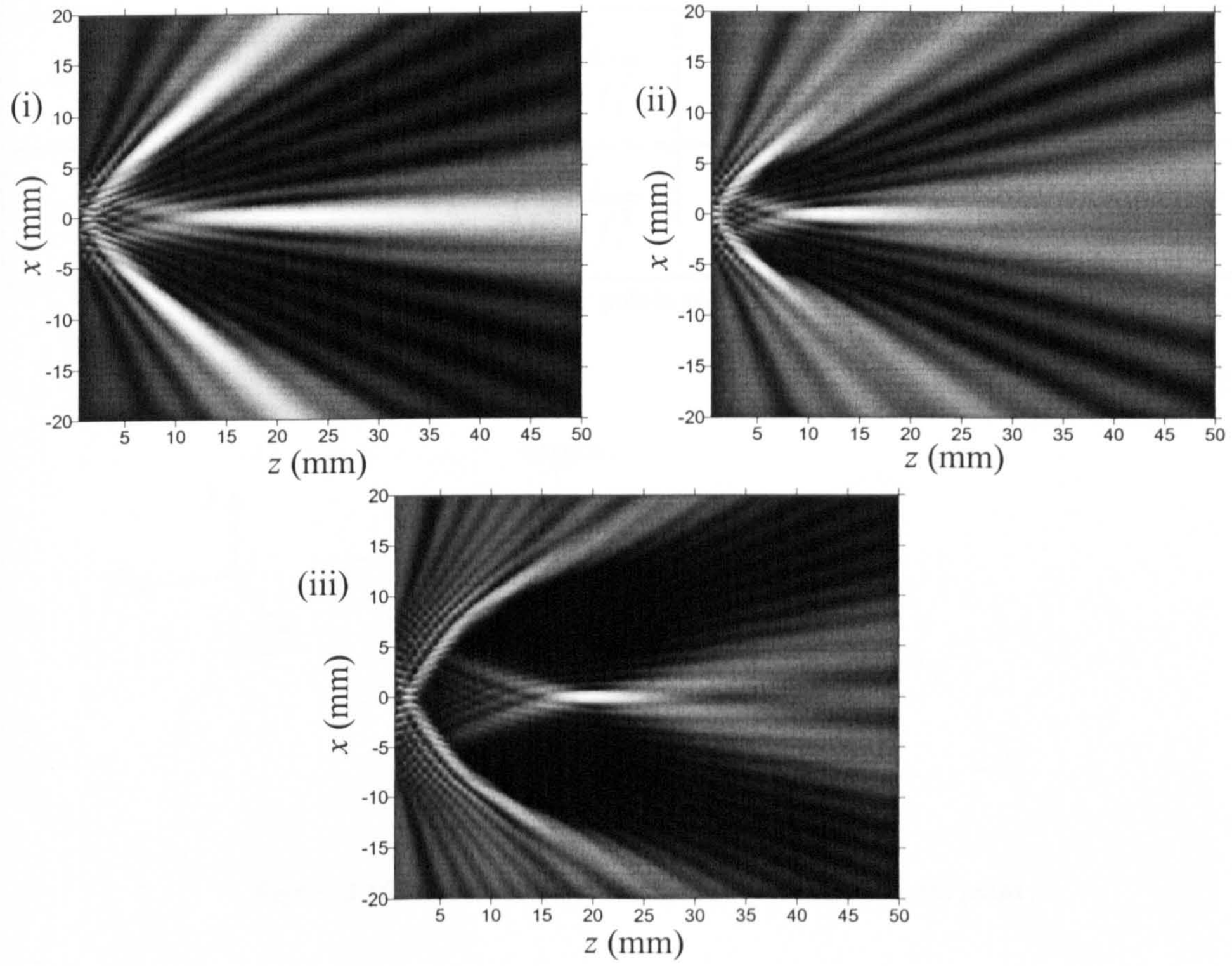

Figure 3.15: The interference fields from an array of conceptual sources on a pitch of 1 mm driven by a phased 500 KHz waveform, in (i) 8 sources are focussed at z = 20mm, in (ii) 8 sources are focussed at 12 mm, and in (iii) 16 sources are focussed at z = 20 mm

This approach can be extended to investigate the area over which a particular size of array of conceptual sources can focus by considering the rate at which the interference drops off as the point of consideration moves away from the focal point, This will be termed the "comparative interference field". The focal point is moved to each point in the field in turn, and at each of these new focal points the phasing is calculated. Four points are then considered around the focal point and compared in

amplitude to the interference value obtained at the focal point. The location of these four points is given in Table 3.1.

Here, d_1 to d_4 is the distance from the focal point to points 1 to 4 respectively. An example of this can be seen in Figure 3.16, the four points considered around the focal point, represented as black dots, are labelled as 1 to 4 as in Table 3.1.

Point:	1	2	3	4
x	$f_x + \frac{d_1 \cdot f_x}{\sqrt{f_x^2 + f_z^2}}$	$f_x + \frac{d_2 \cdot f_z}{\sqrt{f_x^2 + f_z^2}}$	$f_x - \frac{d_3 \cdot f_x}{\sqrt{f_x^2 + f_z^2}}$	$f_x - \frac{d_4 \cdot f_z}{\sqrt{f_x^2 + f_z^2}}$
z	$f_z + \frac{d_1 \cdot f_z}{\sqrt{f_x^2 + f_z^2}}$	$f_z - \frac{d_2 \cdot f_x}{\sqrt{f_x^2 + f_z^2}}$	$f_z - \frac{d_3 \cdot f_z}{\sqrt{f_x^2 + f_z^2}}$	$f_z + \frac{d_4 \cdot f_x}{\sqrt{f_x^2 + f_z^2}}$

Table 3.1: Location of four points surrounding the focal point

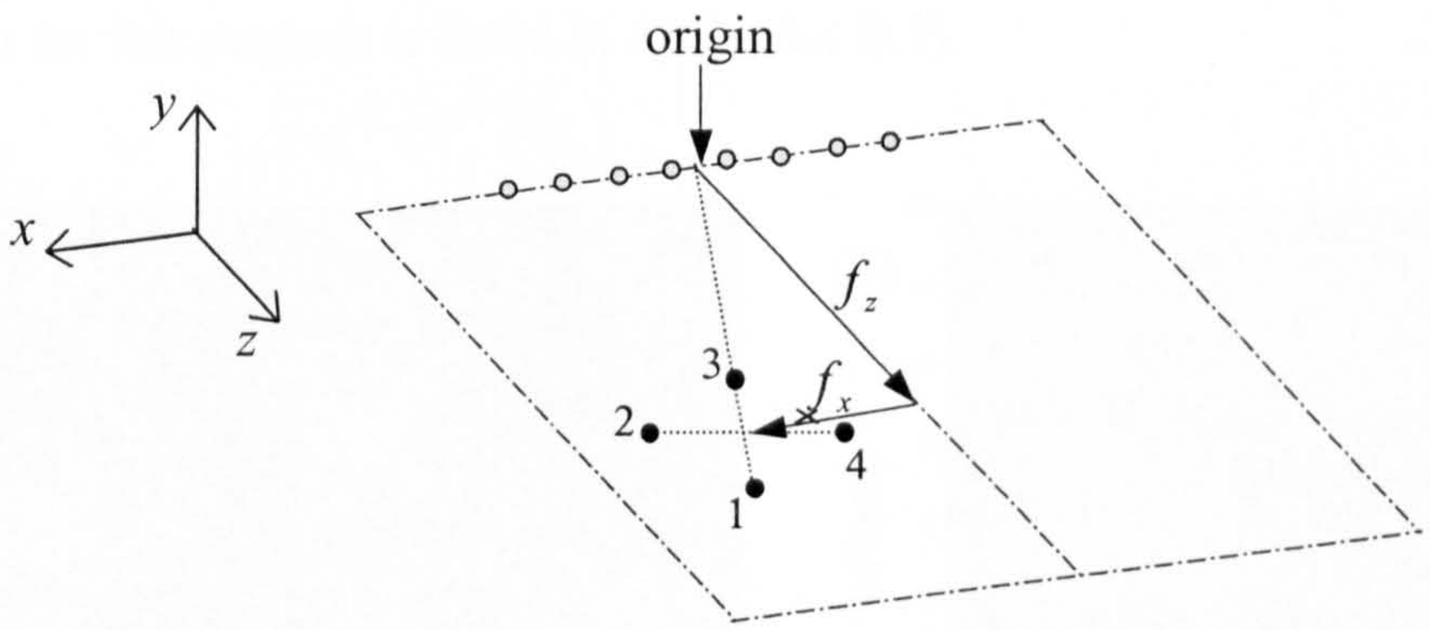

Figure 3.16: The location of four points around the focal point

For an array, which is to be used for locating an object, for example, then it would be necessary to know the area in which a reasonable degree of focussing may be achieved. In such a scenario this method can be used to see the tightness of the interference field. The points labelled as 1 to 4 serve different purposes in Figure 3.16. The effect of the focal point spreading in the direction of point 1 is not so critical as it can be eliminated by considering the time of flight. The time of flight could also be used to lessen the importance of point 3. However, it has been seen that if the interference field has a large focal area in this direction, then the nature of the individual element field may be such as to cause an area of maximum pressure in the incorrect place. Points 2 and 3 govern the tightness of the focal point normally to the line from the centre of the

array to the focal point. Consequently, the image shown in Figure 3.17 (i) is of an 8-element array on a pitch of 1 mm operating at 500 kHz, with d_1 to d_4 set at 8.0, 1.5, 4.0, 1.5 mm respectively. The higher degree of focussing predicted by the interference field is indicated by a lighter shading, the contour changes occur at a drop to 0.25, 0.5, and 0.75 of the interference value at the focal point. In each case the interference value is equated to the lowest value from the four points. Figure 3.17 (ii) shows a similar image with the change that the array now consists of 16 elements. It can be seen that the lighter area extends considerably further for the 16 element case. Looking at a distance of z = 20mm, it can be seen that in the 16 element case there is some degree of focussing, whilst in the 8 element case there is very little possibility. This is in agreement with a real array of finite sources. As shown earlier in Figure 3.13 (iii, iv), an eight element array phased in order to achieve focussing at 20 mm had a maximum pressure at a considerably lower distance, whilst in Figure 3.14 (iii,iv) a sixteen element array was shown to be able to have a focussing effect at 20 mm, (the Matlab program written for this purpose is listed in Appendix B.3).

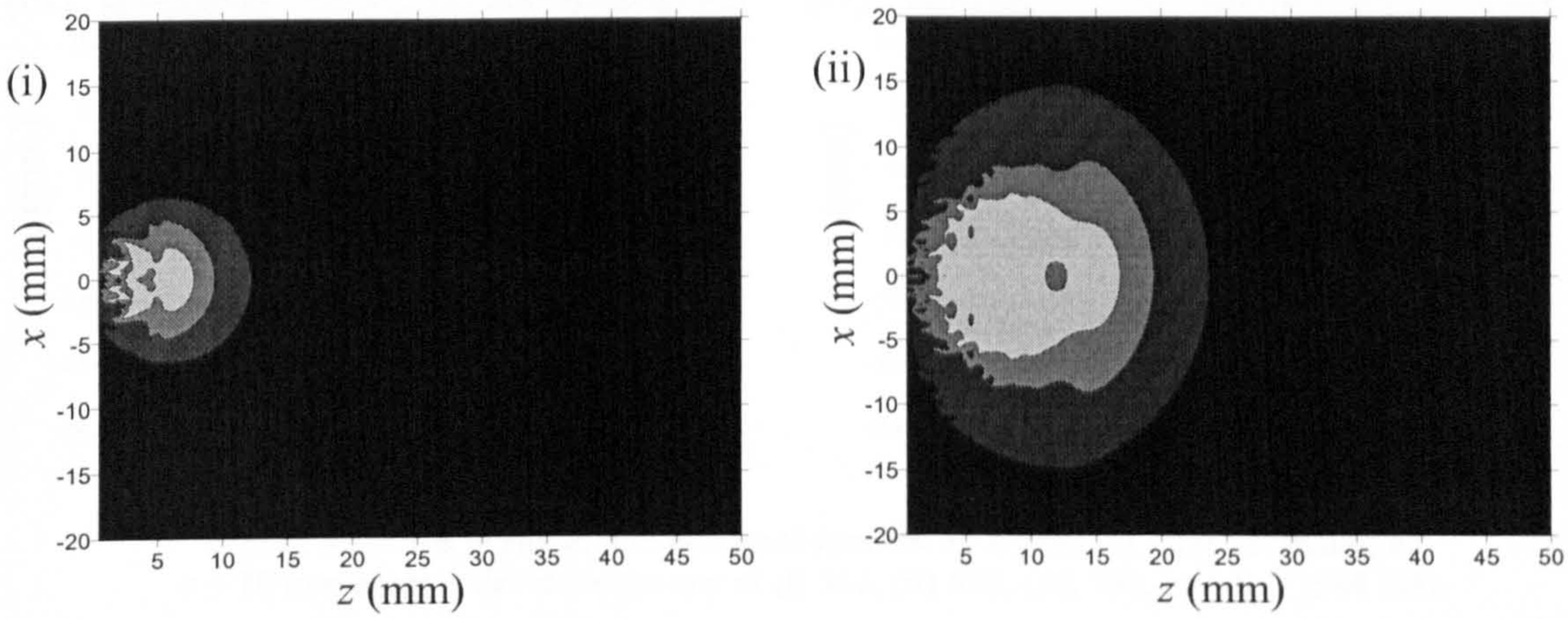

Figure 3.17: Predicting the focussing ability using the interference method for (i) 8 elements on a pitch of 1mm, and (ii) for 16 elements, using in both cases a frequency of 500 kHz

This method of procedure is helpful for the design of arrays if the drive signal applied to each element is a short broadband pulse, in which case the grating lobes can be ignored. However, if a longer pulse is to be used then grating lobes must also be considered. The criteria, which dictate whether grating lobes will be present in the pressure field, will be studied using the interference field.

b) Side lobes

The same array of 8 conceptual sources on a 1 mm pitch has been focussed theoretically on axis at a distance of z = 20 mm, using different frequencies up to 1 MHz. This is shown in Figure 3.18. It can be seen that as the frequency increases the prevalence of side lobes increases.

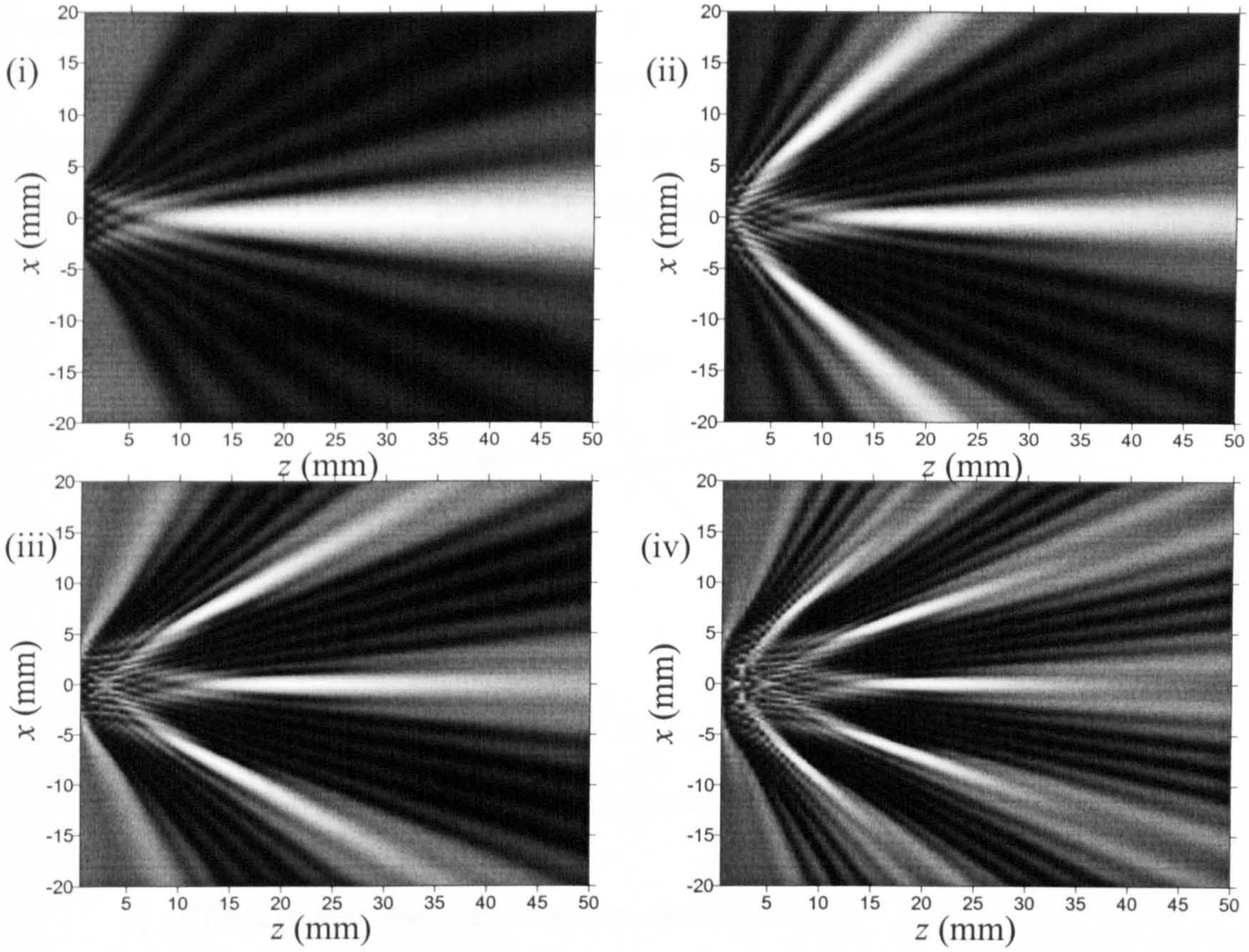

Figure 3.18: An array of 8 conceptual sources on a pitch of 1mm focussing at z = 20 mm using a drive frequency of (i) 300, (ii) 500, (iii) 700, and (iv) 1000 kHz

Side lobes occur when the signal from two devices arrive out of phase at a particular point by one wavelength. If then the frequency is increased, the wavelength is decreased, so side lobes can occur at a lower angle to the main lobe. The case in which most side lobes will occur is when the device is focussed on the array surface at an x value such that it lies outside the array. In this case the difference in phase between adjacent elements is p/c. In order that no side lobes can occur it is therefore necessary to make the pitch $\lambda/2$, as then even at an angle of 90° normally to the array the difference between the two elements is λ. This can be seen more clearly in Figure 3.19 where for the purpose of clarity a two-element array is considered. The focal point is marked with

the purpose of clarity a two-element array is considered. The focal point is marked with a black dot. The phasing is such that element 1 is fired at a time of p/c ahead of element 2. If then a grating lobe is to occur at point P then the signals superimposing from the two elements must be one wavelength out of phase. The arrival time at point P of the signal from element 1 will be d/c, whilst that from element 2 will be $(d+p)/c + p/c$ where the second term is due to the phasing. The time difference is then $2p/c$. For the difference to be a wavelength then the pitch must be $\lambda/2$. So, for no side lobes to occur, then the pitch must be less than $\lambda/2$.

In reality, because of the directivity of the single element, even if a side lobe occurs at a large angle from the normal to the device, the amplitude will be small. Hence, these criteria need not be strictly applied, so long as the area of focus is restricted so that no large lobes appear.

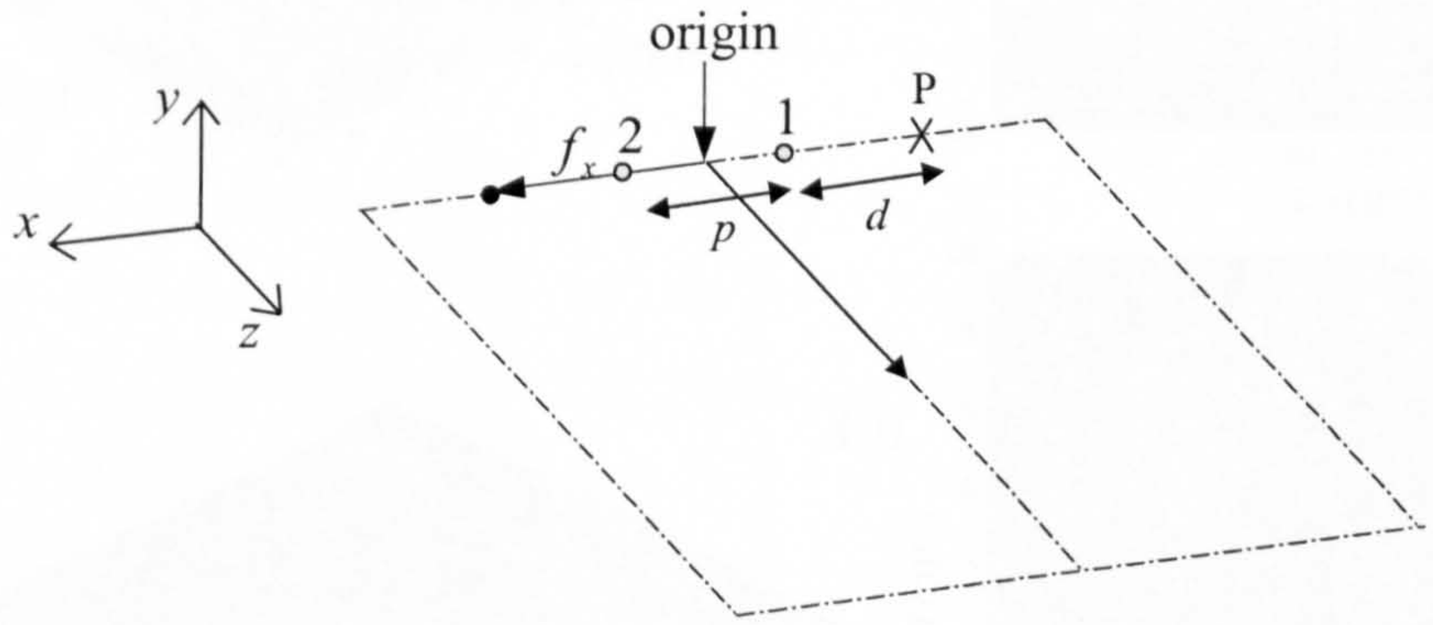

Figure 3.19: Elimination of side lobes

c) Effect of element size on array characteristics

The idealised interference fields have been calculated using arrays of conceptual sources. The comparative interference field has been derived to give an indication of the tightness of the focal point, in order to avoid the occurrence of a maximum pressure at a point other than the intended focal point. However with the use of real finite sources it is also necessary to consider the field pattern of a single source. As the width of a single source is increased the directivity of the source will increase, for a constant frequency. In the case of the interference fields the sources were effectively omnidirectonal, in reality this will not be the case. The directivity of an individual source means that for certain focal points, not all the sources will contribute to the pressure at that point, as it may lay outside the directivity of the individual source, consequently the degree of

focussing will not be as good as the interference field suggests. In this Subsection the way in which the directivity of each individual element limits the ability of the array to focus in certain areas will be investigated.

In Figure 3.20, the field from a single element of 0.8 by 10 mm is shown when driven by a frequency of (i) 500kHz, and (ii) 1 MHz. It can be seen that in the higher frequency case the directivity is significantly greater.

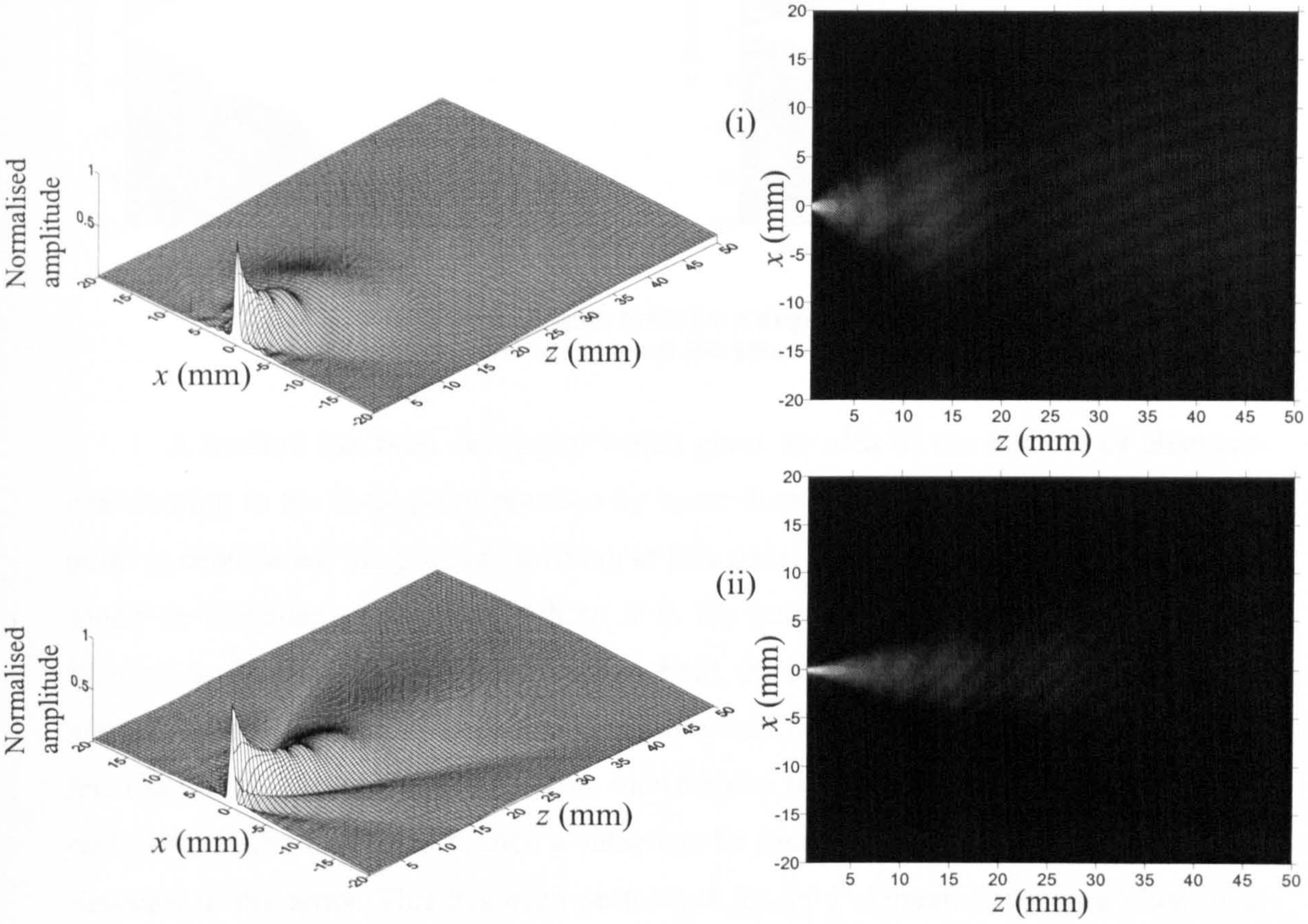

Figure 3.20: The pressure field of a single 0.8 by 10 mm element drive by toneburst signal centred at (i) 500 kHz and (ii) 1 MHz

When this is applied to the use of an array of such elements, then it is clear that the contribution from a particular element to the pressure at the focal point will decrease with distance in the *x* direction, and this is considerably more pronounced for the higher frequency case. Effectively this means that at the focal point the pressure is made up of signals coming from fewer elements than the array consists of. To demonstrate this a further program has been written. This takes the single field and calculates whether the maximum pressure at each point is greater or less than half the maximum pressure at the same z distance on axis. If the pressure is greater than half the axial pressure, then that

point is accorded the value of 1, all other points are 0. This yields a field as shown in Figure 3.21 for the same two elements as were used in Figure 3.20. These are termed "half axial pressure fields".

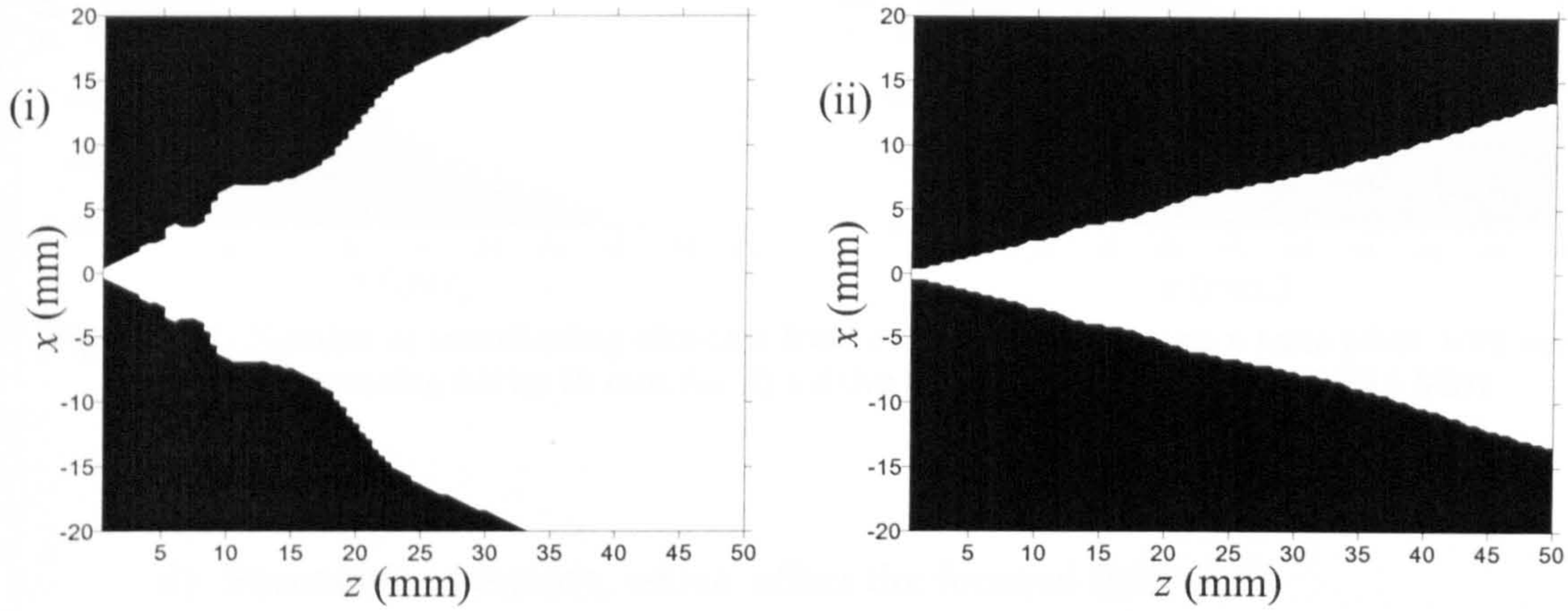

Figure 3.21: Half axial pressure fields for a single element 0.8 by 10 mm, for (i) a drive frequency of 500 kHz, and (ii) 1 MHz

A method has been developed which gives an idea of the number of elements contributing to the focal point pressure by more than half the axial pressure. If a focal point is considered, the pressure arriving at this point from an array of elements can be found by considering N points, where N is the number of elements as explained in Figure 3.9. By using the half axial pressure field, the location of these points shows how many elements are located such that more than half the axial pressure can arrive at the focal point. If, like in the comparative interference fields, the focal point is moved to each point in the field in turn, then a value can be found for the number of contributing elements in the array. This has been performed for an 8 element array on a pitch of 1 mm, each 0.8 by 10 mm. The results are presented in Figure 3.22 for (i) a 500 kHz drive signal, and (ii) a 1 MHz signal, (the Matlab program written to produce these images is listed in Appendix B.4).

It can be clearly seen from Figure 3.22, that the higher frequency (and so more directive) single element pattern causes less elements to contribute to the focal point. As it has already been seen that the number of elements has a large effect on the comparative interference field, it can therefore be deduced that the lower frequency case will be able to focus well over a larger field area.

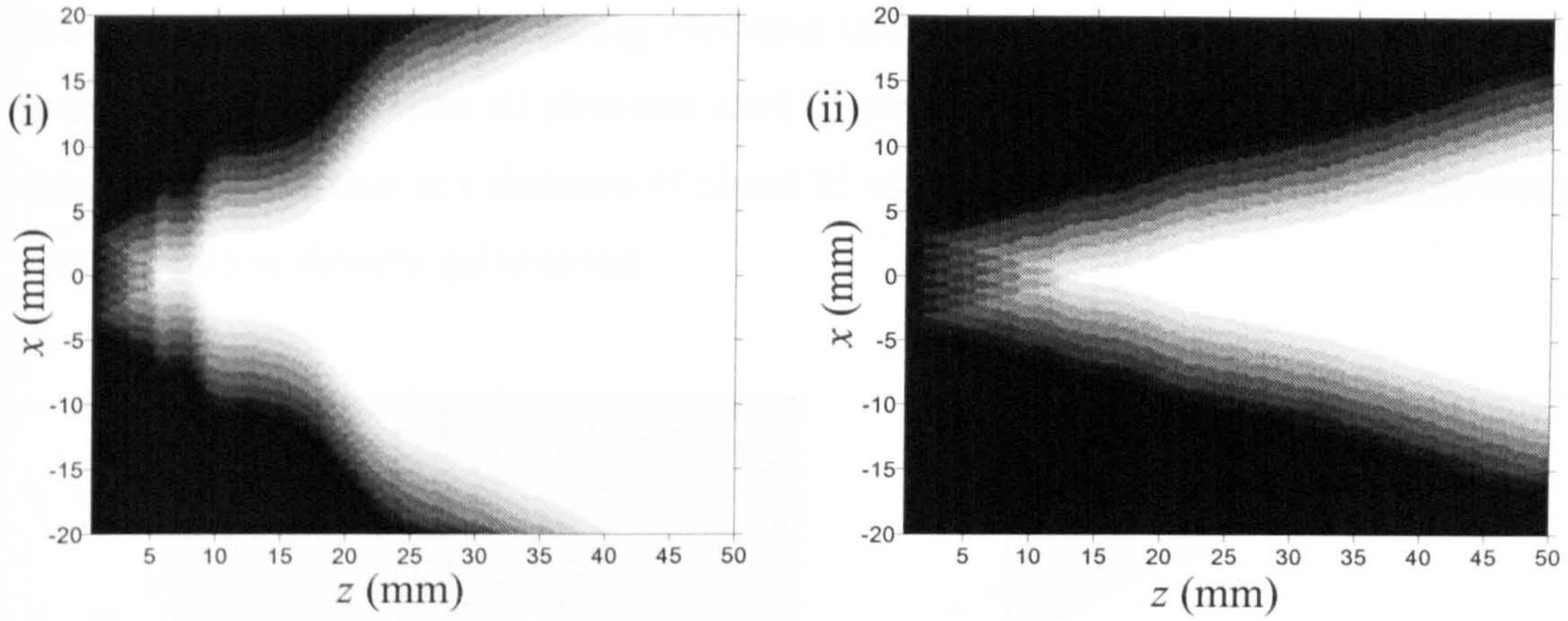

Figure 3.22: Number of contributing elements from an 8 element array on a 1mm pitch, with each element measuring 0.8 by 10 mm, for (i) a drive frequency of 500 kHz, and (ii) 1 MHz

d) Summary of factors, which affect the focused field

Two methods have been developed which are intended to give an indication of the performance of a linear array in focussing operation. The restrictions on the area of focus depends on the inability of the array even in the ideal case of conceptualised sources to focus sharply at certain locations. These were discussed with reference to the interference field, and by studying four points around the focal point, whilst sweeping the focal point through the field. The directivity of the element itself restricts the area of effective focussing, as at certain focal points the array effectively consists of less contributing elements. In addition if a signal is to be used which is not a broadband pulse, then the restriction of either the pitch being less than half the wavelength must be imposed, or the pitch can be greater but the focal point cannot be located in some parts of the field to avoid side lobes.

Several different factors governing the performance of arrays in focussing operations have been discussed in this Chapter. These will be applied to an air-coupled array, which is to be used experimentally in the following Chapter. This is an array of 16 elements on a pitch of 1.1 mm, each measuring 0.8 by 10 mm, driven by a broadband pulse centred at 500 kHz. The theoretical results are shown in Figure 3.23.

Figure 3.23 (i) shows the comparative interference field. It can be seen that this array and using this definition of the lengths d_1 to d_4 (set at 8.0, 1.5, 4.0, 1.5 mm) then a correspondingly sized focal point can be achieved up to a distance of about 25 mm. Figure 3.23 (ii) shows the half pressure field from a single element. Figure 3.23 (iii)

shows the number of contributing elements using the half pressure method described above. It can be seen that all elements start to contribute significantly at a distance of 16 mm on axis, and that at a distance of about 25 mm the area of all elements contributing significantly is already quite broad.

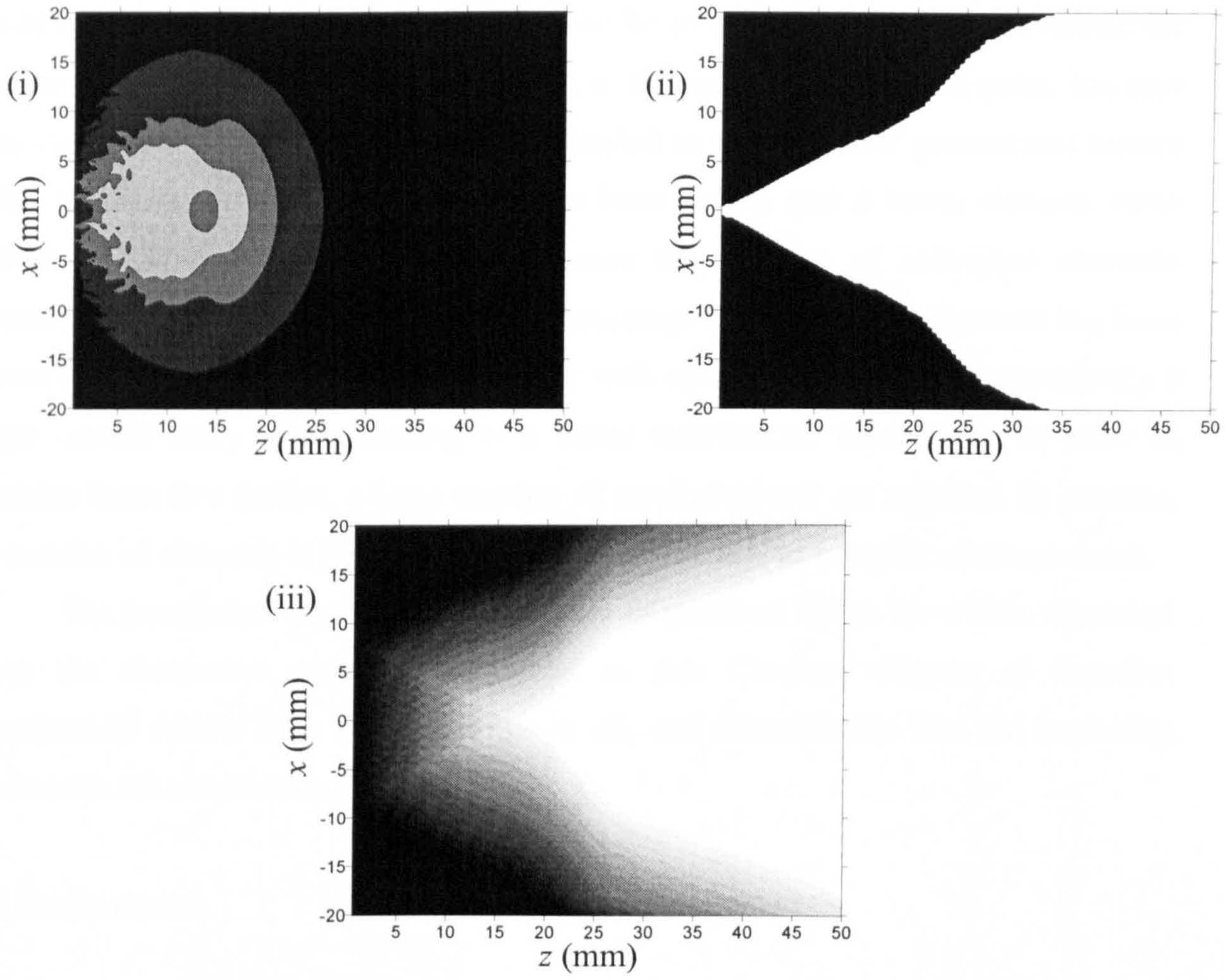

Figure 3.23: The application of the techniques derived in this chapter to a specific array geometry. (i) shows the comparative interference field, (ii) shows the half pressure field of a single element, (iii) shows the number of contributing elements

3.5 Conclusions

Two ways of modelling arrays have been discussed. The first is a farfield approximation used for modelling beam-steering, and the second is an extension of the Impulse Response model. To find the field of a phased array using the Impulse Response method, it has been shown that for each array element a translation in time and space is required. It should be noted that this method is also capable of predicting the field from an array used in the beam-steering mode of operation.

The pressure fields emerging from various phased arrays in air have been shown. In some cases the point of maximum pressure was not at the expected focal point, and the reason for this has been given. In order to indicate the area in which effective focussing may take place a new method has been derived in which idealised sources are used, based purely on the interference taking place. In addition it has been shown how the directivity of each individual element must be considered. A method to indicate the number of elements, which are contributing to the pressure at the focal point, has also been discussed. These two methods are intended to indicate how geometrical factors affect the linear arrays performance. It has been shown that a lower element width (whilst frequency remains constant) increases the merging of individual elements pressure fields, leading to more effective focussing. The number of elements has been shown to affect the interference field greatly, with more elements or more specifically a larger overall array width, leading to a better interference field. Thus, in order to combine these two factors, a large number of small elements are required. In practice, the number of channels is limited, and hence, this will lead to a degree of compromise.

The parameters important in the design of practical arrays have been discussed using the theoretical approach presented in this Chapter. Chapter 4 describes experimental results from phased arrays in air, and demonstrates that the modelling predictions are observed in practice.

3.6 References

[1] D. W. Schindel, "Ultrasonic imaging of solid surfaces using a focussed air-coupled capacitance transducer," *Ultrasonics*, vol. 35, pp. 587-594, 1998.

[2] D. W. Schindel, A. G. Bashford, and D. A. Hutchins, "Focussing of ultrasonic waves in air using a micromachined Fresnel zone-plate," *Ultrasonics*, vol. 35, pp. 275-285, 1997.

[3] T. J. Robertson, D. A. Hutchins, and D. R. Billson, "An air-coupled Line Focused Capacitive Ultrasonic Transducer," presented at IEEE Ultrasonics symposium proceedings, San Juan,Puerto Rico, 2000.

[4] T. J. Robertson, D. A. Hutchins, D. R. Billson, J. H. Rakels, and D. W. Schindel, "Surface metrology using reflected ultrasonic signals in air," presented at 6th biennial joint Warwick/Tokyo nanotechnology symposium, 2000.

[5] W. S. H. Munro and C. Wykes, "Arrays for airborne 100 kHz ultrasound," *Ultrasonics*, vol. 32, pp. 57-64, 1994.

[6] P. Webb and C. Wykes, "High-Resolution Beam Forming for Ultrasonic Arrays," *IEEE Transactions on Robotics and Automation*, vol. 12, pp. 138-146, 1996.

[7] J. L. San Emeterio and L. G. Ullate, "Diffraction Impulse-Response of Rectangular Transducers," *Journal of the Acoustical Society of America*, vol. 92, pp. 651-662, 1992.

[8] S.-C. Wooh and Y. Shi, "Optimum beam steering of linear phased arrays," *Wave Motion*, vol. 29, pp. 245-265, 1999.

[9] C. S. Clay and H. Medwin, *Acoustical Oceanography*, 1 ed: John Wiley & Sons, 1977.

[10] A. Herzenberg, M. M. Woolfson, and J. M. Zimon, *Radiotelescopes*, 1 ed: Cambridge University Press, 1969.

[11] R. A. Monzingo and T. W. Miller, *Introduction to Adaptive Arrays*, 1st ed. New York: Wiley, 1980.

[12] S.-C. Wooh and Y. Shi, "Influence of phased array element size on beam steering behavior," *Ultrasonics*, vol. 36, pp. 737-749, 1998.

[13] S.-C. Wooh and Y. Shi, "A Simulation Study of the Beam Steering Characteristics for Linear Phased Arrays," *Journal of Nondestructive Evaluation*, vol. 18, pp. 39-57, 1999.

[14] S.-C. Wooh and Y. Shi, "Three-Dimensional beam directivity of phase-steered ultrasound," *Journal of the Acoustical Society of America*, vol. 105, pp. 3275-3282, 1999.

[15] P. R. Stepanishen, "Transient Radiation from Pistons in an Infinite Planar Baffle," *Journal of the Acoustical Society of America*, vol. 49, pp. 1629-1638, 1971.

[16] T. J. Robertson, *Advances in Ultrasonic Capacitive Transducer Technology*: PhD Thesis submitted at the University of Warwick, 2001.

[17] J. S. McIntosh, "Advances in Capacitive Micromachined Ultrasonic Transducers (CMUTs)," PhD Thesis submitted at the University of Warwick, 2002.

[18] L. G. Ullate and J. L. S. Emeterio, "A New Algorithm to Calculate the Transient near-Field of Ultrasonic Phased-Arrays," *IEEE Transactions on Ultrasonics Ferroelectrics and Frequency Control*, vol. 39, pp. 745-753, 1992.

Chapter 4: Phased capacitance air-coupled arrays

4.1 Introduction

The previous Chapter contained an explanation of the way in which the Impulse Response model could be extended to model the pressure field emerging from phased arrays. Ways of assessing some of the various criteria effecting the operation of arrays were also developed.

In this Chapter, the practical construction of air-coupled polymer membrane capacitive arrays will be described. An array will be driven with phasing electronics in both beam-steering and focussing modes of operation, and experimental results will be presented and compared to theory.

4.2 Construction

In Chapter 2 the construction of polymer-membrane capacitive devices was discussed. They consist essentially of two key parts, namely the backplate and the membrane. The membrane is typically Mylar, an insulator, coated with a thin conducting layer, and the membrane is typically between 2 and 10 μm in thickness. The drive voltage is applied to the backplate, and the membrane electrode is earthed, thus causing a potential difference between the two. This results in movement of the membrane, and hence the emergence of a pressure waveform. In order to construct an array, the backplate must be divided into electrically isolated elements.

For the arrays used in this work, the backplate was fabricated from PCB technology. Wykes [1] used a similar approach; however the elements were surrounded by a larger area which acted as a source, and the elements themselves were used only as receivers, which could be phased using post-processing. In this work the elements can be used as receivers or as phased sources. The mask required to produce the PCB was drawn using a design package called Eagle.

Each track on the PCB acts as an element, and individual connections were made to a header plug. Prior to attachment of the membrane the backplate was polished. The membrane was positioned over the elements and held in place using adhesive conductive paint, connecting it to the earth plane. The length of the elements was

defined by the separation between two strips of insulating tape applied between the backplate and membrane. This tape had the effect of increasing the distance between the two electrodes (from approximately 3.5 μm, to over 100 μm) and consequently the strength of the electric field in this area was greatly reduced, the effect being that no signal would emerge. Figure 4.1 shows a photograph of (i) the backplate PCB of a 32 elemnt array, and (ii) the finished array where it can be seen that the membrane is connected and held in place by conductive paint at each end, and that the clear insulating tape defines the active area.

(i)

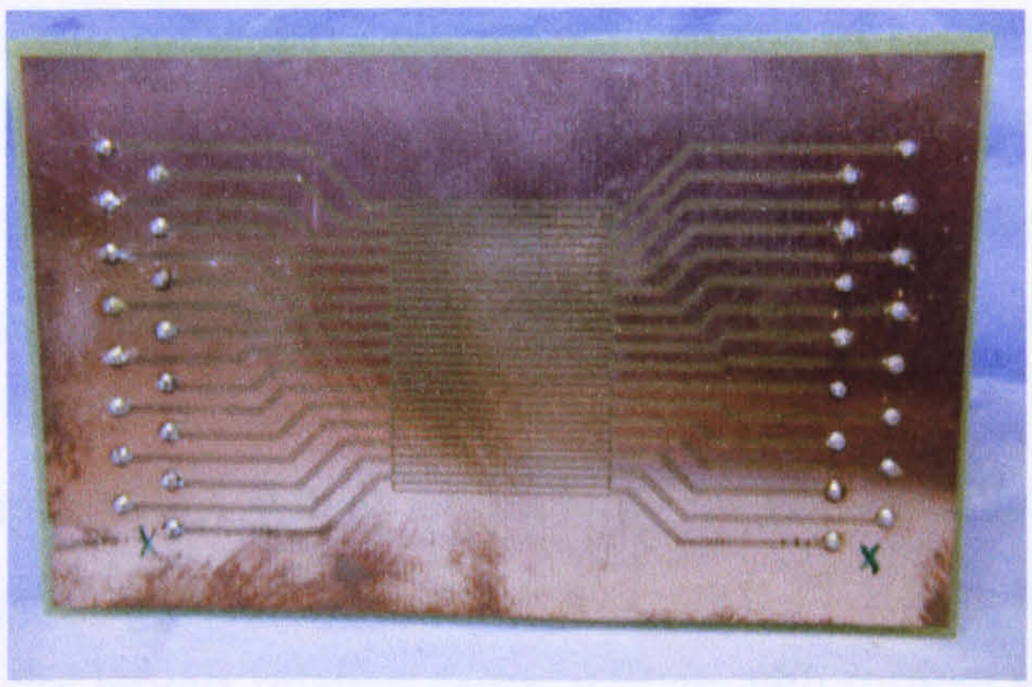

(ii)

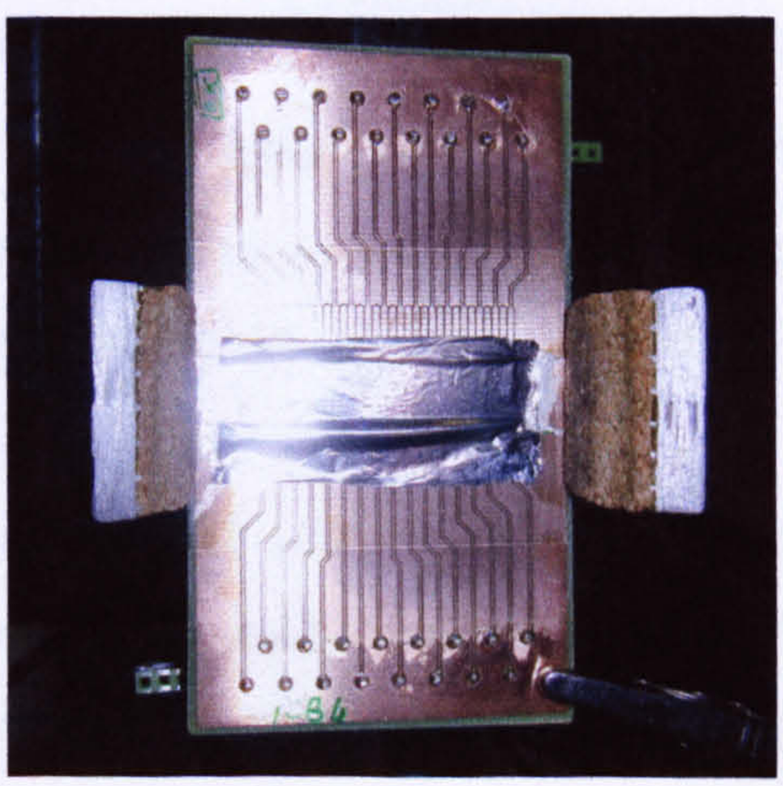

Figure 4.1: Photographs of a capacitive array, (i) the backplate of a 32 element array, and (ii) finished array complete with membrane

The array pictured in Figure 4.1, had 32 elements on a 1.1 mm pitch. Each element was 0.8 mm wide and had a height of 10 mm. The membrane thickness used was 3.5 μm. It can be seen that the tracks joining each element to the relevant connection pin were splayed out. This was to allow the earth plane to pass between each

track. If 16 of the elements are used then this corresponds to the array investigated in Chapter 3, as shown in Figure 3.23.

This method of manufacture is simple, and cheap, but there are restrictions to the geometries used. The main limitation is the thickness of the gap between two elements, and the minimum thickness of any track; both these are limited to approximately 0.3 mm.

4.3 Phasing Electronics

In order to design some drive electronics capable of applying a phased pulse to multiple elements it is first necessary to define the phasing range required. The frequency response of a capacitive transducer with a polished backplate is typically 500 kHz, so the clock speed used in the electronics, which dictates the minimum possible delay between two elements, ought to be considerably higher. It is also necessary to consider the maximum delay, which is likely to be required. To find this, consider focussing off-axis using a 16 element array on a pitch of 1 mm, at a point directly in front of element 16, the largest relative delay will be with respect to element 1. A focal point of 20 mm measured normally from element 16, requires a delay of 14.7 μs, whilst for a focal point at 15 mm, a delay of 18.3 μs is needed. Due to these two considerations, and the limitation imposed by what components are available, a clock speed of 10 MHz and a memory string of 256 bits, which gives a maximum delay of 25 μs, were specified.

The electronics used to drive the phased arrays described in this section had already been constructed as part of another project, and were kindly made available for this work. The phasing circuitry consisted of two parts: a digital circuit which interfaced with a computer, allowing the delays to be set using a LabView program, and an analogue circuit. A block diagram is shown in Figure 4.2. A string of data is defined for each element, and these values are constant except at the time point at which each element must be driven. The PC outputs this data as a long string into the digital circuitry, which is then fed into a shift register where the data is broken back into separate elements. The serial output of the shift register can be used to cascade this circuitry, allowing more elements to be driven. The parallel output of the shift register is connected into an 8 channel FIFO memory, from this location it is re-transmitted at a

pulse rate dictated by an external signal generator. This means that the slow process of downloading data from the PC need not be performed at each pulse repetition. The output of the shift register is connected to the analogue circuitry via a D-type Flip-flop. Both of these components are connected to the 10 MHz clock so dictating that each consecutive data point occurs at intervals of 0.1 μ s. The analogue circuitry consists of a series of mosfet drivers and mosfets, which act as high frequency switches, such that at the time an element requires driving the externally applied DC voltage is connected, so resulting in a voltage spike applied individually to each element at the right phase, resulting in a broadband signal when applied to the transducer element. The circuit allows the addition of a DC bias to the drive signal.

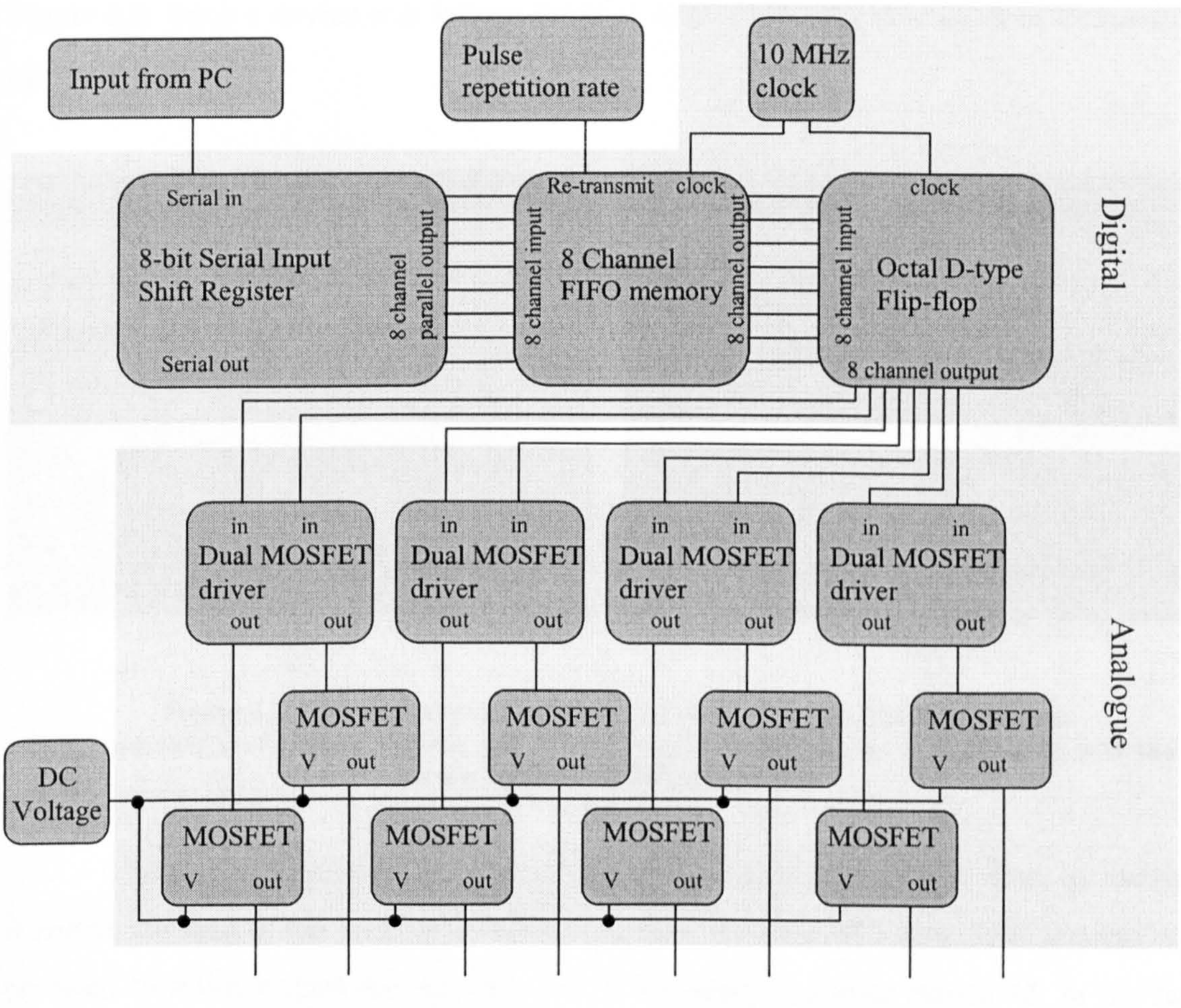

Figure 4.2: Block diagram for the phasing circuitry

4.4 Apodisation of elements

When a voltage change is applied to each of the elements, a pressure waveform will be generated. In this Section, an experiment is described which assesses the differences in the amplitude of these emergent waveforms from each of the elements. While the geometry is the same for each element, there will be certain factors, which vary the output in reality, such as the degree of polish on each element.

A 0.5 mm square micromachined transducer, which has been designed for use as an air-coupled detector, was used as a miniature receiver. A scanning electron micrograph and a photograph of such a device is shown in Figure 4.3 [2]. This was fabricated by QinetiQ (Malvern), and is of a design described earlier in Section 2.5, Figure 2.6. Such a device was known in other work to be sensitive in air at frequencies up to 1.5 MHz [3].

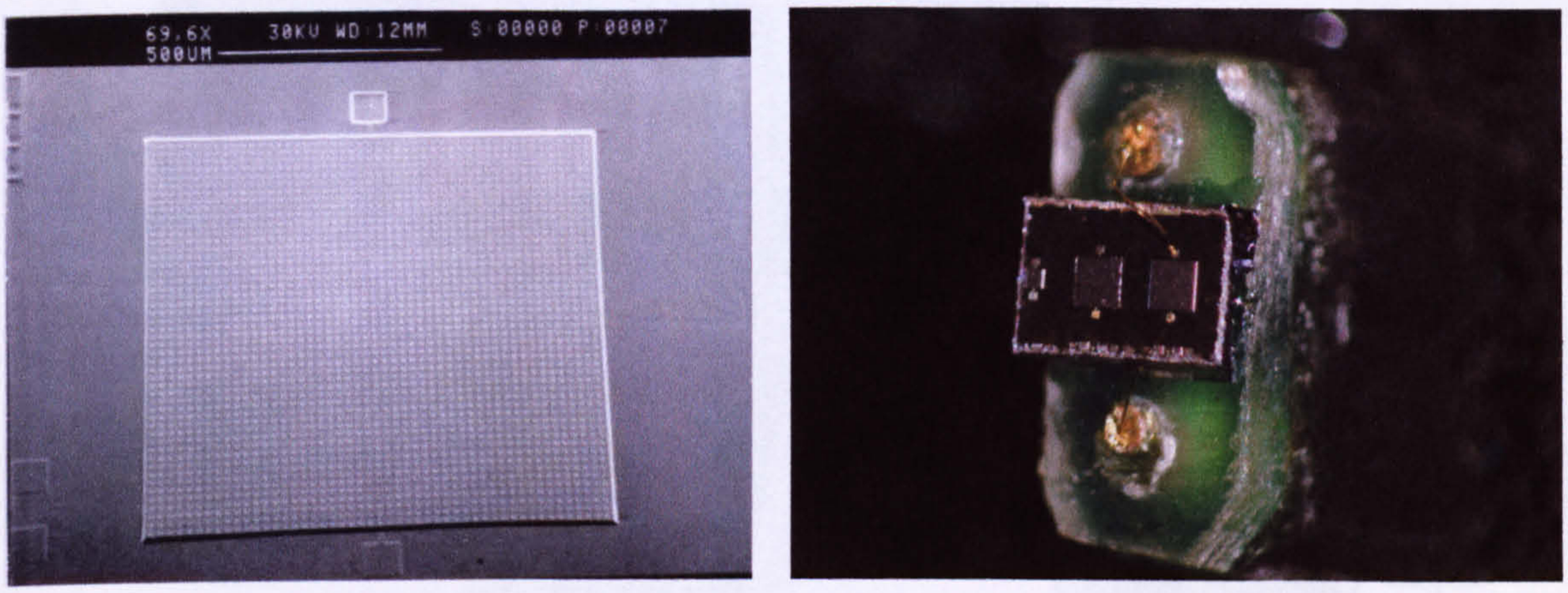

(i) (ii)

Figure 4.3: The miniature micromachined probe tip, (i) a scanning electron micrograph (SEM) of a single element, and (ii) a photograph showing two such elements with the one on the right connected as a receiver

The receiver was used to measure the output of 8 elements at a time, by moving it across the face of the array at a constant normal distance of 3 mm. This process was repeated four times until the output of all 32 elements had been measured. In the first run the elements used were 1, 5, 9, 13, 17, 21, 25 and 29, in each subsequent run the element numbers were increased by 1. This means that each driven element was separated by 3 inactive elements (on which only a DC bias was applied), consequently at a distance of 3 mm the signal detected in front of each element, was solely from that

element, and not the result of interference from the signal emitted from other elements, as the time of flight would have been much larger.

The experimental apparatus used is shown in Figure 4.4, (the specifications for all the experimental equipment used in this thesis are given in Appendix C). It can be seen that two DC supplies are used. One provided the DC voltage for the voltage spike as shown in Figure 4.2, while the other provided the voltage for the constantly present DC bias. In the experiment described in this section the z scanning stage was not used. The x stage moved the receiver to 67 points in 0.55 mm steps. The start point for the receiver was not adjusted for each of the four runs, so that if any misalignment occured between the receiver and the centre of each element, this would at least have been constant.

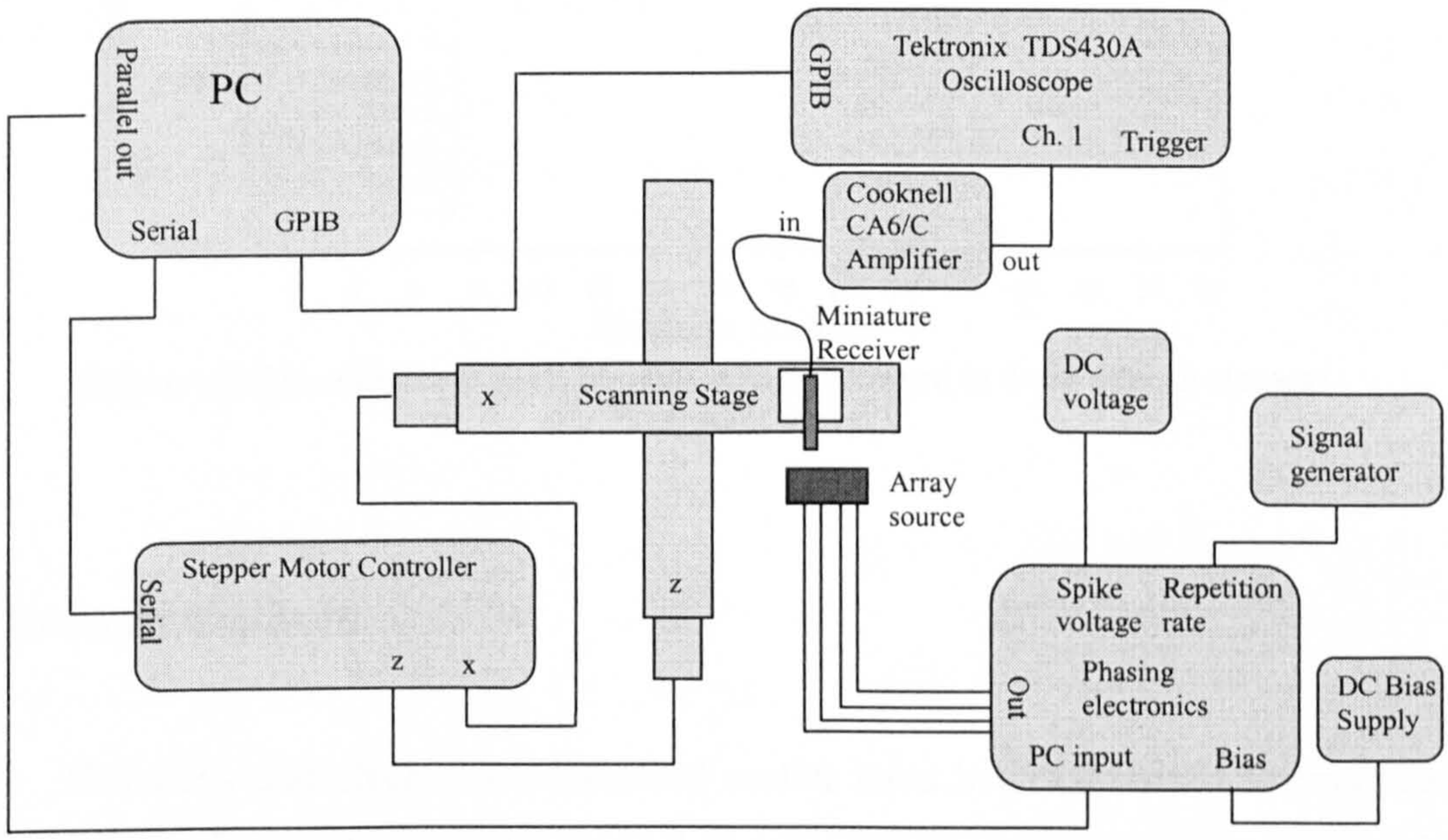

Figure 4.4: Experimental apparatus used to assess the apodisation of the elements of an array

The peak-to-peak voltage received at each of the 67 points on each of the 4 runs has been found. This is presented in Figure 4.5, where, for clarity, only the data in front of, and one step either side of, each active element shown.

It can be seen from Figure 4.5 that the measured output voltage varied considerably for each element, with no obvious pattern. Factors effecting the output include the presence of any dust either between the membrane and backplate, or on the membrane, the presence of small shorts in the membrane, wrinkles occurring in the membrane, the surface of each element in the backplate and variations in the

capacitance of each element which will affect the electrical impedance. The differences in the output from each element varied each time a new membrane was applied. Even with this additional complication, it would be possible to compensate for this phenomenon. However, the similarity in modelled and measured data shown in the next Section indicates that this may not be necessary.

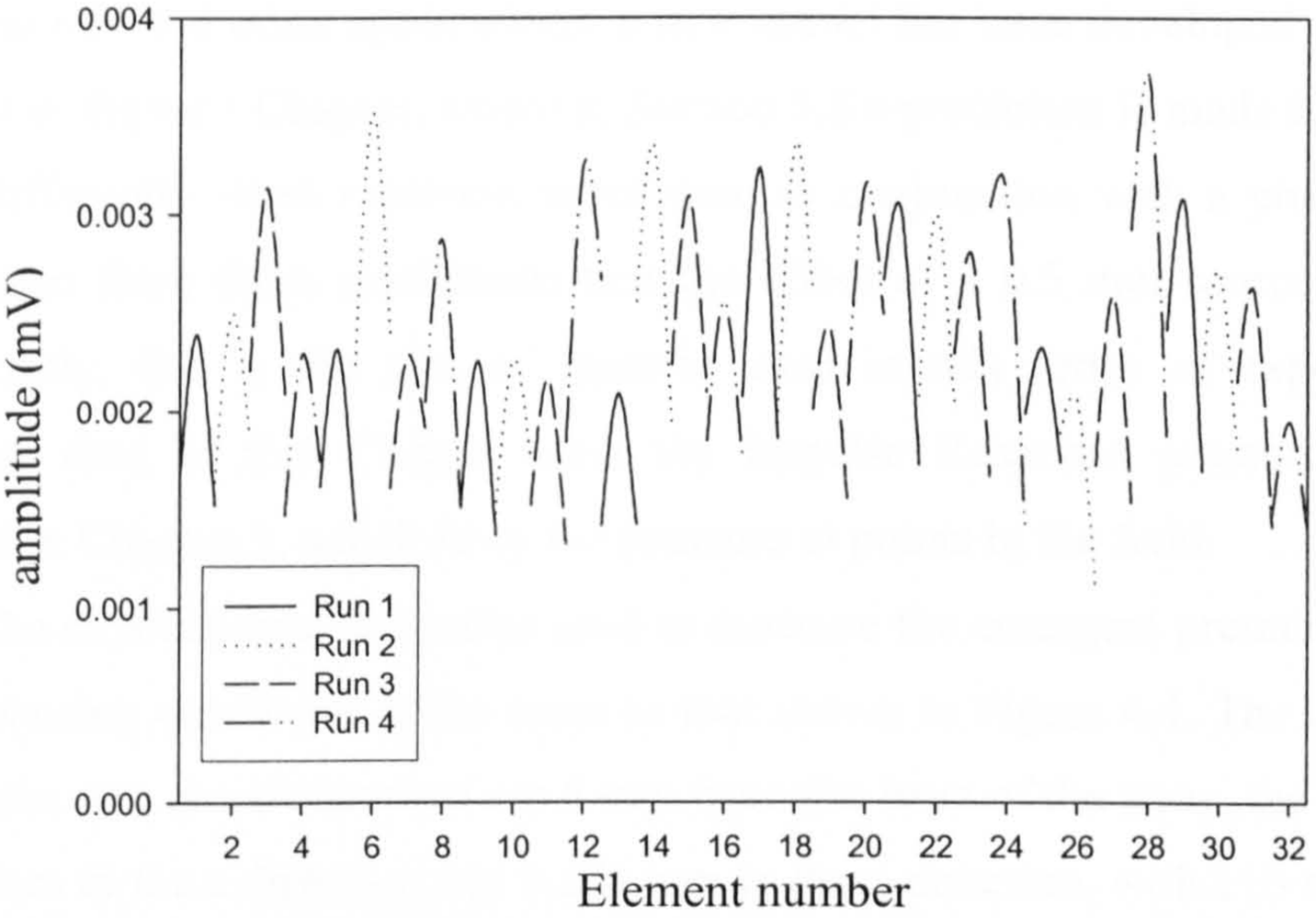

Figure 4.5: The maximum peak-to-peak voltage received in front of each element of a 32 element array

4.5 Focussed source

The array and electronics described earlier have been combined to produce a phased source. In this Section, the applied phasing has been varied to cause focussing and beam steering effects. The focussing effects have been measured, and presented as field scans, graphs of the full width half maximum, and the effect on the focal point of the number of active elements has been investigated. The beam-steering results are displayed as directivity plots, both these and the focussed results correlate well with theory.

4.5.1 Focussed field scans

The applied phasing has been varied to cause focussing in various locations in the field, both on and off-axis. In each case, the field has been scanned and compared to

theoretical results obtained using the impulse response modelling technique applied to arrays as described in Chapter 3.

The receiver used in these experiments was a 0.5 mm square micromachined probe, as was also used in the apodisation experiment. When used to measure a pressure field, that is the pressure obtained at each point in a field, the finite nature of the receiver will have an affect on the results. In order to predict the effect of a finite sized receiver in this and other applications, a new model has been developed. This model is described in the next Chapter, where in Section 5.8 a prediction is made for the affect of several differently sized receivers when used in conjunction with a phased source. It will be seen from these predictions that the effect of a 0.5 mm source is negligible. Consequently, this is the size of receiver used in this series of experiments. The theoretical data in this Chapter used the Impulse Response pressure field model described in Chapter 3, which finds the pressure at points in the field.

The experimental apparatus used to measure the emergent pressure fields under various phasing conditions is the same as that shown in Figure 4.4. The initial position of the probe was at a distance of $z = 5$ mm from the front of the array, the step size used was 0.5 mm in the z direction and 0.275 mm in the x direction, with 110 and 109 points respectively. The step size in the x direction was chosen so that the same value can be used in the theoretical predictions, as it equates to a quarter of the pitch.

Theoretical predictions of the peak-to-peak pressure field have been made using the Impulse Response model described in Chapter 3. In this model, it is necessary to specify the velocity response of the membrane. It is known that the drive voltage is a short voltage spike. However, the response of the array elements is not known. The Impulse Response model states that the pressure waveform emerging from a source at a point is the convolution of the time derivative of the piston velocity, with the scalar impulse response, which is derived geometrically. Therefore, if the output of the source is measured with a second ultrasonic receiver, what is measured is not the same as the piston velocity. In Chapter 1 the concept of plane and edge waves was described, and this showed that, for a short broadband signal, at low z distances form the source it is possible that the plane and edge wave do not interfere. In such a scenario, the plane wave can be measured which relates more closely to the piston velocity, especially as a small broadband receiver is used. However, when an array is used the elements tend to be small in width and consequently the size of the receiver and the distance it would need to be from the element are both prohibitively small.

In order to measure a plane wave, 16 elements were fired simultaneously, and the output was measured using the same 0.5 mm square receiver as used throughout this Chapter. The received signal is shown in Figure 4.6 (i). It can be seen that initially a large negative spike was detected, which was the r.f. pick-up from the driving impulse. Then, at approximately $t = 17\,\mu$s the ultrasonic signal was received, first the plane wave, followed at $t = 21\ \mu$s by the edge wave. A further wave arrived later, which was a reflection. Figure 4.6 (ii) shows the plane wave after filtering (using a second order, Butterworth bandpass filter with a bandwidth of 150 kHz to 1500 kHz, performed in Matlab) and windowing. This can be compared with the waveform used in the simulation which was a 500 kHz signal with a value of $K = 5$. Figure 4.6 (iii) shows a comparison of the Fourier transform of these two waveforms. In Figure 4.6 (ii) and (iii) the simulated data has been offset for clarity. Both sets of data have been normalised. It can be seen that the measured signal, and that used in the simulations to follow, have similar features.

Figure 4.7 shows a comparison of the simulated and experimental results when focussed at (i) $z = 12$ mm and (ii) $z = 20$ mm, both on axis. In the experimental data it can be seen that at low z values the plot has been blacked out. This is because at low distances from a source, r.f. pick-up is received by the micromachined receiver, although this usually lasts a short time as can be seen in Figure 4.6 (i). However, when using phased arrays as different elements are fired at various times, the r.f. pick-up lasts a longer time. The effect this has is that the comparatively small ultrasonic signal is hidden by the pick-up. Consequently, the distance below which, the signal can be resolved is larger. This problem becomes worse, as the time differences at which the elements are fired increases.

It can be seen from the results in Figure 4.7 that the simulation correlates well with the measured results. In addition, the focal point can be seen to become broader as the focal distance increases. The same is true for the results shown in Figure 4.8, for a focal point of (i) $z = 30$ mm and (ii) $z = 40$ mm.

Figure 4.9 shows the theoretical and experiment peak-to-peak pressure fields received when phasing is applied to the 16 elements, in order to cause off-axis focusing. Figure 4.9 (i) shows a focal point of $z = 20$ mm and $x = 5$ mm, and (ii) a focal point $z = 20$ mm and $x = 8$ mm. Again good correlation is seen between theory and experimental results. The size of the focal point can be seen to broaden, as it is moved further off

axis. The way, in which the width of the focal point varies depending on location, will be examined further in the following Section, for a variety of focal points.

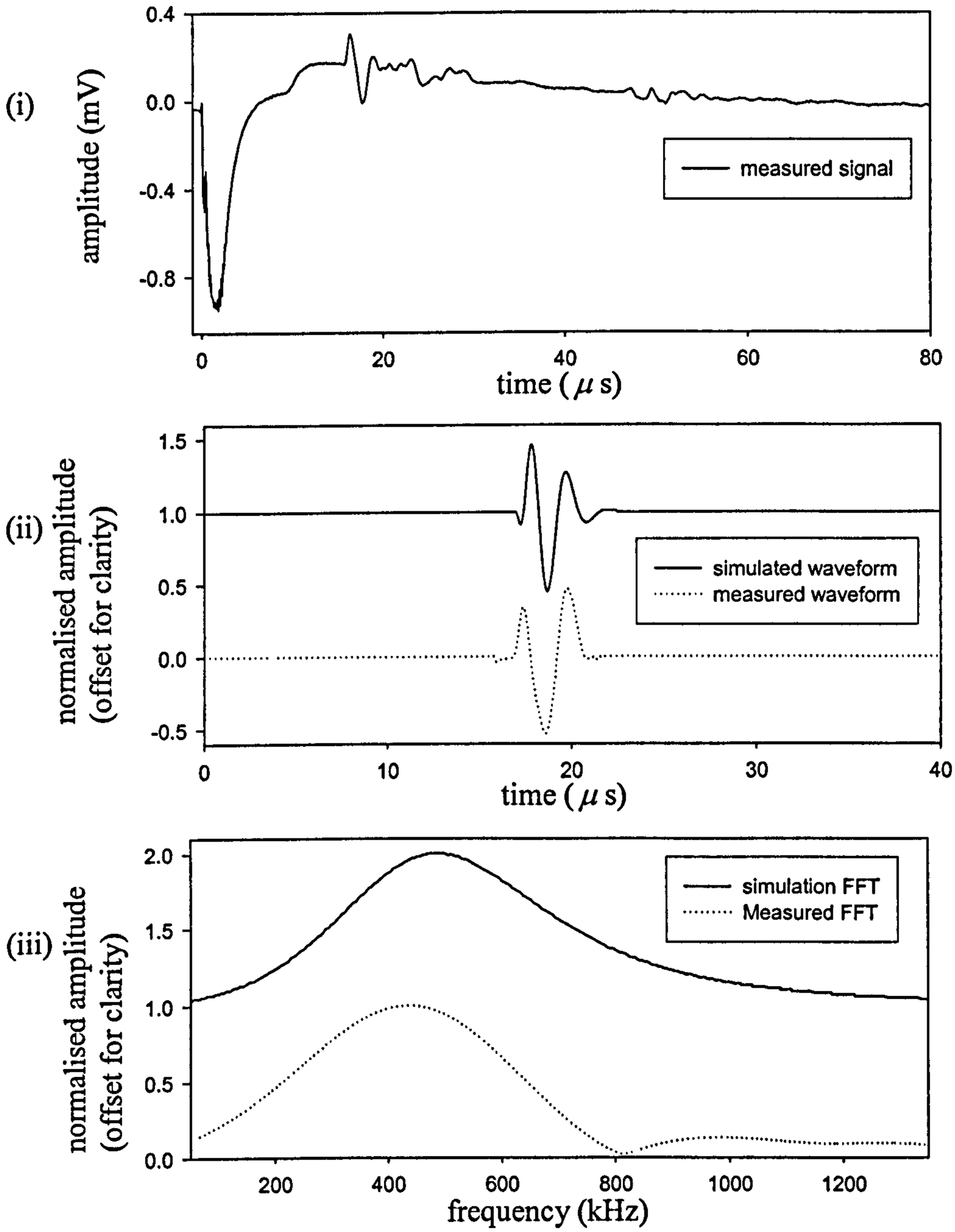

Figure 4.6: A comparison of the measured waveform and that used for the simulation, (i) shows the measured signal, (ii) the windowed waveform and simulated version, and (iii) the Fourier transform of each

axis. The way, in which the width of the focal point varies depending on location, will be examined further in the following Section, for a variety of focal points.

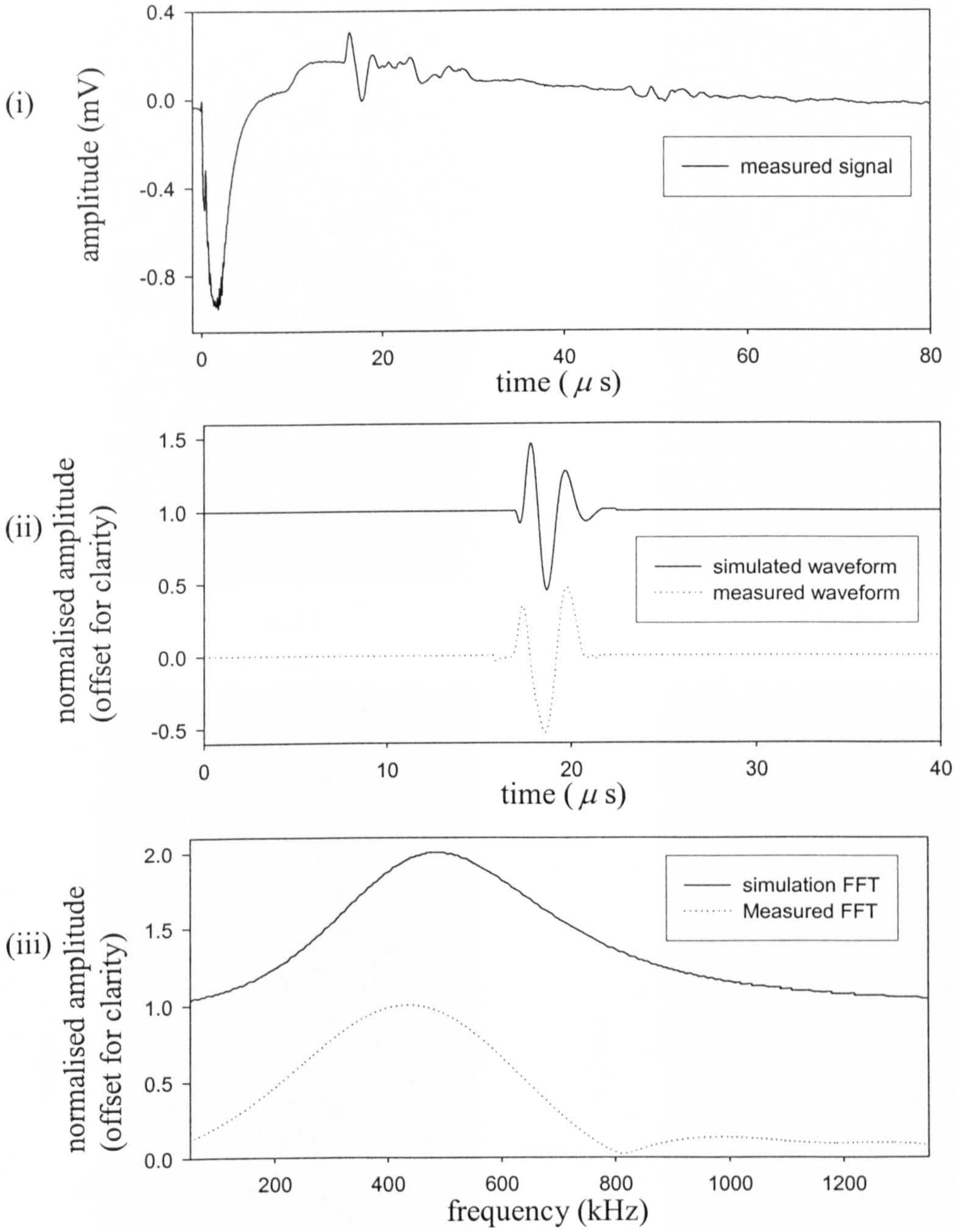

Figure 4.6: A comparison of the measured waveform and that used for the simulation, (i) shows the measured signal, (ii) the windowed waveform and simulated version, and (iii) the Fourier transform of each

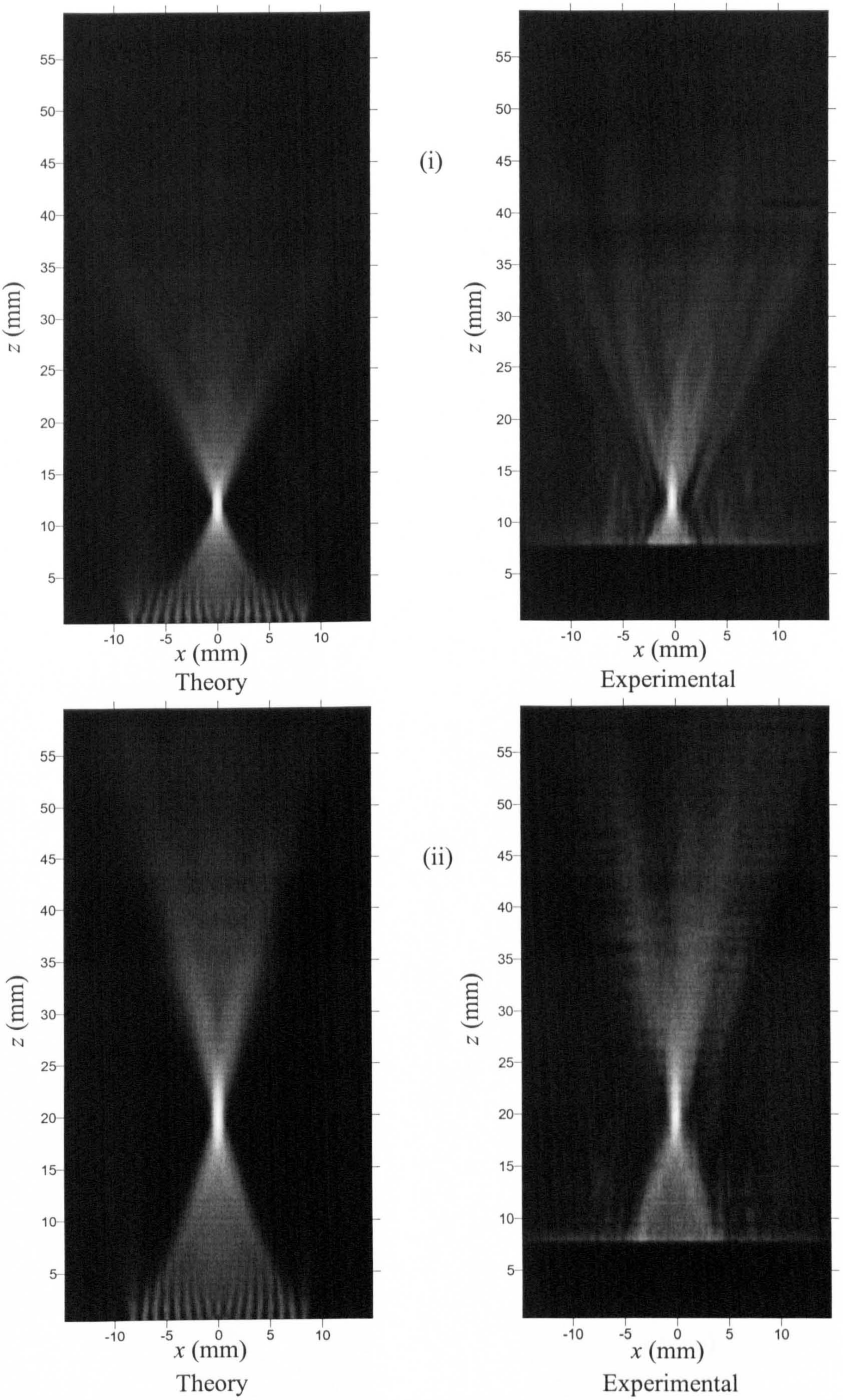

Figure 4.7: Theoretical and experimental maximum peak-to-peak pressure field plots when focussing at (i) $z = 12$ mm, $x = 0$ mm, and (ii) $z = 20$ mm, $x = 0$ mm

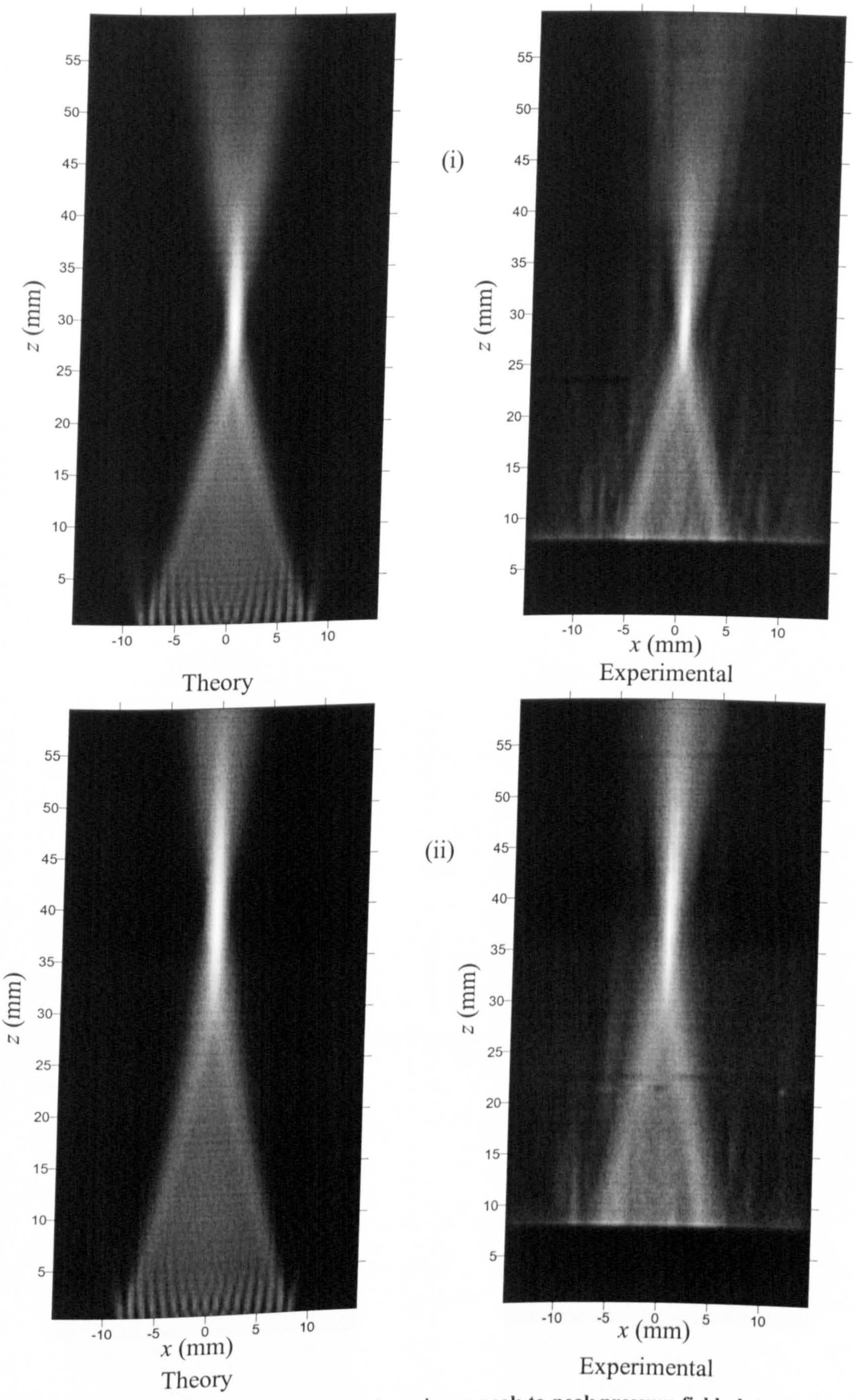

Figure 4.8: Theoretical and experimental maximum peak-to-peak pressure field plots when focussing at (i) $z = 30$ mm, $x = 0$ mm, and (ii) $z = 40$ mm, $x = 0$ mm

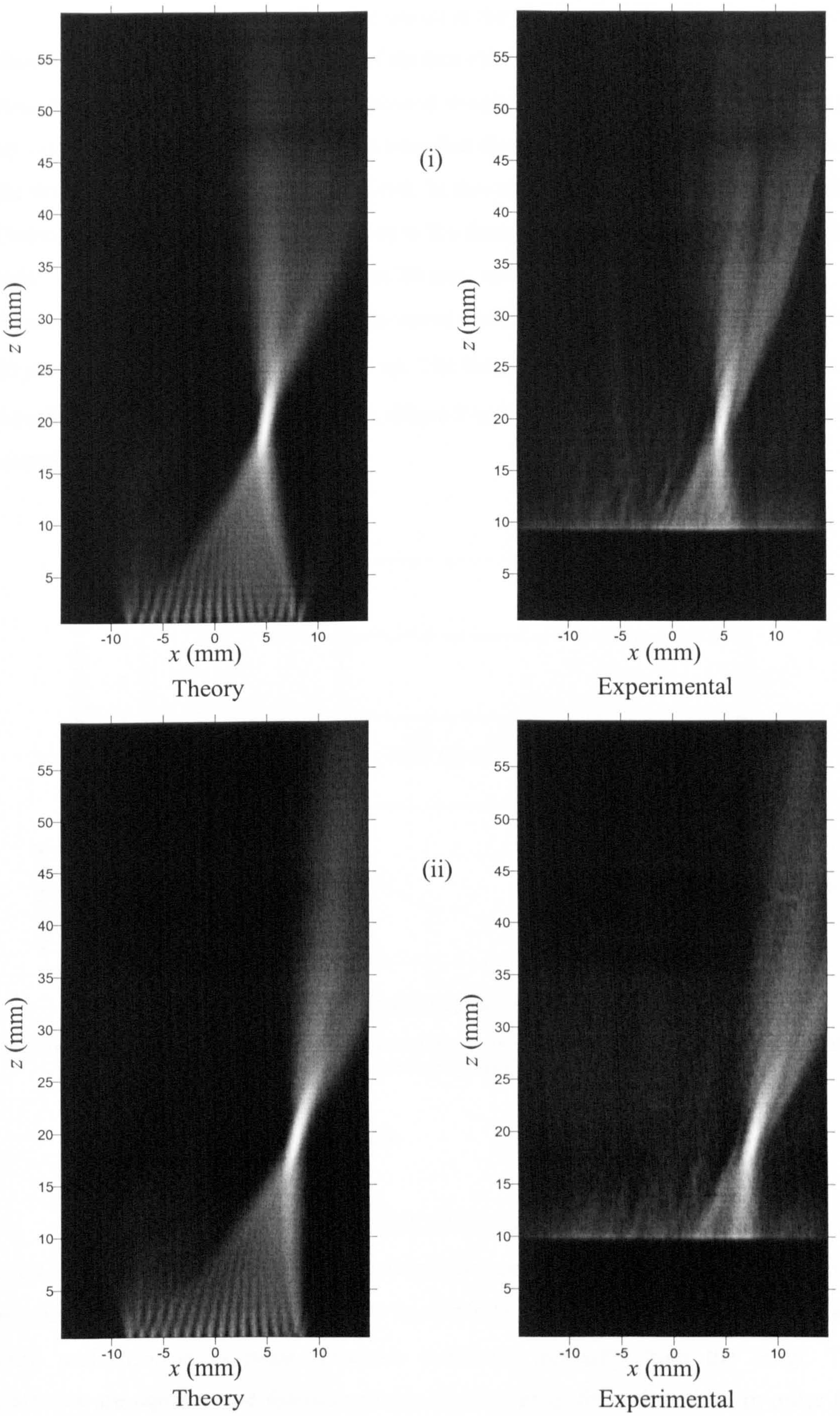

Figure 4.9: Theoretical and experimental maximum peak-to-peak pressure field plots when focussing at (i) z = 20 mm, x = 5 mm, and (ii) z = 20 mm, x = 8 mm

An example of a waveform measured at the focal point of a phased array is shown in Figure 4.10. Here an array of sixteen elements, each measuring 0.8 mm × 10 mm, on a pitch of 1.1.mm have been phased to cause a focus at a distance of $z = 20$ mm on axis. The time scale is based on the time that the scope is triggered which occurs at the time at which the first element is fired. In this case elements 1 and 16 are fired first. Consequently, the time of arrival relates to the distance from these elements to the focal point. This distance is 21.6 mm and not 20 mm, so the time of arrival has been measured as 63.0 μ s not 58.3 μ s. The initial decline in the amplitude measured from 20 μ s to 60 μ s, is due to the r.f. pick-up. The Fourier transform of the measured waveform is shown in Figure 4.10 (ii), where it can be seen to be a broadband signal centred at 500 kHz.

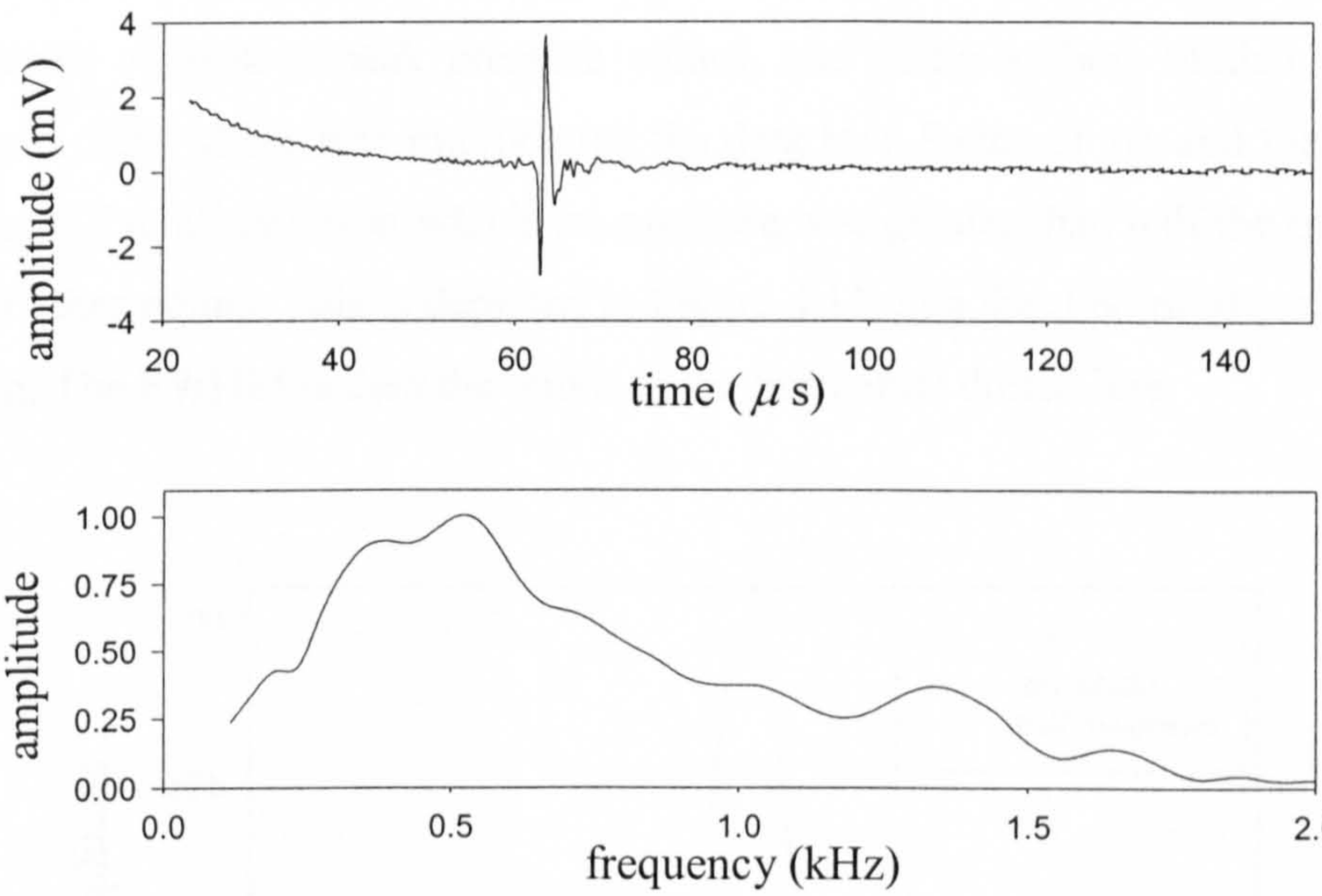

Figure 4.10: An example of (i) a measured waveform and (ii) the frequency spectrum at the focal point, in this case at z = 20 mm, and x = 0 mm

4.5.2 Full width half maximum

The full width half maximum (FWHM) is defined as the distance across a focal point measured between the place at which the peak-to-peak pressure value is half the maximum value. In order to measure the FWHM for various focal points, line scans were performed at constant distances measured normally from the array. These distances are equal to the distance of the focal point in the z direction. In order to do this, the same apparatus was used as shown in Figure 4.4. For each focal point

investigated, the line scan consisted of 61 steps on a pitch of 0.15 mm, the central one of these points lying at the location of the focal point. At each of these points, the peak-to-peak pressure was found. The focal points used were at $z = 12$ mm, $x = 0$, 3 and 6 mm, at $z = 20$ mm, $x = 0$, 3, 6 and 9 mm, at $z = 30$ mm, $x = 0$, 3, 6, 9 and 12 mm and at $z = 40$ and 50 mm, $x = 0$, 3, 6, 9, 12 and 15 mm. In each case 16 elements are used of the array described in Section 4.2. The choice of these focal points was limited by the maximum applicable delay using the phasing electronics, as the z value of the focal point drops and the x value rises, the maximum required delay increases. At points such as $z = 12$ mm, $x = 9$ mm, this required delay exceeds the maximum the electronics can provide, so no scan was possible. Once the receiver was aligned for the first focal point, at the end of each scan the stage was driven to the start point of the next scan. This ensured that any misalignment was as constant as possible in the xz plane.

The FWHM was found by taking the data from each line scan in turn, expressed as a series of peak-to-peak pressure values, and using a short Matlab program (see Appendix B.5) which first interpolated the data by a factor of 10, and then attributed a value of 0.5 to all points at which the pressure was greater than half the maximum, and 0 to all other points. This is depicted in Figure 4.11, at a focal point of $z = 20$ mm and $x = 0$ mm. The FWHM is then the width of the horizontal dotted line.

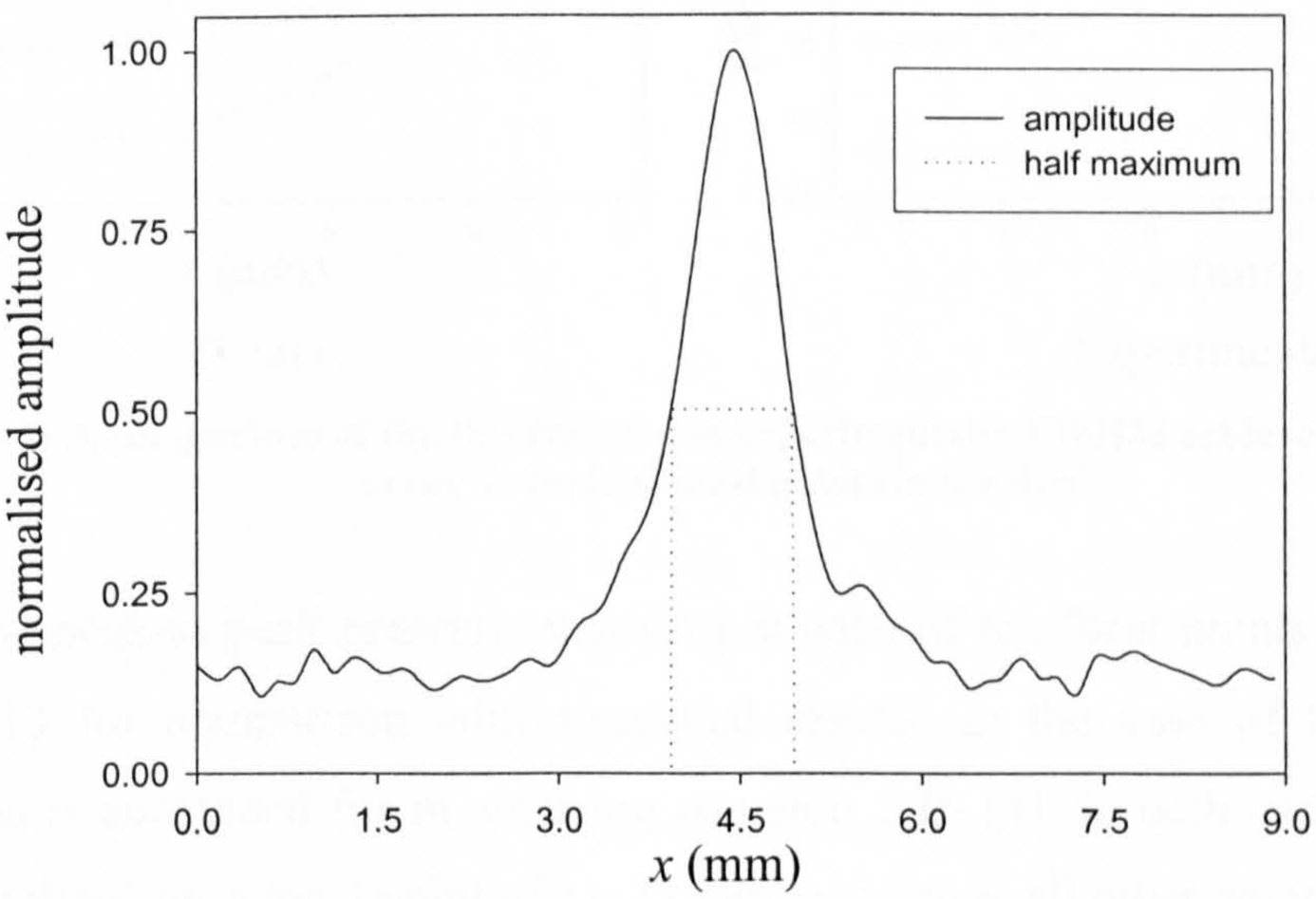

Figure 4.11: The measured peak-to-peak pressure along a line at a constant distance of z = 20 mm from the array

The measured FWHM, and the measured maximum value will be compared to simulated results using the impulse response method described in Chapter 3. The

simulated results are found for a complete grid of focal points, that is for all combinations of z = 12, 20, 30, 40 and 50 mm, and x = 0, 3, 6, 9, 12 and 15 mm. A comparison of the theoretical and experimental results obtained for the FWHM is given in Figure 4.12, each point on the graph relating to a different focal point. It can be seen that as the focal point was moved further away from the array in the z direction, whilst staying on axis (i.e. x = 0 mm), the width of the focal point increased. In Chapter 3 this was discussed in terms of interference fields. However, this trend is reversed for focal points away from the axis, it can be seen, that for focal points with a higher x value the simulated data shows that a point is reached at which a higher z value will result in a narrower focal point, i.e. the lines on the graph can be seen to cross. This is due to the directivity of the individual elements. At greater angles from the normal of the array then effectively some elements will not contribute much to the focal point signal. This was described earlier in more detail in Section 3.4.3. It can be seen from the data that the simulation and experimental results are in good agreement.

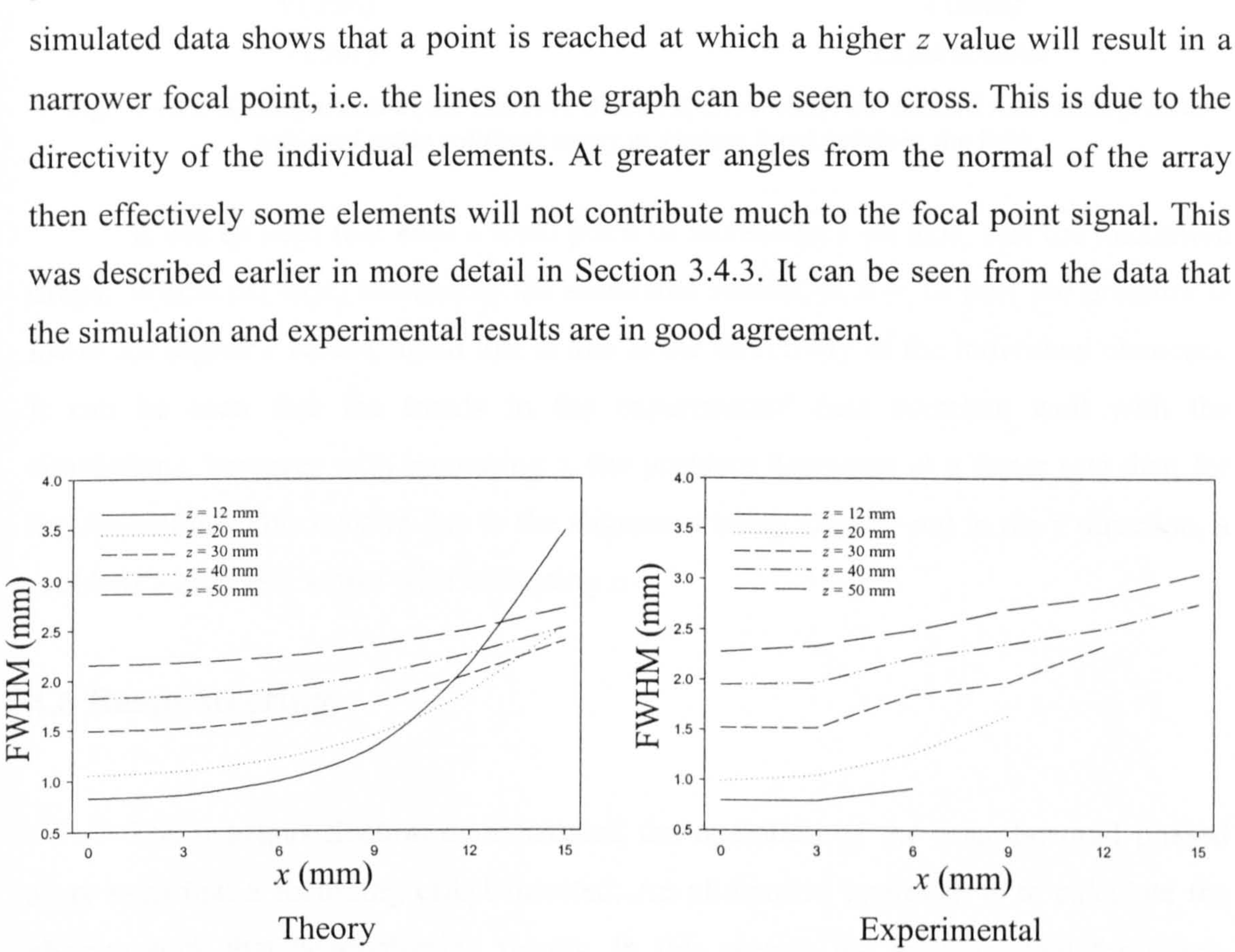

Figure 4.12: A comparison of the theoretical and experimentally FWHM achieved using a phased array at various focal points in the field

The peak-to-peak pressure measured at each of the focal points is presented in Figure 4.13 for comparison with simulated results. In the case of the simulations attenuation is accounted for in air using equation 1.10 [4]. In both cases the data has been normalised for a focal point of z = 12 mm, x = 0 mm, all other points are relative to this.

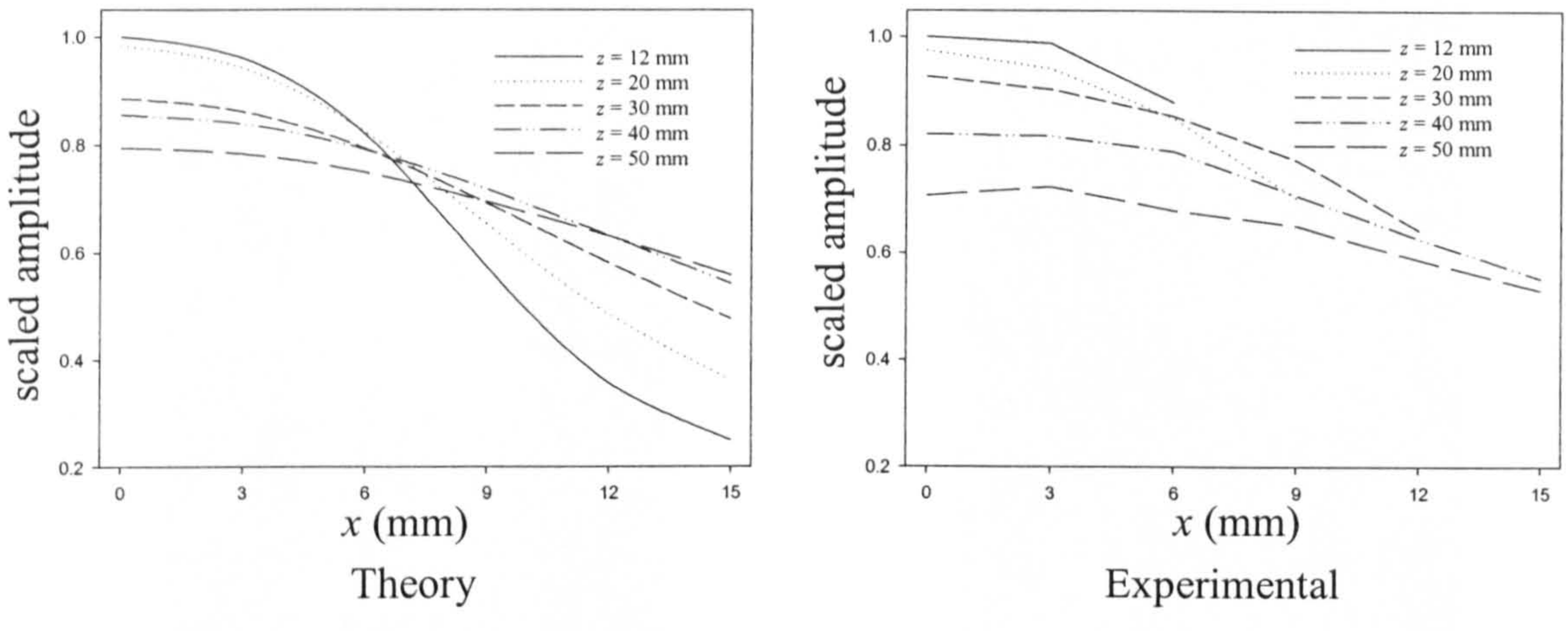

Figure 4.13: A comparison of the theoretical and experimentally normalised maximum pressure achieved using a phased array at various focal points in the field

It can be seen that with a focal point of increasing z on axis, that the maximum drops. Whilst off axis, examining the simulated results, at x = 15 mm the pressure is lower for higher z values, again this is due to the directivity of the individual elements. It can be seen that the trends in the experimental data correlate well with the simulations, however with increasing z, the pressure decreases at a faster rate than for the simulation. This may be due to the alignment being slightly out in the y direction, a problem which gets worse with increasing z.

4.6 Beam-steering

The previous Section demonstrated the operation of the manufactured phased array such that a focussing effect resulted. An alternative approach is to calculate the phasing such that beam-steering results. In this section the array is used for beam-steering, and the experimental results are compared to theory. The theoretical model used in the extension to the Impulse Response model described in Chapter 3. The experimental apparatus used is the same as that shown in Figure 4.4.

Figure 4.14 (i) shows the peak-to-peak pressure field emerging form the 16 active elements of the array when no phasing was applied. The resultant measured field lies entirely within the nearfield of the device. In Figure 4.14 (ii) phasing has been applied such that the beam is steered through an angle of 15°.

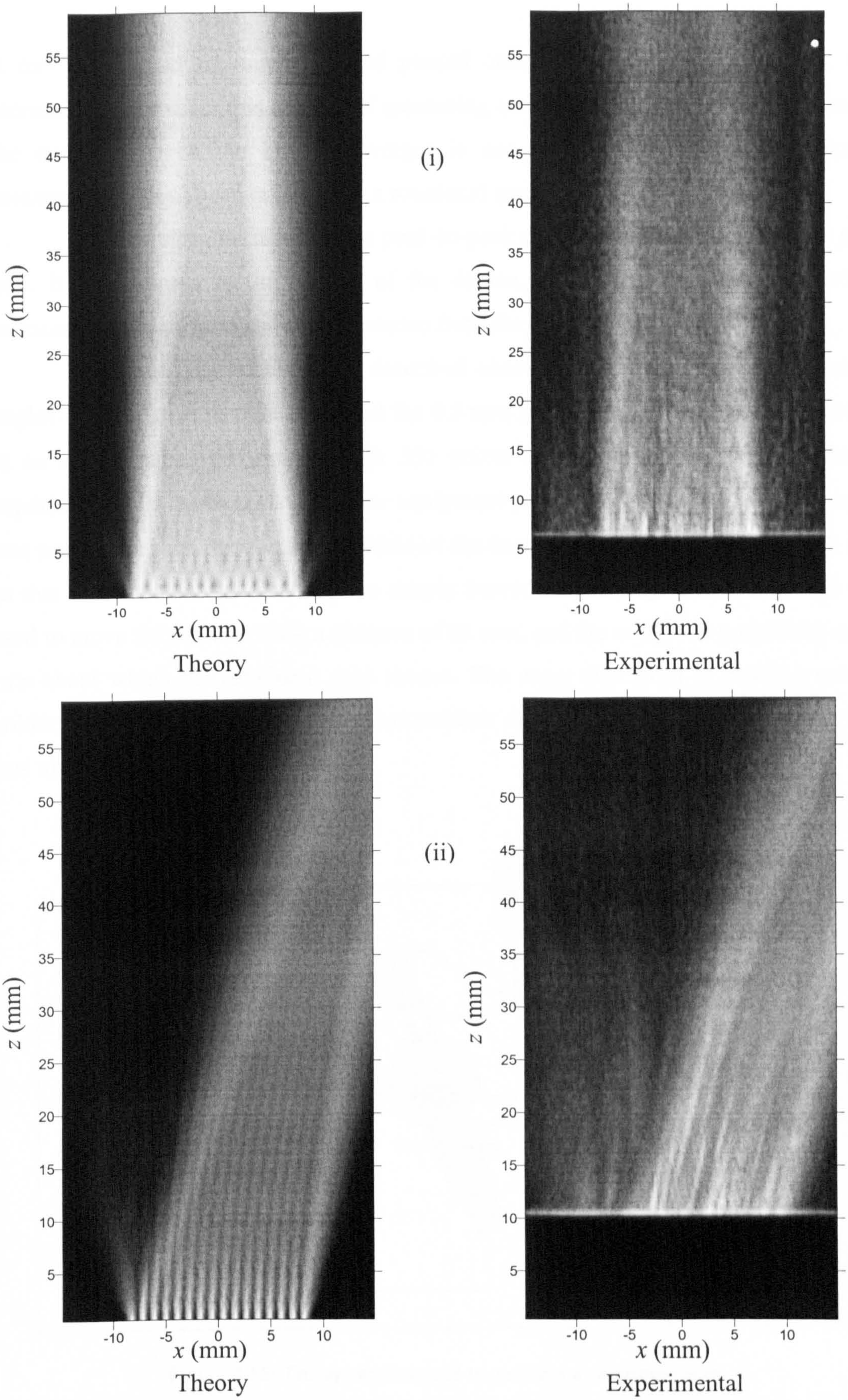

Figure 4.14: A comparison of theoretical and experimental field plots, for (i) an unphased source, and (ii) phasing through as angle of 15°

It can be seen in the unphased and phased cases, that the beam converges, with increasing z. However this method of measuring and presenting the data is not clear, as the angle at which the beam converges is not obvious. For this reason, further measurements have been taken using a rotational stage.

A directivity plot displays the peak-to-peak pressure relative to angle as a polar plot. It is measured in the farfield of the device, a region in which the directivity remains the same regardless of the distance from the source.

The directivity of the array described above was found for different steering angles. Eight elements were used, and the 0.5 mm micromachined receiver was moved in an arc of radius 65 mm, through 360 points on a pitch of 0.5°. This series of experiments was performed using the equipment shown in Figure 4.15. The receiver was positioned such that the front surface of the transducer was at a radius of $r = 0$ mm, so that when rotated the front surface simply moved rotationally. The r stage was then used to move the receiver back a distance of 65 mm, and the array was positioned on the axis about which the rotational scan moves. The array was fixed in position using a holder, which did not protrude the front surface of the device, so that the sound field was unaffected.

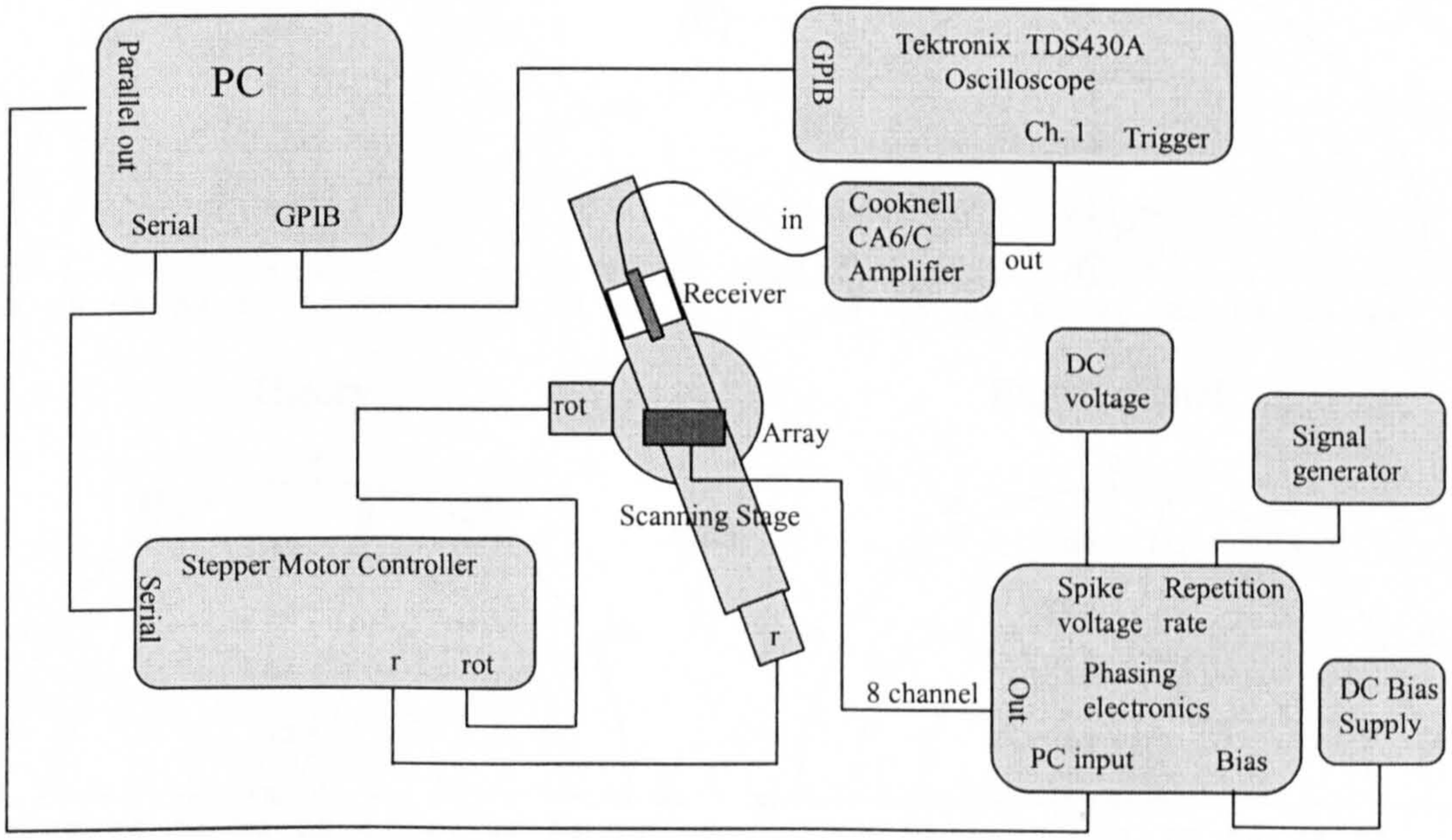

Figure 4.15: The apparatus used to perform a rotational scan

The theoretical and experimental results can be compared in Figure 4.16, for the cases of no phasing and a steering angle of 10° and -10°. For the theoretical work the radial distance is on a normalised scale, whilst for the experimental data it is in mV. It should be noted that for the unphased or 0° steering angle case, a Panametrics PR5055 pulser was used instead of the phasing electronics. It can be seen that in all three cases the angle and approximate width of the main lobe shows good agreement between theoretical and experimental results. It can also be seen that there is good similarity between the 10° and -10° cases, showing that the beam can be steered in either direction. However in all three cases it can be seen that a comparison of the predicted and measured grating lobes shows a considerable difference. This will be returned to at the end of the Section.

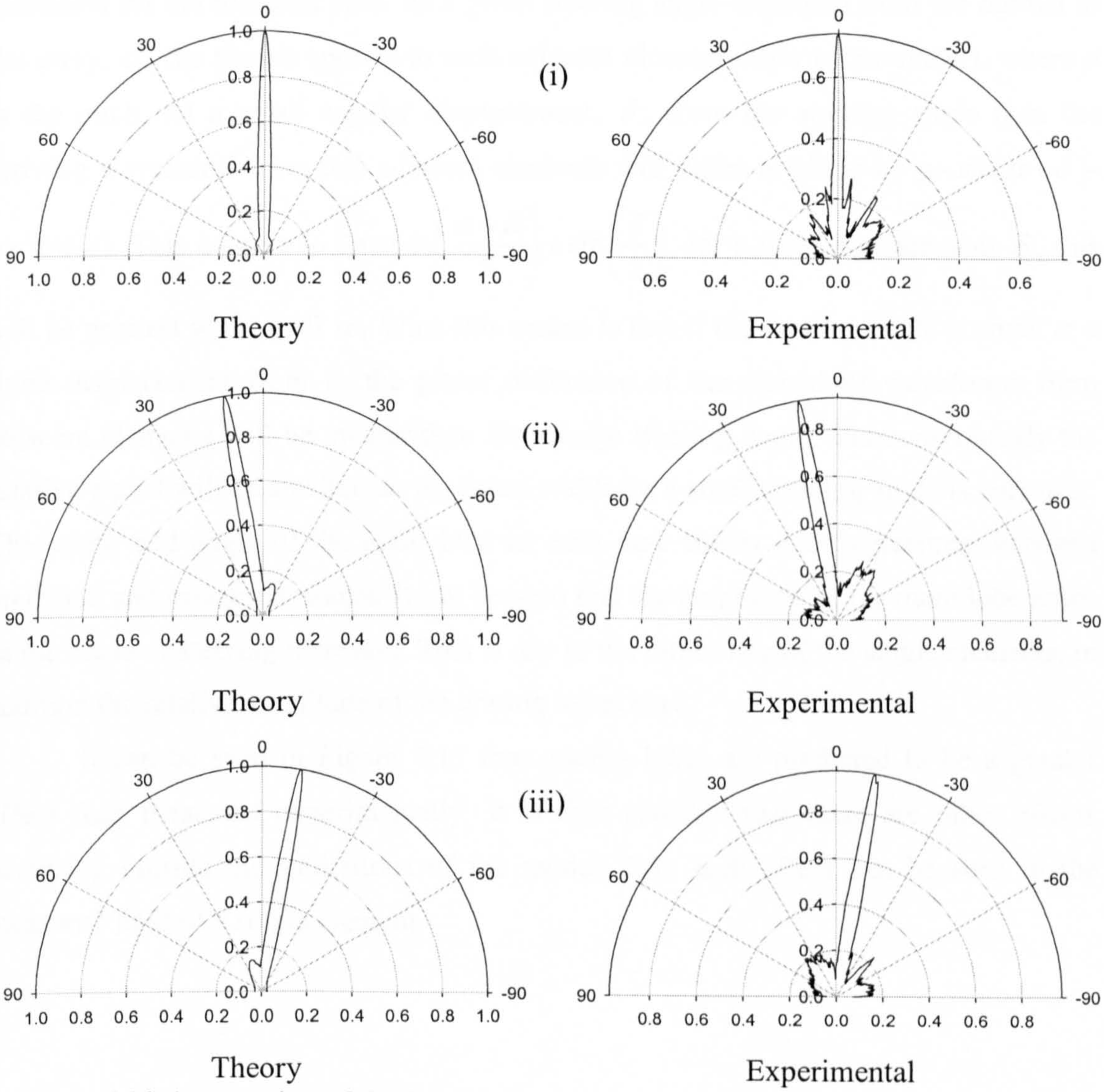

Figure 4.16: A comparison of the theoretical and experimental directivity of an array steered by (i) 0°, (ii) 10°, and (iii) –10°

It can be seen from Figure 4.16, that by steering the main lobe through an angle of 10° it increases slightly in width. As the steering angle gets larger this effect can be seen to get stronger. This can be seen in Figure 4.17, which shows the theoretical and experimental directivity plots when phasing is applied to the same array to cause steering to an angle of (i) 20°, (ii) 30°, (iii) 40° and (iv) 50°. In each case it can be seen that the main lobe increases in width. When the width of the focal point was seen to vary due to location, two factors were discussed in Chapter 3. One was the ability to focus discussed using interference fields, the other the directivity of single elements discussed using half axial pressure fields. In this case, because beam-steering is a farfield effect the directivity of single elements dictates the maximum peak but not the beam width. The beam width is affected in a way similar to the interference fields discussed for the focussed case. At a given steering angle measured from the normal to the array, α, the phases applied to each adjacent element differ by $p\times\sin(\alpha)$, where p is the pitch. At a small angular displacement, δ, from the steering angle then the arriving waveforms from two adjacent elements will differ in phase by $p\times\sin(\alpha+\delta)$-$p\times\sin(\alpha)$. This equates to $2p\times\cos\left(\frac{\alpha+\delta}{2}\right)\times\sin\left(\frac{\delta}{2}\right)$, for a fixed displacement δ, this will be greatest with small α. What this means is that if the steering angle is small at a fixed displacement from it, the phase difference of the arrival of waveforms from adjacent elements will be greater than for a large steering angle, and consequently the relative signal will be smaller, so the beam width for a small steering angle is narrower. The width and angle of the main lobe in each case shows good agreement between predicted and measured results. It can be seen that the amplitude of the main lobe drops as the angle of steering increases. This is due to the directivity of the single elements, in addition the relative amplitude of the grating lobes rises.

It can be seen in Figure 4.17 that grating lobes are predicted to be a greater effect than measured experimentally. It is thus possible that there are other effects occurring outside the limitations of the model. One such effect can be seen in the measured field of a single element.

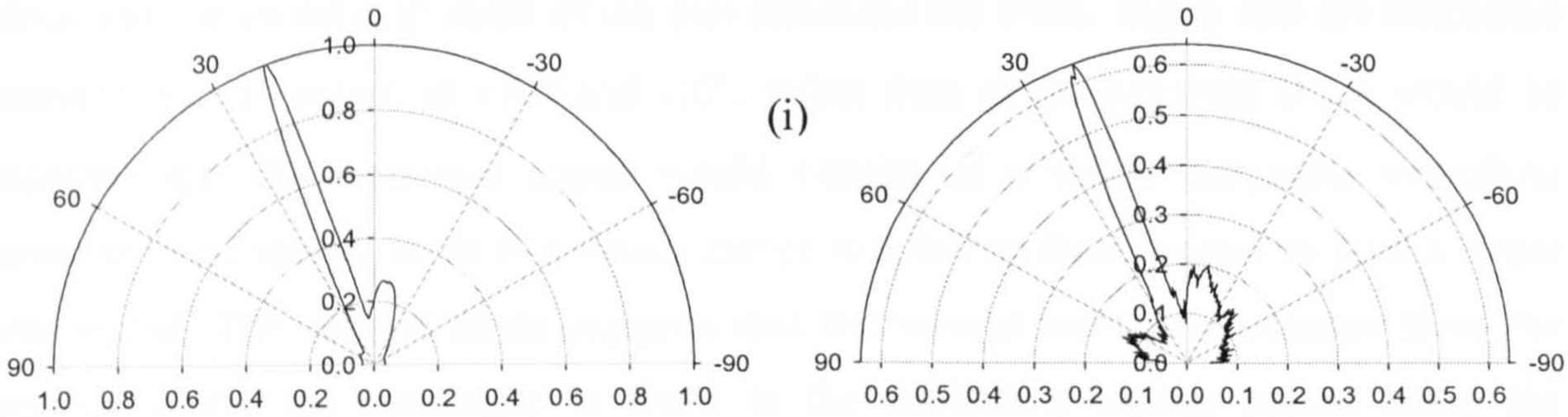

Theory Experimental

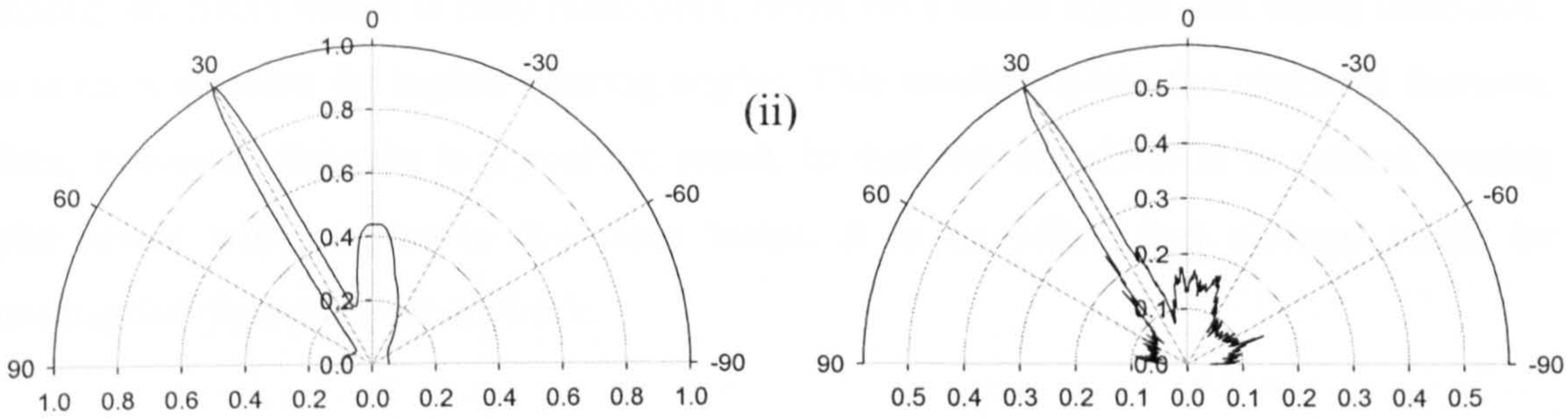

Theory Experimental

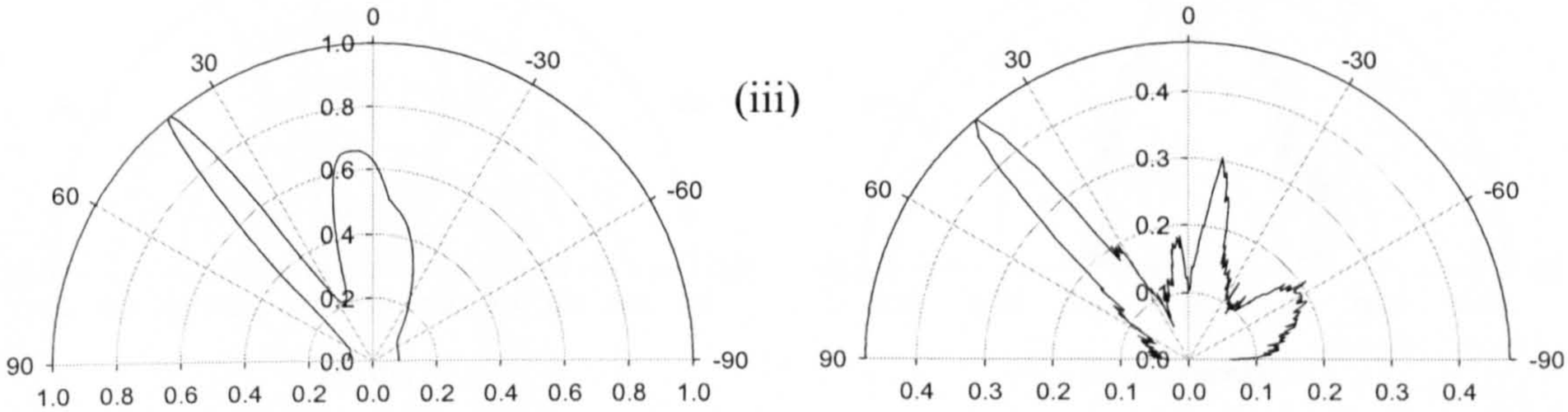

Theory Experimental

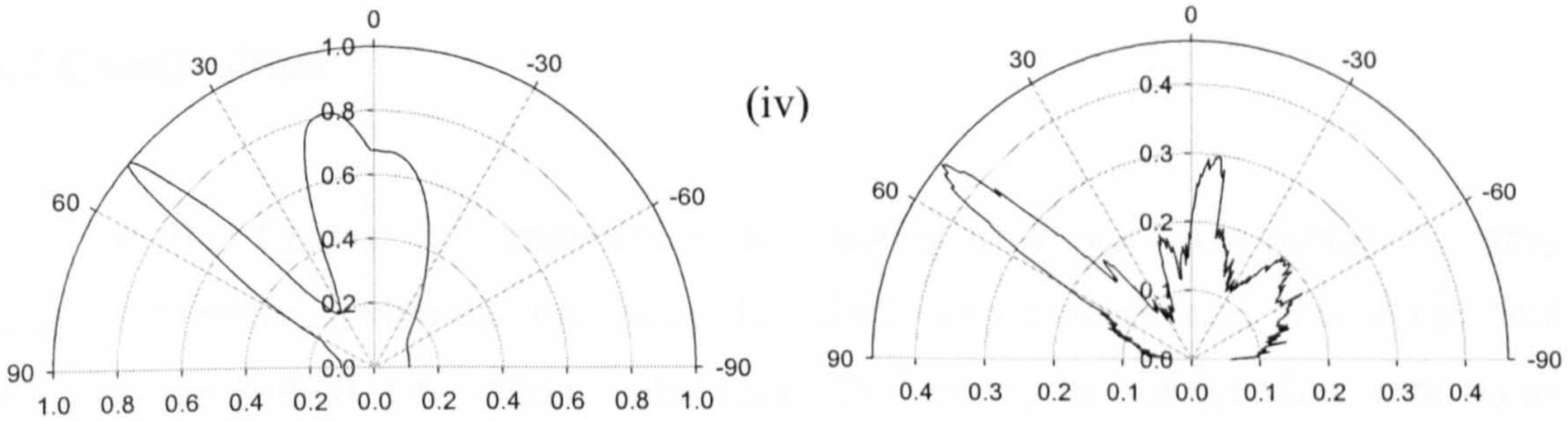

Theory Experimental

Figure 4.17: A comparison of the theoretical and experimental directivity of an array steered by (i) 20°, (ii) 30°, (iii) 40° and (iv) 50°

Figure 4.18 shows the theoretical and experimental results for a single element. It can be seen that they have some different features. Firstly the signal to noise ratio is poor, resulting in a jagged edged plot. However this experiment was performed several

times and the underlying shape of the plot remained the same, that is that the maximum pressure was measured at +10° and -10°, rather than at the expected 0°. It would be expected that the measured signal would consist of a single ultrasonic waveform however there appear to be two which merge together at these angles to give a larger total signal. The time of flight suggests that the second waveform emerges from the location where the membrane is fixed to the backplate, having passed along the membrane. It may be possible that a similar effect occurs when the whole array is phased, an effect which is only noticeable, when very small signals are being measured, so is more relevant for higher steering angles. This would explain the observed features. Note, however, that this is a positive result, in that the net effect is to reduce grating lobe levels with respect to the main beam. It is an effect that perhaps could be investigated further in future work.

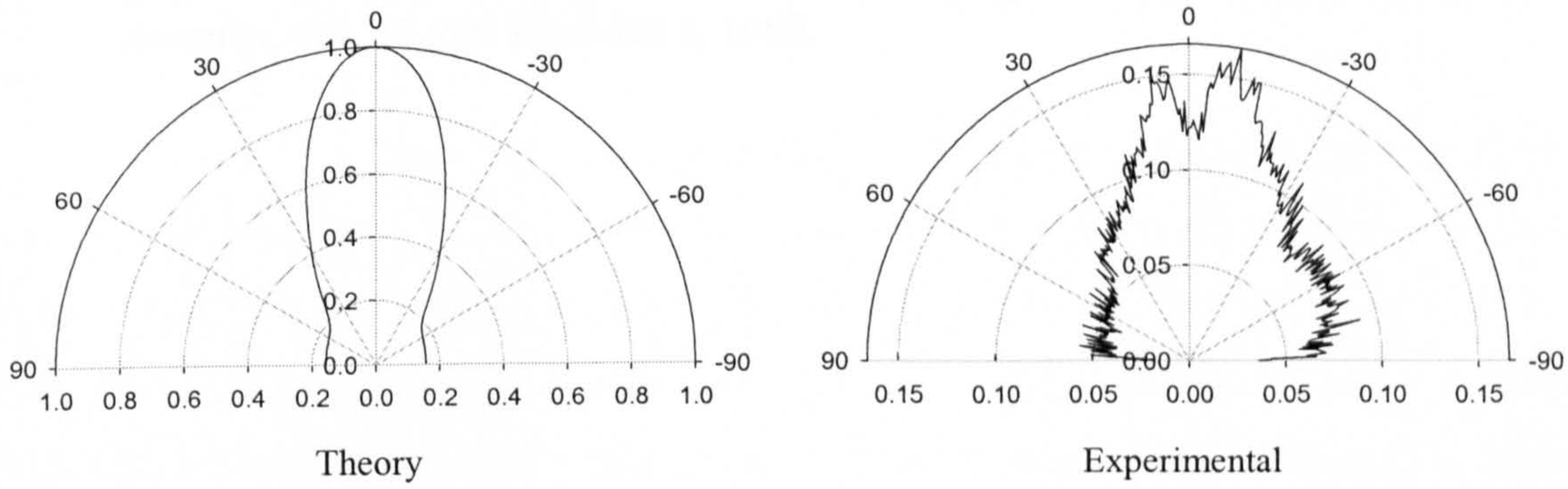

Figure 4.18: A comparison of the theoretical and experimental directivity of a single element

4.7 Conclusions

In this Chapter, the manufacture and testing of a capacitive transducer array using a polymer membrane has been described. The manufacture was cheap and accurate using PCB fabrication techniques. This array, in combination with some phasing electronics, has been used to cause focussing and beam steering using different phasing regimes. A good correlation has been shown between theoretical predictions based on the work of the previous Chapter and experimental results. The degree of focussing has been shown to vary with the focal point location, and similarly the width of a steered beam has been shown to vary with steered angle. Both agreeing well with simulated results. This agreement indicates that, even though the measured output for

each individual element varies, (as was shown in the apodisation section), the resultant fields can be modelled in a satisfactory way by assuming a uniform output amplitude across the array.

4.8 References

[1] W. S. H. Munro and C. Wykes, "Arrays for airborne 100 kHz ultrasound," *Ultrasonics*, vol. 32, pp. 57-64, 1994.

[2] R. A. Noble, A. D. R. Jones, T. J. Robertson, D. A. Hutchins, and D. R. Billson, "Novel, wide bandwidth, micromachined ultrasonic transducers," *IEEE Transactions on Ultrasonics Ferroelectrics and Frequency Control*, vol. 48, pp. 1495-1507, 2001.

[3] J. S. McIntosh, D. A. Hutchins, D. R. Billson, T. J. Robertson, R. A. Noble, and A. D. R. Jones, "The characterization of capacitive micromachined ultrasonic transducers in air," *Ultrasonics*, vol. 40, pp. 477-483, 2002.

[4] L. J. Bond, C. H. Chiang, and C. M. Fortunko, "Absorption of ultrasonic waves in air at high frequencies (10-20 Mhz)," *Journal of the Acoustical Sociey of America*, vol. 92, pp. 2006-2015, 1992.

Chapter 5: A theoretical model for the effect of a finite-size receiver

5.1 Introduction

The standard approach to the characterization of the radiated field of an ultrasonic transducer is to scan a miniature hydrophone throughout the field, and to plot spatial variations in the received amplitude. This hydrophone can take many different forms, including those using a PVDF or PZT element [1] or by using a thin polymer PVDF membrane with etched electrodes to define the measurement area [2]. More accurate calibration work uses a metallized membrane, together with laser interferometry, to get absolute measurements [3]. In all cases, however, the basic assumption is that the receiver diameter is small compared to the shortest wavelength likely to be encountered.

It is often the case that the receiver does not conform to the above criteria. This will be especially true in air where, for a given frequency, wavelengths are smaller when compared to water. In such cases, the directivity pattern of the receiver will not be equivalent to that received by a point receiver, and so the measured field will deviate from that which actually exists. The received waveform at any location will also be different to that from a point receiver. It is therefore of interest to be able to predict the effect of a finite sized receiver on the measured field from a source. This has been investigated previously for the case where a source and receiver are moved apart axially, as this is a common procedure for measuring attenuation and acoustic velocity. A "diffraction correction" [4] is then predicted to account for the effects of the finite receiver. However, there does not appear to be a solution in the literature for the general case where a finite size receiver is moved throughout the field of a transducer under transient excitation.

In this Chapter, the Impulse Response model, as described in Chapter 1, will thus be used to derive a model to find the pressure signal arriving at a finite rectangular receiver from a rectangular source.

In a comprehensive review of transient field theory, Harris [5] includes three models of finite receivers, but in each case these are limited to two circular transducers aligned on axis. He also states that it is common practice to equate the received signal to

the average pressure over the receiver area [5]. This is taken as the basis for the model presented here. The assumption is made that the scalar impulse response can be integrated over the face of the receiver, and that this total system impulse response can be convolved with the time differential of the piston velocity waveform, to give the pressure waveform. The present finite receiver model is developed by deconstructing a model proposed by San Emeterio [6] which finds the pressure waveform at a point in space from a rectangular receiver, and readdressing the problem in such a way that the integral over the receiver area can be performed.

In the following, the model is compared to a method in which the receiver is replaced by an evenly distributed grid of points across the finite area, with the pressure at each being summed to give the total pressure. This comparison aims to show that the new finite receiver model is accurate and is computationally considerably faster than the addition of multiple point receivers. In addition, the model is verified by using it to produce simulated peak-to-peak pressure fields, which are compared to experimentally obtained results.

5.2 Overview

It is informative to give an initial summary of the steps necessary to solve the general problem. The objective of the work presented in this Chapter is to produce a model of the pressure emitted by a rectangular source as measured by a finite rectangular receiver. This will be done by taking an existing model, the Impulse Response model, and altering it such that integration can be performed over the face of the receiver.

San Emeterio [6] has produced an approach based on a convolution method, capable of predicting the pressure at each field point from a rectangular source. The problem is reduced to finding a time-stepped impulse response for each field point, this is proportional to the angle subtended by an arc in the plane of the source. Hence the problem is geometrical in nature. For the purpose of the model developed here, the first step is to produce a geometrical solution to the same problem (that of a point receiver) using a different method. This new method treats each edge of the source separately. The advantage of the new method is that when a finite receiver is considered, it allows

the required integration to be performed. An idea is also introduced, termed planar time, which simplifies the problem.

Having described the new geometrical approach for a point receiver in a specific region of the field, attention is turned to how to perform an integral over the area of the receiver. If the impulse response can be found for a point receiver by considering each edge in turn, then the same is true for a finite receiver providing the integration is set up correctly. To this end, three different integral types are devised, termed the corner limited, edge limited and planar integrals. The solution of each of these integrals is found using generalised variables.

The total impulse response of the finite receiver can be found using the three integrals described. However, their implementation varies depending on where the receiver is located in relation to the source. Consequently, it is first necessary to define regions in the field, and to segment the receiver so that each segment lies wholly in one region.

The impulse response for each segment can then be found by use of the three integral types. This is done by finding the correct values for each of the generalised variables used, for each edge in turn.

The total impulse response can then be found by summing that calculated for each of the segments. The result is a time stepped impulse response for a finite receiver.

An overview of the model, which produces a scalar impulse response averaged across a finite receiver, is as shown in Table 5.1.

Step 1:	Write a new form for the impulse response in terms of planar time, considering each edge of the source in turn.	Section 5.3
Step 2:	Consider three integrals: corner limited, edge limited and planar.	Sections 5.4.1 to 5.4.3
Step 3:	Produce a generalised integral for each of these cases over the area of the receiver.	Section 5.4.4
Step 4:	Segment the receiver	Section 5.5
Step 5:	Construct the source, from the generalised solution of the three integrals.	Section 5.6
Step 6:	Sum for each Segment of the receiver	
Result:	Time stepped scalar impulse response	

Table 5.1: Overview of finite receiver model

5.3 A new geometrical approach to finding the scalar impulse response

In Section 1.5.2 the impulse response method of modelling the pressure emerging from a plane piston was described. The pressure at a point is related to the impulse response and piston velocity by equation 1.17. It was shown that the impulse response is proportional to the angle of the arc which intersects the plane piston, termed $\Omega(\bar{r},t)$, subtended at the point P' as given in equation 1.19. Where the point P' is the projection of any field point P onto the plane containing the planar piston, as shown in Figure 5.1. As the $\Omega(\bar{r},t)$ angle will be referred to, in this work, as being with reference to a point P defined in Cartesian coordinates, it is not necessary to also use the $\bar{r}$ term to define the location of the point. Figure 5.1 shows the location of P as being located at coordinates x, y, z, with the origin being located at the centre of the piston.

Hence the problem is reduced to one of geometry, where $\Omega(t)$ must be found at sequential time steps. The problem need only be considered in two dimensions, if the time is redefined as an equivalent time, referred to as planar time (t_p), within the xy plane according to

$$t_p = \frac{\sqrt{c^2t^2 - z^2}}{c}. \tag{5.1}$$

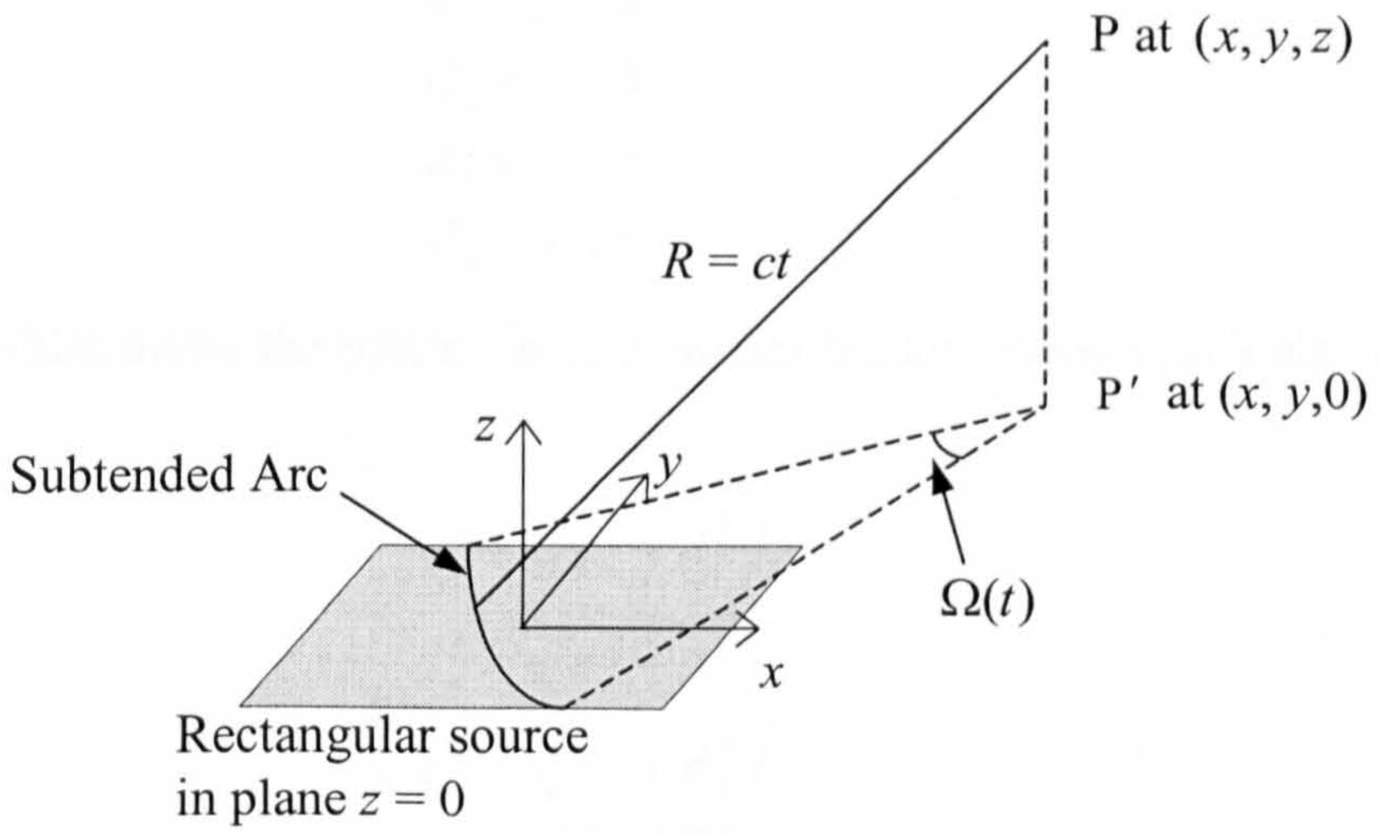

Figure 5.1: Arc subtended at the projection of point P onto the plane of the piston

A model has been developed by San Emeterio [6] which finds the angle $\Omega(t)$ at a given point, P′. An example of this in the region that lies outside the projection of edges AB and BC (that is for $x \geq b$ and $y \geq a$) is shown in Figure 5.2. Arcs centred at P′ for two different points in time are shown, and the radius of each arc is given by ct_p.

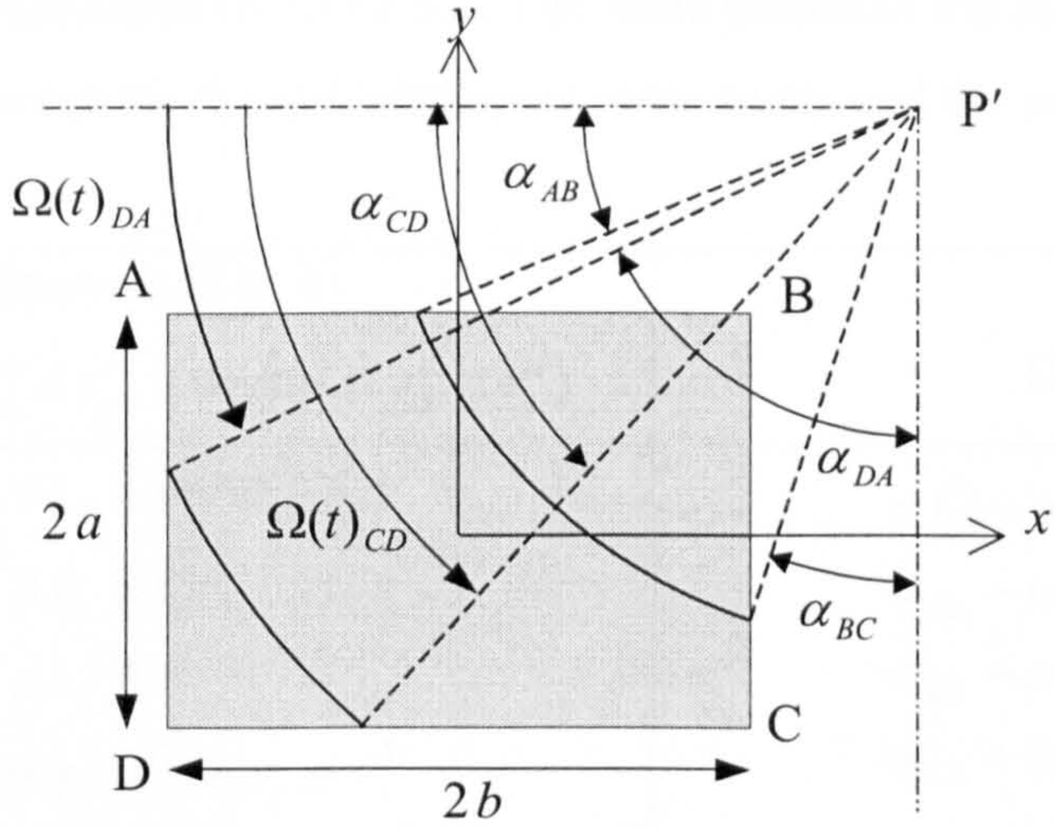

Figure 5.2: Definition of angles in the z = 0 plane

The geometry can be considered more easily using four variables, which can be defined as

$$\begin{aligned} d_1 &= y - a \\ d_2 &= x - b \\ d_3 &= y + a \\ d_4 &= x + b. \end{aligned} \tag{5.2}$$

These variables allow the planar times at which the arc crosses each piston corner to be defined as

$$\begin{aligned} t_p^A &= \sqrt{d_4^2 + d_1^2}\,/c \\ t_p^B &= \sqrt{d_1^2 + d_2^2}\,/c \\ t_p^C &= \sqrt{d_2^2 + d_3^2}\,/c \\ t_p^D &= \sqrt{d_3^2 + d_4^2}\,/c \end{aligned} \tag{5.3}$$

The angles, α_{AB} to α_{DA}, shown in Figure 5.2, can then be found as

$$\begin{aligned}\alpha_{AB} &= \sin^{-1}(d_1 / ct_p)\\ \alpha_{BC} &= \sin^{-1}(d_2 / ct_p)\\ \alpha_{CD} &= \sin^{-1}(d_3 / ct_p)\\ \alpha_{DA} &= \sin^{-1}(d_4 / ct_p)\end{aligned} \tag{5.4}$$

By using these angles, $\Omega(t)$ can be found for a point, which has been projected onto the $z = 0$ plane, P′ located at (x, y), and lies outside the piston (that is for $x \geq b$ and $y \geq a$), using the equations presented in Table 5.2. The table produces the same result as that of San Emeterio [6], except for the redefinition of some terms and the use of planar time.

	Time intervals (1 to 4) (2 occurs if $t_p^A \leq t_p^C$, 3 occurs if $t_p^C \leq t_p^A$)	$\Omega(t)$
1	$t_p^B \leq t_p \leq \min(t_p^A, t_p^C)$	$\pi/2 - \alpha_{AB} - \alpha_{BC}$
2	$t_p^C \leq t_p \leq t_p^A$	$\alpha_{CD} - \alpha_{AB}$
3	$t_p^A \leq t_p \leq t_p^C$	$\alpha_{DA} - \alpha_{BC}$
4	$\max(t_p^A, t_p^C) \leq t_p \leq t_p^D$	$\alpha_{CD} + \alpha_{DA} - \pi/2$

Table 5.2: Piston considered as a whole

The approach described above treats the source as a whole. However it is possible to use an approach, which treats each edge separately. When such a method is used, the relationship between t_p and $\Omega(t)_{Edge}$ can be found using Table 5.3.

Time intervals	$\Omega(t)_{Edge}$
$t_p^B \leq t_p \leq t_p^A$	$\Omega(t)_{AB} = \alpha_{AB}$
$t_p^B \leq t_p \leq t_p^C$	$\Omega(t)_{BC} = \pi/2 - \alpha_{BC}$
$t_p^D \leq t_p \leq t_p^C$	$\Omega(t)_{CD} = \alpha_{CD}$
$t_p^A \leq t_p \leq t_p^D$	$\Omega(t)_{DA} = \pi/2 - \alpha_{DA}$

Table 5.3: Piston considered as series of edges

The term $\Omega(t)_{Edge}$ relates to the angle from a reference line, which passes through P′ in the negative x direction, for a particular edge (e.g. AB, BC, etc). As an example the

angles $\Omega(t)_{DA}$ and $\Omega(t)_{CD}$ are labelled in Figure 5.2. Outside the time interval defined for each edge in Table 5.3, $\Omega(t)_{Edge} = 0$. The subtended angle at a point in time, $\Omega(t)$, can then be found using,

$$\Omega(t) = -\Omega(t)_{AB} + \Omega(t)_{BC} + \Omega(t)_{CD} - \Omega(t)_{DA} \tag{5.5}$$

This new approach has two major advantages when applied to a finite receiver model, but it is first necessary to define two terms. The terms inactive and active will be used to describe certain regions of the plane within which the source lies. A point in the $z = 0$ plane is considered to be active, at time point t_p, if a section of an arc of radius ct_p centred at that point lies within the source, so that for that point $\Omega(t_p) \neq 0$; conversely, $\Omega(t_p) = 0$ is true for any point lying within the inactive area.

To illustrate the first advantage of this approach, consider Figures 5.3 and 5.4. In Figure 5.3, as in later ones, the source has been labelled as ABCD, and arcs centred at these corners of the source and of radius ct_p have been labelled A`, B`, C` and D` respectively. In addition in this figure, these arcs have been used to divide a region of the $z = 0$ plane into segments, labelled as β, γ, δ, ε, ζ and η. The time interval which applies to any point in these segments at this specific point in time, t_p, are given in the inserted table. Figure 5.3 thus shows which time interval, using the whole piston approach (Table 5.2), is applicable to each segment of the region $x \geq b$ and $y \geq a$ at a point in time. Consequently, for point P_1 (as labelled in Figure 5.3), time interval 2 applies, so $\Omega(t) = \alpha_{CD} - \alpha_{AB}$, whilst point P_2 falls into the area where time interval 4 applies, and consequently $\Omega(t) = \alpha_{CD} + \alpha_{DA} - \pi/2$. It can be seen then that, across the area of the receiver shown in Figure 5.3, three different time intervals apply in this example. Whilst such an approach is suitable for a point receiver model, this is impractical for a finite rectangular receiver. At this point in time, the areas labelled γ, δ, ε, and ζ are active.

Segment	Time Interval
β	Inactive
γ	1
δ	2
ε	3
ζ	4
η	Inactive

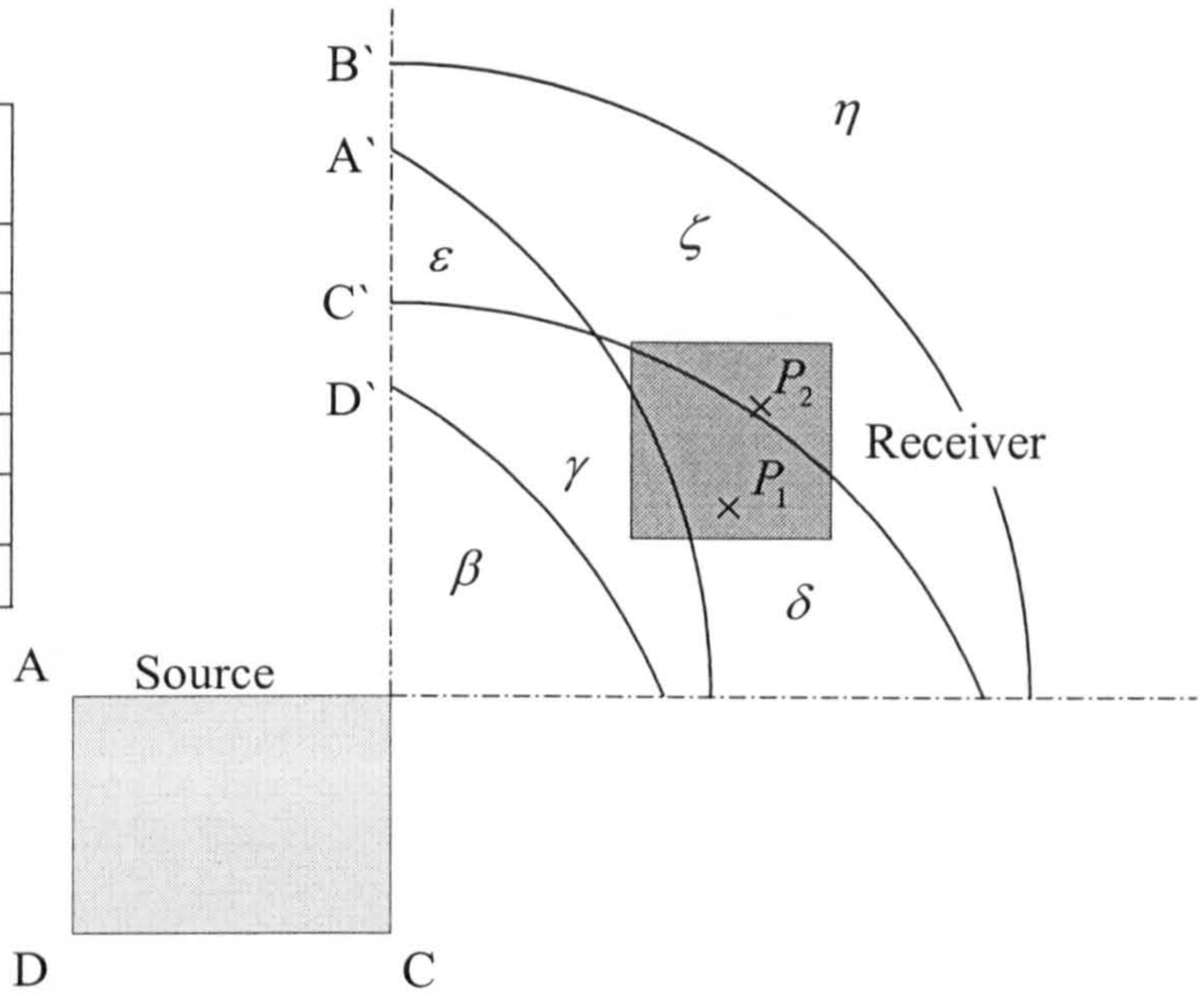

Figure 5.3: Region Segmentation, Whole Piston Approach

Figure 5.4 shows the active and inactive segments of the region shown in Figure 5.3, where $x \geq b$ and $y \geq a$, at a fixed point in time. When each edge is considered separately (in this example edge AB is considered), just one equation applies within the active region. Consequently, whereas the equations required to find $\Omega(t)$ at points P_1 and P_2 in Figure 5.3 were different, in this new approach only one equation applies, $\Omega(t)_{AB} = \alpha_{AB}$ (see Table 5.3). This is clearly better-suited to the problem of modelling the field of a rectangular source detected by a rectangular receiver, as any point on the receiver need be considered as falling into the active or inactive area, rather than any one of the 4 areas within the active area as was shown in Figure 5.3.

The second advantage of using the new approach, is that the angle $\Omega(t)_{edge}$ remains constant for all points within the active region along a line parallel to the edge being considered, so the integration over the area of the receiver can be reduced to a integral in either the x or y direction, depending on which edge is being considered. This is shown in Figure 5.5 for edge AB, where it can be seen that the arc of radius ct_p centred on a point on the line EF, intersects the source at an angle $\Omega(t)_{AB}$, and that this angle is the same for all points on the line EF.

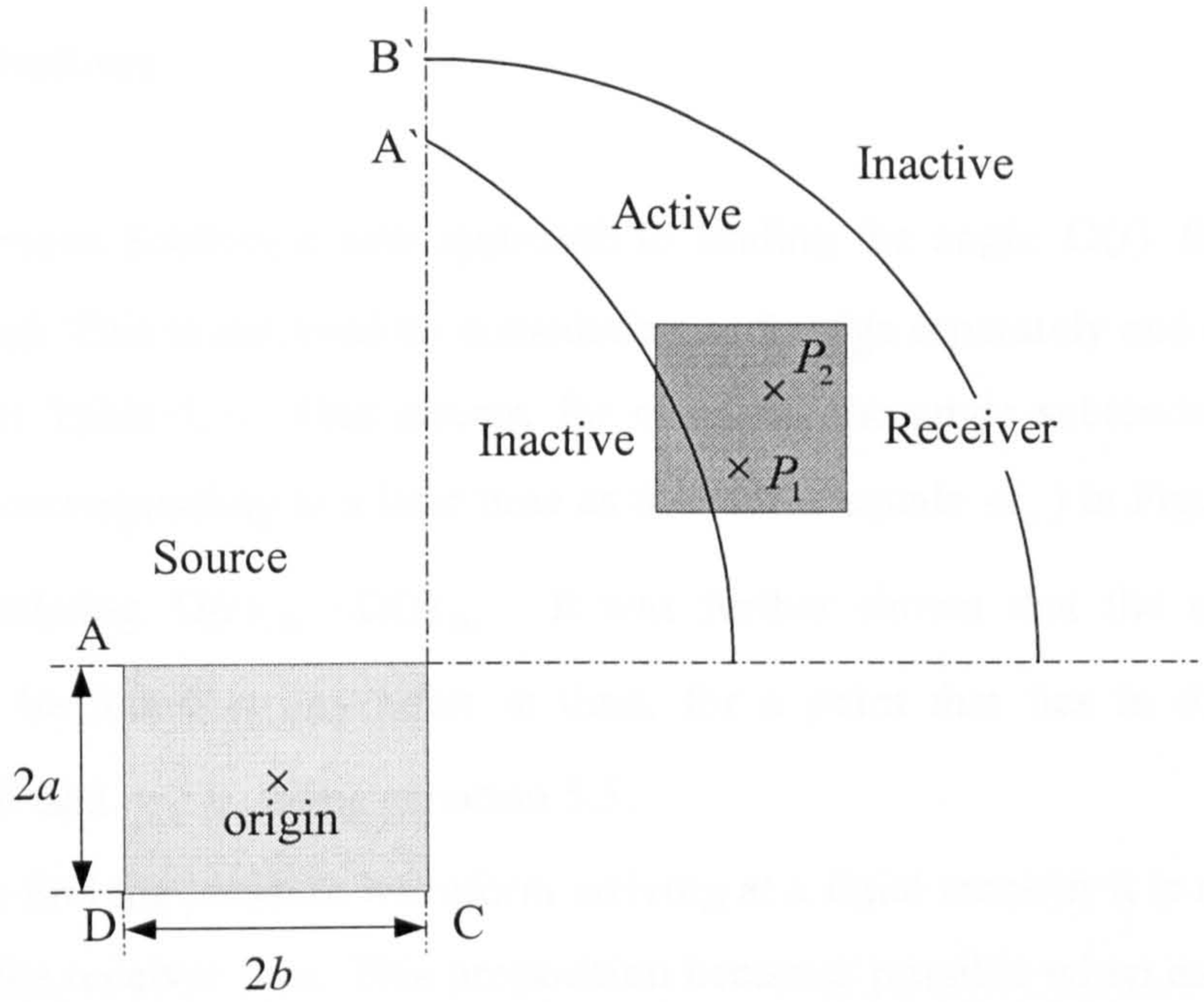

Figure 5.4: Region Segmentation for edge AB

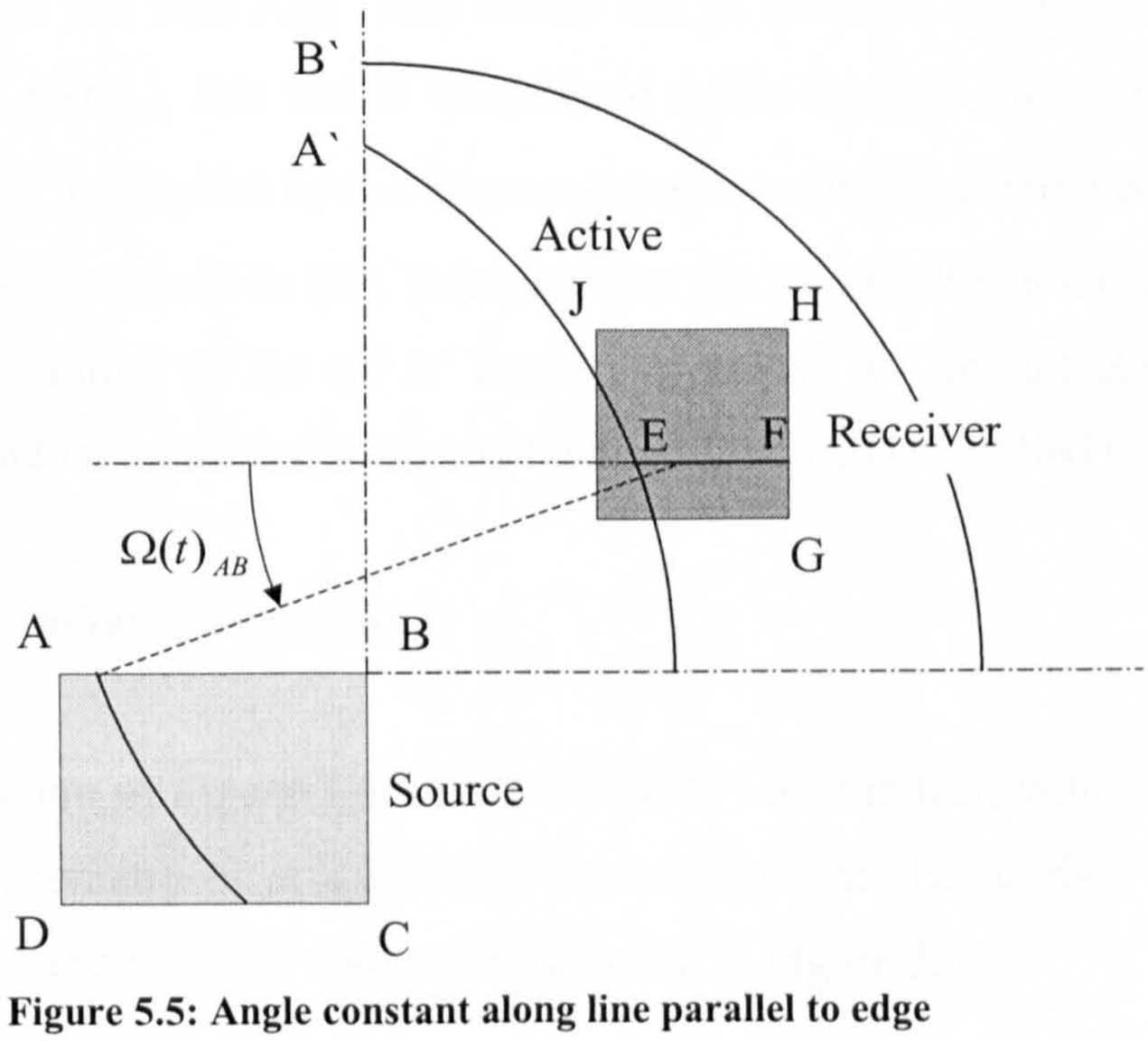

Figure 5.5: Angle constant along line parallel to edge

If a different edge were to be considered, the same would be true, for example consider edge AD, the angle would be constant for any point within the active part of the receiver on a line parallel to HG. Consequently, for the edge AB, a line integral needs to be performed in the y direction and for edge AD a line integral in the x direction must be performed.

5.4 General solutions

In the previous Section, a new approach to finding the angle $\Omega(t)$ for a field point was described. This is achieved by considering each edge separately and using the equations given in Table 5.3. This allows, for example, the angle subtended by the larger radius arc (corresponding to a later time as the radius equals ct_p) in Figure 5.2 to be found by calculating $\Omega(t)_{CD} - \Omega(t)_{DA}$. It was further shown that the subtended angle, $\Omega(t)$, can be found at any point in time, for a point that lies in the region described by $x \geq b$ and $y \geq a$, using equation 5.5.

In order to find the pressure waveform arriving at a finite receiver it is necessary to integrate over the receiver area. This proposition becomes possible when each of the angles, relating to each of the edges as given in Table 5.3, are considered separately. Figure 5.5 shows how these angles remain constant along lines parallel to the edge under consideration (in this case AB). This means that in terms of an integration over the receiver area for $\Omega(t)_{AB}$, this would simplify to a line integral over the distance from H to G, of $\Omega(t)_{AB}$ multiplied by the distance parallel to the edge being considered (in the example given this would be EF). It is clear that the length EF is not equal to the length JH, but rather limited by the arc A` centred on corner A. This integration will now be considered, and the term "corner-limited integration" will be applied to it.

5.4.1 Corner limited integration

From examination of Figure 5.5, it is possible to imagine that, with a different source and receiver geometry or at a different moment in time the receiver could be crossed by both arc A` and B`. Such a situation is shown in Figure 5.6.

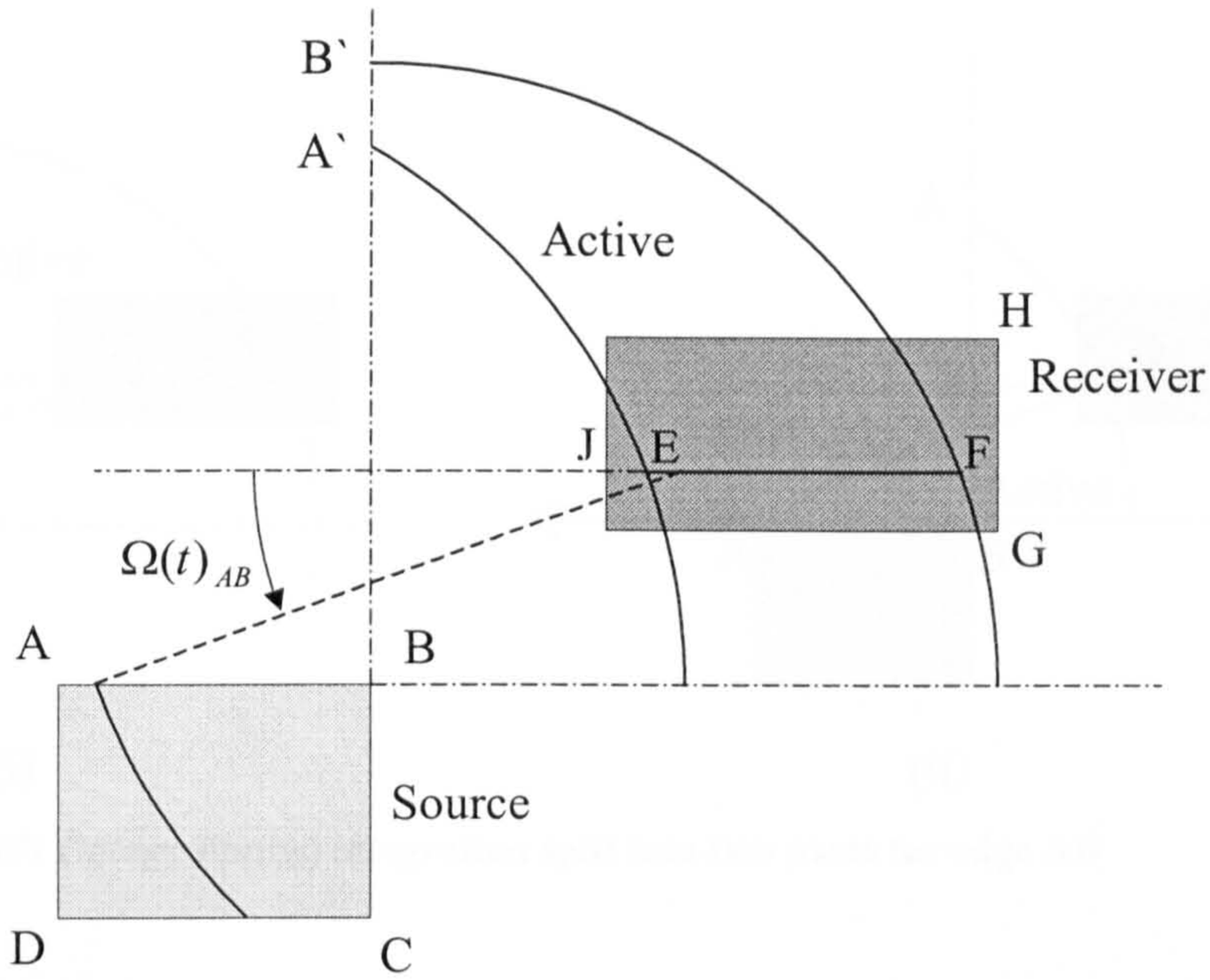

Figure 5.6: Corner limited integration, when the receiver is crossed by both A`, and B`

In order to avoid having to integrate the product of length EF and $\Omega(t)_{AB}$, over the range of G to H, it is easier to consider the integral of the product of JF and $\Omega(t)_{AB}$, minus the integral of product of JE and $\Omega(t)_{AB}$, over the same range. Firstly, consider the integral involving JF. To alter what is seen in Figure 5.6, to an integral over the length JF, it would be necessary to remove arc A`, this can be done notionally by moving point A away from B towards infinity. In such a scenario the arc B` would be the only boundary to the active area. Secondly, consider the integral involving JE. For the line JE to be in the active area, then a notional edge extending from A towards infinity away from B, would need to be considered, as this would result in the active area being limited only by arc A`. Consequently, the problem is changed to that shown in Figure 5.7, the result required being the result from Figure 5.7 (i) minus that from Figure 5.7 (ii). It can be seen that the problem posed by both of these cases is essentially the same.

This conceptual construct of the integral of $\Omega(t)_{edge}$ over the area of the receiver limited by an arc centred at the end of a line stretching to infinity, is termed the corner limited integral, and a generalised solution will be found.

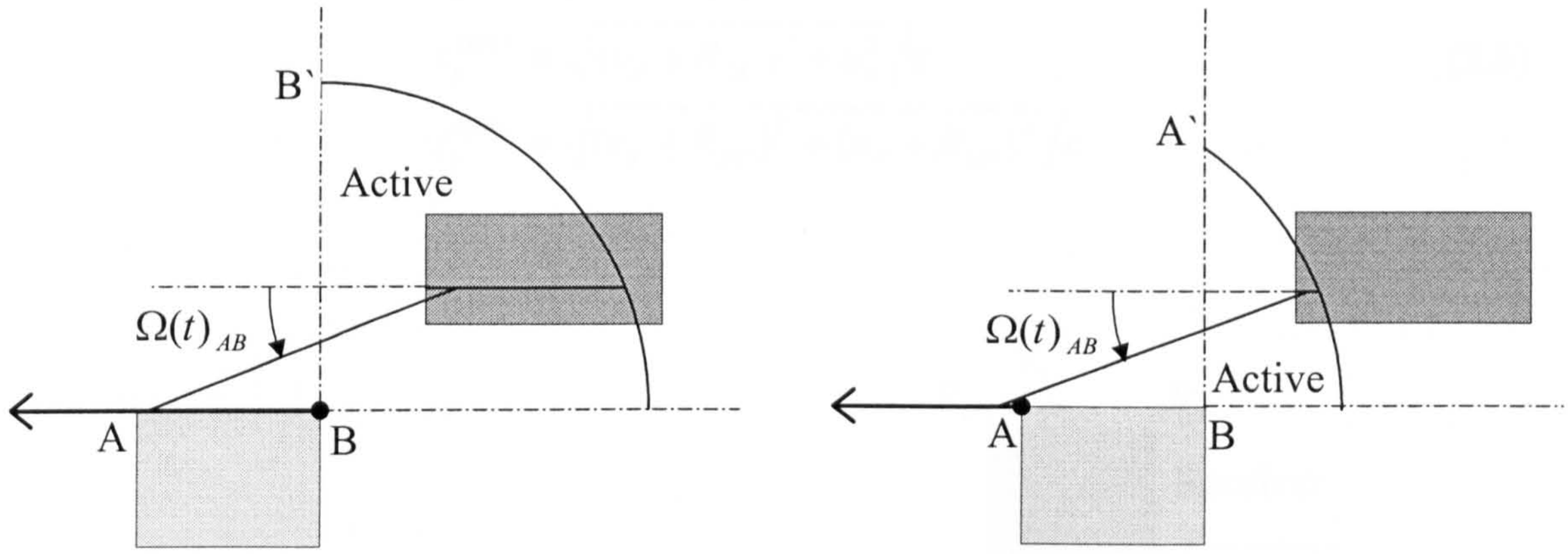

(i) (ii)

Figure 5.7: Corner limited integration split into two parts for edge AB

The dimensions used to solve the corner limited integral are shown in Figure 5.8. These are u_1 which is the length perpendicular to the edge to the line of the receiver being considered, v_1 which is the length of the receiver at u_1 which falls within the active part of the field at any given t_p, u_d which is the perpendicular distance from the considered edge to the receiver, and v_d which is the length from the corner of the source (that is the tip of the infinite line) to the receiver parallel to the edge being considered. In Figure 5.8, the arc shown is centred on the end of the line. In addition, it is necessary to define R_{DC} as the distance between the receiver corners R_D and R_C, and R_{DA} the distance between R_D and R_A. The integration will be performed over the area of the receiver within the arc of radius ct_p, centred at the tip of the infinite line, labelled source corner.

In Figure 5.8, the arc is shown intersecting the two nearest edges of the receiver, although in general there are four combinations of receiver, edges which could be crossed at a point in time, shown in Figure 5.9. To describe these it is also necessary to define four planar times: t_p^{start} the time at which the leading corner of the receiver becomes active; t_p^{switch} the time at which $v_1 = R_{DC}$ at $u_1 = u_d$; t_p^{stable}, the time at which the whole of the receiver is active, (given in equation 5.6), and finally t_p^{end} which will be covered later when the edges are pieced together. The first three of these are given by

$$t_p^{start} = \sqrt{u_d^2 + v_d^2}\,/c$$
$$t_p^{switch} = \sqrt{(v_d + R_{DC})^2 + u_d^2}\,/c \qquad (5.6)$$
$$t_p^{stable} = \sqrt{(v_d + R_{DC})^2 + (u_d + R_{DA})^2}\,/c.$$

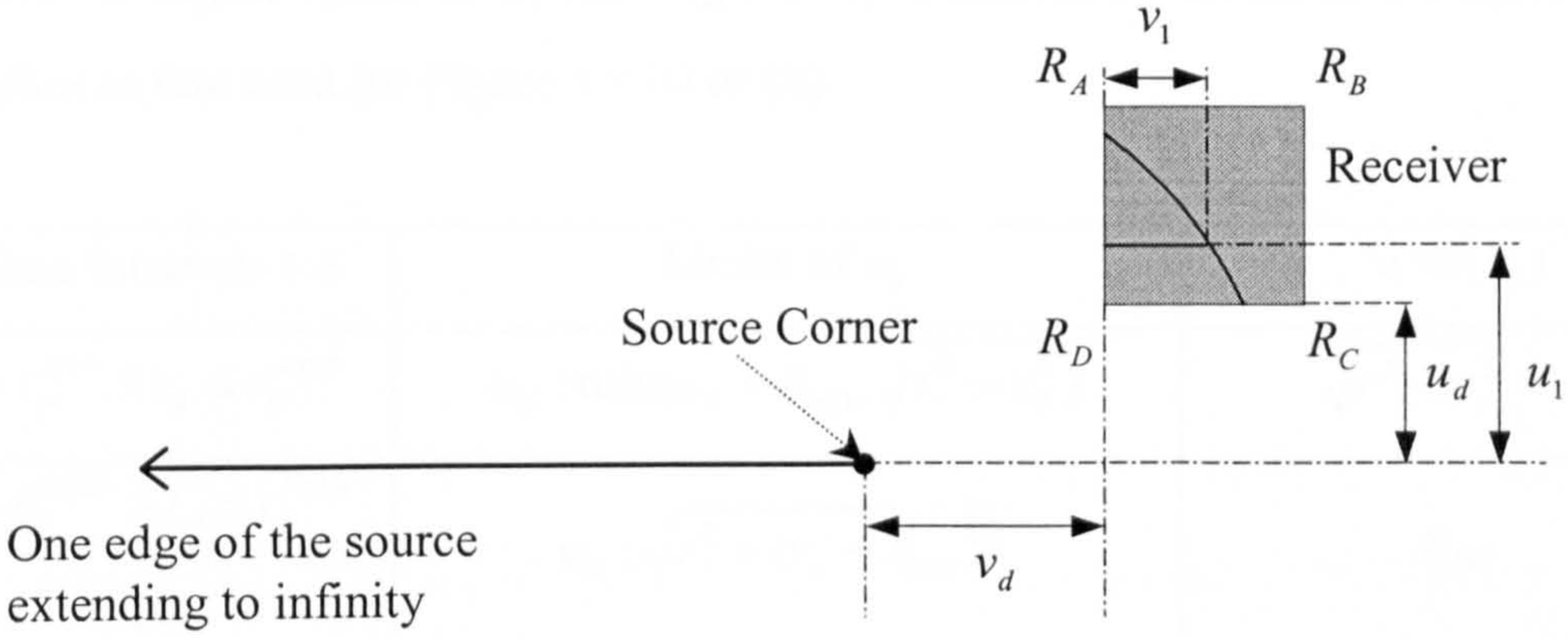

Figure 5.8: Dimensions used in deriving corner limited integral

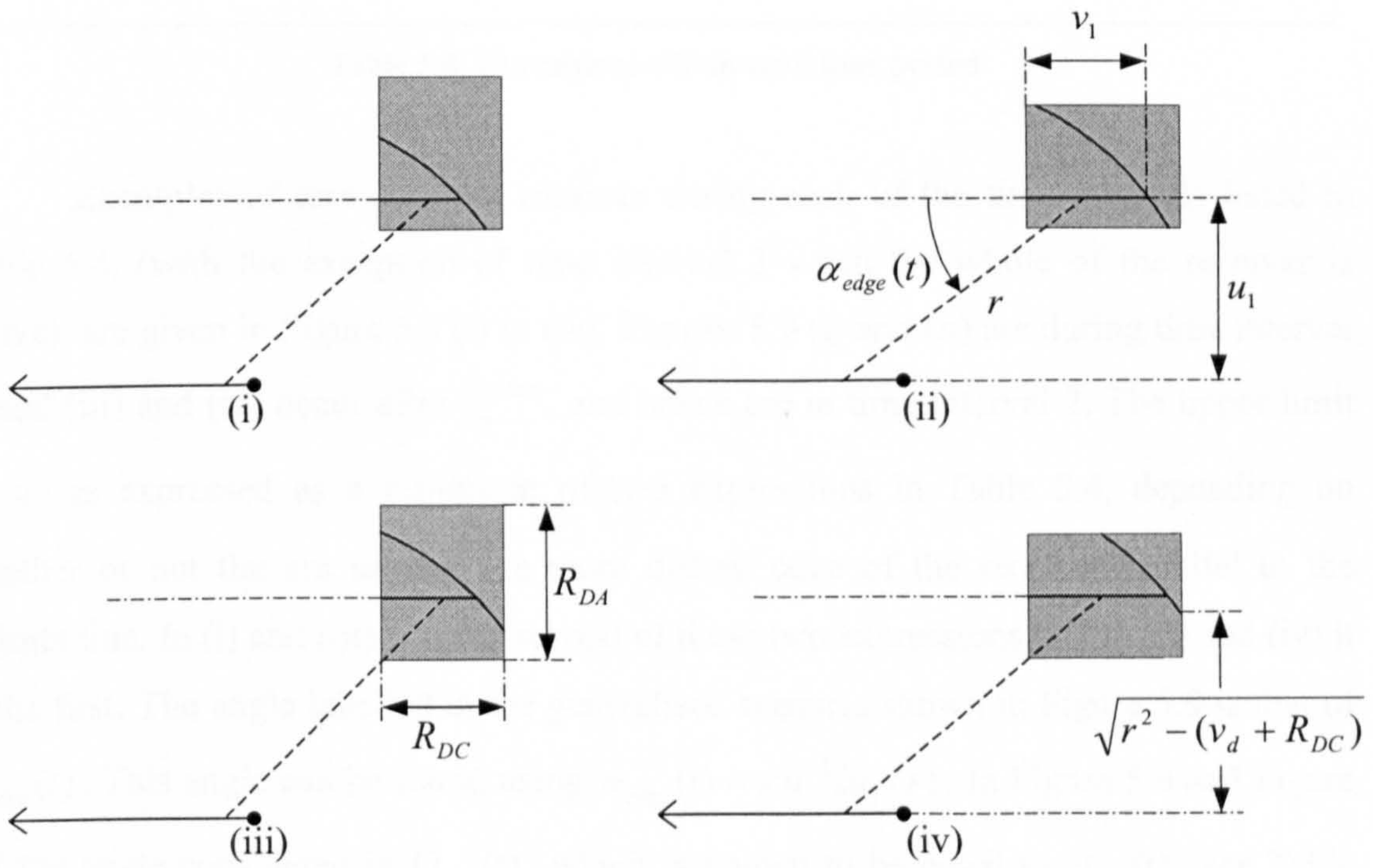

Figure 5.9: Receiver at various time intervals

The four planar times can be used to define three time intervals in each of which the limits of u_1 can be found, and v_1 can be found as a function of u_1 within these

limits. These are found with reference to r which is defined as ct_p, and are listed in Table 5.4. It can be seen from Table 5.4 that between t_p^{switch} and t_p^{stable}, v_1 must be expressed in two different ways, (i) and (ii). The reason for this can be seen in Figure 5.9 (iv). For $u_1 < \sqrt{r^2 - u_1^2} - v_d$, the length v_1 is equal to the length of the receiver, whilst for higher values of u_1 the length of v_1 is limited by the arc so the same equation applies as that used for Figure 5.9 (i) or (ii).

Time Intervals 1:3	Limits of u_1	$v_1 = \mathrm{f}(u_1)$
1) $t_p^{start} \le t_p \le t_p^{switch}$	$u_d : \min(u_d + R_{AD}, \sqrt{r^2 - v_d^2})$	$\sqrt{r^2 - u_1^2} - v_d$
2) $t_p^{switch} \le t_p \le t_p^{stable}$ (i)	$u_d : \sqrt{r^2 - (v_d + R_{DC})^2}$	R_{DC}
(ii)	$\sqrt{r^2 - (v_d + R_{DC})^2} :$ $\min(u_d + R_{AD}, \sqrt{r^2 - v_d^2})$	$\sqrt{r^2 - u_1^2} - v_d$
3) $t_p^{stable} \le t_p \le t_p^{end}$	$u_d : u_d + R_{AD}$	R_{DC}

Table 5.4: Dimensions within each time period

Examples of arcs across a receiver during each of the time intervals listed in Table 5.4, (with the exception of time interval 3 when the whole of the receiver is active), are given in Figure 5.9 (i) to (iv). Figures 5.9 (i) and (ii) are during time interval 1, and (iii) and (iv) occur after t_p^{switch}, and hence are in time interval 2. The upper limit of u_d is expressed as a minimum of two expressions in Table 5.4, depending on whether or not the arc crosses the more distant edge of the receiver parallel to the infinite line. In (i) and (iii) it is the second of these two expressions and in (ii) and (iv) it is the first. The angle labelled in the generalised scenario shown in Figure 5.9 is that of $\alpha_{edge}(t)$. This angle can be found using $\alpha_{edge}(t) = \sin^{-1}(u_1 / r)$. In Figure 5.6 and Figure 5.7 the angle considered is $\Omega_{AB}(t)$, which is known to be equal to $\alpha_{AB}(t)$, see Table 5.3. It can also be seen from Table 5.3, that the relationship between $\alpha_{edge}(t)$ and $\Omega_{edge}(t)$ differs for other edges, so, for the generalised solution, it is necessary to introduce a couple of variables, C_a and C_b, such that $\Omega_{edge}(t) = C_a + C_b \alpha_{edge}(t)$. By

altering the values of C_a and C_b the correct value for the case for each edge in Table 5.3 can be found. This means that in the generalised form

$$\Omega_{edge}(t) = C_a + C_b \sin^{-1}(u_1/r). \tag{5.7}$$

The values for C_a and C_b in each case will be discussed later. The contribution due to a finite edge can then be found using the corner limited integral from the furthest corner of the edge subtracted from that of the nearest corner, the only difference in the expressions being the value of v_d, t_p^{start}, t_p^{switch}, t_p^{stable} and t_p^{end}. This will be covered later.

For the particular case shown, the whole integration could be performed using this geometrical approach. However this is not the case in general for other relative positions of source and receiver, i.e. when the whole of the receiver does not lie in the region described by $x \geq b$ and $y \geq a$. It is therefore necessary to define further geometries to describe the general solution. Firstly an integral limited by an edge rather than an arc centred on a corner will be defined, and then an integral termed the "planar integral" must be defined for the case when receiver lies within the boundaries of the source.

5.4.2 Edge limited Integral

In regions outside that described by $x \geq b$ and $y \geq a$, the projection of the receiver onto the $z = 0$ plane will be alongside two edges of the source, as shown in Figure 5.10. In this case, in order to find the effect of such an edge it will be necessary to define the "edge limited integral".

If the point P′ in Figure 5.10 is considered, then it can be seen that at a given instant in time, which is depicted then the arc centred at P′ crosses the nearest edge twice. Hence, whereas previously it was sufficient to consider one angle per edge as given in Table 5.3, it is now necessary to consider two, which can be dealt with separately.

As previously, the angles must be integrated over the active section of the receiver. These are shown in Figure 5.11, for each of the two angles, as the darker areas of the receiver. For angle $\alpha_1(t)$, the active area is limited by being within the distance r measured normally to the edge under consideration (here AB), and by being more distant than r away from point A. In this situation then the integral of $\alpha_1(t)$ over the

active area of the receiver, can be equated to the integral $\alpha_1(t)$ over the area within a distance of r from the edge of the source, minus a corner limited integral centred on A. So it is necessary to find the first of these, termed an edge limited integral, which is equivalent to the case when the edge of the source is infinitely long, as then there would be no intersecting arc. It is possible to perform the integral of $\alpha_2(t)$ in a similar manner.

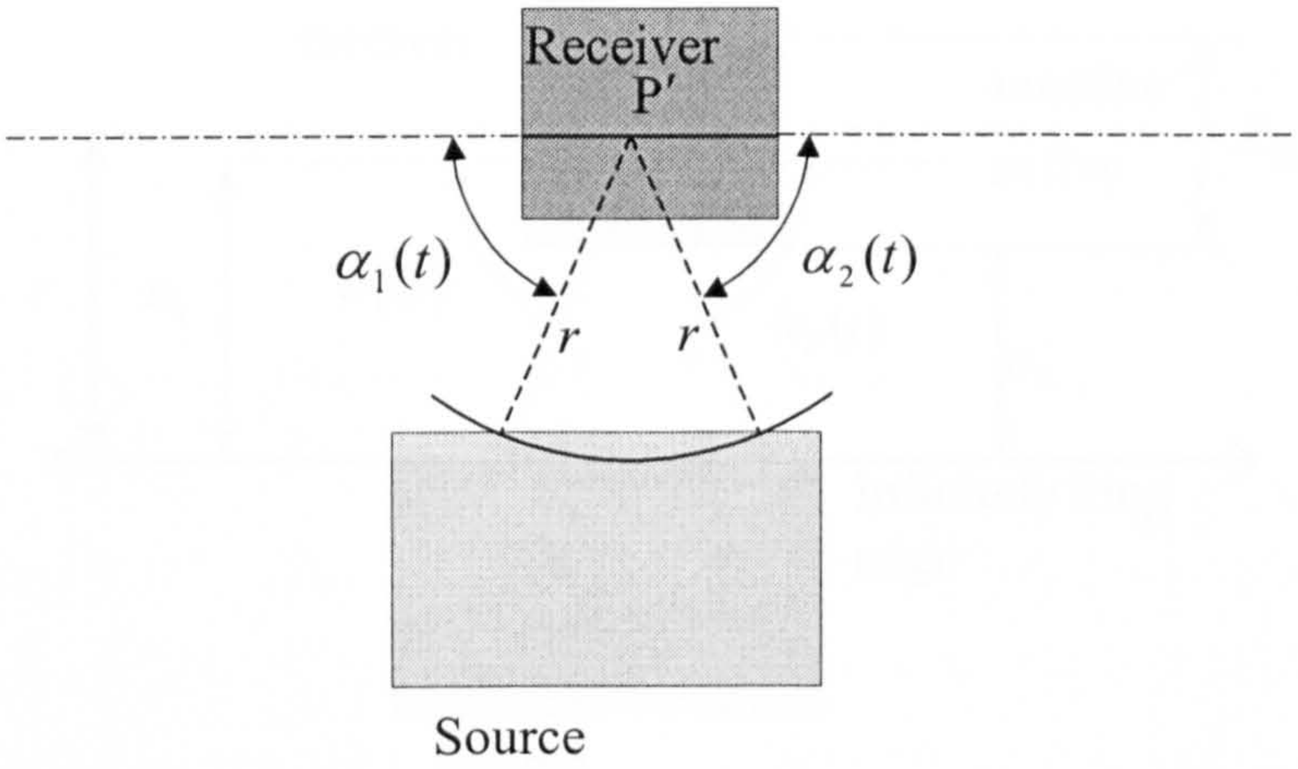

Figure 5.10: Demonstrating the need to define an edge limited integral

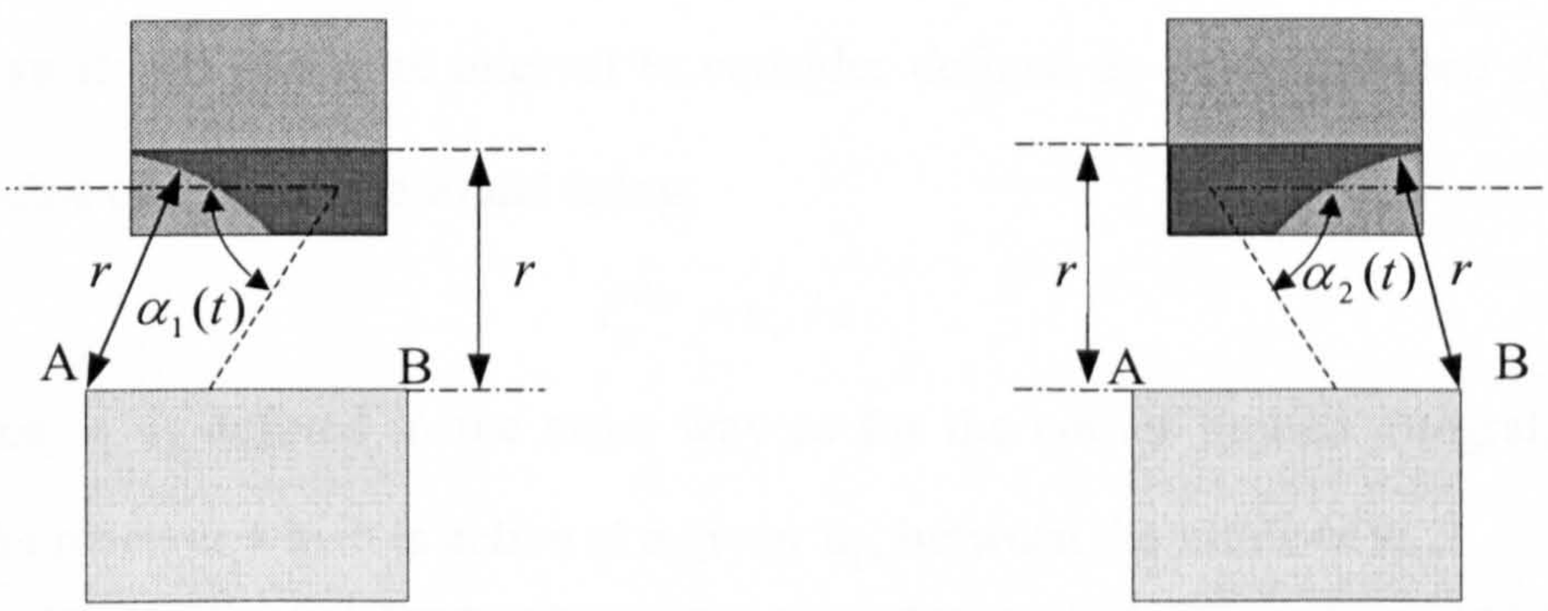

Figure 5.11: Active area for an edge limited integral

The edge limited integral is defined as the integral limited by an infinite line alongside the receiver. It can be seen from Figure 5.10, that the angles $\alpha_1(t)$ and $\alpha_2(t)$ are equal in magnitude. However, they must be considered separately, because when these different integrals are combined all the angles $\Omega_{edge}(t)$ must be with reference to the same line, meaning that the values of C_a and C_b relating $\Omega_{edge}(t)$ to $\alpha_{edge}(t)$ will differ (see equation 5.7).

The variables used are given in Figure 5.12, which shows a receiver alongside an infinite line. It can be seen that the length v_1 is equal to the length of the receiver in the direction parallel to the infinite edge, so equates to R_{DC}, and the integral limits of u_1 in this illustration are $u_d : r$.

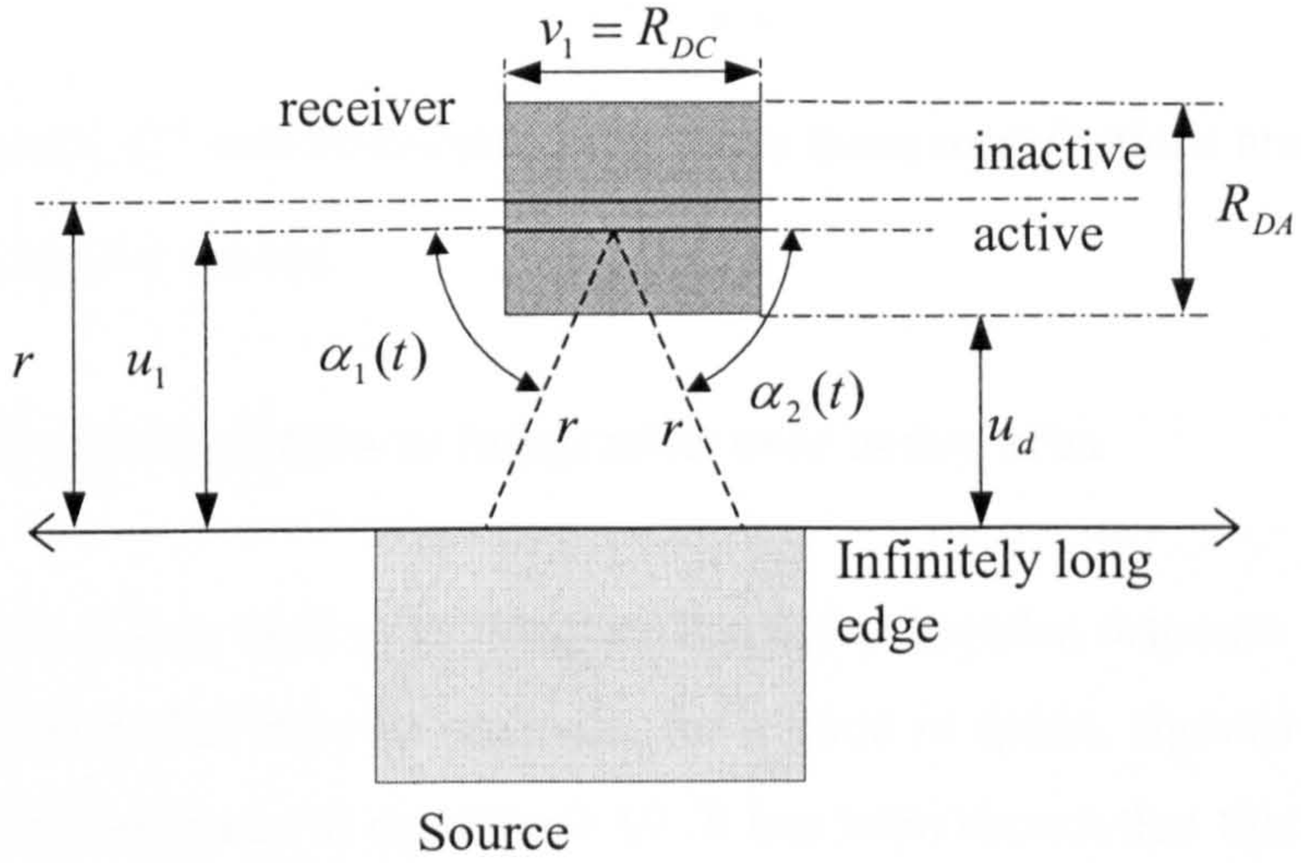

Figure 5.12: Edge limited integral

There is just one time interval to consider defined as being between t_p^{edge} and t_p^{end}. The value of t_p^{edge} can be found using,

$$t_p^{edge} = u_d / \mathrm{c} . \tag{5.8}$$

The distance v_1 is defined in the same way as for the corner limited integral, as the length of the receiver which is active at a given u_1, between the limits of u_1,

Time Interval	Limits of u_1	v_1	(5.9)
$t_p^{edge} \le t_p \le t_p^{end}$	$u_d : \min(u_d + R_{DA}, r)$	R_{DC}	

The two preceding geometric constructs, the corner and edge limited integrals, can be used to model the case shown in Figure 5.12, however one further integral is required so that a solution can be found for a receiver lying in any region.

5.4.3 Planar Integral

When the projection of the receiver onto the plane of the source is such that the two overlap, then the planar integral must be considered. If a point is considered which

falls into this region, then it will subtend an arc, $\Omega(t) = 2\pi$, until r is such that the arc crosses the nearest edge. As with the corner and edge limited integrals it is useful to consider an extension of the source, so that is covers an infinite plane. This would mean that during the time interval $t_p^{plane} \le t_p \le t_p^{end}$, the whole of the area of the receiver, $R_{DA} \times R_{DC}$, subtends an arc of $\Omega(t) = 2\pi$, where,

$$t_p^{plane} = 0 \tag{5.10}$$

and as previously, t_p^{end} will be covered later when these contributions are pieced together to form a rectangular source.

5.4.4 General solution to integration over active area

The aim of this work is to integrate the scalar impulse response over the area of the receiver. The scalar impulse response, for a point in space, equates to a function in terms of the $\Omega(t)$ as given in equation 1.19. It has been shown that this time dependent angle can be found by considering each edge in turn, and for each edge a new angle is defined, $\Omega_{edge}(t)$. The integration of this angle can be performed over the active area of the receiver by using a combination of the three limited integrals previously described in Sections 5.4.1 to 5.4.3, namely the corner limited integral, the line limited integral and the planar integral. Once these integrals have been solved, the results can be used to form a summation of each $\Omega_{edge}(t)$ in a similar way as was described for a point, (see equation 5.5). These three integrals have been defined in terms of the limits over which they must be performed and the function to be integrated. In this Section, a general solution will be found.

In order to average the impulse response, $h(\bar{r},t)$, over the area of the receiver, equation 1.19 must be amended so that the subtended arc, $\Omega(t)$, is integrated over the area of the receiver for each successive time point and by dividing by the area of the receiver, giving,

$$h(\bar{r},t) = \frac{c}{2\pi . R_{DA} . R_{DC}} . \iint \Omega(t) dv_1 du_1 , \tag{5.11}$$

here the vector, $\bar{r}$, relates the location of the receiver with respect to the source.

By considering the angle to each edge separately, and with the realisation that along lines of constant u_1, this angle, $\Omega_{edge}(t)$ is constant as defined in Figure 5.8, the integral needed for the edge and corner limited integrals is reduced to a line integral. This does not yield the answer to $h(\bar{r},t)$, as the angle considered is different, but can be used to calculate it. The result will be termed $h_{general}(\bar{r},t)$, and is given at any given t_p in the form,

$$h_{general}(\bar{r},t) = \frac{c}{2\pi.R_{DA}.R_{DC}} . \int_{u_1^{lower}}^{u_1^{upper}} \Omega_{edge}(t).v_1 du_1 \qquad (5.12)$$

If a generalised solution capable of being implemented for both edge and corner limited integrals is to be found then a way must be found to express v_1 for any case, to this end the constants C_c and C_d are introduced, such that v_1 becomes $C_c.\sqrt{r^2-u_1^2}+C_d$. Using this and equation 5.7, the generalised form becomes,

$$h_{general}(\bar{r},t) = \frac{c}{2\pi.R_{DA}.R_{DC}} . \int_{u_1^{lower}}^{u_1^{upper}} (C_a + C_b.\sin^{-1}(u_1/r)).(C_c.\sqrt{r^2-u_1^2}+C_d)du_1 \qquad (5.13)$$

Then one integral will be valid for both the corner and edge limited integrals, over all time intervals, (although for time interval 2 in the corner limited integrals the integration must be performed twice, that is for (i) and for (ii), see Table 5.4), provided the correct values of C_a, C_b, C_c, C_d are used.

This becomes more manageable by multiplying out the brackets, and separating, such that,

$$h_{general}(\bar{r},t) = \frac{c}{2\pi.R_{DA}.R_{DC}} (A+B+C) \qquad (5.14)$$

where,

$$A = C_b.C_d . \int_{u_1^{lower}}^{u_1^{upper}} \sin^{-1}(u_1/r)du_1 \qquad (5.15)$$

$$= C_b.C_d . \left[u_1.\sin^{-1}(u_1/r) + \sqrt{r^2-u_1^2} \right]_{u_1^{lower}}^{u_1^{upper}}$$

and

$$B = C_b.C_c . \int_{u_1^{lower}}^{u_1^{upper}} \sqrt{r^2-u_1^2}.\sin^{-1}(u_1/r)du_1 \qquad (5.16)$$

$$= C_b.C_c . \left[\frac{r^2}{4}.(\sin^{-1}(u_1/r))^2 + \frac{u_1}{2}.\sin^{-1}(u_1/r).\sqrt{r^2-u_1^2} + \frac{r^2}{8} - \frac{u_1^2}{4} \right]_{u_1^{lower}}^{u_1^{upper}}$$

and finally

$$\begin{aligned} C &= C_a \cdot \int_{u_1^{lower}}^{u_1^{upper}} C_c \cdot \sqrt{r^2 - u_1^2} + C_d du_1 \\ &= C_a \left[C_c \cdot \left\{ \frac{u_1}{2} \cdot \sqrt{r^2 - u_1^2} - \frac{r^2}{2} \cdot \cos^{-1}(u_1 / r) \right\} + C_d \cdot u_1 \right]_{u_1^{lower}}^{u_1^{upper}}, \end{aligned} \tag{5.17}$$

these integrals are performed in Appendix D.

The plane integral can be solved with reference to equation 5.12, and yields a simple result of,

$$h(\bar{r}, t) = \mathrm{c} \tag{5.18}$$

because the angle, $\Omega(t)$ is constant at, 2π over the whole area of the receiver.

These three definite integrals are well suited to a computer program, which would solve the equations in sequential time steps. However it is first necessary to find the values of the constants, C_a, C_b, C_c and C_d, and to define t_p^{end}, for each corner and line limited integral, so that the solution can be pieced together.

5.5 Regions

As described above, the line limited integral and planar integral are only required for certain parts of the plane in which the piston source lies. Hence, this plane must be divided into regions, and the receiver segmented if it lies across the boundary of these regions. The four different regions that need be considered are shown in Figure 5.13. The segmentation of a receiver overlapping these different Regions is shown in Figure 5.14.

For a prediction of the pressure field at any point, the symmetry of the system means that only the area described by $x \geq 0$ and $y \geq 0$ need be considered, so that regions 1-4 are required. With a finite area receiver, the possibility that in either the x or y direction, or in both, the receiver is larger than the source, means that even if $x \geq 0$ and $y \geq 0$, some part of the receiver may lie within the additional Sectors 5-9. However, any segment of the receiver lying within Sectors 5-9 can be reflected into Regions 1-3, hence the reason for different terms being used. It is also necessary to divide Region 4 into four Zones, this will be discussed further in Subsection 5.6.3. The Sectors, Regions and Zones are shown in relation to the source in Figure 5.13.

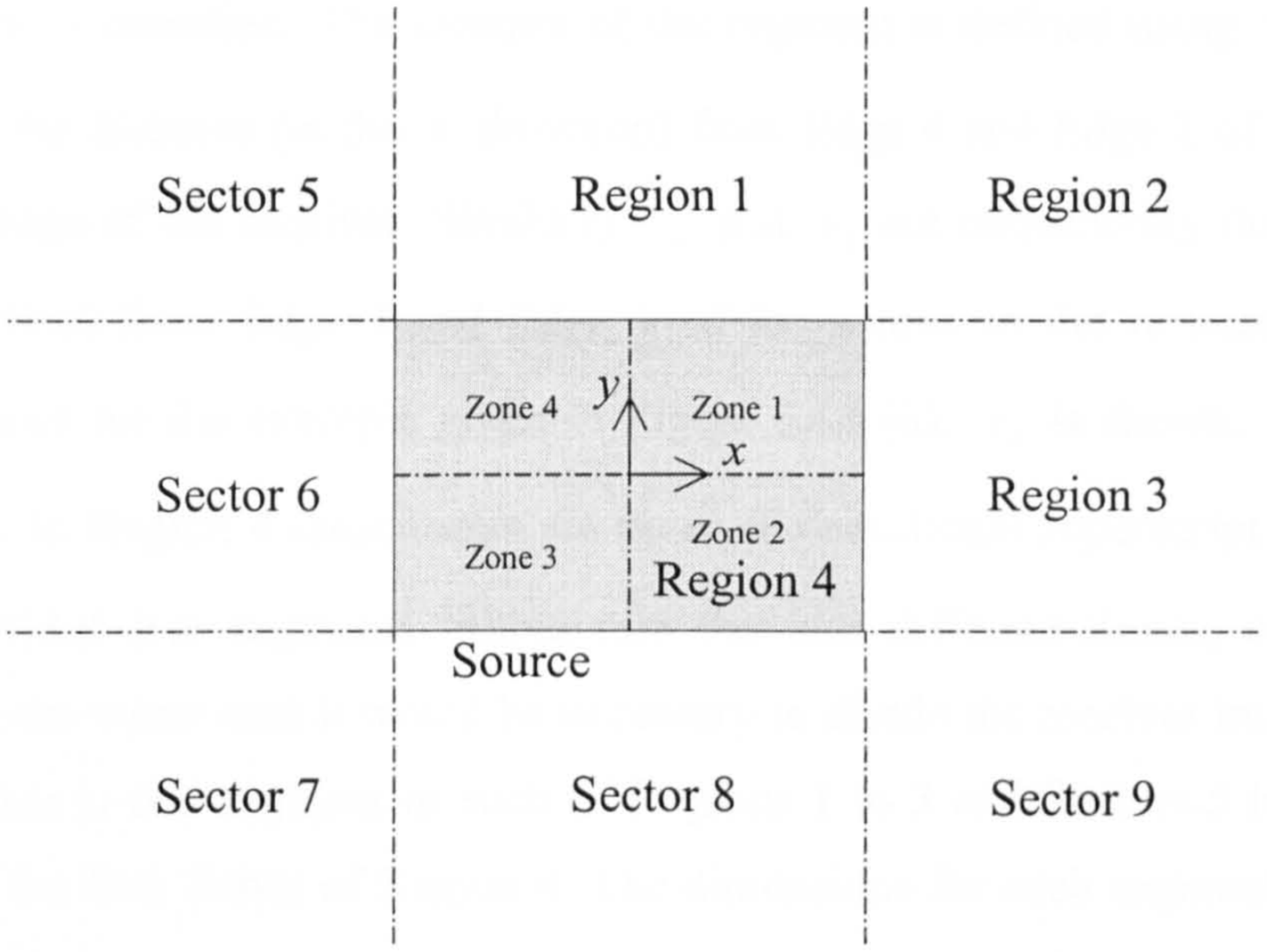

Figure 5.13: Regions and Sectors

The way in which the receiver overlaps the various Regions and Sectors, when projected onto the plane of the source, defined as $z = 0$, depends on the size of the source and receiver, and the location of the receiver, which is expressed as the coordinate x_r, y_r, relating the centre of the source to the centre of the receiver. When the receiver lies within two or more Regions it is necessary to divide it into parts, each part lying in just one Region. For this segmentation of the receiver to be possible, it is necessary to define some terms for the size of the source, $2b \times 2a$, and the receiver, $2e \times 2d$, these are shown in Figure 5.14, which gives an example of the segmentation of the receiver. In this case the receiver, shown in Figure 5.14 (i), falls into four Regions, (regions 1 to 4), and hence is divided into four segments shown in Figure 5.14 (ii) to (v) (shown at half the scale of Figure 5.14 (i)) which can then be considered separately. It can be seen that the four edges of the source have been labelled, Edge 1 to Edge 4 respectively in Figure 5.14 (i).

After segmentation, the parts of the receiver are considered separately for each sector. By using the same terms to describe the geometry of the receiver segment in each sector, any computer program written to numerically implement this model is simplified, as it could loop through the sectors simply changing the values of these terms. The size of the receiver segment is defined using the terms r_x in the x direction,

and r_y in the y direction. The location of the segment is defined using x_a and x_b as respectively the distance (in the x direction) from Edge 4 and Edge 2 of the source to the nearest edge of the receiver. Similarly y_a and y_b are respectively the distance (in the y direction) from Edge 3 and Edge 1 of the source to the nearest edge of the receiver. Hence for the example given in Figure 5.14 (ii), x_a is shown, y_a is $2a$, x_b and y_b are 0. In Region 4 these terms are given the additional superscript ^{whole} prior to being subdivided into segments falling into the four different Zones, compromising Region 4. In the worst case it would be necessary to divide the receiver into 13 separate segments. That is one segment in each of Regions 1 to 3 and Sectors 5 to 9, and four segments in the four Zones of Region 4. The dimensions for each segment are given in Table 5.5.

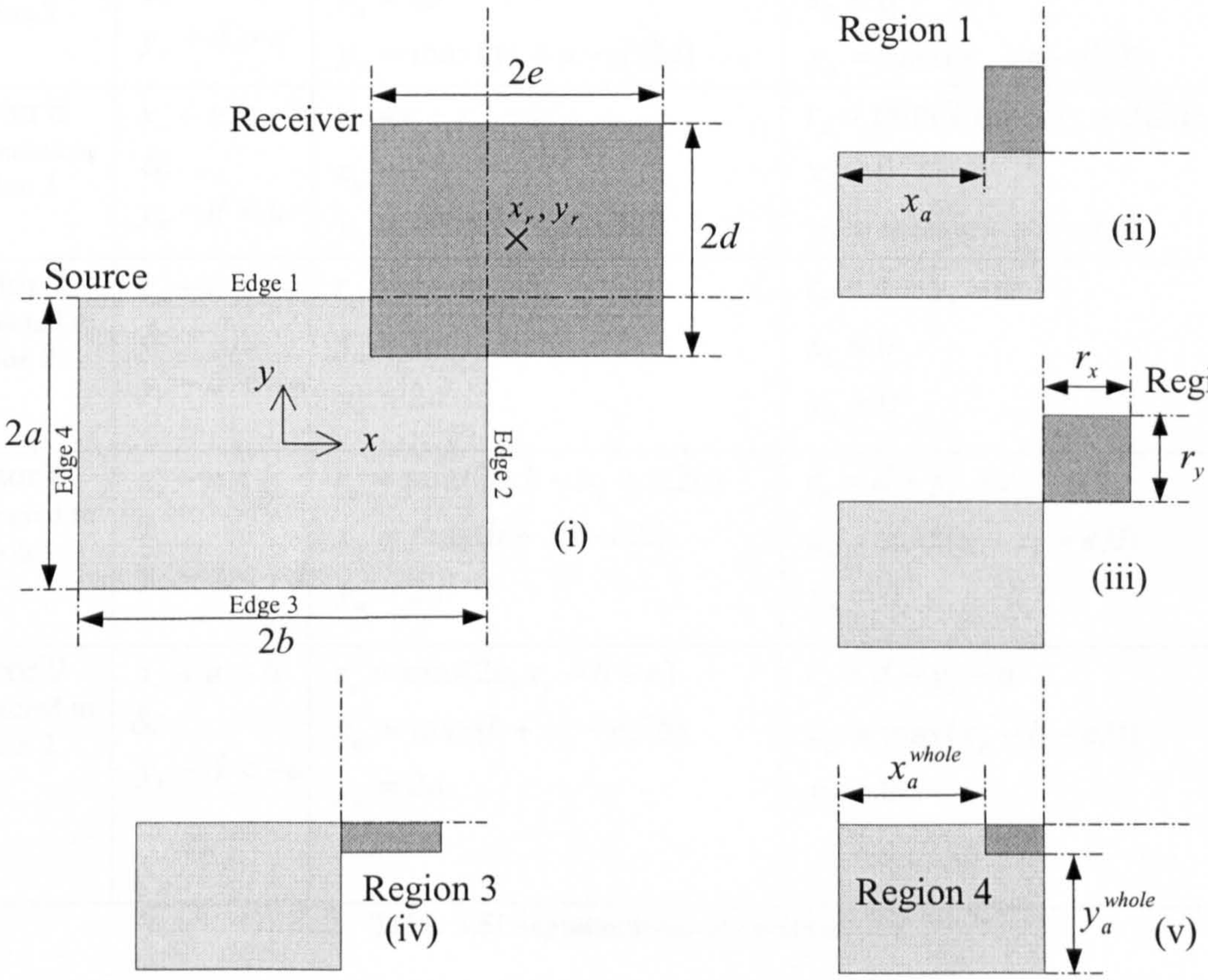

Figure 5.14: An example of segmentation, the whole receiver (i), is divided into four parts: (ii), (iii), (iv) and (v).

	Occurs if:		
Region 1	$x_r - e < b$ & $y_r + d > a$	$r_x = \min(2e, b - x_r + e, 2b)$ $x_a = \max(b + x_r - e, 0)$ $y_a = \max(y_r + a - d, 2a)$	$r_y = \min(2d, y_r + d - a)$ $x_b = \max(b - x_r - e, 0)$ $y_b = \max(y_r - a - d, 0)$
Region 2	$x_r + e > b$ & $y_r + d > a$	$r_x = \min(2e, x_r - b + e)$ $x_a = \max(b + x_r - e, 2b)$ $y_a = \max(y_r + a - d, 2a)$	$r_y = \min(2d, y_r + d - a)$ $x_b = \max(x_r - b - e, 0)$ $y_b = \max(y_r - a - d, 0)$
Region 3	$x_r + e > b$ & $y_r - d < a$	$r_x = \min(2e, x_r - b + e)$ $x_a = \max(b + x_r - e, 2b)$ $y_a = \max(y_r + a - d, 0)$	$r_y = \min(2d, a - y_r + d, 2a)$ $x_b = \max(x_r - b - e, 0)$ $y_b = \max(a - y_r - d, 0)$
Region 4 (prior to zoning)	$x_r - e < b$ & $y_r - d < a$	$r_x^{whole} = \min(2e, b - x_r + e, 2e)$ $x_a^{whole} = \max(b + x_r - e, 0)$ $y_a^{whole} = \max(y_r + a - d, 0)$	$r_y^{whole} = \min(2d, a - y_r + d, 2a)$ $x_b^{whole} = \max(b - x_r - e, 0)$ $y_b^{whole} = \max(a - y_r - d, 0)$
Sector 5 Reflected to Region 2	$x_r - e < -b$ & $y_r + d > a$	$r_x = e - x_r - b$ $x_a = 2b$ $y_a = \max(y_r + a - d, 2a)$	$r_y = \min(2d, y_r + d - a)$ $x_b = 0$ $y_b = \max(y_r - a - d, 0)$
Sector 6 Reflected to Region 3	$x_r - e < -b$ & $y_r - d < a$	$r_x = e - x_r - b$ $x_a = 2b$ $y_a = \max(y_r + a - d, 0)$	$r_y = \min(2d, a - y_r + d, 2a)$ $x_b = 0$ $y_b = \max(a - y_r - d, 0)$
Sector 7 Reflected to Region 2	$x_r - e < -b$ & $y_r - d < -a$	$r_x = e - x_r - b$ $x_a = 2b$ $y_a = 2a$	$r_y = d - y_r - a$ $x_b = 0$ $y_b = 0$
Sector 8 Reflected to Region 1	$x_r - e < b$ & $y_r - d < -a$	$r_x = \min(2e, b - x_r + e, 2b)$ $x_a = \max(b + x_r - e, 0)$ $y_a = 2a$	$r_y = d - y_r - a$ $x_b = \max(b - x_r - e, 0)$ $y_b = 0$
Sector 9 Reflected to Region 2	$x_r + e > b$ & $y_r - d < -a$	$r_x = \min(2e, x_r - b + e)$ $x_a = \max(b + x_r - e, 2b)$ $y_a = 2a$	$r_y = d - y_r - a$ $x_b = \max(x_r - b - e, 0)$ $y_b = 0$

Table 5.5: Segmentation of receiver

Note that the segments in each of the Sectors have been reflected into Regions, and that the equations have been simplified by imposing the restriction $x_r \geq 0$ and $y_r \geq 0$ which utilises the symmetry of the pressure field (as in a point receiver model). It should be noted that any segment in Sector 5 can be reflected to Region 2, Sector 6 to Region 3,

Sector 7 to Region 2, Sector 8 to Region 1 and Sector 9 to Region 2. When part of the receiver lies within Region 4 then it gets subdivided into Zones using the equations in Table 5.6, all these segments have been reflected into Zone 1.

	Occurs if:		
Zone 1	Always	$r_x = \min(r_x^{whole}, r_x^{whole} - b + x_a^{whole})$ $x_a = \max(b, x_a^{whole})$ $y_a = \max(a, y_a^{whole})$	$r_y = \min(r_y^{whole}, r_y^{whole} - a + y_a^{whole})$ $x_b = x_b^{whole}$ $y_b = y_b^{whole}$
Zone 2	$y_a^{whole} < a$	$r_x = \min(r_x^{whole}, r_x^{whole} - b + x_a^{whole})$ $x_a = \max(b, x_a^{whole})$ $y_a = a$	$r_y = a - y_a^{whole}$ $x_b = x_b^{whole}$ $y_b = y_a^{whole}$
Zone 3	$y_a^{whole} < a$ & $x_a^{whole} < b$	$r_x = b - x_a^{whole}$ $x_a = b$ $y_a = a$	$r_y = a - y_a^{whole}$ $x_b = x_a^{whole}$ $y_b = y_a^{whole}$
Zone 4	$x_a^{whole} < b$	$r_x = b - x_a^{whole}$ $x_a = b$ $y_a = \max(a, y_a^{whole})$	$r_y = \min(r_y^{whole}, r_y^{whole} - a + y_a^{whole})$ $x_b = x_a^{whole}$ $y_b = y_b^{whole}$

Table 5.6: Subdivision of the receiver within Region 4

5. 6 Reconstruction of the source

It is now possible to reconstruct the source from the corner limited, edge limited and planar integrals, within each defined region. This is done by finding the correct value for v_d, u_d, R_{DA}, R_{DC}, C_a, C_b, C_c, C_d and t_p^{end} in each case, and is performed for both corners of each edge in turn. The labelling of these points are shown in Figure 5.15, where it should be noted that each corner of the source has two different labels depending on the edge being considered. This allows a simplification, as when the integrals are summed, all those from Pt 1s are positive, and all those from Pt 2s are negative.

Three examples will now be given for receiver segments lying in different regions. Firstly for Region 2, where only corner limited integrals are required, then for Region 3 where in addition it is necessary to include edge limited integrals, and finally for a case in Region 4 where corner limited, edge limited and planar integrals must be

considered. Note that the approach used for Region 1 is the same as that used for Region 3.

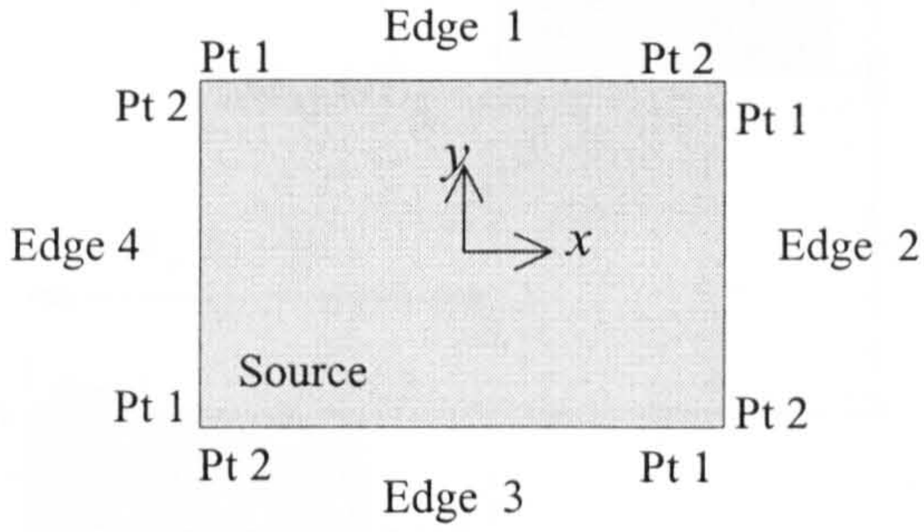

Figure 5.15: Labelling of the source

5.6.1 An example of source reconstruction in Region 2

An example will now be given, for a receiver segment lying in Region 2. Figure 5.16 shows two arcs across the receiver, of radius r. These arcs originate from edge 1, Pt 1, and edge 1, Pt 2 on the source. The dimensions given in this figure are for Edge 1.

The total contribution of Edge 1 can be found using the corner limited integrals (the time intervals and limits from Table 5.4, integrated over the area in equations 5.14-5.17), of Pt 1 and Pt 2. The corner limited integral has been described as relating to a line starting at a point and extending to infinity. Consequently the contribution from Edge 1 can be found by the following:

$$h_{edge1}(\bar{r},t) = h^{corner}_{edge1\,pt2}(\bar{r},t) - h^{corner}_{edge1\,pt1}(\bar{r},t) \tag{5.18}$$

at any given t value, where h is presented with a superscript relating to the type of integral (corner limited, line limited or planar), and a subscript relating to the point on the source under consideration.

The subtraction in equation 5.18 will equal 0, once the whole of the receiver is within the active region for both Pt 1 and Pt 2, as $h^{corner}_{edge1\,pt2}(\bar{r},t)$ will equal $h^{corner}_{edge1\,pt1}(\bar{r},t)$. This condition occurs at t_p^{stable} for the more distant point, in this case Pt 1. Consequently, t_p^{end} for both points on edge 1 is defined as equal to this value.

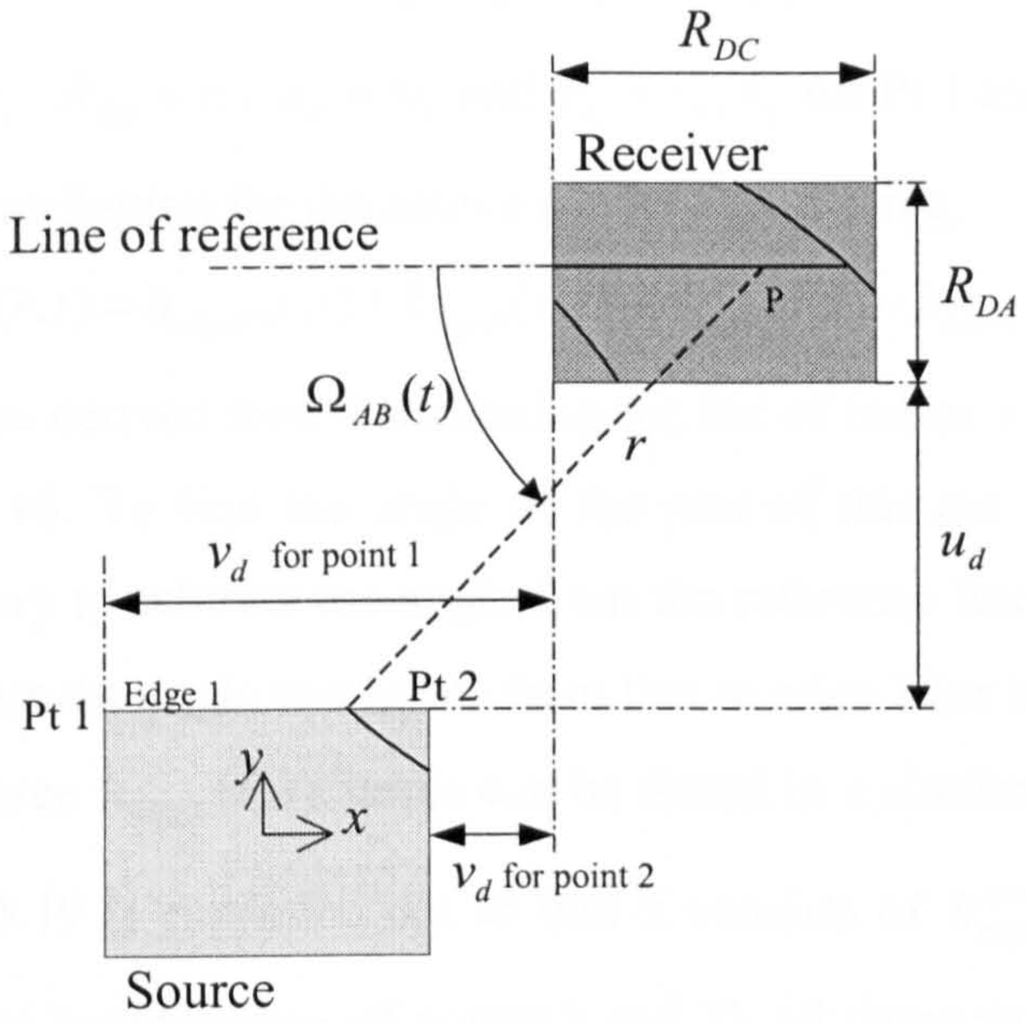

Figure 5.16: An example in Region 2 for Edge 1

The angle $\Omega_{edge}(t)$ must be defined consistently for the summation of different integrals to be valid. For Regions 1 to 3, the reference line is defined as the line passing through the point on the receiver being considered in the negative x direction along a line parallel to the x axis, as shown in Figure 5.16. The angle runs from $-\pi$ to $+\pi$ (in these three regions the discontinuity across the line which passes from $-\pi$ to $+\pi$ is not crossed). This allows both C_a and C_b, (as used in equation 5.13 which integrates the angle at a point over the area of the receiver), to be found for edge 1. In fact for edge 1, $C_a = 0$ and $C_b = 1$ for both Pt 1 and Pt 2 (similarly for edge 4, $C_a = \pi/2$ and $C_b = -1$).

In equation 5.13, the distance v_1 (shown in Figure 5.9) is expressed as $C_c \cdot \sqrt{r^2 - u_1^2} + C_d$, and v_1 is given for each time interval in Table 5.4. Consequently, for time intervals 1, 2 (i), 2 (ii), and 3 respectively, C_c is 1, 0, 1, 0 and C_d is $-v_d$, R_{DC}, $-v_d$, R_{DC}, for all corner limited integrals.

In Figure 5.16, where u_d, v_d, R_{DC} and R_{DA} are shown, the definitions are taken from the general case shown in Figure 5.8. The values for these four variables can be found for edge 1, for the segment of the receiver within region 2 (in this example the whole receiver). This can be done in terms of the dimensions of the segment (r_x and r_y),

and the values defined to locate it x_a, x_b, y_a and y_b, which are given in Table 5.5. This gives, $R_{DC} = r_x$, $R_{DA} = r_y$, $u_d = y_b$ and $v_d = x_a, x_b$ for Pt 1 and Pt 2 respectively.

The total contribution for the source can be found using,

$$h_{source}(\bar{r},t) = h_{edge2}(\bar{r},t) + h_{edge3}(\bar{r},t) - h_{edge1}(\bar{r},t) - h_{edge4}(\bar{r},t) \qquad (5.19)$$

This equation can be derived from considering the arc of radius r from some point P as shown in Figure 5.16. To find the angle of the part of this arc which lies within the source, it is necessary to subtract the angle from the reference line to edge 1 (or later in time when r is longer the angle to edge 4) from that to edge 2 (or later edge 3).

The other three $h_{edgeX}(\bar{r},t)$ terms can be found in a similar way to that for Edge 1. When equation 5.19 is expanded out so that it consists of $h^{corner}_{edgeXptY}(\bar{r},t)$, (relating to the individual corner contributions of points 1 and 2), all those terms related to Pt 1 are positive, and Pt 2 negative.

5.6.2 An example of source reconstruction in Region 3

Finding the total contributions from edges 2 and 4, when a segment of the receiver is in Region 3, requires the use of the edge limited integral. Edge 4 will be used in this example, the dimensions of which are shown in Figure 5.17. From this diagram it can be seen that for the point shown, P, that the angle at that specific time can be found by subtracting the angle to the intersection of edge 1 from that to the intersection of edge 4 point 2, and adding this to the result of subtracting the angle to the intersection relating to edge 4 point 1 from the angle to the intersection of edge 3. The integration, over the area of the receiver, of the angle subtended by each point in the receiver can be built up in a similar manner, so long as only the active region of the receiver is considered for each edge in turn.

When the edge limited integral was introduced, it was stated (see Figure 5.10) that the angles of each of the two lines of length r which intersect the edge from the point under consideration (P in Figure 5.17), must be treated separately, despite being of the same absolute size, so that they could be made with reference to the same line. Figure 5.18 shows each angle separately and the active area for each. It can be seen that the active area for each angle is that of the edge limited integral minus that of the corner limited integral.

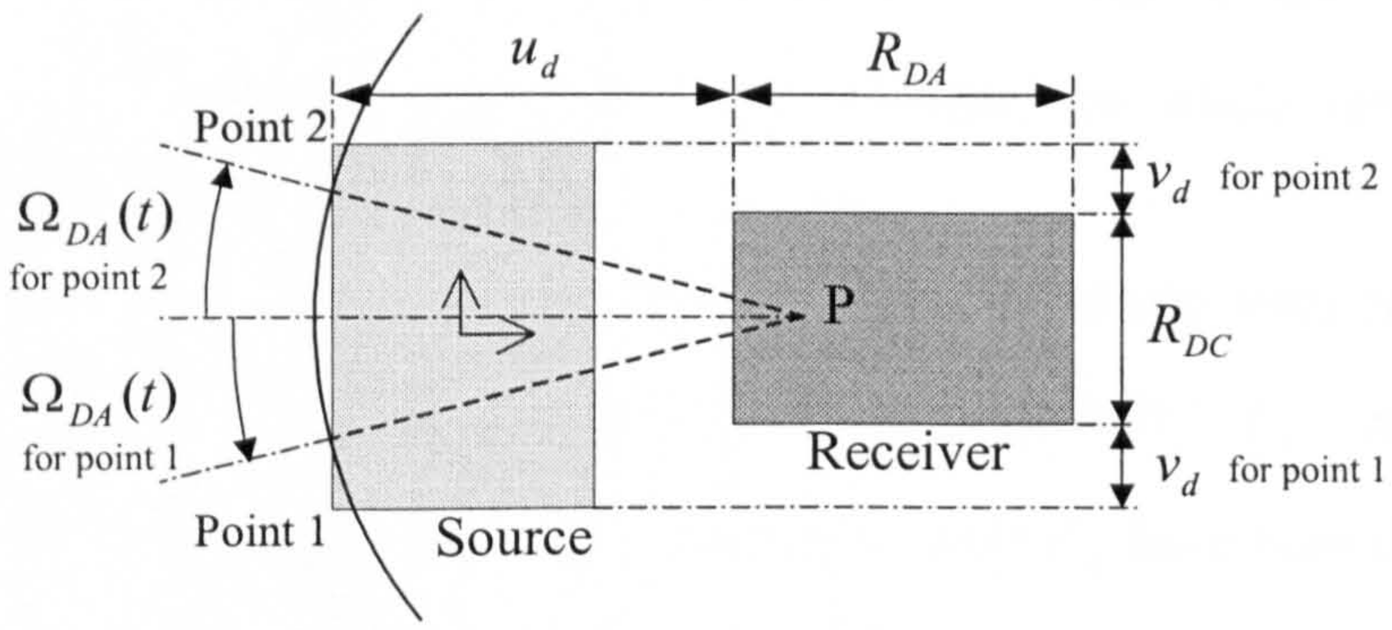

Figure 5.17: Example in Region 3, for Edge 4

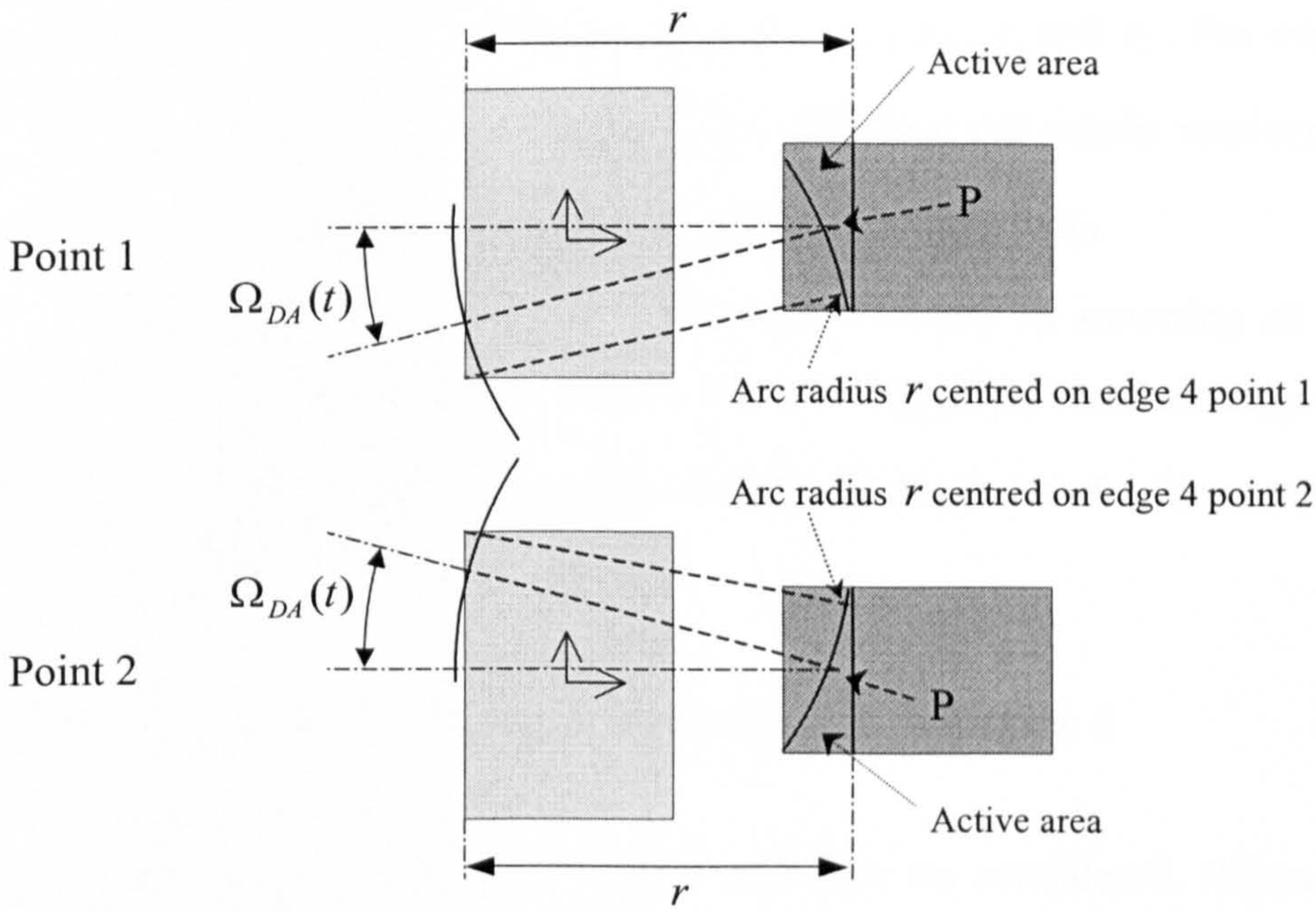

Figure 5.18: Edge 4, point 1 and point 2

As the angle has been defined as measured from the negative x direction from $-\pi$ to π, the contribution from edge 4, is given by,

$$h_{edge4}(\bar{r},t) = \{h^{edge}_{edge4\,pt2}(\bar{r},t) - h^{corner}_{edge4\,pt2}(\bar{r},t)\} - \{h^{edge}_{edge4\,pt1}(\bar{r},t) - h^{corner}_{edge4\,pt1}(\bar{r},t)\} \qquad (5.20)$$

It can be seen again that in equation 5.20 the corner limited integral due to Pt 1 is positive, and that due to Pt 2 is negative, it can also be seen that in both cases the sign of the edge limited integral is the opposite to the corner limited integral.

For both the edge and corner limited integrals, t_p^{end} is defined as equal to the value of t_p^{stable} for each point respectively. As at this point in time the corner limited integral is calculated using an active area covering the whole receiver, and hence cancels out the edge limited integral.

As before C_a and C_b are used to define the angle with respect to a fixed reference line, by relating $\Omega_{edge}(t)$ to $\alpha_{edge}(t)$, for edge 4 Pt 1 $C_a = \pi/2$ and $C_b = -1$, and for Pt 2, $C_a = -\pi/2$ and $C_b = 1$. Note that C_c and C_d have been described for each time interval in the corner limited integral in the previous example and remain the same. For the edge limited integral they are 0 and R_{DC} respectively.

Again u_d, v_d, R_{DC} and R_{DA} must be defined in terms of the values used to locate the receiver after segmentation, x_a, x_b, y_a, y_b, r_x and r_y. For edge 4, for the segment of the receiver within region 3 (in this case the whole receiver), $R_{DC} = r_y$, $R_{DA} = r_x$, $u_d = x_a$ and $v_d = y_a, y_b$ for Pt 1 and Pt 2 respectively.

The total contribution for the source can be found by summing all the different integrals for each edge in turn as before. With the $h_{edge}(\bar{r},t)$ term for edge 2 found in a similar way to that just described, and the terms for edges 1 and 3 found using the same method as used for Region 2.

5.6.3 An example of source reconstruction in Region 4

An example in Region 4, Zone 1 will now be considered. When considering Region 4, it is necessary to include the planar integral. The problem must be treated differently because when the angles are added together to find the total for a point, care must be taken that the addition does not cross the discontinuity occurring between $-\pi$ to $+\pi$. It is for this reason that the region must be subdivided into zones, and that the angles must be defined differently. In Figure 5.19 the arc for two points, projected onto the plane of the source, are shown at four different times relating to radii r_1, r_2, r_3 and r_4, one point P within Zone 1 the other, Q, outside Zone 1. In Figure 5.19, Zone 1 is indicated with two dot-dashed lines.

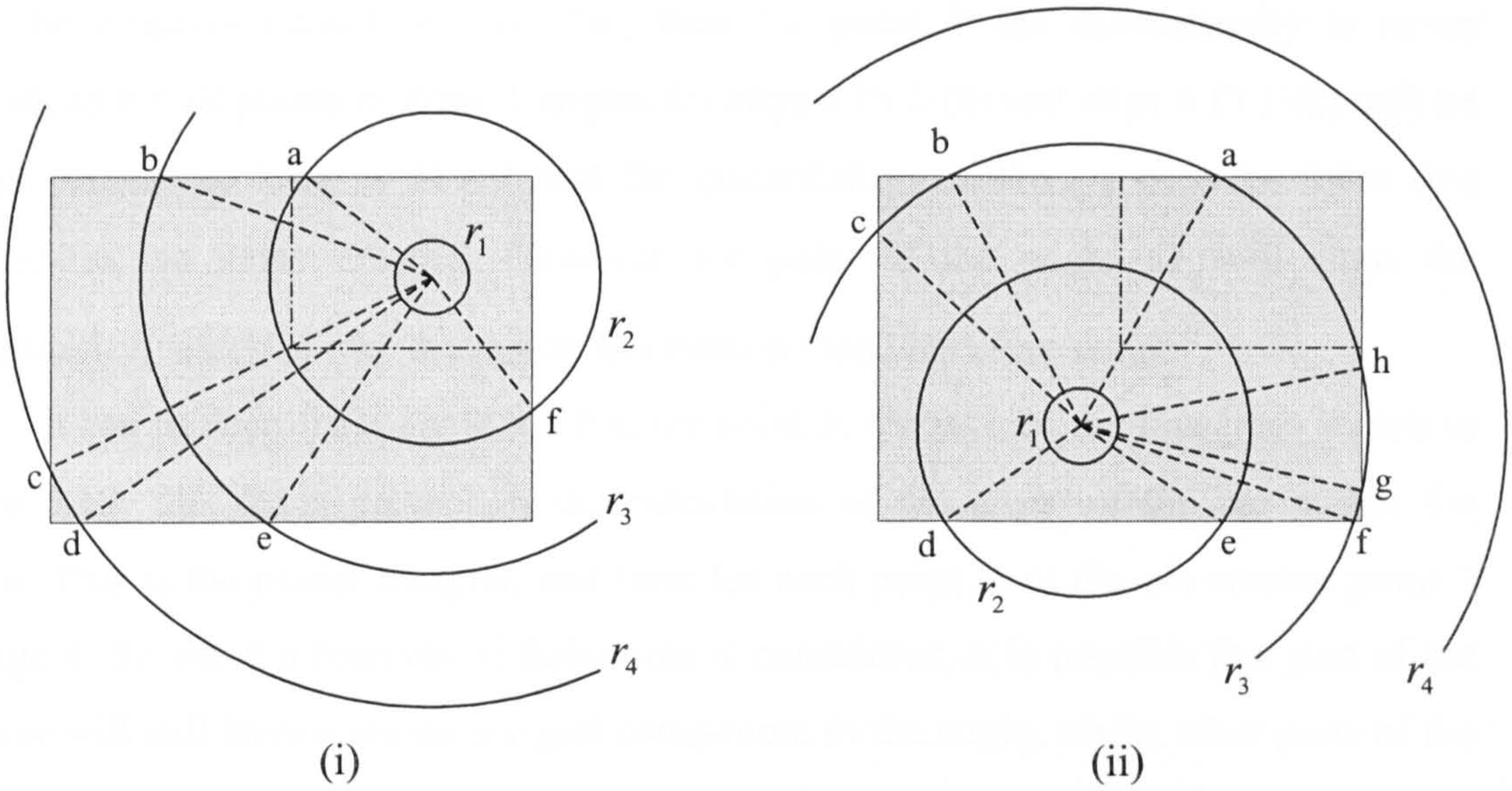

Figure 5.19: Two Points within Region 4 for (i) point P, and (ii) point Q

For each of the arcs considered the angle subtended at P and Q can be found using the equations given in Table 5.7, where the notation Ω_{ab} means the angle between the lines intersecting the edge of the source at points a and b measured anticlockwise, (and is unrelataed to $\Omega_{AB}(t)$). Note that the angles to be found are those subtended by the arcs lying outside the source.

	Point P	Point Q
r_1	2π	2π
r_2	$2\pi - \Omega_{fa}$	$2\pi - \Omega_{de}$
r_3	$2\pi - \Omega_{eb}$	$2\pi - \Omega_{ab} - \Omega_{cf} - \Omega_{gh}$
r_4	$2\pi - \Omega_{dc}$	0

Table 5.7: Angles subtended at Point P and Q

If the definition of the angle is from a reference line passing through the point P in the negative x direction, then the angle Ω_{fa} will cross the discontinuity between $-\pi$ to $+\pi$. However if for Region 4 the angle is defined as from 0 to 2π from the negative x direction, with the exception of edge 4 Pt 1 (labelled c) which is measured as the angle

from the negative x direction plus 2π, then for point P the discontinuity is never crossed, as for all points in Zone 1 angles for edge 3 Pt 2 (d) and edge 4 Pt 1 (c) will be always present so long as $\Omega \neq 0$ and the discontinuity is always between these two intersection, so never crossed. However for point Q the angle Ω_{cf} will cross the discontinuity, which is why the region has been divided into four zones.

It can be seen from Table 5.7 that for point P, for each of the four lines shown in Figure 5.19, that 2π is present in the calculation of the angle of the arc within the source. This is the planar integral, and lasts for each point until the arc crosses point 1 on edge 4. So when a receiver of finite size is considered, it is possible that part of the receiver will still have a planar integral component in the angle, whilst other parts of the receiver may at the same time be 0. The planar integral however, only allows for the integration of 2π over the whole area of the receiver. It is therefore necessary to amend this, by deducting from it the area of the receiver where the angle is 0. This is illustrated in Figure 5.20.

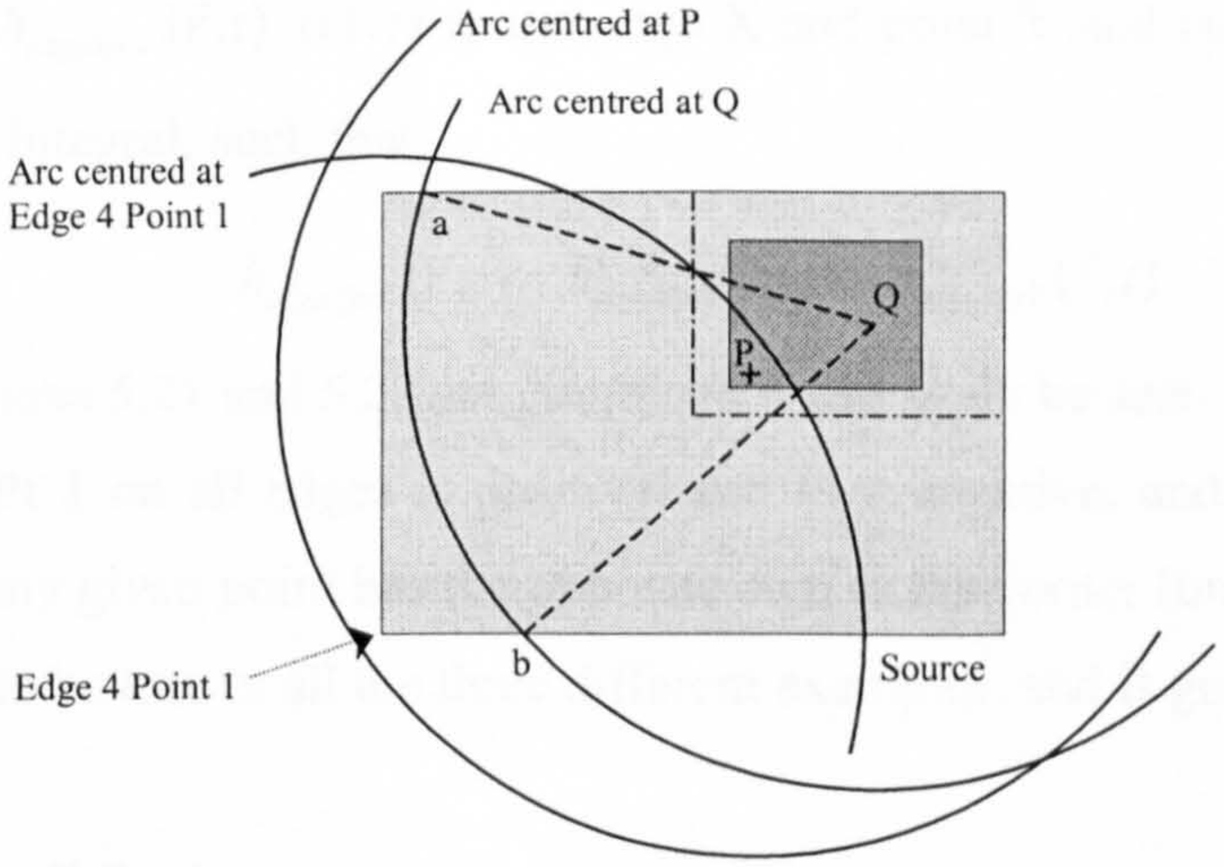

Figure 5.20: Amending the Plane contribution

It can be seen that for point Q, the angle of the arc within the source is $2\pi - \Omega_{ba}$, whilst for point P it is 0. So the angle at Q will be found from the plane contribution, and edge contributions of edge 1 and 3 (as in the previous example). However, unless the plane contribution is amended, the angle for P will be calculated as 2π as this is the value found for the whole area of the receiver. It is therefore necessary to deduct from the plane contribution the area of the receiver in which at any given time the arc of radius r

does not lie within in the source (i.e. $\Omega = 0$), these are all points within an arc of radius r from edge 4 Pt 1. This is most easily done using a corner limited integral from edge 4 Pt 1 where the only change is that the angle is set as 2π, so $C_a = 2\pi$ and $C_b = 0$.

The total value of the impulse response can be found at any given time using the planar integral, with the amendment just described, and by treating all four edges of the source as edge 4 in the Region 3 example. In equation 5.20 the total contribution of edge 4 is found using, an edge limited integral minus a corner limited integral for both Pt 1 and Pt 2 on that edge, the total impulse response would then be found by considering each edge in turn. The sign of the contributions depend on the way the angle has been defined, in this case the angle is 2π minus the angle of the arc lying outside the source. Hence,

$$\begin{aligned} h(\bar{r},t) = \quad & h^{plane}(\bar{r},t) - h^{plane\_amend}(\bar{r},t) - \{h_{edge1\,pt1}(\bar{r},t) - h_{edge1\,pt2}(\bar{r},t) \\ & + h_{edge2\,pt1}(\bar{r},t) - h_{edge2\,pt2}(\bar{r},t) + h_{edge3\,pt1}(\bar{r},t) - h_{edge3\,pt2}(\bar{r},t) \\ & + h_{edge4\,pt1}(\bar{r},t) - h_{edge4\,pt2}(\bar{r},t)\} \end{aligned} \tag{5.21}$$

where each $h_{edgeXptY}(\bar{r},t)$ refers to the edge X and point Y and consists of a corner and edge limited integral, such that,

$$h_{edgeXptY}(\bar{r},t) = h^{edge}_{edgeXptY}(\bar{r},t) - h^{corner}_{edgeXptY}(\bar{r},t) \tag{5.22}$$

When equations 5.21 and 5.22 are combined it can again be seen that the corner limited integral for Pt 1 on all edges is positive, and Pt 2 negative, and that the edge limited integral for any given point has the opposite sign as the corner limited integral. This has been shown to be true in all the three different examples, and is generally true.

5.6.4 All Regions

By following the procedure outlined above, the source can be recombined for all Regions, using the corner limited, edge limited and planar integrals. This requires calculating the contribution from both points on each edge in turn, and from the amended plane contribution. All that is necessary for this to be possible, is for the constants, in each case, to be defined for whichever integral must be considered. The integrals which must be included depends on the Region, so that for example edge limited and planar integrals are not needed in Region 2. The constants required are the

geometrical values describing the location and size of the segment of the receiver, v_d, u_d, R_{DA} and R_{DC}, the terms which are required for the generalised integral, C_a, C_b, C_c and C_d, the end of the time intervals, t_p^{end} and the sign of the integral when it is added to the rest, which is shown in equations 5.21 and 5.22.

The location and size of these terms are dictated by the way that the generalised form (see Figures 5.8 and 5.10) must be rotated for each edge, and so they are the same for any given edge and point in all Regions, for both the corner limited and edge limited integral. R_{DA}, R_{DC} and u_d are the same for both points on each edge, v_d, however is not. The values are given, in Table 5.8, using the terms used to describe the receiver after segmentation (as shown in Figure 5.14).

Edge	R_{DA}	R_{DC}	u_d	v_d Pt 1	v_d Pt 2
1	r_y	r_x	y_b	x_a	x_b
2	r_x	r_y	x_b	y_b	y_a
3	r_y	r_x	y_a	x_b	x_a
4	r_x	r_y	x_a	y_a	y_b

Table 5.8: Location and Size constants

The first two of the generalised integral constants, C_a and C_b, are used to describe the angle with respect to a reference line, these are the same for both edge limited and corner limited integrals for any given edge and point combination. They are dictated by the rotation required to superimpose the angle $\alpha_{edge}(t)$ used in the generalised solution (they are defined in equation 5.7) on the edge and point under consideration, and so vary for each point and edge combination. The values of C_a and C_b are given in Table 5.9.

The other two constants used in the generalised integral, namely C_c and C_d, are used to define the length of the receiver parallel to the edge which is active, v_1, as a function of time and perpendicular distance from the edge, u_1, (see Table 5.4, Figure 5.8 and equation 5.13). These values are constant for all Regions and edges. They are also constant for the edge limited integral at C_c is 0 and C_d is R_{DC}. They are irrelevant

for the planar integral (as were C_a and C_b). They vary only with the time interval, (as defined in Table 5.4) for the corner limited integral, and are as given in Table 5.10.

	Region 1		Region 2		Region 3		Region 4	
	C_a	C_b	C_a	C_b	C_a	C_b	C_a	C_b
Edge 1 Pt 1	0	1	0	1	0	-1	2π	-1
Edge 1 Pt 2	π	-1					π	1
Edge 2 Pt 1	$\pi/2$	1	$\pi/2$	-1	$-\pi/2$	1	$3\pi/2$	-1
Edge 2 Pt 2					$\pi/2$	1	$\pi/2$	1
Edge 3 Pt 1	π	-1	0	1	0	1	π	-1
Edge 3 Pt 2	0	1					0	1
Edge 4 Pt 1	$\pi/2$	-1	$\pi/2$	-1	$\pi/2$	-1	$5\pi/2$	-1
Edge 4 Pt 2					$-\pi/2$	1	$3\pi/2$	1

Table 5.9: C_a and C_b

Time interval	C_c	C_d
1	1	$-v_d$
2(i)	0	R_{DC}
2(ii)	1	$-v_d$
3	0	R_{DC}

Table 5.10: C_c and C_d

Finally, the time at which Ω returns to 0 has to be considered, and is termed t_p^{end}. When the edge under consideration lies parallel to the receiver, it is treated as an edge limited integral minus a corner limited integral for each end (Pt 1 and Pt 2) of the edge, as in the example for Region 3 and 4, in this case Ω returns to 0 when the corner limited integral is equal to the edge limited integral, which will occur when the arc of radius $r = ct_p$ cast from the point on the edge encompasses the whole of the receiver, so t_p^{end} is t_p^{stable} for both Pt 1 and Pt 2. When the edge is not alongside the receiver, as is always the case in Region 2, the edge is treated as a corner limited integral from the

nearest edge minus a corner limited integral from the furthest point, in this case Ω returns to 0, when the arc cast from the furthest point encompasses the whole of the receiver, so for both points t_p^{end} is the same as t_p^{stable} for the furthest point.

So t_p^{end} is equal to t_p^{stable} (so time interval 3 in Table 5.4 does not occur), except for edges where there is no edge contribution when t_p^{end} for the nearest point is as given in Table 5.11.

Region	Edge	Point	t_p^{end}
2 and 3	1	2	$t_p^{end} = \sqrt{(v_d + R_{DC} + 2b)^2 + (u_d + R_{DA})^2}\,/\,c$
	3	1	
1 and 2	2	1	$t_p^{end} = \sqrt{(v_d + R_{DC} + 2a)^2 + (u_d + R_{DA})^2}\,/\,c$
	4	2	

Table 5.11: Exceptions for t_p^{end}

When these edges are considered in these regions, there is no edge effect, so for the purpose of programming it is useful to deactivate the edge limited integral part of the program, similarly it is only necessary to activate the plane limited integral (including the amendment, based on a corner limited integral) of the program when Region 4 is considered and only for edge 4 Pt 1 (from where the corner limited integral used to amend the planar integral is centred). The next section describes an algorithm intended to aid the writing of a program using this model.

5.7 Algorithm

A summary of the steps taken in an algorithm, which is suitable for this model is given in Table 5.12. This algorithm finds the impulse response of a finite receiver, from a finite source, in a given position. Depending on which are activated, as described at the end of the last section, it finds the corner limited, edge limited and planar integrals for each segment, edge and point in turn, and reconstructs the source by summing the integrals using an equation derived from equation 5.21 and 5.22. Here the corner limited integral for each Pt 1 is positive, and Pt 2 negative, whilst the edge limited integral is always of the opposite sign. The result then is a value of $h(\bar{r},t)$, for each time step,

which can be convolved with the time differential of the source excitation velocity, and multiplied by the medium density, to give a predicted received pressure waveform. A program has been written in Matlab based on this algorithm (this program is listed in Appendix B.6).

1. Input	z, x_r, y_r, a, b, c, d	Size and location of source and receiver	Figure 5.14
2. Segment Receiver	$x_a, x_b, y_a, y_b, r_x, r_y$	Size and location of segment of receiver	Table 5.5 and Table 5.6
3. Loop - Segments		For each sector or region in which part of the receiver falls	
4. Loop – Edges		1 to 4	
5. Loop – Points		1 to 2	
6. Define Constants	$R_{DC}, R_{DA}, u_d, v_d, t_p^{end}$, C_a, C_b, C_c, C_d	Constants for reconstructing source	Evaluated in Tables 5.8-5.11. Defined in Figure 5.8 and equation 5.13.
7. Activate		Activate whichever of the corner limited, edge limited and planar integrals are relevant for this region, edge and point.	
8. Loop - time			
9. General Integral	$h^{corner}, h^{edge}, h^{plane}, h^{plane\_amend}$	Use general integral result to find these values	Equations 5.14-5.17
11. End time loop			
12. Sum	$h = h + (-1)^{point+1}.(h^{corner} - h^{edge}) + h^{plane} - h^{plane\_amend}$	As the program loops, h becomes the total for all previous segments, edges and points.	Based on Equations 5.21,5.22
13. End all loops			

Table 5.12: A schematic table of the steps required for an algorithm

5.8 Finite receiver model predictions

The original motivation for the investigation of finite-sized receivers was in the context of measuring the pressure fields from phased array transducers. The field from a single element similar to that used in the phased array of Chapter 4 has been modelled theoretically, assuming three different sizes (0.5, 1, and 2 mm) of square receiver. These predicted peak-to-peak pressure amplitude fields have been compared to those modelled for a point receiver in Figure 5.21. The element measures 0.8 × 10, and this simulation assumes a broadband drive signal centred at 500 kHz ($K = 5$). As would be expected the larger the receiver the greater the effect on the measured pressure field, as the directivity of the device will increase with size.

In Figure 5.22 an array has been considered, the array has 16 elements of 0.8 × 10 mm elements, on a pitch of 1.1 mm, and hence has the same geometry as the array used in Chapter 4. In the simulation phasing has been applied to the elements such that a focal point occurs at x = 0, y = 0, and z = 20 mm. Again the simulation has been performed for receivers measuring 0.5, 1 and 2 mm square, and these results can be compared to a point receiver in Figure 5.22. It can be seen that for a 0.5 mm receiver, there is only a negligible difference to the point receiver.

Figure 5.23 shows a cross-section through the field of both the single element and the focussed array at a distance of $z = 20$ mm, again using a receiver measuring 0.5, 1 and 2 mm to compare against a point receiver. For the focussed case, Figure 5.23 (ii), the cross-section passes through the focal point. It can be seen that for a single element, that there is considerable difference in the pressure predicted at this distance, as measured by the different receivers. Though again, as would be expected from their relative directivity, the smaller the receiver the better the correlation to a point receiver. For the case of a focussed 16 element array, as shown in Figure 5.23 (ii), the measured focal point is broader for the larger receivers, however for a 0.5 mm square receiver the approximation to a point receiver is good. Consequently, this was the receiver size used to measure the fields from the focussed arrays in the previous Chapter.

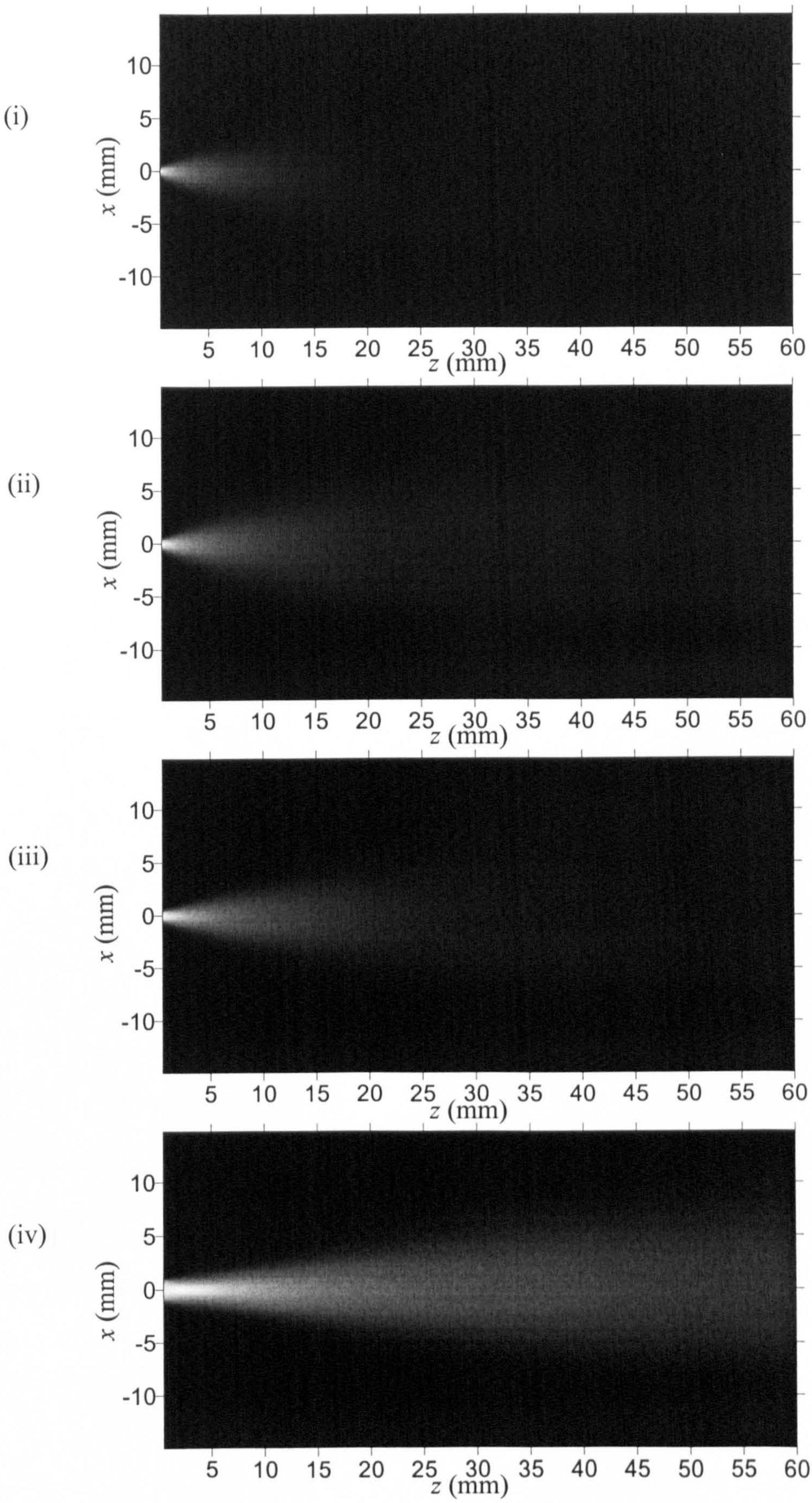

Figure 5.21: The pressure field from a single element, for (i) a point receiver, and for (ii) a 0.5 mm, (iii) a 1 mm and (iv) a 2mm square receiver

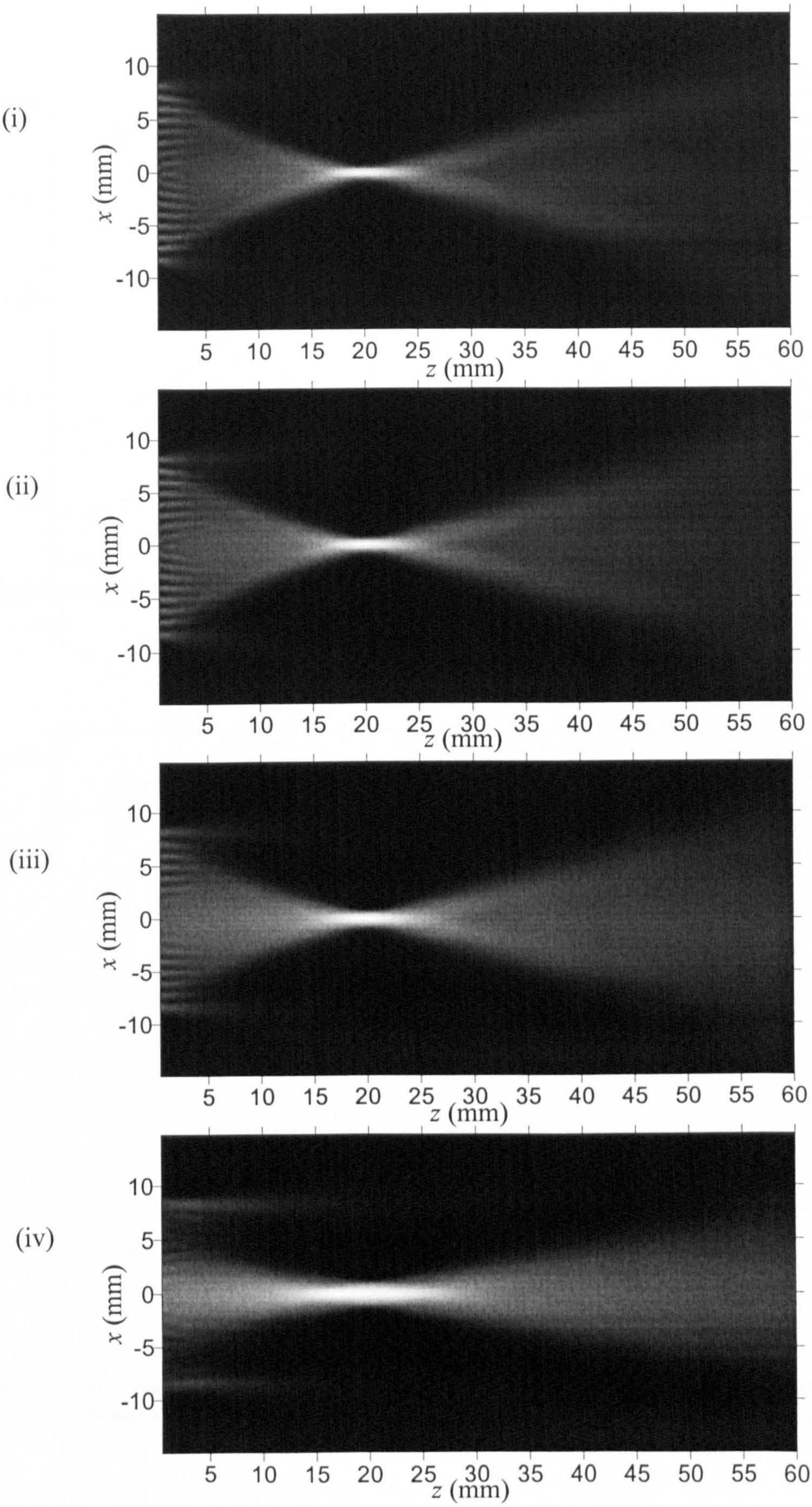

Figure 5.22: The pressure field from a 16 element array focussed at $z = 20$ mm, for (i) a point receiver, and for (ii) a 0.5 mm, (iii) a 1 mm and (iv) a 2mm square receiver

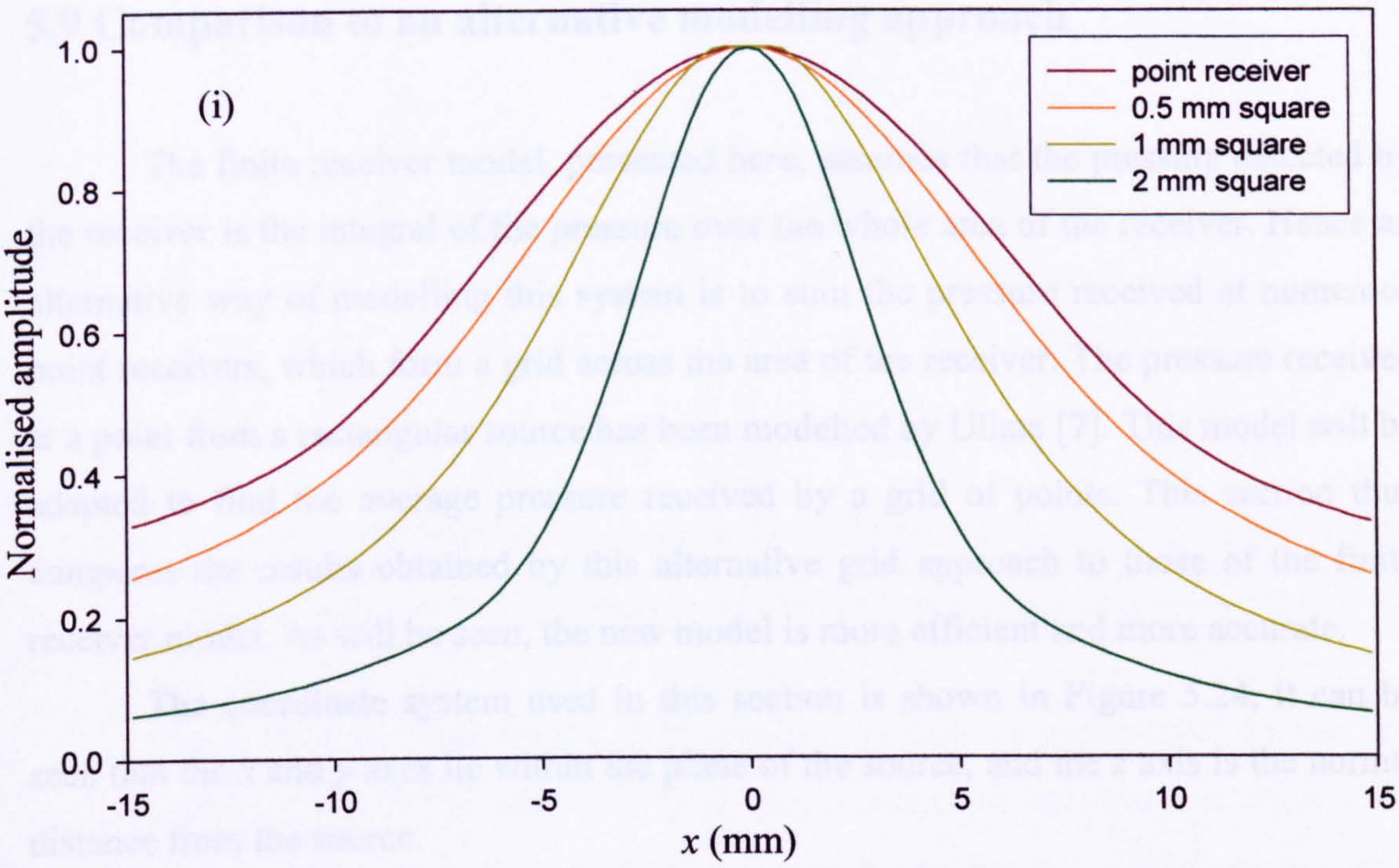

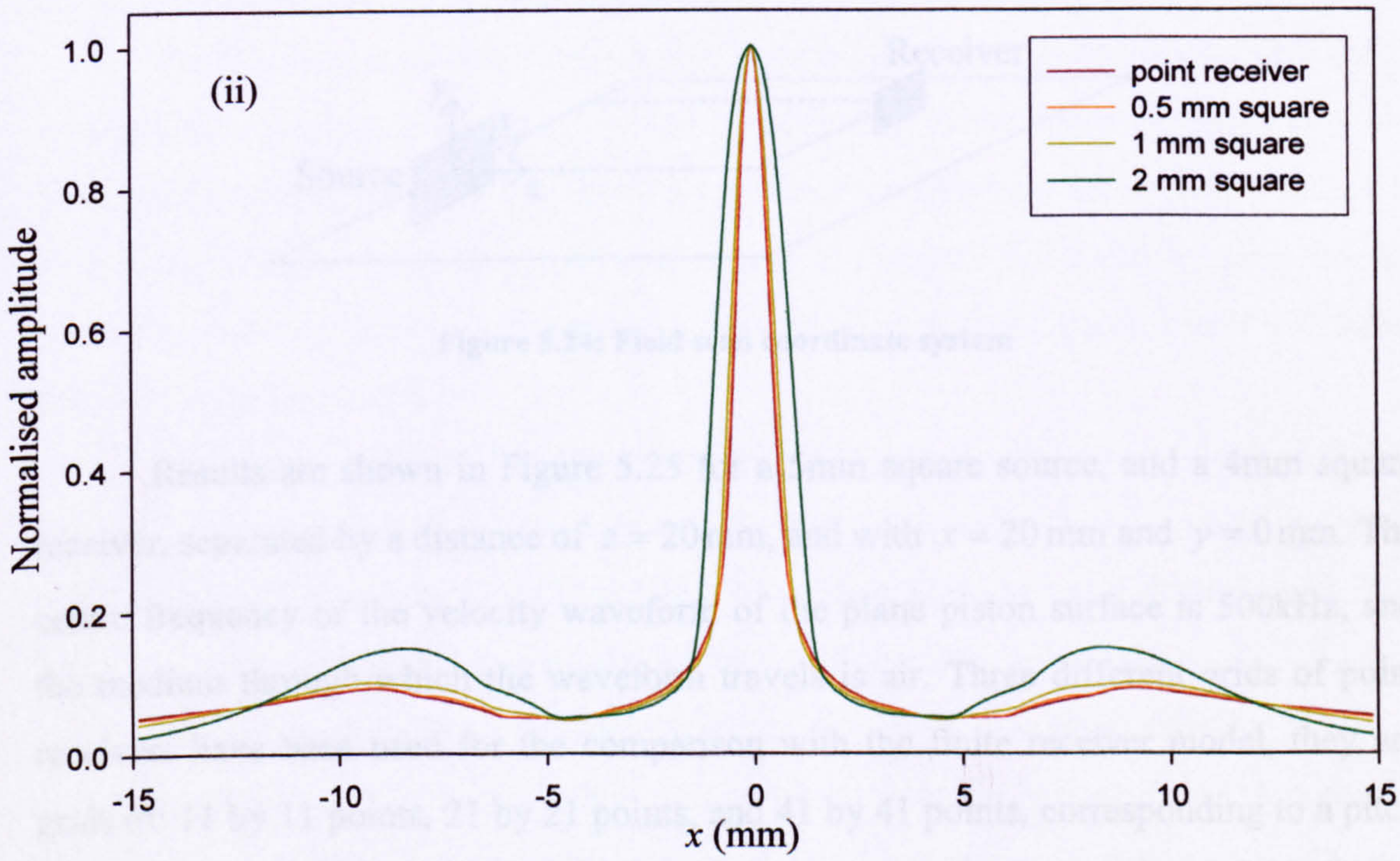

Figure 5.23: A cross-section through the pressure field at z = 20 mm, for (i) a single element, and (ii) a 16 element array focussed at z = 20 mm, for in both cases a point receiver, and receivers measuring 0.5, 1, and 2 mm square

5.9 Comparison to an alternative modelling approach

The finite receiver model, presented here, assumes that the pressure detected by the receiver is the integral of the pressure over the whole area of the receiver. Hence an alternative way of modelling this system is to sum the pressure received at numerous point receivers, which form a grid across the area of the receiver. The pressure received at a point from a rectangular source has been modelled by Ullate [7]. This model will be adapted to find the average pressure received by a grid of points. This section thus compares the results obtained by this alternative grid approach to those of the finite receiver model. As will be seen, the new model is more efficient and more accurate.

The coordinate system used in this section is shown in Figure 5.24, it can be seen that the x and y axes lie within the plane of the source, and the z axis is the normal distance from the source.

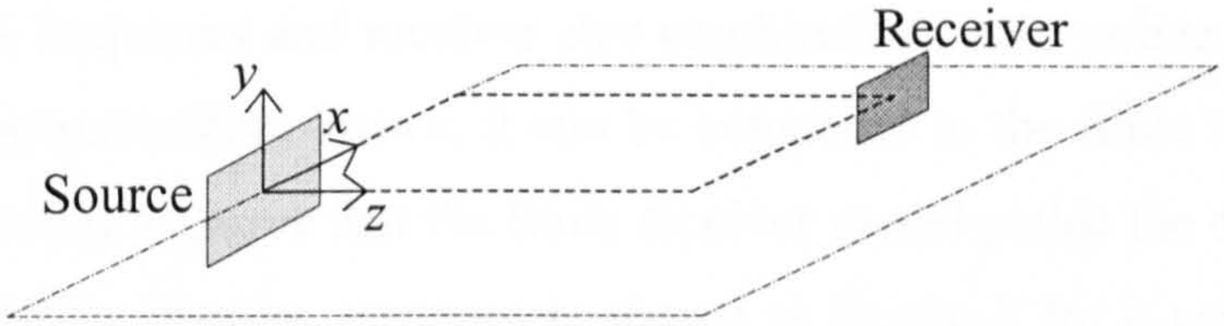

Figure 5.24: Field scan coordinate system

Results are shown in Figure 5.25 for a 5mm square source, and a 4mm square receiver, separated by a distance of $z = 20\,\text{mm}$, and with $x = 20\,\text{mm}$ and $y = 0\,\text{mm}$. The centre frequency of the velocity waveform of the plane piston surface is 500kHz, and the medium through which the waveform travels is air. Three different grids of point receivers have been used for the comparison with the finite receiver model, they are grids of: 11 by 11 points, 21 by 21 points, and 41 by 41 points, corresponding to a pitch of approximately 0.6, 0.3 and 0.15 wavelengths, respectively. In Figure 5.25 (i) the scalar impulse response, $h(t)$, is shown, and in Figure 5.25 (ii) the results of the convolution of the scalar impulse response with the 500kHz waveform V, resulting in pressure waveforms are shown.

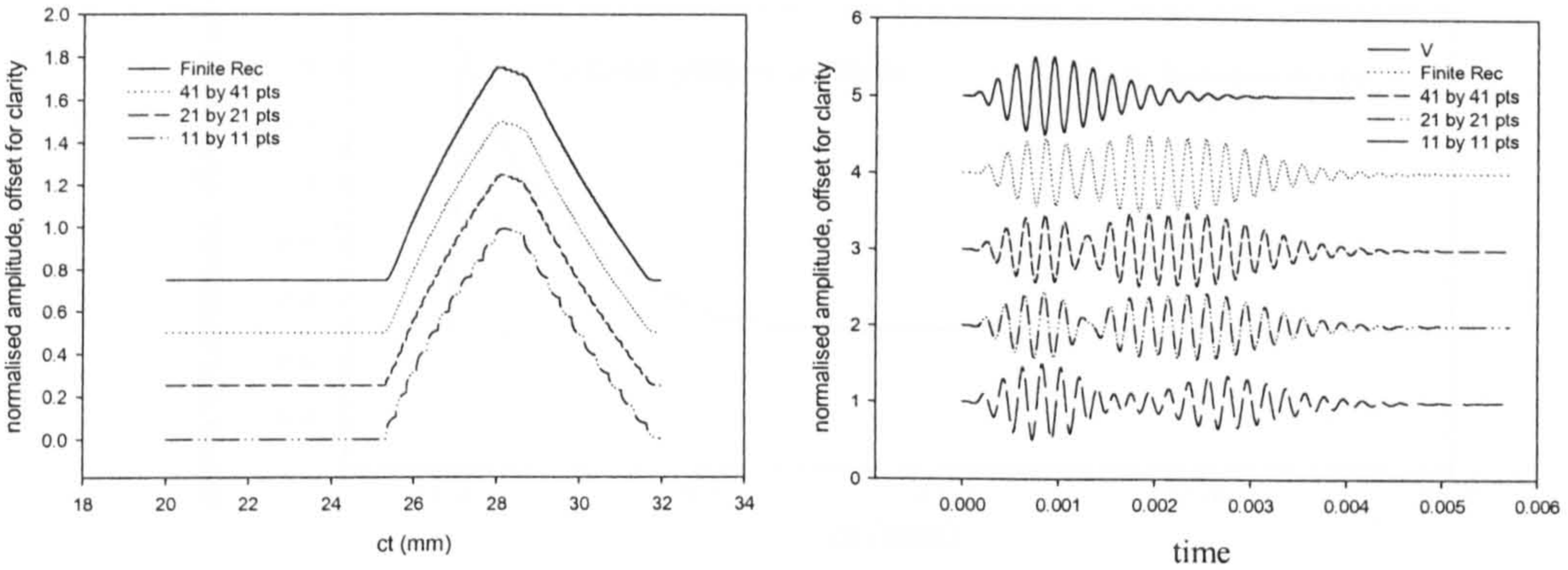

(i) (ii)

Figure 5.25: A comparison of predictions from the Finite Receiver model with those from a grid of points approach, using a 5mm square source and a 5mm square receiver: V is the velocity waveform at the source surface, (i) shows the impulse response, and (ii) the pressure waveform

It can be seen from Figure 5.25 that the number of points used in the grid approximating to the finites receiver affects the closeness of this approximation to the finite receiver model, and as expected an increase in the number of grid points causes the approximation to tend towards the finite receiver model prediction.

For this frequency and receiver size combination, a 41 points square grid offers an adequate approximation. Hence, it can be compared to the finite receiver model for three field positions to prove that the finite receiver model yields the correct results. For each case the scalar impulse response is shown in Figure 5.26. It can be seen that the agreement between the two approaches is very good in all three cases, hence validating the finite receiver model.

In order to compare the computing efficiency of the finite receiver model, and the grid of points approximation, Table 5.13 gives the times it took to model the three grid points used above on a PC. This had a 700MHz processor, and 128Mbyte of RAM, using programs written to be as similar in format as possible, in Matlab.

As can be seen from the running times presented, the finite receiver model is faster for all three field positions than even the least accurate grid of 11 by 11 points. It can also be seen that if the grid of points approach were to be used, with a 41 by 41 grid, then the running time would be extremely slow in comparison to the finite receiver model.

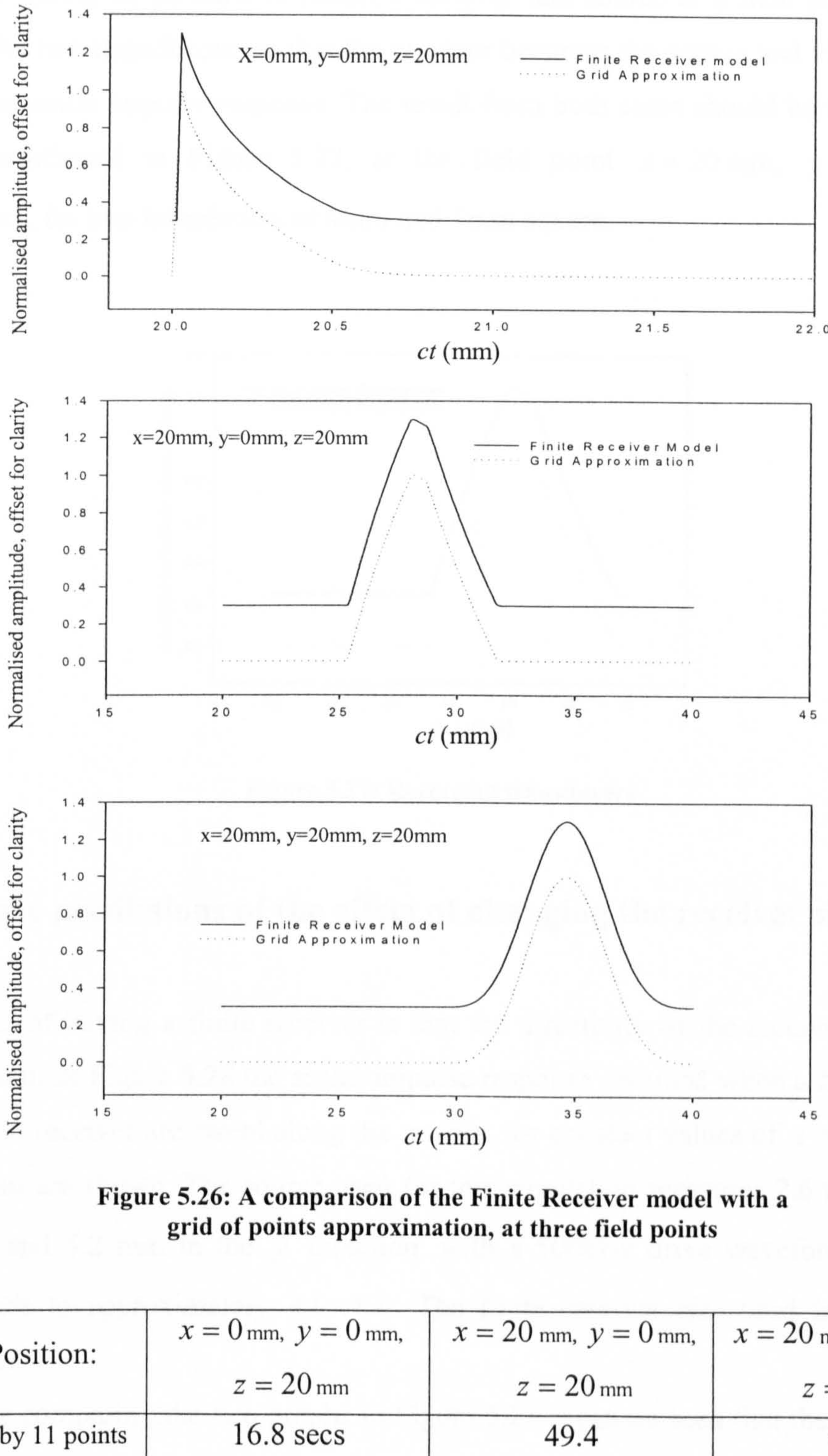

Figure 5.26: A comparison of the Finite Receiver model with a grid of points approximation, at three field points

Field Position:	$x = 0$ mm, $y = 0$ mm, $z = 20$ mm	$x = 20$ mm, $y = 0$ mm, $z = 20$ mm	$x = 20$ mm, $y = 20$ mm, $z = 20$ mm
Grid of 11 by 11 points	16.8 secs	49.4	88.6
Grid of 21 by 21 points	59.3	180.0	320.8
Grid of 41 by 41 points	222.4	684.5	1214.5
Finite receiver model	13.1	16.5	18.9

Table 5.13: Comparison of running time

It should be possible to model a receiver and source at a field point, and then reverse the two transducers, so that the receiver becomes the source and vice versa, and model the scalar impulse response. The result from both cases should be the same, and this is confirmed in Figure 5.27, at the field point $x = 20\,\text{mm}$, $y = 0\,\text{mm}$, and $z = 20\,\text{mm}$, for two transducers of 4mm and 5mm square.

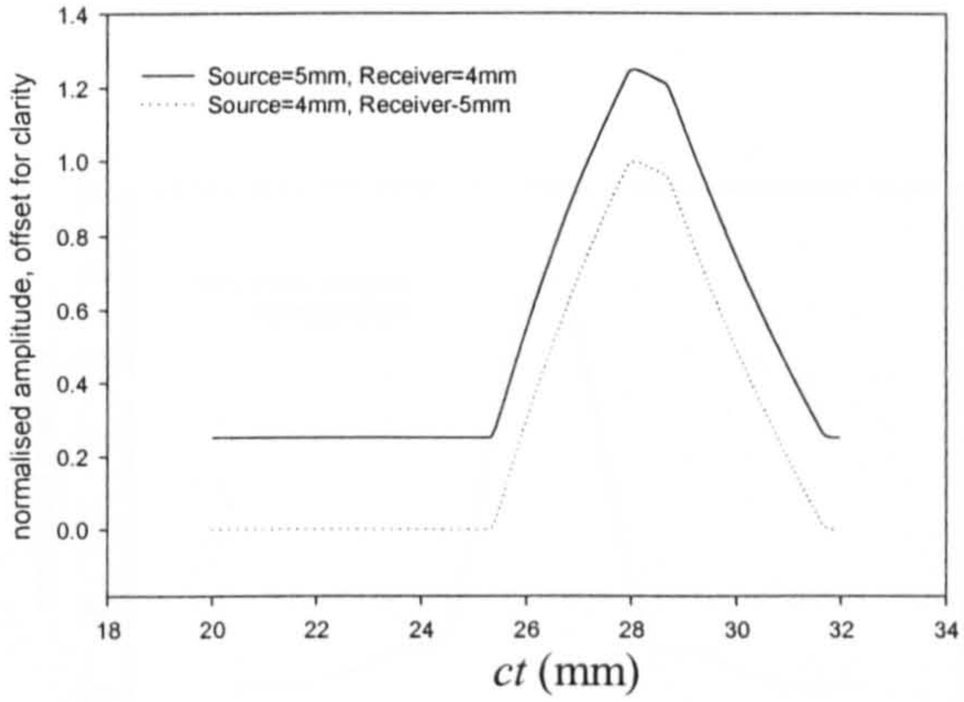

Figure 5.27: Reversing transducers

5.10 Some predictions of the effect of changing the receiver size

The effect of having a finite receiver is that the directivity of the receiver affects the field pattern. In Figure 5.28 the scalar impulse response obtained when a finite receiver and a point receiver are swept along the x axis, for constant values of $z = 20$ mm and $y = 0$ mm are shown. The source used for this simulation measures 2.6 mm in the x direction and 5.2 mm in the y direction, with a 500kHz drive waveform in air this corresponds to approximately $4\lambda \times 8\lambda$. The finite receiver size used is 1.3 mm or 2λ square.

By comparing the two graphs in Figure 5.28 it can be seen that the effect of the finite receiver is to smooth the discontinuities of the point receiver, which is due to the integration over an area over which the time of arrival varies. The effect this has on the peak-to-peak amplitude of the pressure can be seen in Figure 5.29, where the same geometrical values are used, and the piston velocity, V, is as in Figure 5.25 (i).

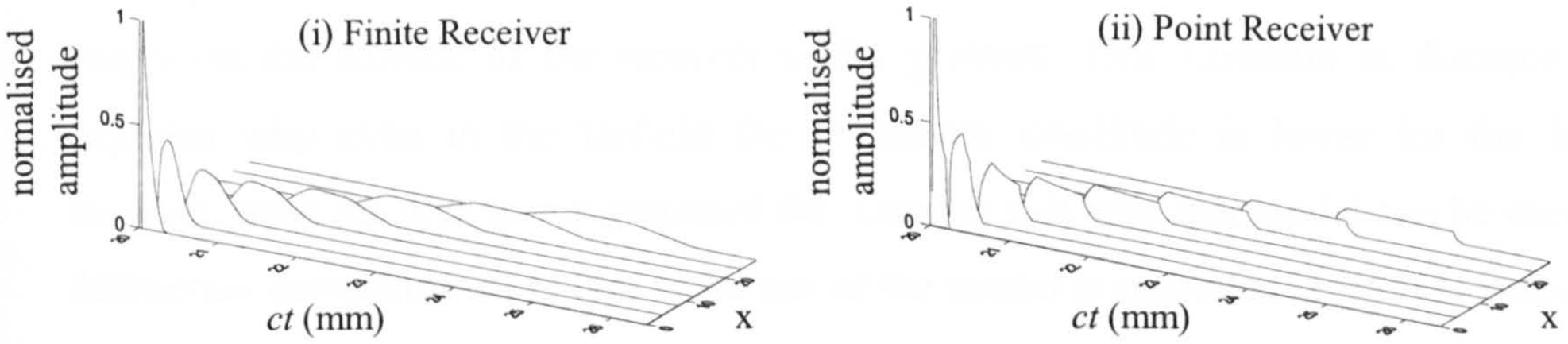

Figure 5.28: Increasing x from 0 to 28mm in 4mm steps, for (i) a finite receiver, and (ii) a point receiver

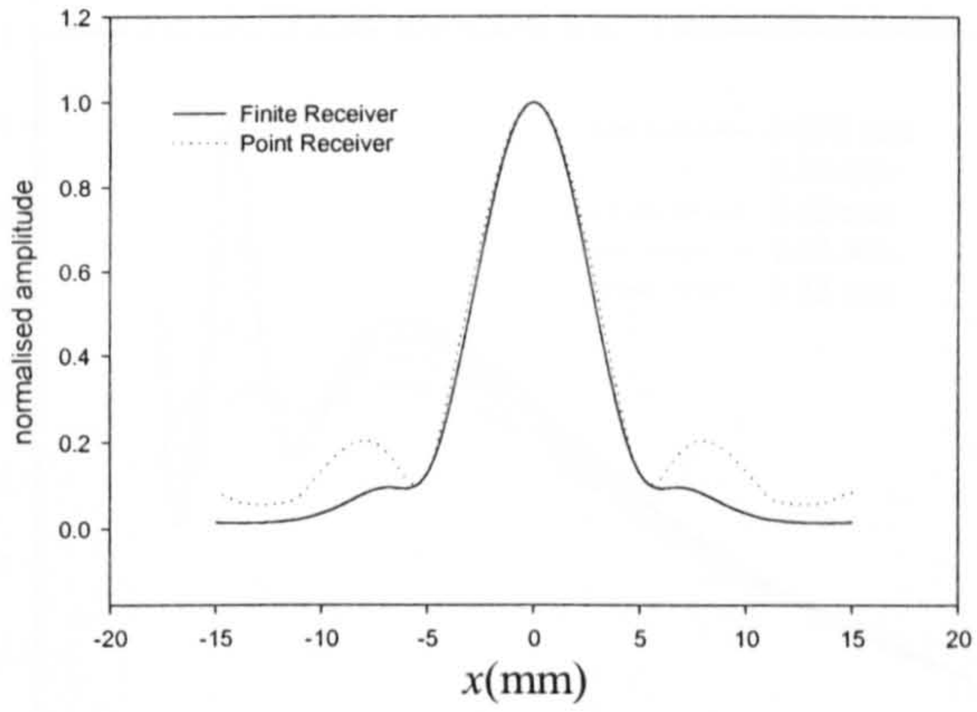

Figure 5.29: The effect on pressure amplitude of a finite receiver

It can be seen that the effect of the finite receiver is greater as x rises, as the directivity of the receiver causes the side lobes to be smoothed out. In this case, the amplitude has been normalized in both cases for that fixed z value using the maximum value which occurs on axis. However, as z varies, the use of a finite receiver will also have an effect, which will compound the difference shown in Figure 5.29 at certain distances from the source transducer. The effect of varying the size of the receiver as the two transducers are moved apart on axis is shown in Figure 5.30. In this example, the source dimensions used are as for the results shown in Figure 5.28 and Figure 5.29, as is the piston velocity waveform. The receiver dimensions are 0.068 mm, 0.34 mm, 0.68 mm, 1.02 mm and 1.36 mm square, corresponding to 0.1λ, 0.5λ, 1λ, 1.5λ and 2λ. The distances x and y are fixed at 0mm, whilst z varies from 0.4mm to 32mm.

The data for the smallest receiver has been normalized, and the data for all other receivers has been related to this by scaling to compensate for differences in area. It can be seen from Figure 5.30 that the greatest effect of increasing the size of the receiver is within the nearfield, (the nearfield / farfield boundary of the source is at approximately

12 mm), where the relative difference in the distance that the signal covers to various points on the surface of the receiver is the greatest. This variation of distance also explains why even in the farfield the maximum amplitude is lower for the larger receiver, once the area is compensated for. Used in this way this model can be used for diffraction correction. Note that if the use of the model is restricted to on-axis response, then considerable simplification can be made, by the use of symmetry, to the Zones, Regions and Sectors, which need be considered.

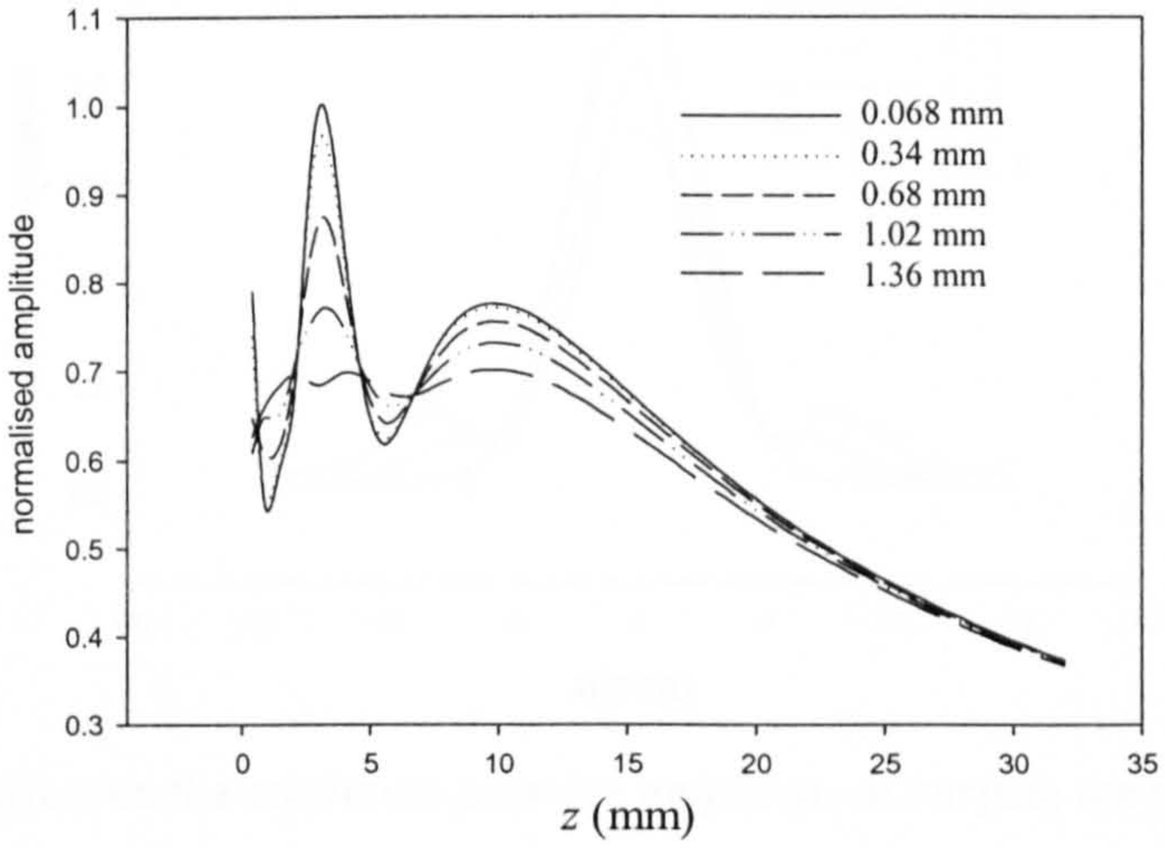

Figure 5.30: Comparison of receiver sizes, with varying z on axis

The effect on the maximum pressure of changing the shape of the receiver whilst the area is maintained constant is shown in Figure 5.31. As before the source is 2.6 mm (x) × 5.2 mm (y), or $4\lambda \times 8\lambda$ in size. The distances z and y are fixed, at 20 mm, and 0mm respectively, whilst x is varied between -15 mm and 15 mm. Five different receiver are modelled with dimensions of $8\lambda \times 0.5\lambda$, $4\lambda \times 1\lambda$, $2\lambda \times 2\lambda$, $\lambda \times 4\lambda$, and $0.5\lambda \times 8\lambda$, expressed as width ($x$) × length ($y$). The amplitude received in the $2\lambda \times 2\lambda$ case is normalized, and then the data for the other receivers is scaled using the same factor. It can be seen that the square transducer, positioned on axis, receives the maximum pressure amplitude for which the difference in the maximum and minimum time of flight from any point on the source to any point on the receiver is least. The $4\lambda \times 1\lambda$ sized receiver has the second largest on axis peak-to-peak pressure, followed by $\lambda \times 4\lambda$, $8\lambda \times 0.5\lambda$, and least of all $0.5\lambda \times 8\lambda$. This can be explained in terms of the time of flight differences over the receiver. The time of flight differences as described for the square receiver as varying least on axis, will be less for less

elongated transducers, hence the two transducers of aspect ratios 16:1 have a lower maximum pressure than those two of 4:1 aspect ratio. The directivity of the source is greater in the y direction than in the x direction, hence those receivers which are more directional in the x direction will have a larger maximum received pressure, so, for example, the $4\lambda \times 1\lambda$ receiver has a greater maximum pressure than the $\lambda \times 4\lambda$ receiver.

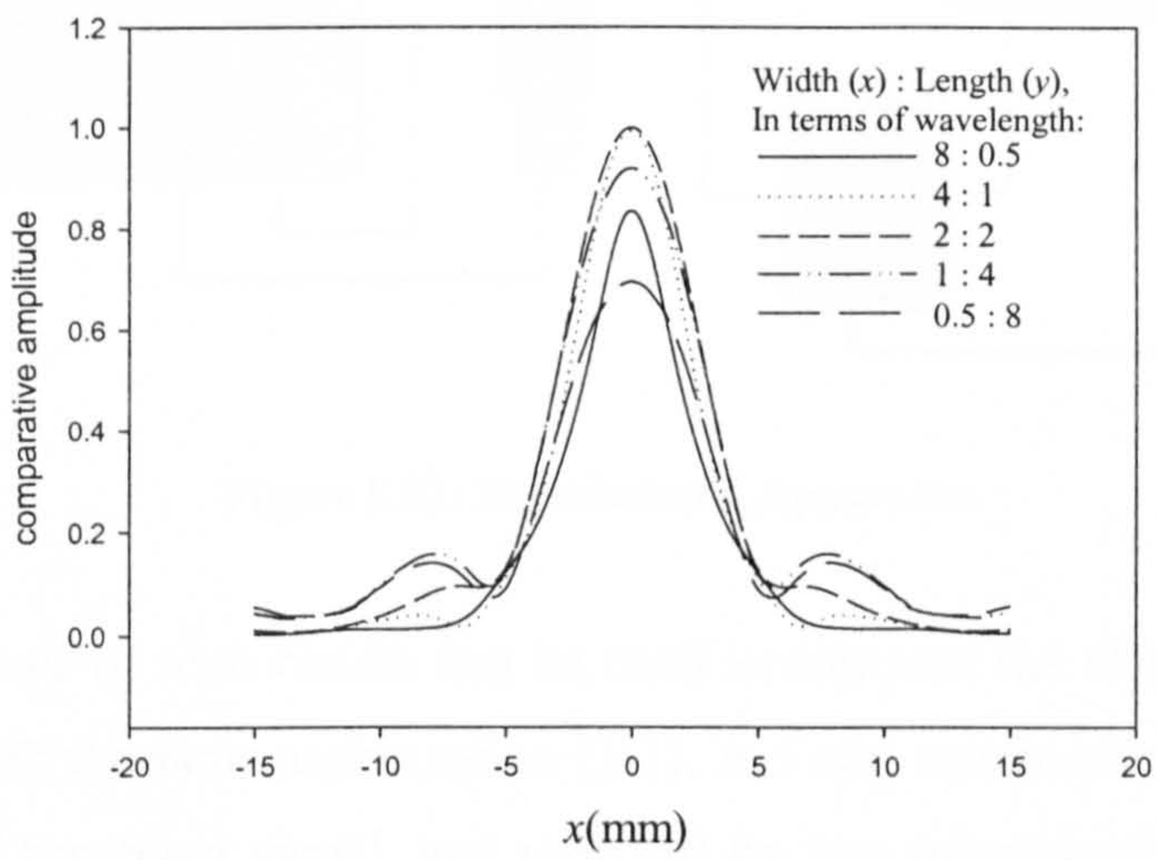

Figure 5.31: The effect on the maximum pressure amplitude of varying the shape of the receiver

The width of the main lobe at this z distance also varies, the narrowest is for the $8\lambda \times 0.5\lambda$ at 4.55 mm (FWHM), rising progressively to 6.40 mm for the $0.5\lambda \times 8\lambda$ receiver. Showing that the FWHM is greatest, when moving in the x direction, for the receiver, which is least directive, in the x direction. A similar explanation can be used to discuss the suppression of the sidelobes present in the field of the source, when a more directive receiver transducer is used.

5.11 Comparison of model predictions to experimental measurements

In the previous Section, the effects of the receiver shape and overall surface area were discussed. These two effects will now be studied by comparing the theoretical field plots of maximum pressure amplitude to experimental data obtained in air.

A scanning stage was used to move the receiver, with respect to the source, in the xz plane (see Figure 5.24). The experimental apparatus is shown in Figure 5.32.

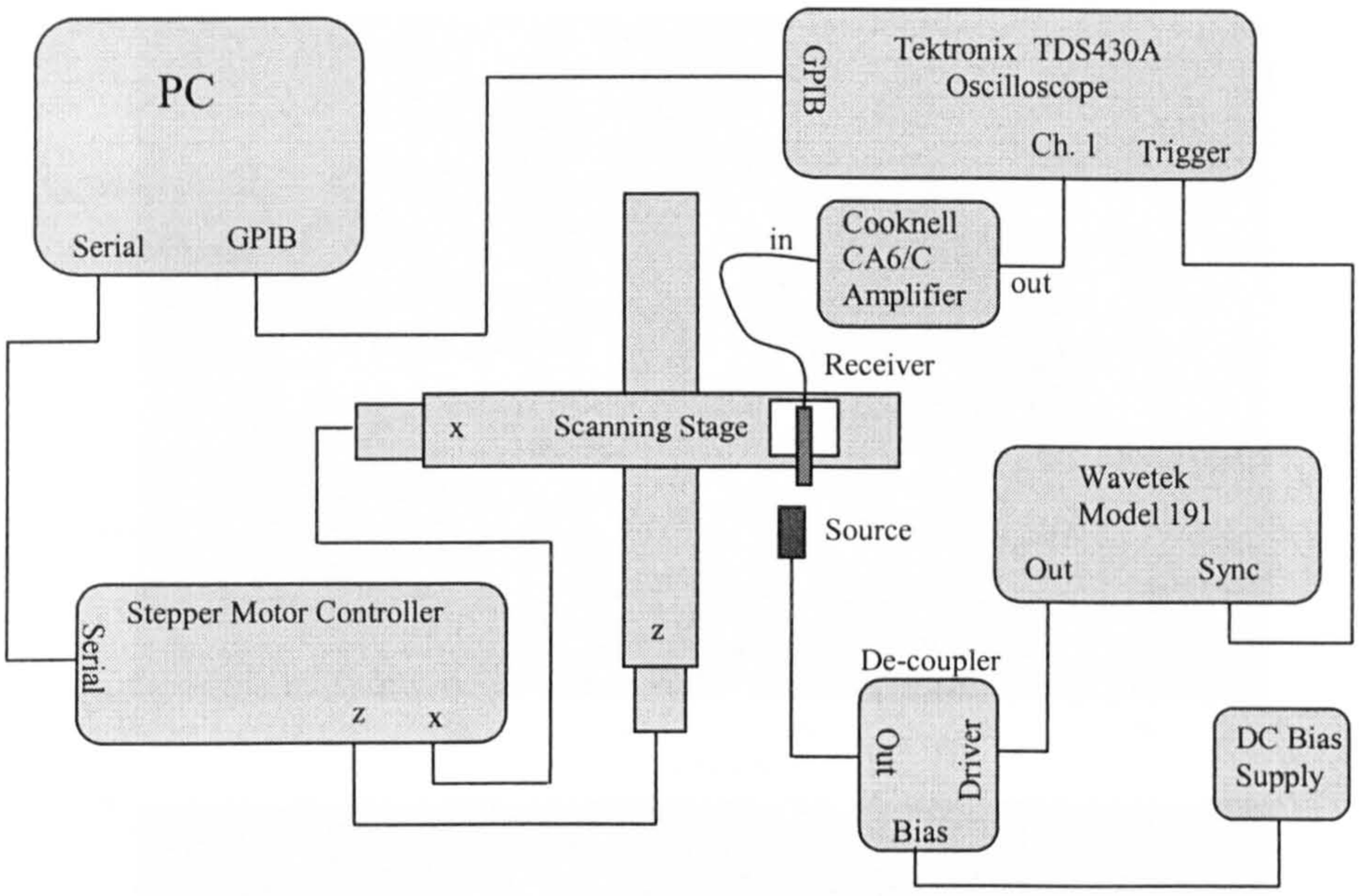

Figure 5.32: Experimental Apparatus

The first pair of scan results can be used to compare the effect of two different sized receivers with the same aspect ration (1:1). A 5 mm square source was driven by a 5 cycle, 500 kHz toneburst signal, and received by two transducers of different sizes: 0.5 mm square and 4 mm square. For the source and larger receiver, paper apertures of the appropriate size were fitted to the front surface of two 10mm diameter air-coupled transducers with micromachined backplates, as described in Chapter 2. A micromachined transducer [8] was used for the smaller 0.5mm receiver.

The scans were performed using a 0.5mm step size in the x direction, and a 1 mm step size in the z direction. The maximum pressure amplitude obtained experimentally for a 0.5 mm receiver can be compared to the theoretical simulation in Figure 5.33, and the same comparison can be made for a 4 mm receiver in Figure 5.34. Figure 5.35 shows the theoretical field, from a source of the same size, driven under the same conditions, for a point receiver. The data is displayed as a greyscale image, where a lighter shade indicates regions of higher amplitude.

It can be seen in Figure 5.34 the use of a larger, more directional receiver has the effect of suppressing the sidelobes as was also seen in the previous section. A comparison of Figure 5.33 and Figure 5.35 shows that the 0.5mm square receiver has a negligible effect on the measured pressure field, showing that the receiver is now sufficiently small that the effect of the finite receiver aperture has not affected the measured field unduly.

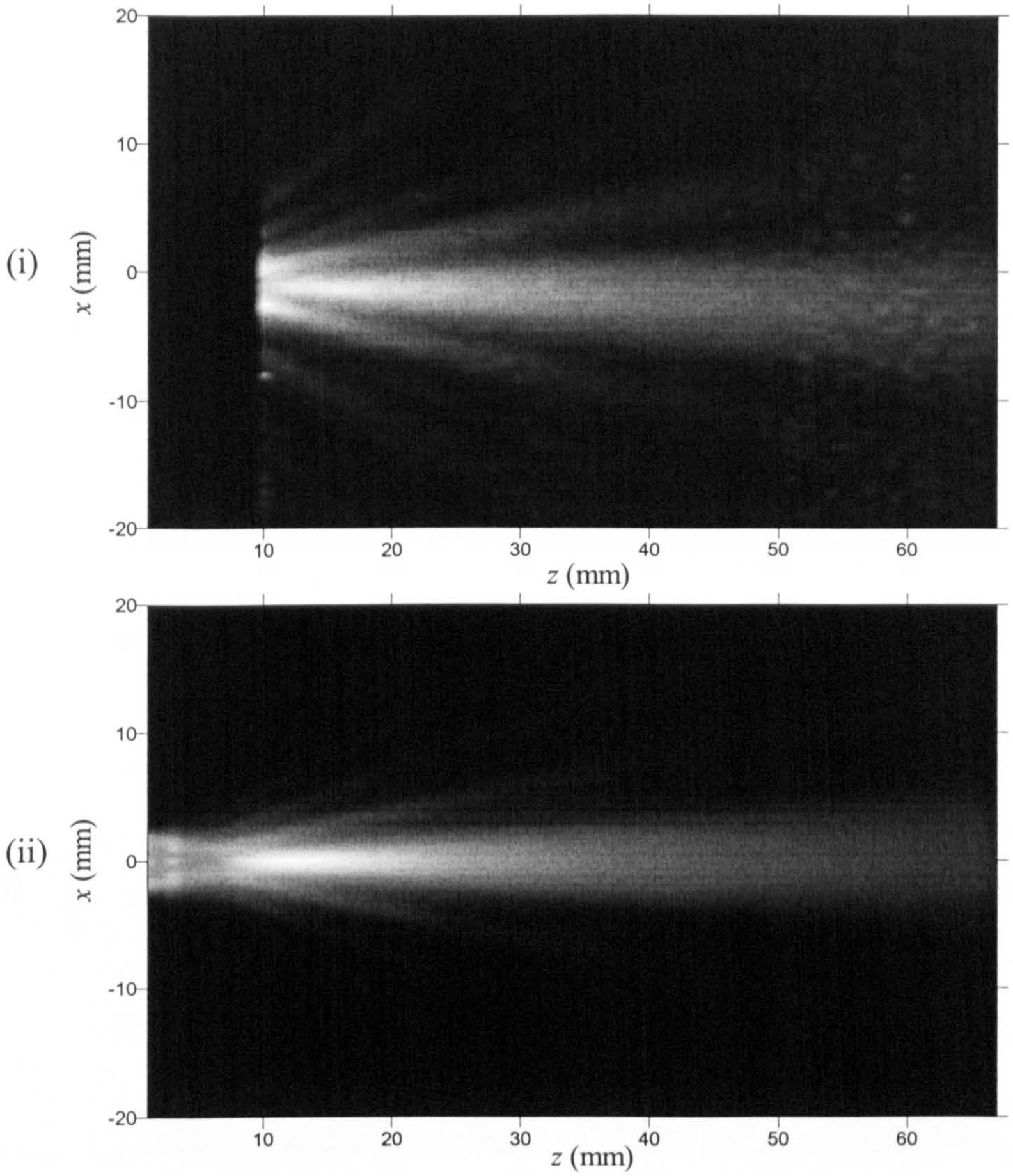

Figure 5.33: 5 mm square source and 0.5 mm square receiver, (i) experimental, (ii) theoretical for finite receiver

The apparatus shown in Figure 5.32 was also used for a second set of scans, which were used to compare the effect of using two receivers of the same area but different aspect ratio. The transducers used were the same 10 mm diameter metalized polymer membrane devices, constrained with paper apertures. The source aperture was 6 mm wide (x) and 4 mm long (y), the receiver used had an aperture of 8 mm wide (x) × 1 mm long (y) and was then rotated to give an aperture of 1 mm wide (x) × 8 mm long (y). The drive signal applied to the source was a 5 cycle 625 kHz toneburst, again the experiment was performed in air. The maximum pressure amplitude can be compared in Figure 5.36 for the 1:8 ($x:y$) receiver, and in Figure 5.37 for the 8:1 receiver. Whilst, Figure 5.38 shows the theoretical field for a point receiver.

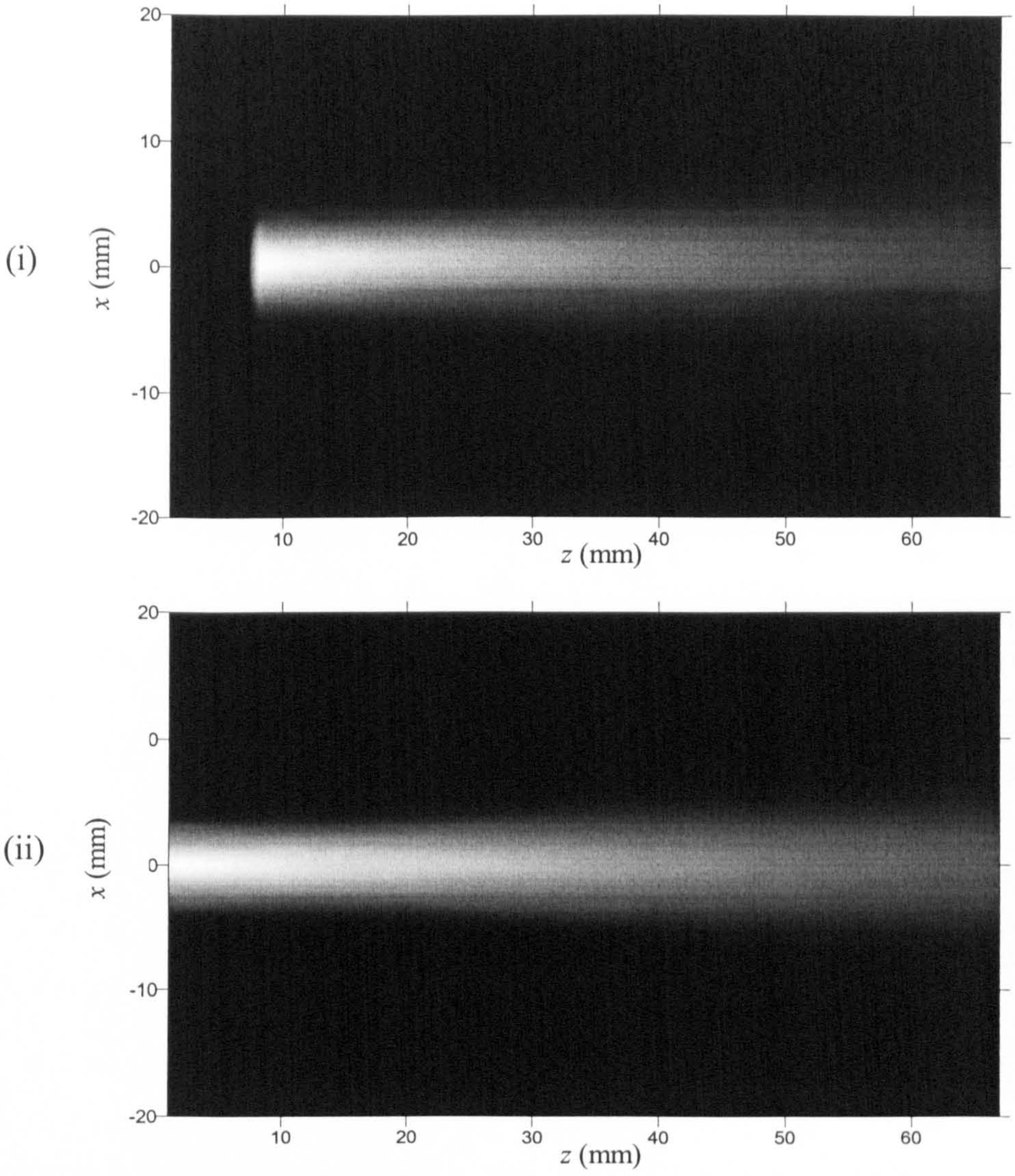

Figure 5.34: 5 mm square source and 4mm square receiver, (i) experimental and (ii) theoretical

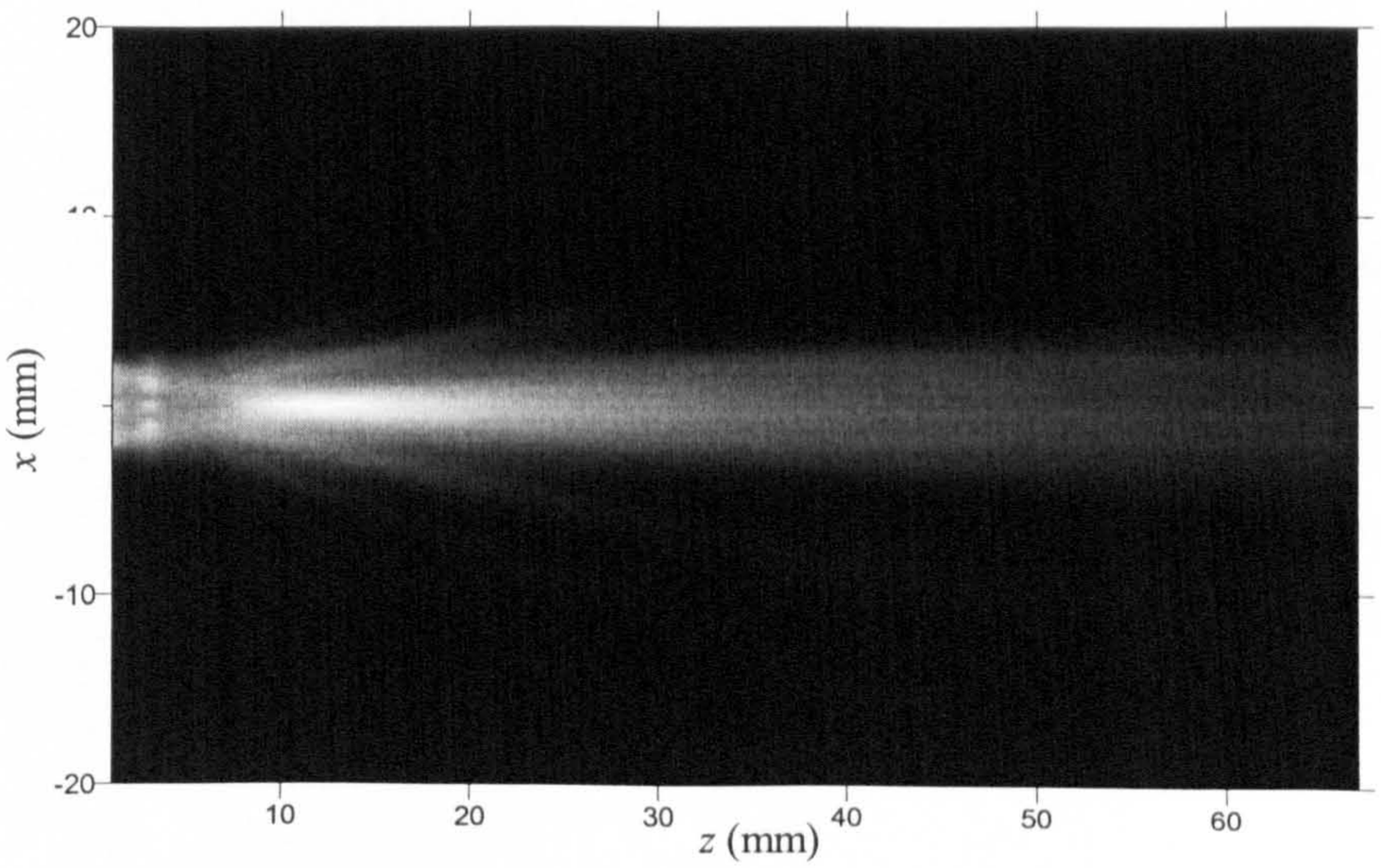

Figure 5.35: Theoretical field for a 5 mm square source and a point receiver

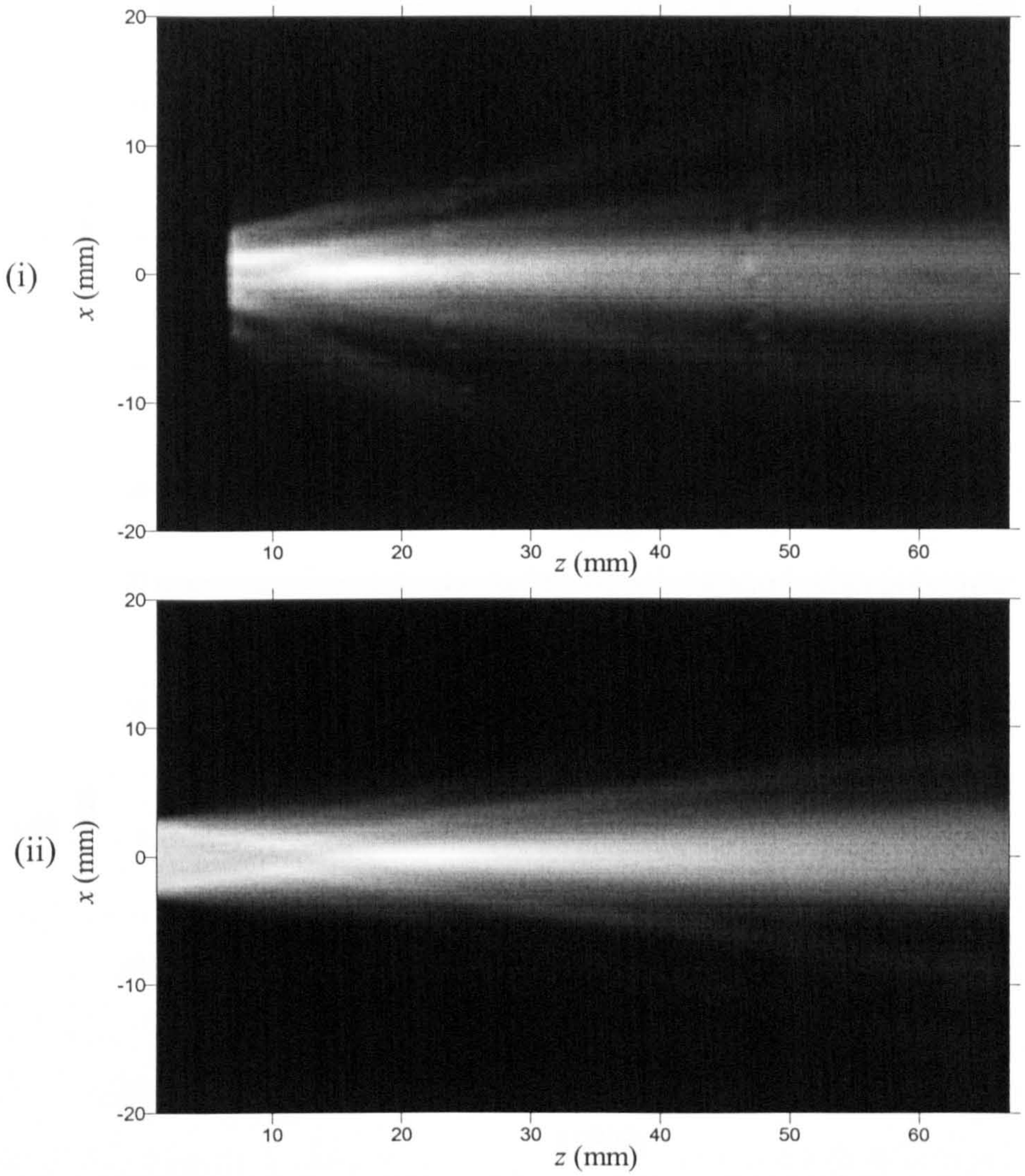

Figure 5.36: 6mm × 4 mm source and 1 mm × 8 mm receiver (x,y), (i) experimental and (ii) theoretical field plots

The effect of the rotation of the receiver, from being a 8 × 1 mm to 1 × 8 mm receiver, is as explained in the previous section, namely that the more directional receiver in the x direction has resulted in reduced detection of the sidelobes emitted from the source, as can be seen by comparing Figure 5.36 with Figure 5.37. In addition, it can be seen in Figure 5.38 that whilst the sidelobes of the field are slightly reduced in amplitude by the size of the receiver, and the amplitude of the mainlobe increased, the biggest difference between a point receiver and one of finite size occurs very close to the source.

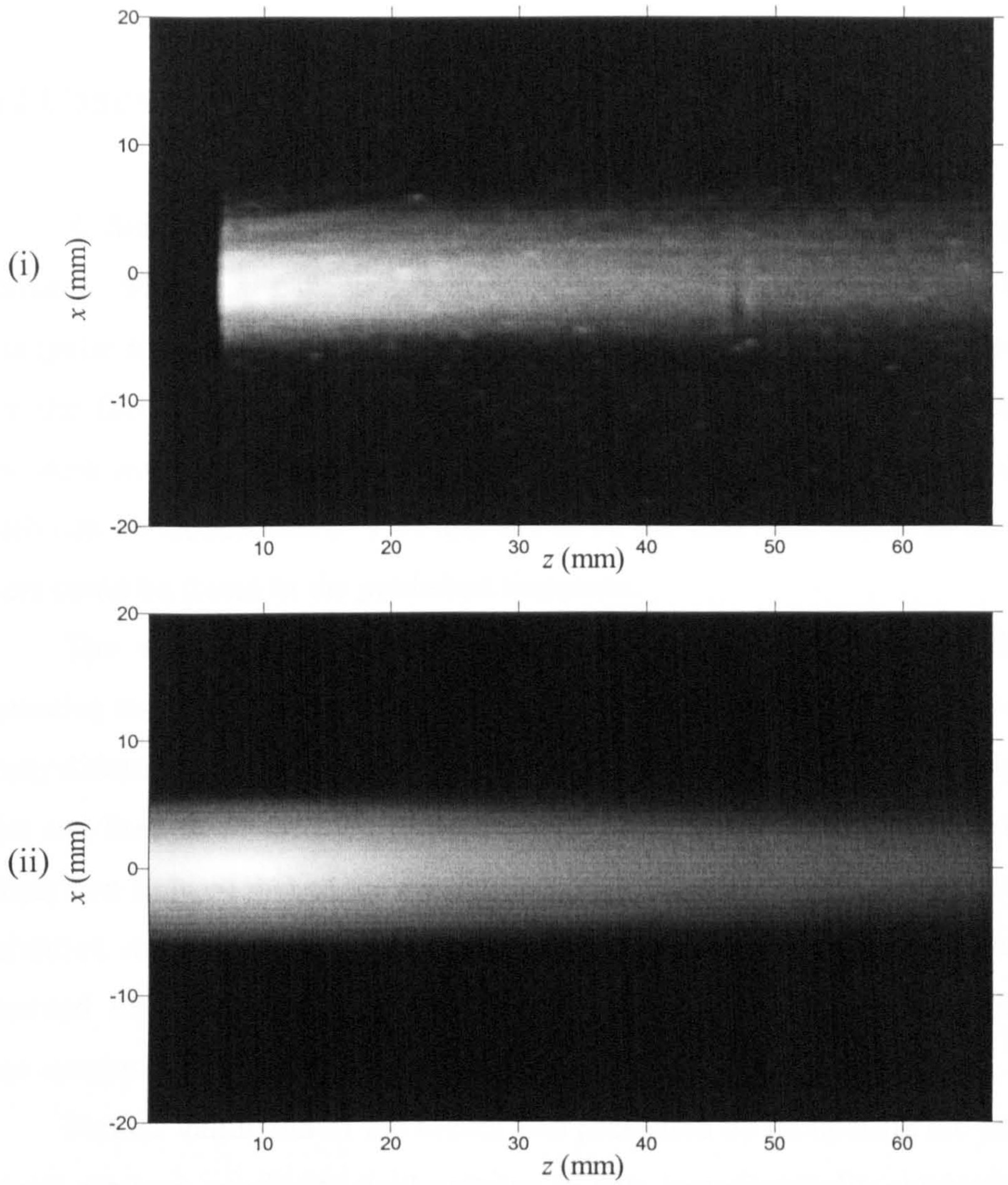

Figure 5.37: 6 mm × 4mm source and 8mm × 1mm receiver (x,y), (i) experimental and (ii) theoretical

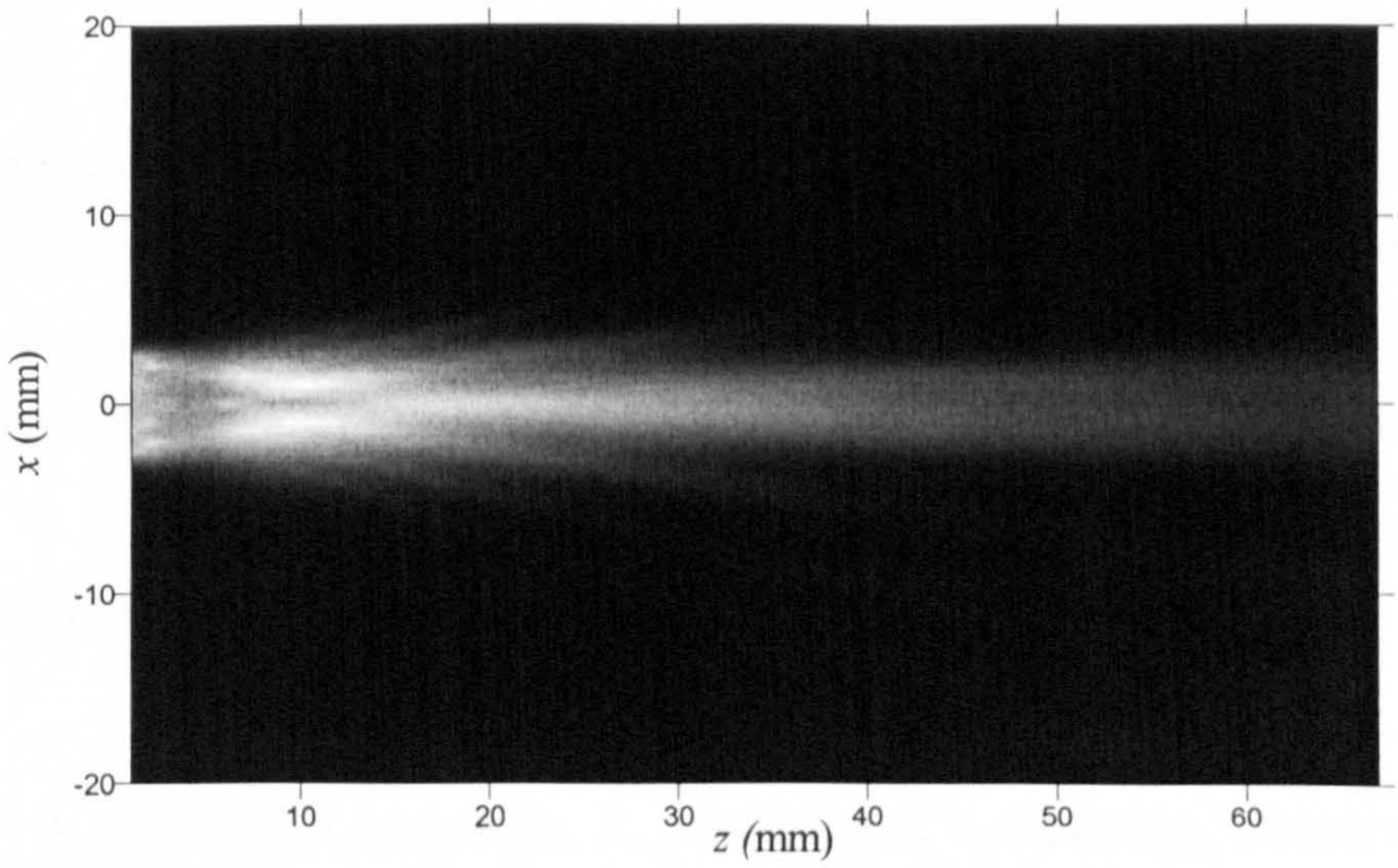

Figure 5.38: Theoretical field for a point receiver from a 6×4 mm source

5.12 Conclusions

A finite receiver model has been developed, based on the Impulse Response approach, which is capable of predicting the pressure transmitted between two rectangular transducers. This has been done by integrating the scalar impulse response over the face of the receiver. To obtain such an integral, an alternative method of procedure was developed, in which the receiver is treated as a series of components which can be reconstructed. This appears to be the first such model to be described; no others could be found in the published literature.

The model presented here has been validated by a comparison with an alternative method. This alternative method approximates the finite receiver to a grid of evenly distributed points covering the receiver face; the scalar impulse response at each point can then be found by summation of each of these scalar impulse response. This comparison showed that as the number of points constituting the grid is increased, in the alternative model, the result tends towards that given by the finite receiver model presented here. However, the alternative approximation was computationally much more intense.

Further validation of the model was presented by comparing the predicted peak-to-peak pressure amplitude field patterns to data experimentally obtained in air. These results showed good correlation and have been discussed in relation to the size and aspect ratio of the receiver and source transducers.

This model can be used to asses the effect of various sized receivers on the measured pressure field and if required determine the size needed such that the effect is negligible. It can also be used to account for diffraction correction, as two transducers are moved apart on axis in an analogous way to that calculated for circular pistons [5]. The model is thus likely to have applications in many ultrasonic measurements.

5.13 References

[1] P. A. Lewin, G. Lypacewicz, R. Bautista, and V. Devaraju, "Sensitivity of ultrasonic hydrophone probes below 1 MHz," *Ultrasonics*, vol. 38, pp. 135-139, 2000.

[2] H. L. W. Chan, S. T. Lau, K. W. Kwok, Q. Q. Zhang, Q. F. Zhou, and C. L. Choy, "Nanocomposite ultrasonic hydrophones," *Sensors and Actuators A: Physical*, vol. 75, pp. 252-256, 1999.

[3] D. R. Bacon, "Primary Calibration of Ultrasonic Hydrophones using Optical Interferometry," *IEEE Transactions on Ultrasonics Ferroelectrics and Frequency Control*, vol. 35, pp. 152-161, 1988.

[4] A. S. Khimunin, "Numerical Calculation of the Diffraction Corrections for the Precise Measurements of Ultrasonic Absorption," *Acustica*, vol. 27, pp. 173-181, 1972.

[5] G. R. Harris, "Review of Transient Field-Theory for a Baffled Planar Piston," *Journal of the Acoustical Society of America*, vol. 70, pp. 10-20, 1981.

[6] J. L. San Emeterio and L. G. Ullate, "Diffraction Impulse-Response of Rectangular Transducers," *Journal of the Acoustical Society of America*, vol. 92, pp. 651-662, 1992.

[7] L. G. Ullate and J. L. S. Emeterio, "A New Algorithm to Calculate the Transient near-Field of Ultrasonic Phased-Arrays," *IEEE Transactions on Ultrasonics Ferroelectrics and Frequency Control*, vol. 39, pp. 745-753, 1992.

[8] R. A. Noble, A. D. R. Jones, T. J. Robertson, D. A. Hutchins, and D. R. Billson, "Novel, wide bandwidth, micromachined ultrasonic transducers," *IEEE Transactions on Ultrasonics Ferroelectrics and Frequency Control*, vol. 48, pp. 1495-1507, 2001.

Chapter 6: Focussing in air using a parabolic mirror

6.1 Introduction

Ultrasound can be focussed in a variety of ways, including the use of phased arrays as in Chapter 4, contoured transducers such as conical sources [1], Fresnel plates [2, 3], and reflective mirrors [4]. In this Chapter a parabolic mirror, which reflects ultrasound produced by a circular source, and hence has a focussing effect, is modelled. The model produced is capable of predicting the emerging pressure field from such mirrors, so is able to aid the design process. To this aim different variables are altered to examine the effect on the size of the focal point.

When considering reflection, it is usual to first think of the incident angle equalling the emergence angle, one of the results predicted by Snell's Law. This is however, only true for a plane wave. Here the incident wave consists of more than a simple plane wave, as it is the diffraction field of a transducer. Hence, such an approach is not applicable. Snell's Law for reflection, can be derived by considering the pathlength travelled, this must be constant across the wavefront, a criteria which is satisfied when the incidence angle is equal to the emergence angle, (see Chapter 1).

The model presented here approximates the mirror surface to a grid of point reflectors. Each of these point reflectors will have an incoming waveform, which can be found from the Impulse Response model. This incoming waveform is reflected. The reflected pressure waveform, which arrives at a point in the field, can be found by summing these reflected waveforms once the variation in pathlength is accounted for by a time shift.

It would appear that no such predictions exist in the literature for the case of reflection and focussing of a beam from a planar piston. Here, the particular case of a reflection of the beam from a circular source by a parabolic mirror will be investigated.

6.2 The Impulse Response model for a circular piston

The impulse response model has been discussed in Chapter 1. It is used to predict the pressure waveform arriving at a field point from a planar source, which is located within an infinite rigid baffle. The problem reduces to the pressure being equal

to the propagation medium density, ρ, multiplied by the time differential of the convolution of the velocity of the piston source, $v(t)$, with the scalar impulse response, $h(\bar{r},t)$, as given in equation 1.17. The scalar impulse response is found from equation1.19, using $\Omega(\bar{r},t)$, the angle subtended in the plane of the infinite baffle by the source (as shown in Figure 1.3). Stepanishen [5] has found this angle as a time stepped function for a uniform circular source operating in a homogenous propagation medium. The variables used are shown in Figure 6.1.

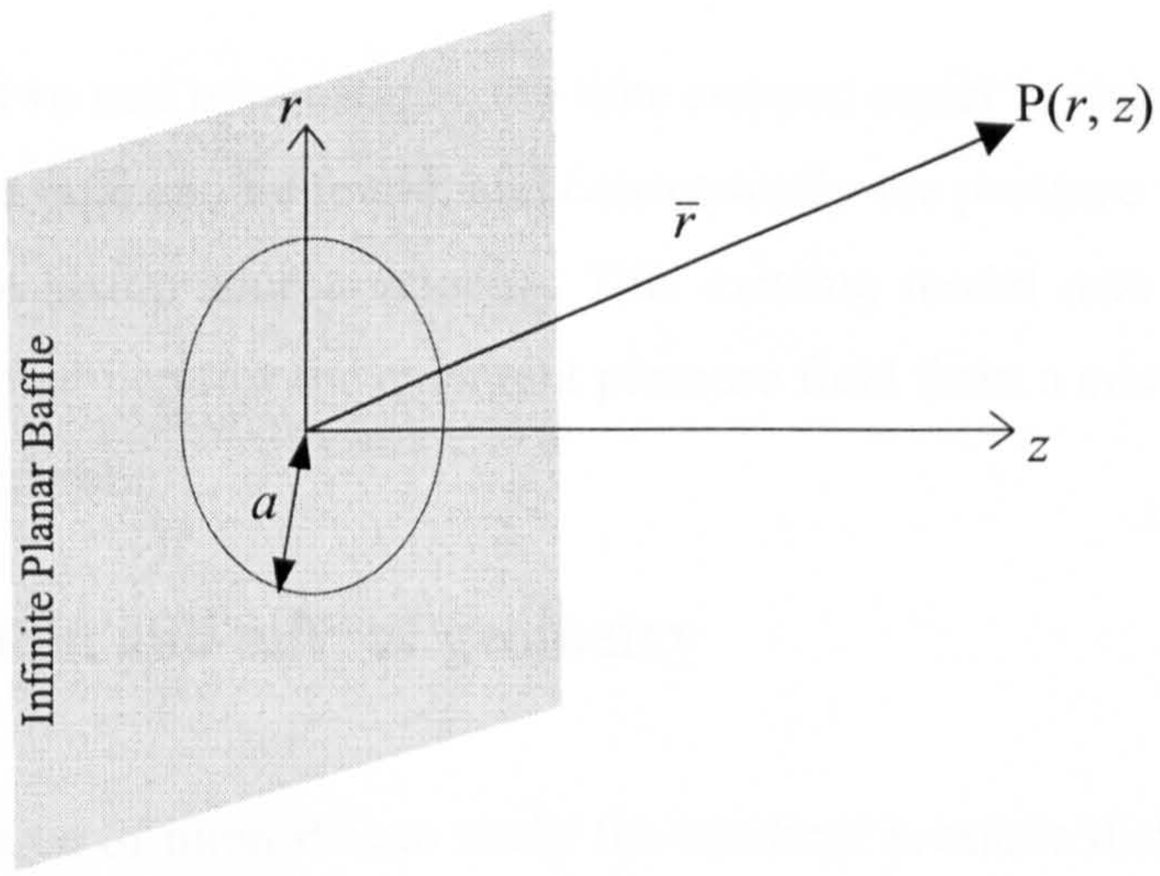

Figure 6.1: Variables used to model a circular source

The point P, located at $\bar{r}$, can be defined by cylindrical coordinates r and z, from the centre of the circular source. Where r is the radial distance, and z the distance normal to the plane in which the source lies. The radius of the source is a. The time stepped value of $h(\bar{r},t)$ for the case of $a>r$, is given by:

$$
\begin{aligned}
h(\bar{r},t) &= 0, && ct<z, \\
&= c, && z<ct<R`, \\
&= \frac{c}{\pi}\cos^{-1}\left\{\frac{(ct)^2 - z^2 + r^2 - a^2}{2r\left[(ct)^2 - z^2\right]^{1/2}}\right\}, && R`<ct<R, \\
&= 0, && ct>R,
\end{aligned}
\tag{6.1}
$$

where c is the speed of sound in the propagation medium, $R`=\left[z^2+(a-r)^2\right]^{1/2}$, and $R=\left[z^2+(a+r)^2\right]^{1/2}$. For the case where $a \le r$, then $h(\bar{r},t)$ is given by:

$$\begin{aligned} h(\bar{r},t) &= 0, && ct < R`, \\ &= \frac{c}{\pi}\cos^{-1}\left\{\frac{(ct)^2 - z^2 + r^2 - a^2}{2r\left[(ct)^2 - z^2\right]^{1/2}}\right\}, && R` < ct < R, \\ &= 0, && ct > R. \end{aligned} \tag{6.2}$$

Using these two sets of equations, the time stepped scalar impulse response at any point, P(r, z), in the field can be found, and consequently the pressure waveform can be found from a given piston source velocity. This existing model acts as the first step in the model described here for the emergent pressure field from a circular source focussed by a parabolic mirror.

6.3 Reflection and mirror geometry

The area of interest is to study the resultant pressure distribution when the field of a planar piston is reflected at a boundary. At the interface of two media in which sound waves are propagating, some of the energy is transmitted and some reflected. Equation 1.7 gave the reflection coefficient for an interface, in terms of the acoustical impedances of the two media, when the sound wave travels normally to the interface. This equates to a value of $R = 0.99997$, when the interface is between air (acoustical impedance, Z, is $414\text{kgm}^{-3}\text{s}^{-1}$) and steel ($Z = 51\times10^{6}\text{kgm}^{-3}\text{s}^{-1}$). Consequently only a very small proportion of the energy is transmitted from the air into the steel. This indicates the extent of the validity of the assumption used in this model of a reflecting surface, i.e. that the pressure wave, which arrives at a point on the mirror surface, is wholly reflected.

If the reflector is a point, then the pressure wave emerging from it will diffract in all directions, according to Huygens' principle (the basis of the Impulse Response model). This results in a drop of pressure amplitude proportional to $1/R$, where R is the distance from the point reflector [6].

The basis of the model presented here is that a reflector placed in front of a circular source can be modelled as a fine grid of point reflectors. The pressure waveform emerging from any one of these points can be equated to the pressure waveform arriving from the circular source at that point, found using the Impulse Response method. An additional assumption that is made is that the waveform arriving at any field point has first been reflected from the mirror, so that if any phase change occurs during reflection it is a constant factor and hence can be ignored. This Chapter will investigate the specific case of a parabolic mirror, which can be used for focussing, and a comparison will be presented between the predicted peak-to-peak pressure amplitude fields and experimental scan results of the field of this device in air. The geometry and a photograph of the device studied here is shown in Figure 6.2. This device uses a planar polymer-membrane capacitive transducer of the type described in Chapter 2, fitted with a parabolic mirror, and which has been designed to operate in air. The device was manufactured by Microacoustic Instruments Inc, (Ottawa, Canada). The dotted line, in Figure 6.2 (i), shows the angle at which the mirror is intended to be aligned during operation, and is at 90^0 to the line from the central axis of the mirror to the focal point. The casing has been designed to fit within this line. The model will be written so that the pressure field from this product can be modelled, although the variables are defined so that the modelling of other parabolic mirrors is possible.

In Section 1.5, the concept of a plane and edge wave emerging from a circular source was discussed. The plane wave exists only for the case of $a>r$, and except for points on-axis, it is greater in size than the edge wave. The plane wave arrives at the time of $t = z/c$, so for a point on the mirror, the plane wave arrives having travelled a distance of z, which is the distance normal to the source (see Figure 6.1). The focal point will occur when these plane waves are reflected so that they arrive in phase. If a point on the mirror surface is considered, the total pathlength from the source to the focal point via this point on the mirror, is the distance of the point on the mirror to the source measured normally, added to the distance from the point on the mirror to the focal point. The shape of the mirror is dictated by the criteria that this pathlength must be equal across all points on the mirror surface.

(i)

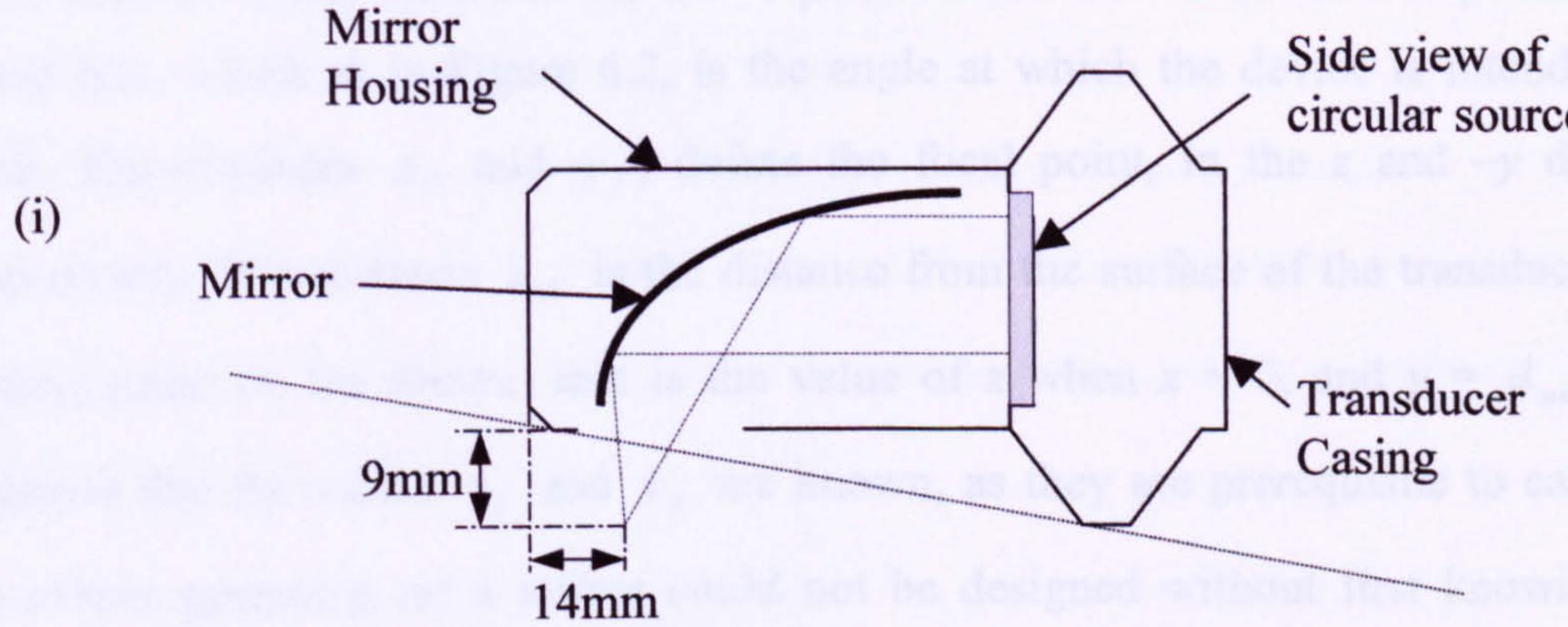

(ii)

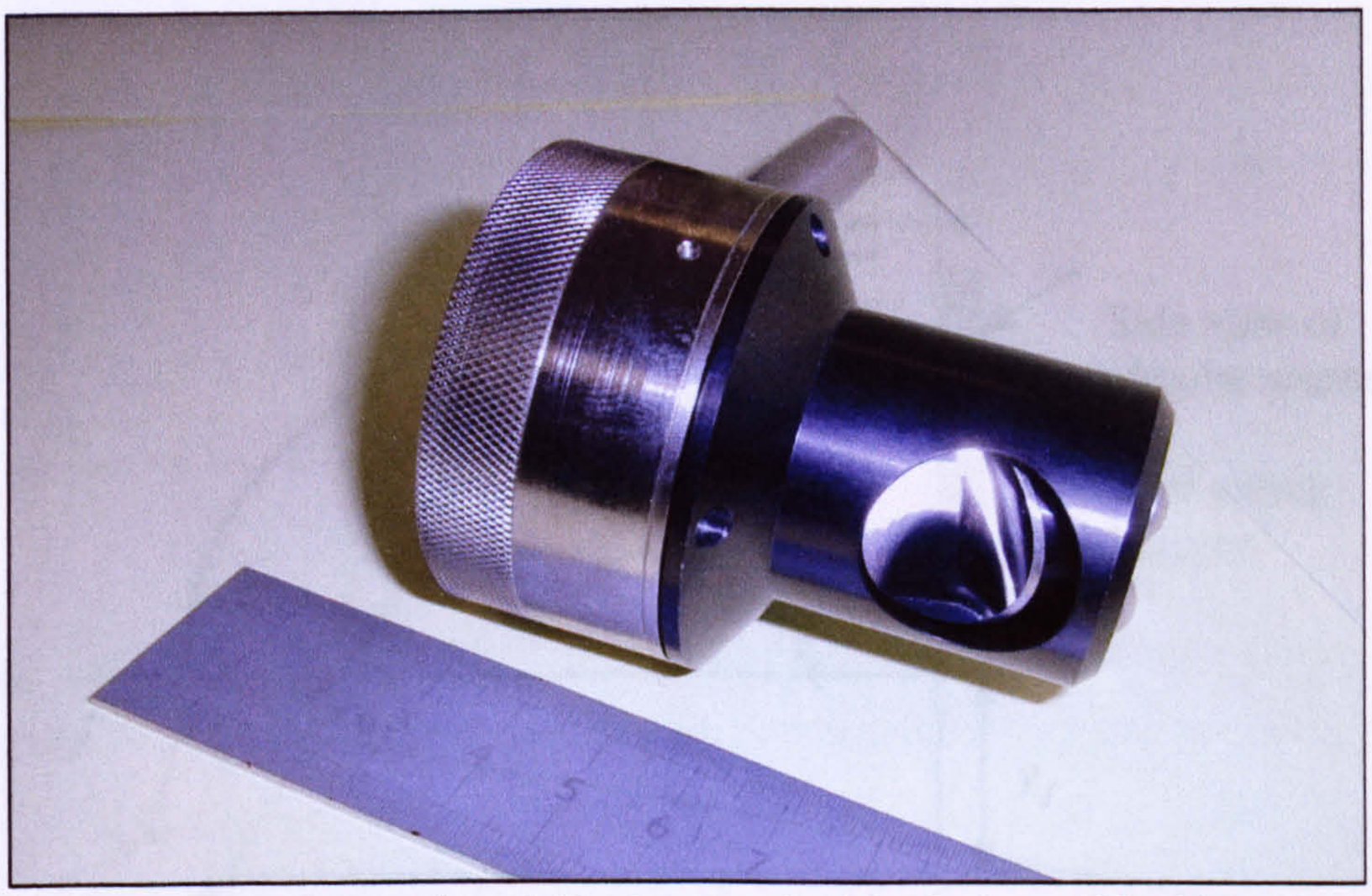

Figure 6.2: (i) Schematic and (ii) photograph of the device used in this work

In the case where the mirror is greater in diameter than the transducer, then no plane wave arrives at some parts of the mirror. This is the case for the current device, where the mirror and source have diameters of 24.6 mm and 22 mm respectively. However this is ignored and the shape of the mirror is calculated as stated above across the whole surface.

To find a point on the mirror surface it is first necessary to define the axes used these are shown in Figure 6.3. The x axis completes the orthogonal set with the y and z axes, the diagram in Figure 6.3 shows the $x = 0$ plane which cuts the source and mirror thorough their centres, and so is a plane of symmetry. The source face lies in the $z = 0$ plane. The most distant tip of the mirror is defined as occurring at $y = 0$. The mirror and source are aligned coaxially, and have diameters of d_{mirror} and d_{source} respectively. The w axis completes the orthogonal set with the u and v axis, consequently it is parallel to

the x axis, the plane shown is the $w = 0$ plane. The u axis is defined as parallel to the doted line, which as in Figure 6.2, is the angle at which the device is intended to be used. The distances z_f and y_f, define the focal point, in the z and $-y$ directions respectively. The distance z_{off} is the distance from the surface of the transducer to the nearest point on the mirror, that is the value of z when $x = 0$, and $y = d_{mirror}$. It is assumed that the values z_f and y_f are known, as they are prerequisite to calculating the mirror geometry, so a mirror could not be designed without first knowing these values. In addition the value of d_{mirror}, d_{source} and z_{off} must be specified.

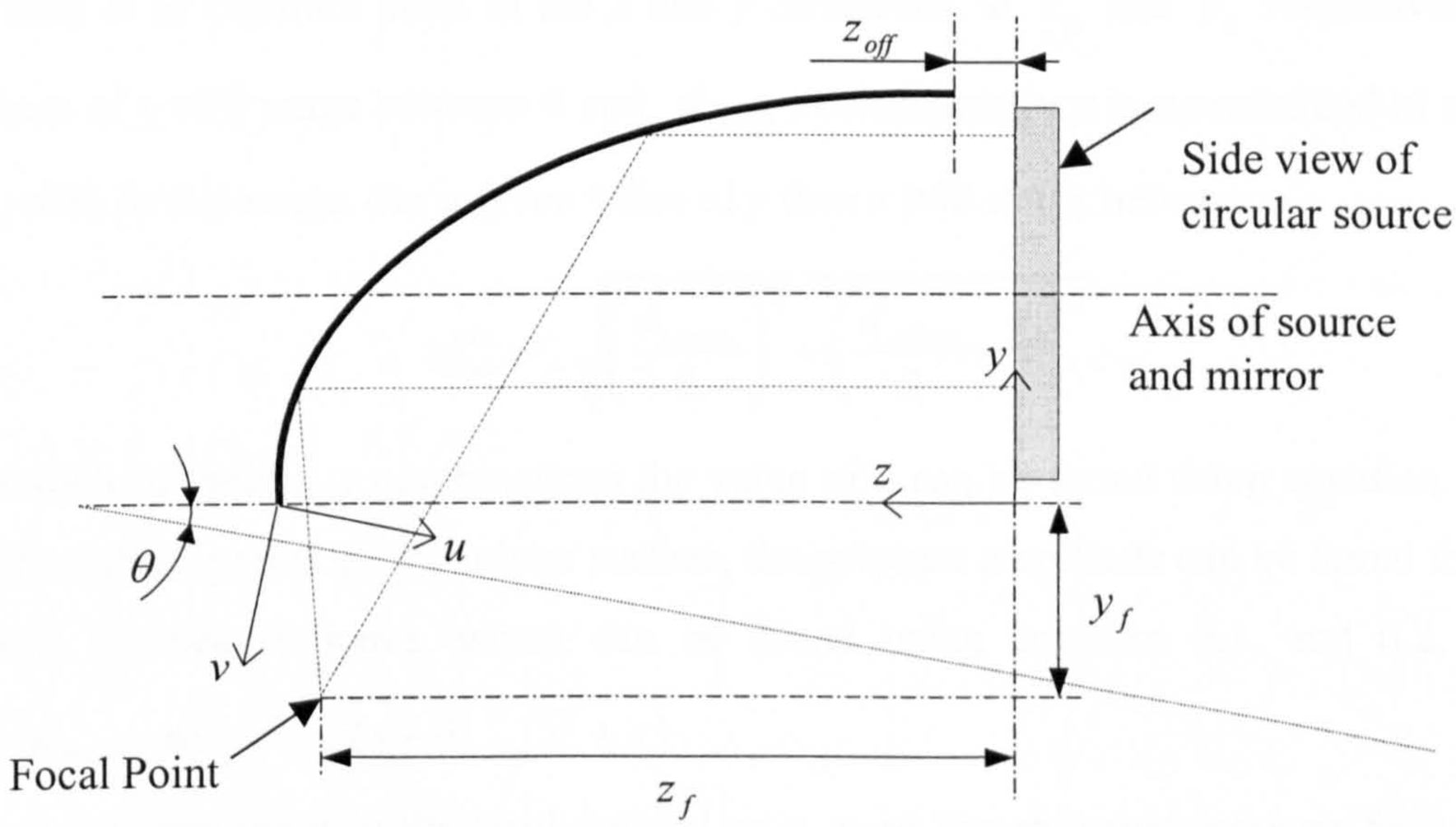

Figure 6.3: Definition of terms used to define the reflecting mirror

The only known point on the mirror is z_{off}, so this will be used to calculate the path length to the focal point, which will be constant for all x, y, z coordinates on the mirror surface. It can be seen from Figure 6.3 that the path length to the focal point is given by,

$$pl_f = z_{off} + \sqrt{(z_f - z_{off})^2 + (y_f + d_{mirror})^2}. \tag{6.3}$$

If x and y define a line passing through the mirror then the value of z such that the point x, y, z lies on the mirror surface can be found from the path length using,

$$z = \frac{pl_f^{\,2} - z_f^{\,2} - (y_f + y)^2 - x^2}{2(pl_f - z_f)}. \tag{6.4}$$

Using this method, any point on the surface of the mirror can be found.

The dimension z_{tip} is defined as the length, in the z direction, to the further most tip of the mirror, this occurs at $x = y = 0$. As with all other points on the mirror the value of z can be found from equation 6.5, giving,

$$z_{tip} = \frac{pl_f^{\,2} - z_f^{\,2} - y_f^{\,2}}{2(pl_f - z_f)}. \tag{6.5}$$

It has been stated that the reflecting surface will be modelled by an approximation to a grid of point reflectors on the surface of the mirror. The grid which is used is of constant pitch in the x and y directions, at x_p and y_p respectively. The values of y will range between 0 and d_{mirror}, consequently y is incremented at steps of y_p with in this range. For a given value of y then x will range between:

$$x_{\max}^{\min} = \overset{-}{+} \sqrt{\left(\frac{d_{mirror}}{2}\right)^2 - \left(\frac{d_{mirror}}{2} - y\right)^2}. \tag{6.6}$$

For each of these x, y combinations the value of z can be found using equation 6.4. At each of these points on the mirror surface, the pressure amplitude can be found from the scalar impulse response, which can be found using equation 6.1, and 6.2, where $r = d_{mirror}$, and $a = \sqrt{(y - d_{mirror})^2 + x^2}$.

At any point in the field defined as u, v, w, the reflected pressure from all the grid points will arrive. The total arriving pressure is proportional to the sum of the reflected pressures after the phase and effect of diffraction are considered. As stated previously, the pressure amplitude of a point source drops with $1/R$, where R is the distance from the source. Consequently, the pressure waveform emerging from one of the grid points, (x, y, z), which arrives at a field point (u, v, w), is proportional to the emerging waveform divided by R, where R is given by,

$$R = \sqrt{(w - x)^2 + (y + u.\sin\theta + v.\cos\theta)^2 + (z_{tip} - u.\cos\theta + v.\sin\theta - z)^2}, \tag{6.7}$$

where θ is the angle shown in Figure 6.3.

The geometry of the mirror is such that the path length is constant for any point reflector on the mirror surface, at the focal point. However, for field points other than the focal point, the path length will differ for each point reflector, and consequently a

phase shift is introduced. It is therefore necessary to calculate the path length from the source to the point on the grid, (x, y, z), to the field point (u, v, w), this is given by

$$pl = z + R. \tag{6.8}$$

The change in the actual path length, from point to point, can be used to find a time shift by dividing by the speed of sound, c. In addition the length pl can be used to account for absorption in the propagation medium, as this is the total distance travelled from the source to the point in the field. However, in the predictions shown here the absorption has been ignored, as the path length differences are not great, and the pressure field is in any case normalised.

In order to find the pressure field emerging from a parabolic mirror using this method, a computer program has been written. The results presented in this work have been calculated using a program written in Matlab, which is listed in Appendix B.7.

When a simulated field in the uv plane is considered it is possible to use the symmetry of the system, and consider only points on the mirror, which have a positive x value. So x^{min} in equation 6.6 becomes 0. Symmetry can also be used when the pressure arriving in points in the uw plane are considered, here it is only necessary to consider field points in which w is positive.

The model states that the pressure waveform reflected from each point on the mirror surface must be added after phasing and diffraction are accounted for. However the pressure waveform is the result of the convolution of the scalar impulse response with the time differential of the piston velocity waveform multiplied by the density, as given in equation 1.17. This convolution increases the length of the data string, it is therefore more efficient only to perform the convolution at the end of the program, and until then deal only with scalar impulse responses. In addition to shorter data strings this means the convolution need only be performed once for each field point.

In order to show the mirror focussing, the system has been simplified to a circular source and eleven point reflectors as shown in Figure 6.4 (i). Figure 6.4 (ii) shows the scalar impulse response at each of the eleven points on the surface of the mirror described above. The points are at $x = 0$, and $y = 0 : 22.4$ mm in 2.24 mm steps. These points on the mirror are plotted in Figure 6.4 (i), as y against z.

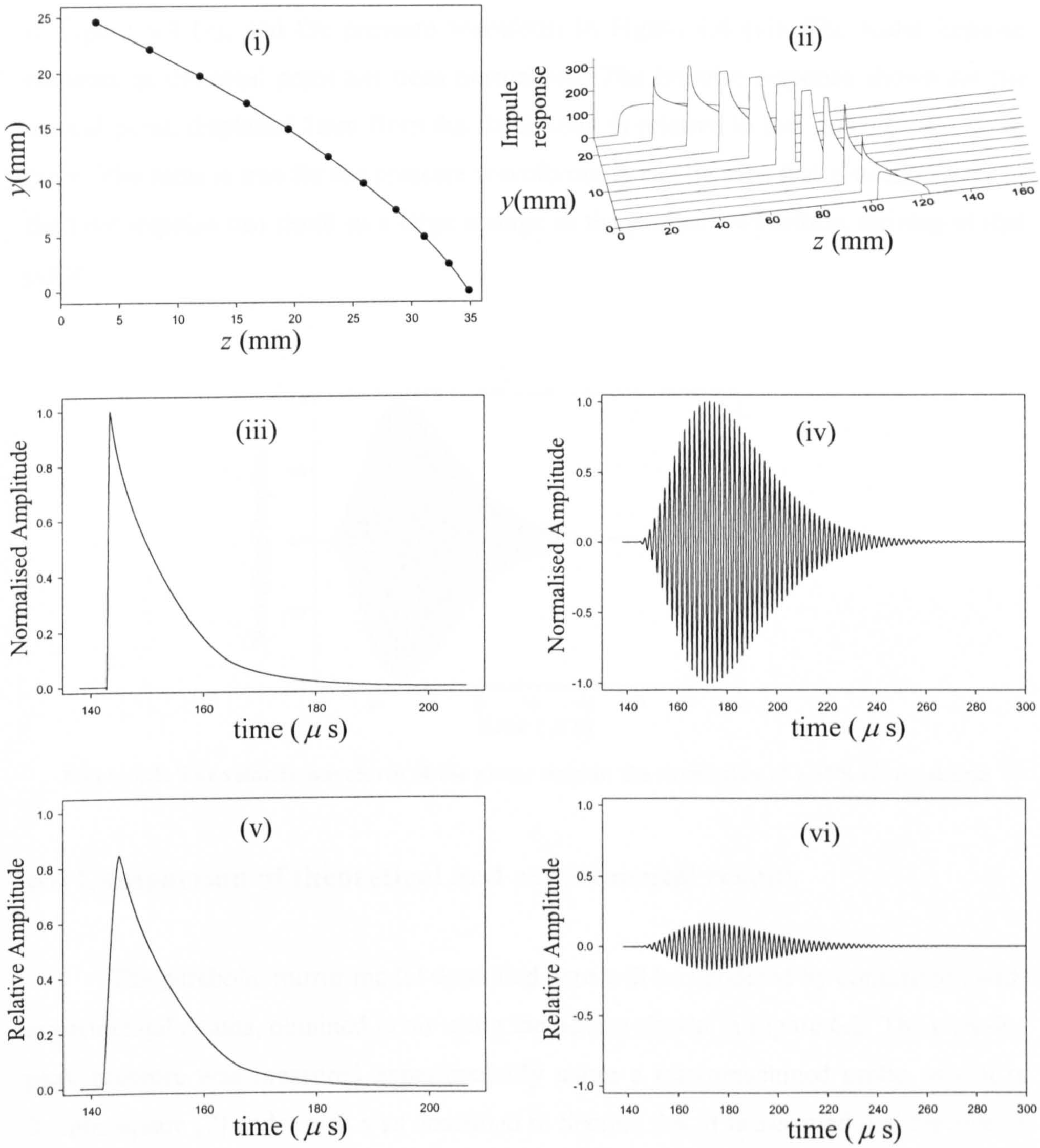

Figure 6.4: The impulse response at eleven points on the mirror, and the resulting total scalar response and pressure waveforms at two points in the field, the first being the focal point, and the second displaced by 1mm. (i) shows the eleven points, (ii) the scalar impulse response at each of the points, (iii) shows the total impulse response at the focal point, and (iv) shows the resulting waveform, (v) shows the total impulse response at 1 mm from the focal point, and (vi) the corresponding pressure waveform

The total scalar impulse response of the whole mirror has been calculated at the focal point as shown in Figure 6.4 (iii), this has been convolved with the piston velocity, to give the pressure waveform arriving at the focal point, this is shown in Figure 6.4 (iv). The piston drive signal used here is a 500 kHz toneburst (K = 0.2, see equation 2.1), as shown in Figure 6.5. The same has been done for a point 1mm from the focal

point in the positive u direction, for this point the total scalar impulse response is given in Figure 6.4 (v), and the pressure waveform in Figure 6.4 (vi). The scalar impulse response at the focal point has been normalised. The impulse response shown for the second point, displaced 1mm from the focal point is relative to that given for the focal point. The same is true for the pressure waveforms. It can be seen that a small change in the total impulse can result in a large change in the pressure waveform arriving at that point.

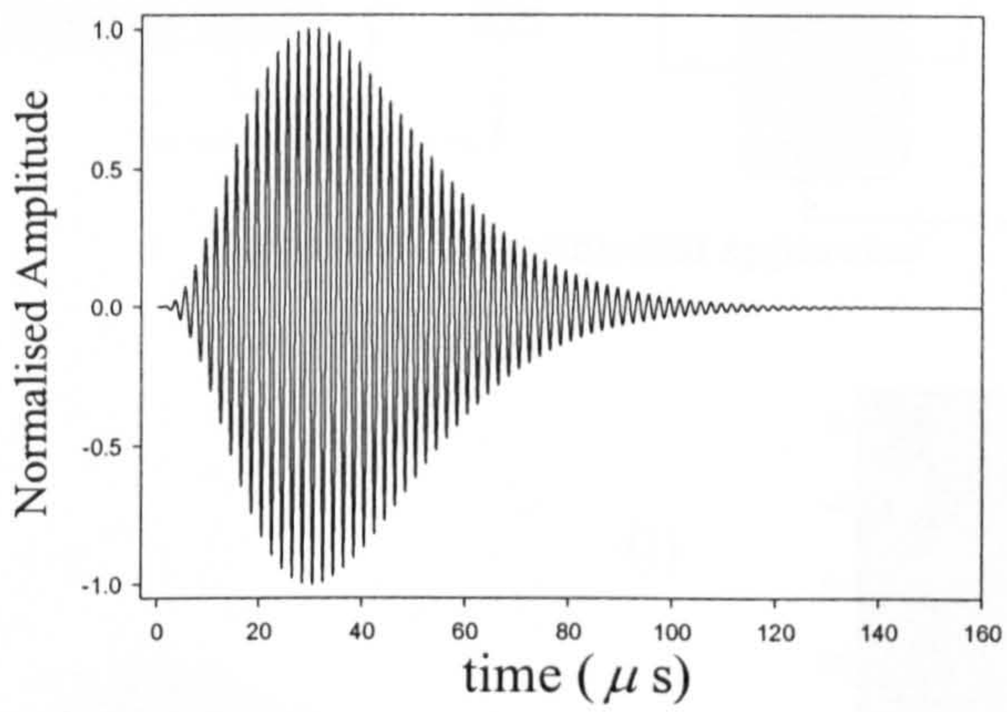

Figure 6.5: The velocity waveform of the piston used in the simulation of a 500kHz toneburst

6.4 Comparison of theoretical and experimental results

The parabolic mirror model described here will be validated by comparison with experimental results, obtained in air using the device shown in Figure 6.2. The peak-to-peak pressure was measured experimentally using a micromachined probe, which is 0.5mm square [7] and which was described in Section 4.4. It is assumed that the size of this probe has no discernible effect on the experimental data. This probe is used as a receiver and moved in the u and v direction with respect to the mirror, in the $w = 0$ plane. The experimental apparatus used is shown in Figure 6.6.

Figure 6.7 shows the normalised peak-to-peak pressure amplitude when the source is driven by a 500kHz toneburst ($K = 0.2$, see equation 2.1). The theoretical results here are produced using a gird of points on the mirror surface at a pitch of $x_p = y_p = 0.06\,\text{mm}$, (which for the case of the 1MHz drive waveform, the highest frequency simulated here, corresponds to approximately one fifth of a wavelength).

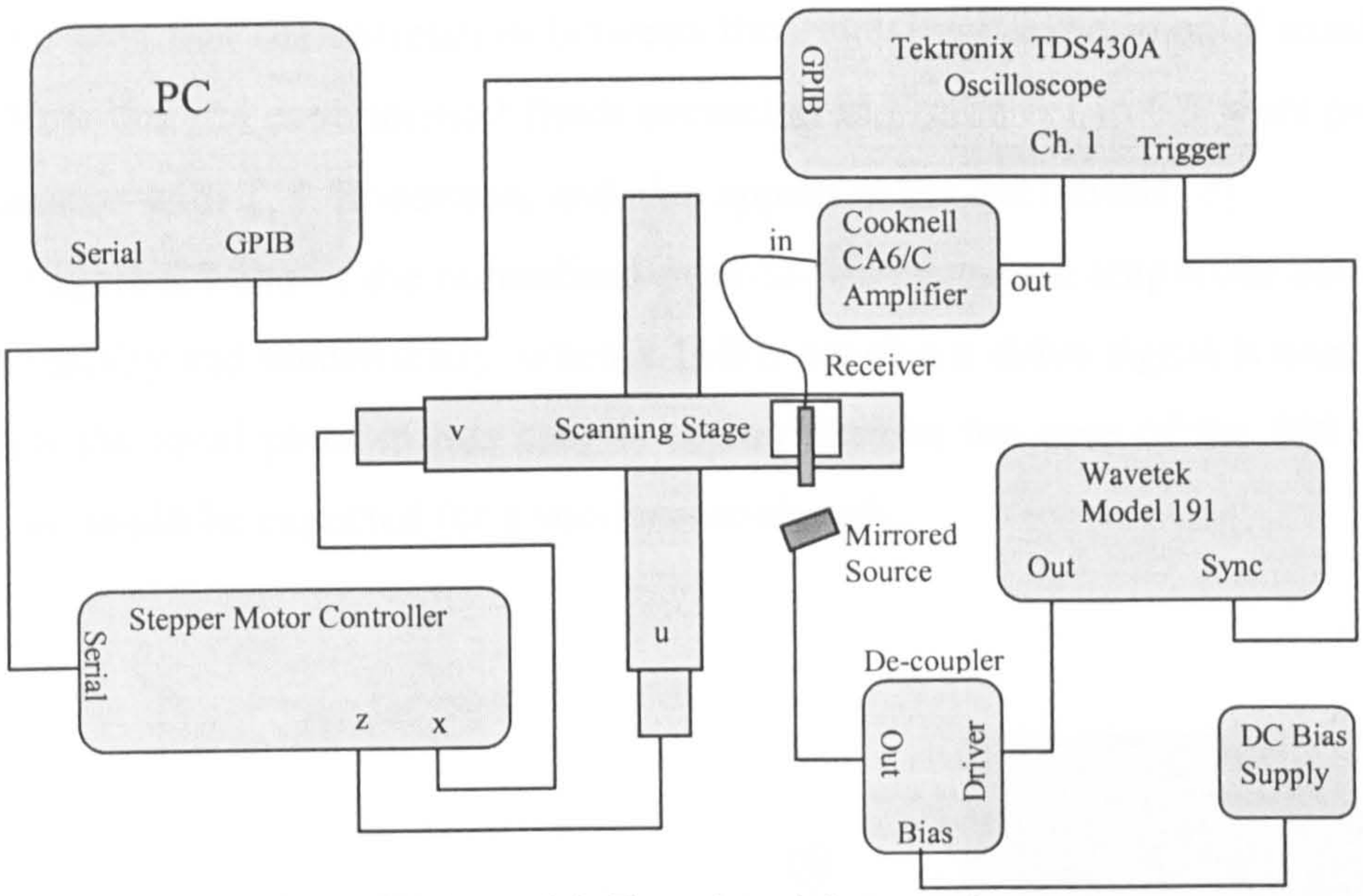

Figure 6.6: Experimental apparatus

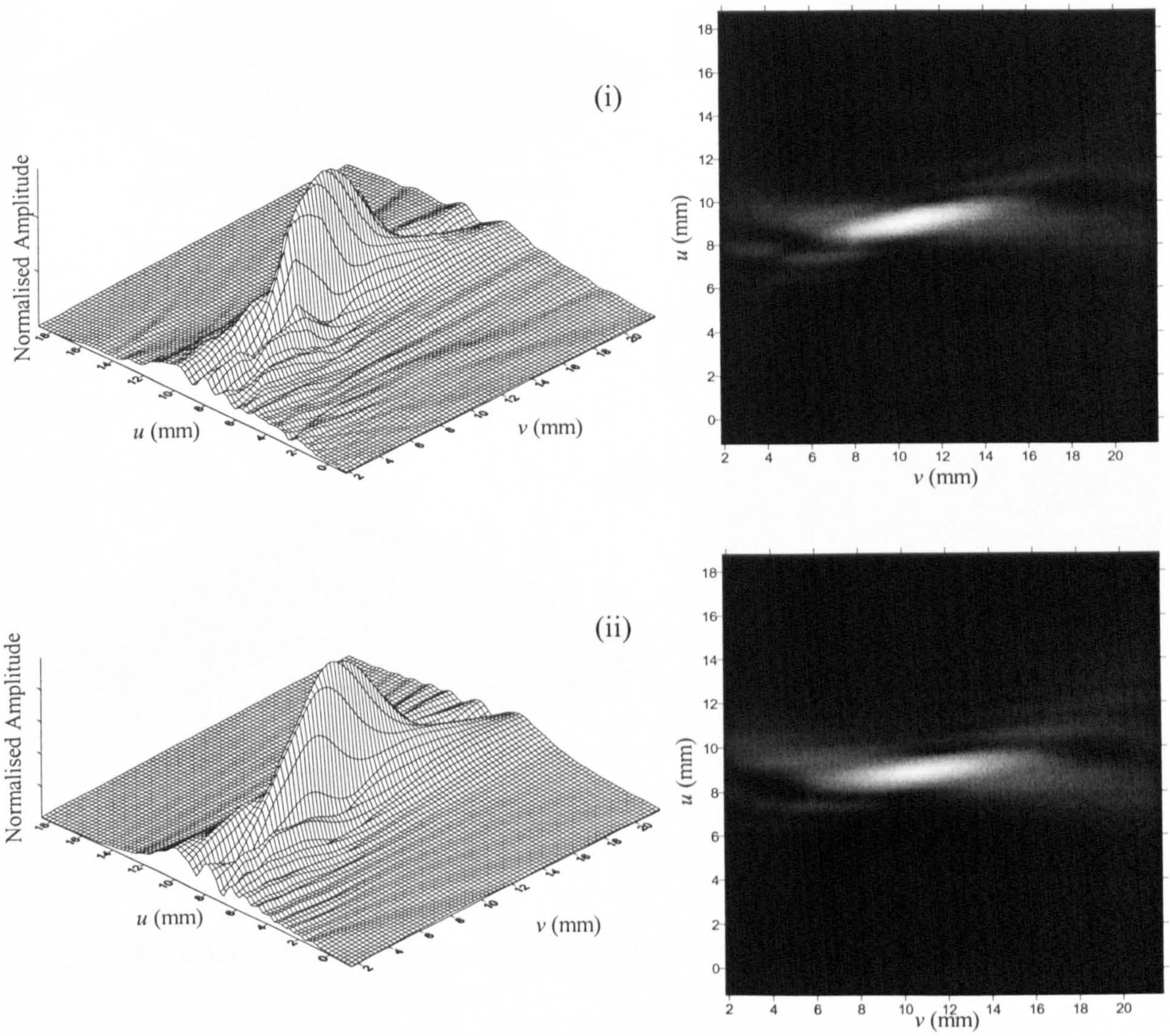

Figure 6.7: Comparison of (i) experimental and (ii) theoretical results with 500 kHz toneburst drive signal

It can be seen that the correlation between theoretical and experimental results is very good. Note that the experimental fields presented in Figure 6.7 to 6.9 were produced in collaboration with T. J. Robertson, and also appear in his PhD thesis [8].

Figure 6.8 shows the normalised peak-to-peak pressure amplitude obtained both experimentally and theoretically, when a 1MHz toneburst drive signal is used. It can be seen that the focal point in this case is tighter than in the case of the 500 kHz drive signal, as would be expected for a shorter wavelength.

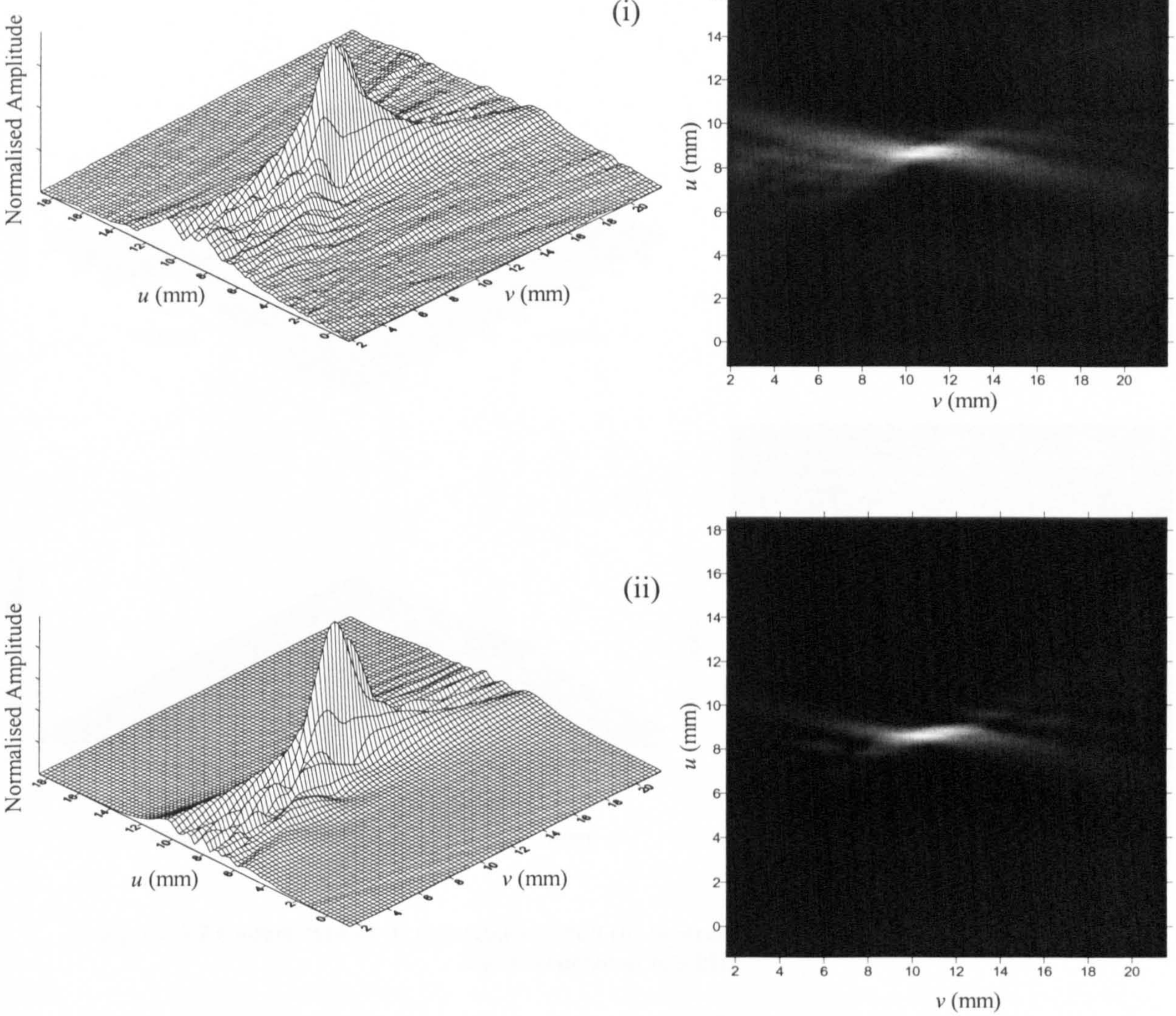

Figure 6.8: Comparison of (i) experimental and (ii) theoretical results with 1 MHz toneburst drive signal

Figure 6.9 shows the peak-to-peak pressure amplitude when a broadband drive signal (K = 3.5, see equation 2.1) is used to drive the source. The apparatus used in this experiment was the same as that shown in Figure 6.6, except that the Wavetek signal generator, was replaced by a Panametrics PR5055 pulser. The response of the transducer was found to be centred at 625kHz so the theoretical simulation uses a short signal centred at the same value. It can be seen that with this shorter waveform there were less ripples in the field than with the longer toneburst signals, and that the size of the focal point was between that of the 500 kHz and 1 MHz cases.

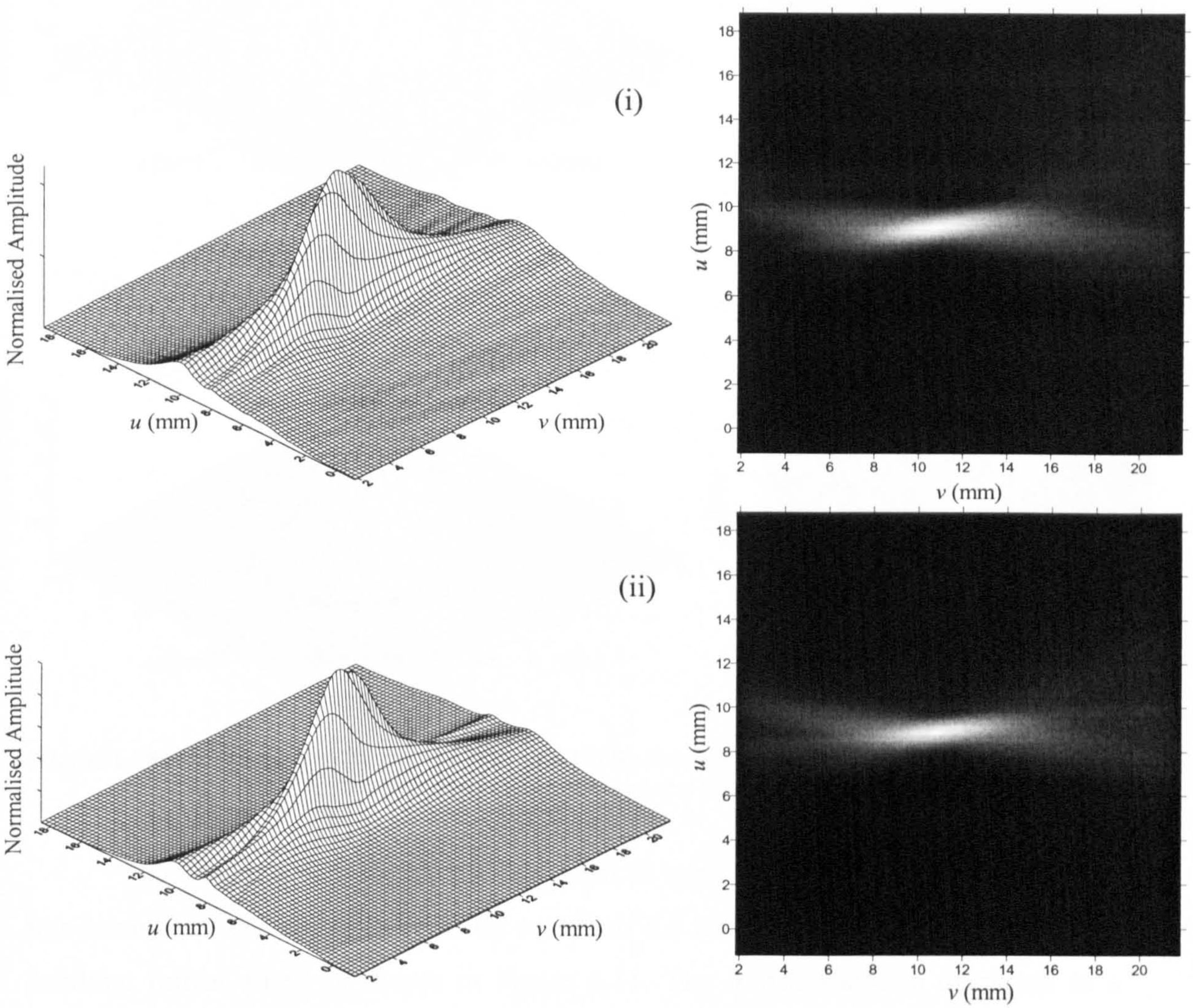

Figure 6.9 Comparison of (i) experimental and (ii) theoretical results with a broadband drive signal centred at 625 kHz

An application of the focussed air-coupled transducer is the non-destructive testing of samples using through-transmission. In this application it is useful to know the pressure field in the plane of the front surface of the sample, which is the *uw* plane passing through the focal point. Figure 6.10 shows a comparison of the experimental

and theoretical pressure fields in this plane, when a 500kHz toneburst drive signal is used. The apparatus used is as shown in Figure 6.6, except that the transducers are re-orientated such that the stages operate in the *uw* plane.

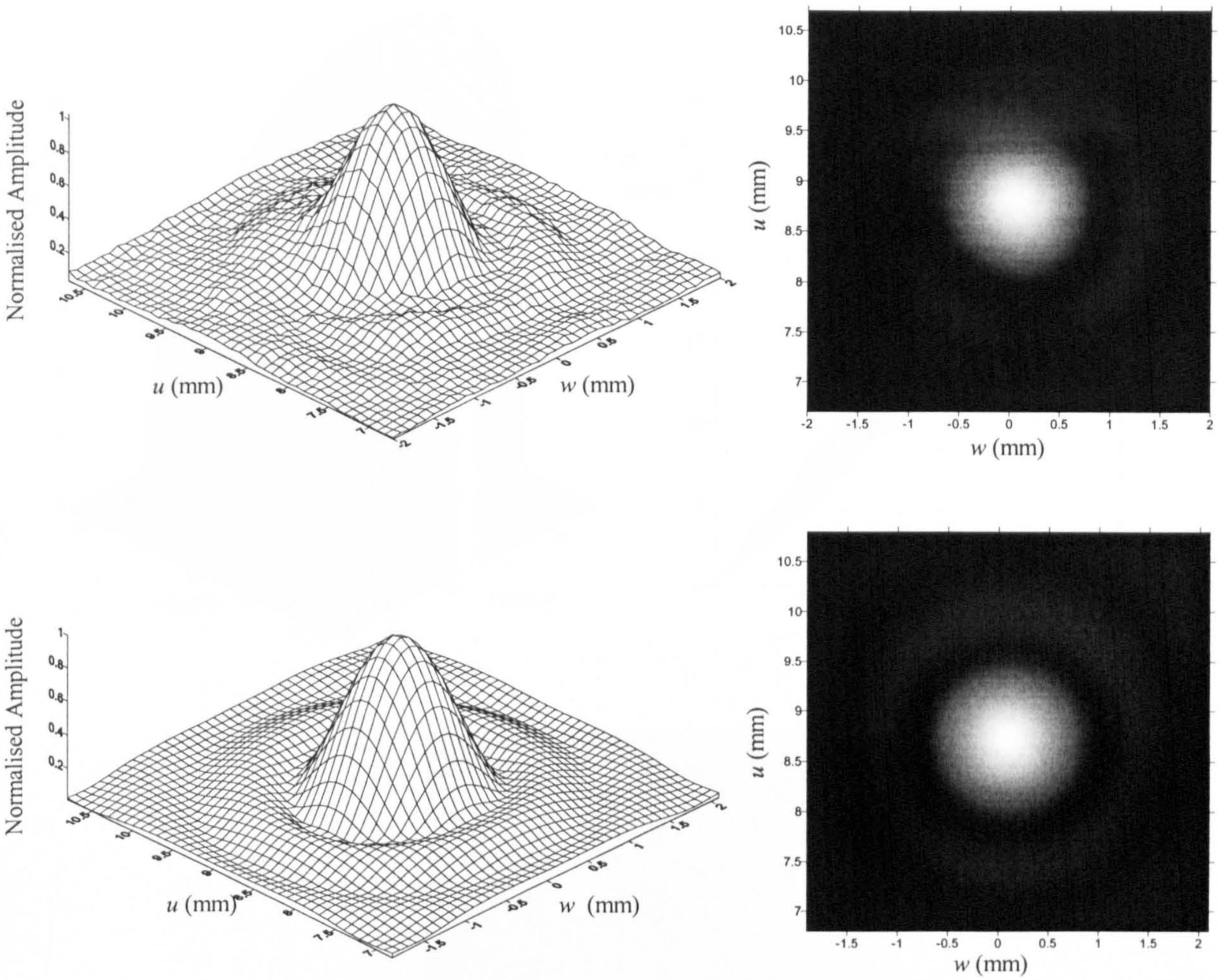

Figure 6.10: Comparison of (i) experimental and (ii) theoretical results with a 500kHz toneburst, in the *uw* plane passing through the focal point.

The way in which the grid points, used to approximate to the mirror surface in this model, are calculated is by using equations 6.3 and 6.4 as already described. The resulting mirror shape is shown in Figure 6.11. The mirror shape is displayed as a wireframe in Figure 6.11 (i), a cross section through the $x = 0$ plane in Figure 6.11 (ii), and a contour plot of the xy plane such that the contours refer to the z height, in Figure 6.11 (iii).

It can be seen from the contour plot of the mirror presented as Figure 6.11 (iii) that the lines of equal height, that is of equal z, are arcs. At the focal point the path length is equal regardless of the location of the point reflector on the mirror surface, as

equation 6.10 gives the path length as equal to the sum of z and R, then for all points of constant z the distance to the focal point must be a constant value of R. So all these are arcs are sections of circles centred on the focal point.

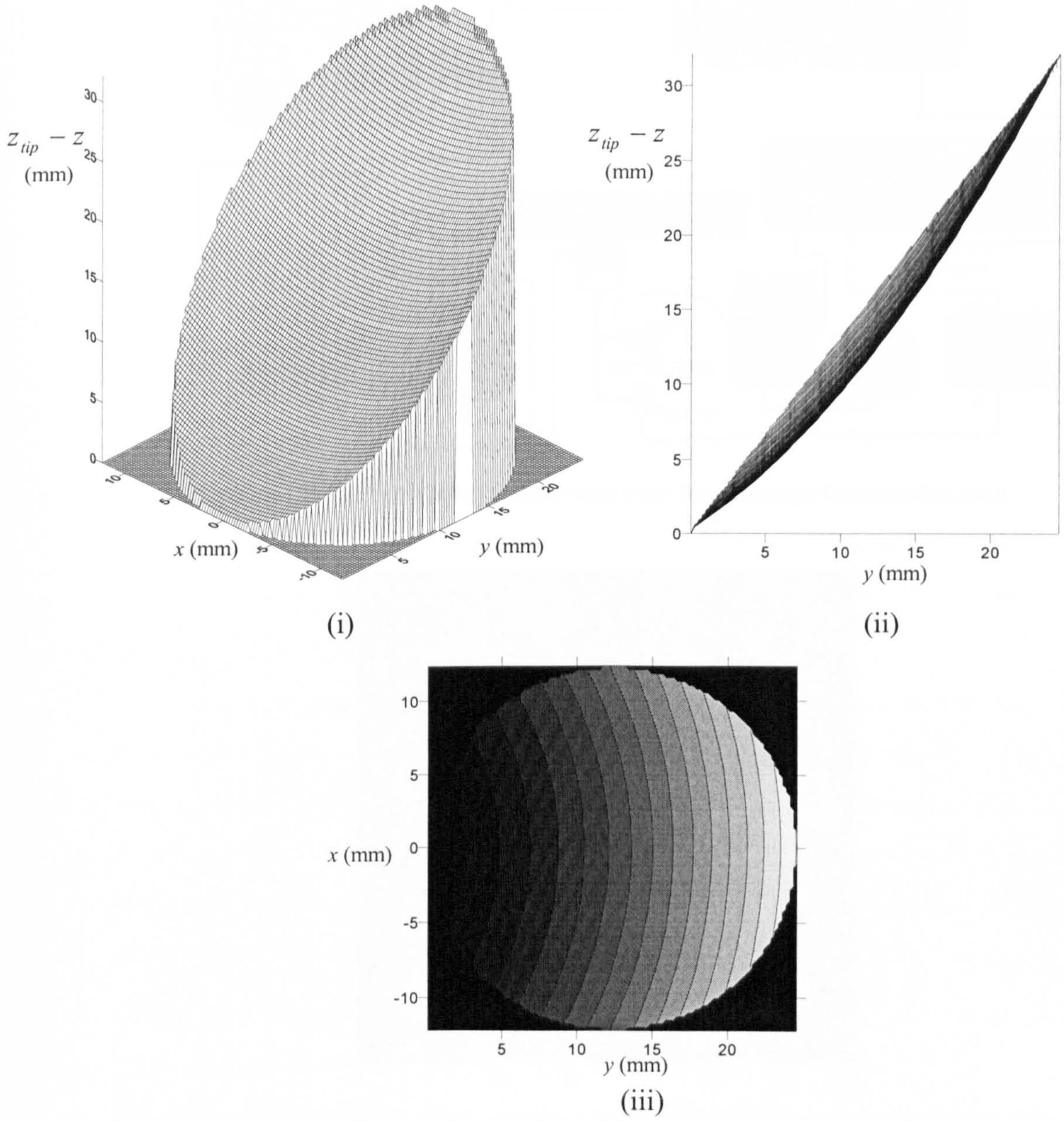

Figure 6.11: Mirror shape used to simulate the experimental device, (i) wireframe, (ii) cross section through the x =0 plane, (iii) contour plot.

The parabolic mirror focussed device has been used to produce a through-transmission image of a 25 mm square defect in a composite plate. The experimental apparatus used is shown in Figure 6.12. Figure 6.13 shows a scan of a composite plate,

using through transmission. The source used was the parabolic mirror described above, and the receiver was a 10 mm circular device. These where both moved with reference to the sample, at 0.3 mm steps.

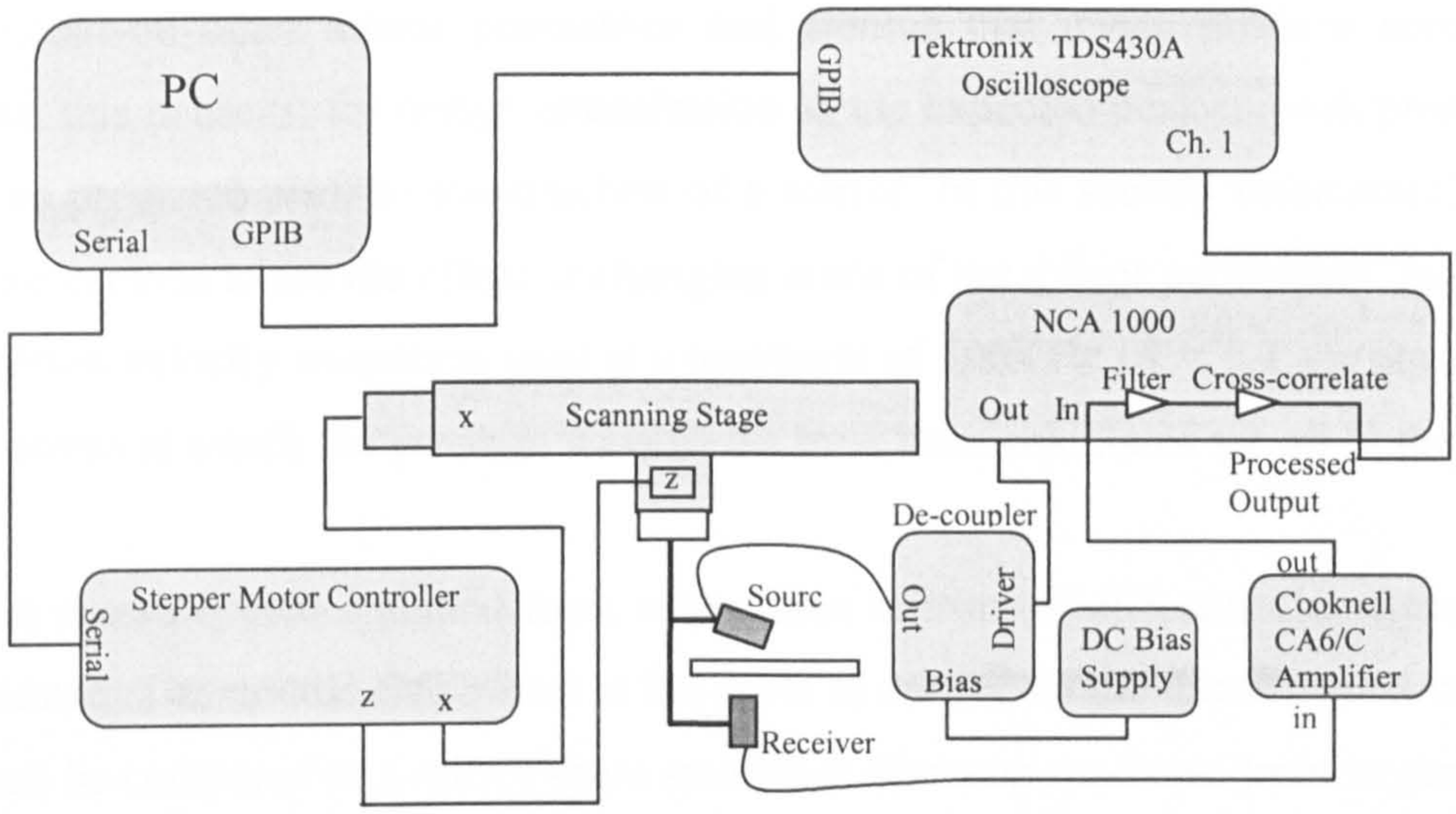

Figure 6.12: The experimental apparatus used for a through transmission scan

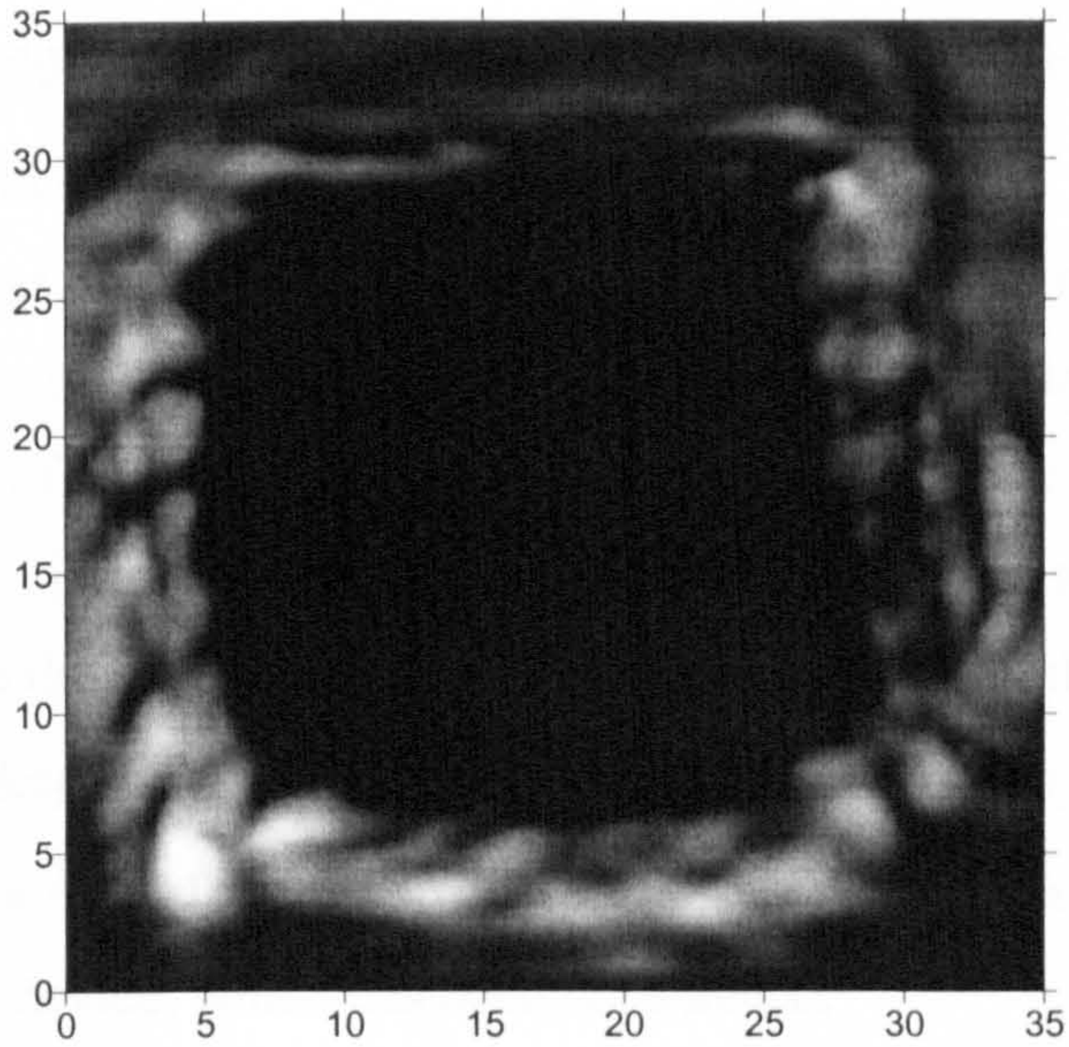

Figure 6.13: Through transmission scan of a composite plate (axes in mm) containing a 25 mm square defect

The drive signal used was a chirp, of 500 kHz centre frequency, 500 kHz bandwidth and 1000 μ sec duration. Upon reception, after amplification using the Cooknell charge amplifier, the NCA 1000 filtered and cross-correlated the signal.

6.5 The effect of changing the mirror parameters

It has been shown that the model presented here has provided simulations which correlate well to experimentally obtained results. As this is the case it is reasonable to use the model on other mirror geometries and assume that it can produce accurate predictions, this is useful for design optimisation as the expected peak-to-peak pressure field can be predicted prior to manufacture of a mirror. In this section some simulated results are produced to see the effect of changing some of the mirror parameters. In each case the piston velocity waveform used is a toneburst of 500KHz ($K = 0.2$ see equation 2.1). The points at which the pressure waveforms have been calculated are all in the $w = 0$ plane.

The pressure field obtained from using three mirrors of different diameters has been simulated. The middle size mirror is the same as earlier for the experimental work, and this can be compared to a mirror 4mm smaller in diameter, and one 4mm larger, for both of which the mirror diameter, d_{mirror}, is equal to the transducer diameter, d_{source}. The focal point of each mirror has been calculated such that the shape of smaller mirror is the same as the middle mirror for $y = 2$mm : d_{mirror} -2mm, and the larger mirror is also of the same profile but extends 2mm further in all directions.

The model has been written such that the pressure waveform can be predicted at various points, these points are described by the u, v, w coordinate system the origin of which is at the tip of the mirror most distant from the source. Here, however, the pressure is predicted in the $w = 0$ plane, and the values of u, and v have been translated so that in each of the three mirrors the origin is at the tip of the middle size device. The variable z_{off} is also kept fixed. The simulated pressure field from each of these mirrors is presented in Figure 6.14. The amplitude given in the wireframe plot is relative to the result for the present device, which has been normalised.

It can be seen from the peak-to-peak pressure fields presented in Figure 6.14, that the mirror diameter has a strong effect on the focal point size. Unsurprisingly, a larger diameter mirror causes a tightening the focal point, and a higher relative maximum peak-to-peak pressure.

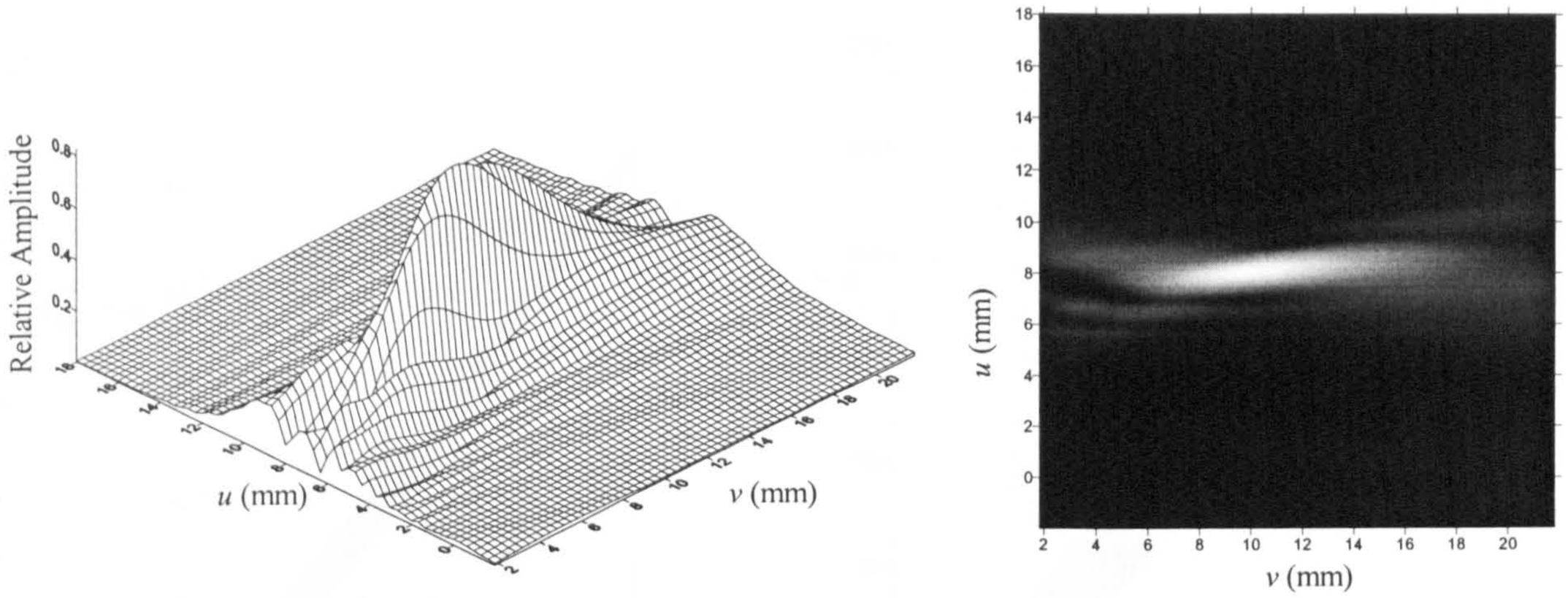

Smaller mirror: d_{mirror} =20.6mm

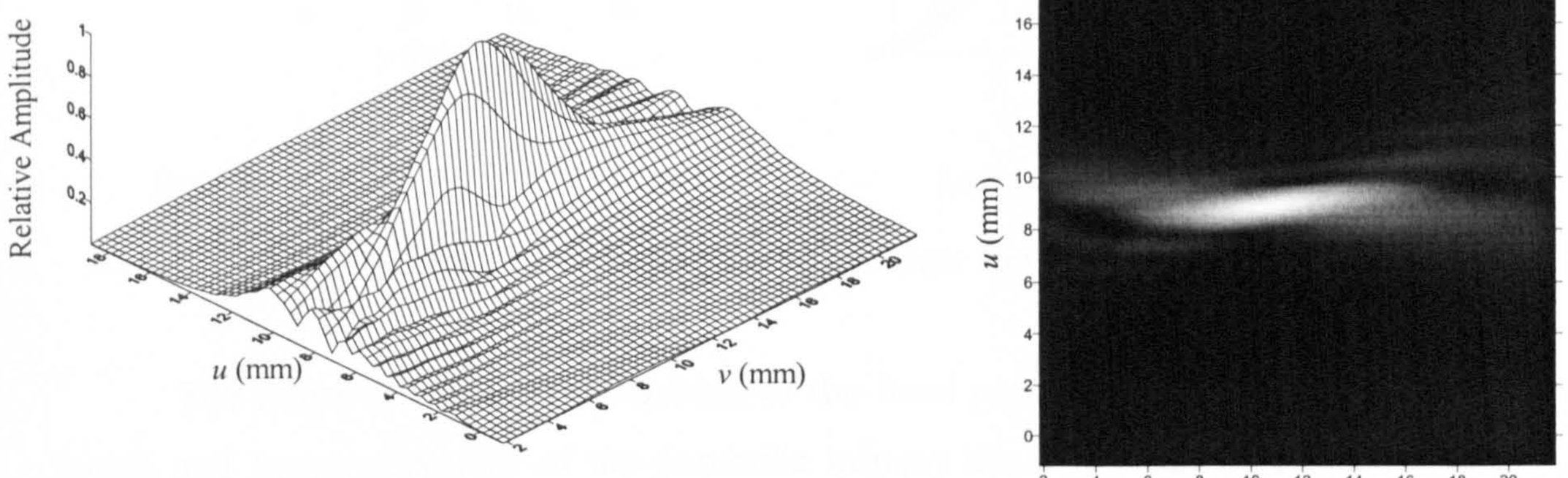

Present: d_{mirror} =24.6 mm

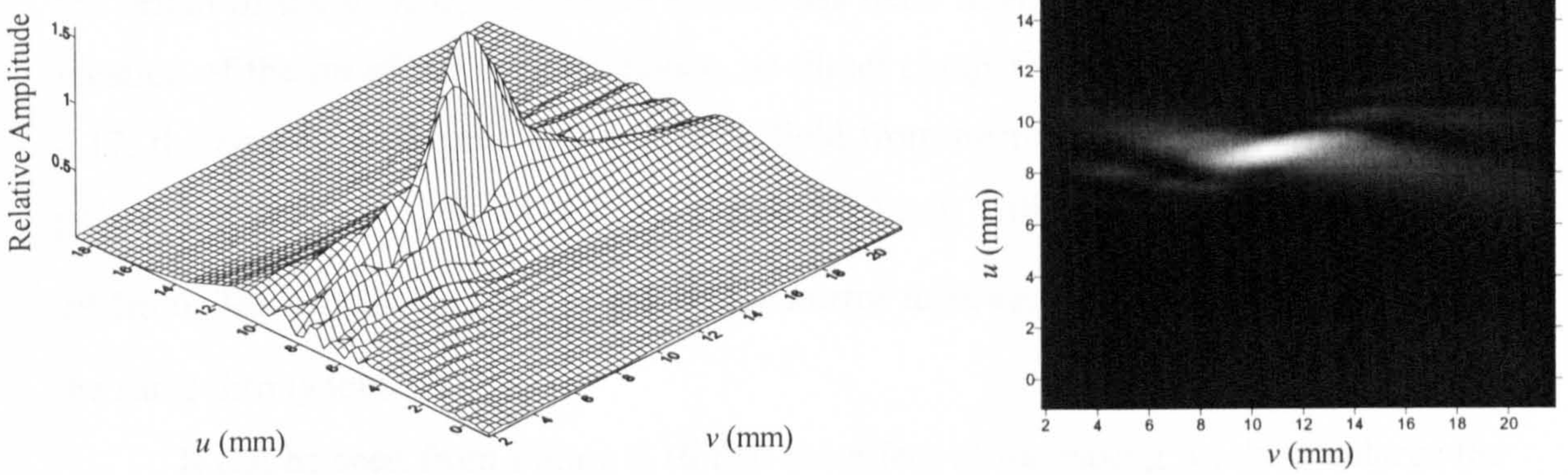

Larger mirror: d_{mirror} =28.6 mm

Figure 6.14: A comparison of the predicted pressure field of three different mirror diameters, displayed as wireframe and image plots

Figure 6.15 shows the cross-section through the $x = 0$ plane of the larger and smaller mirrors, and these can be compared to that for the middle size device shown earlier in Figure 6.9.

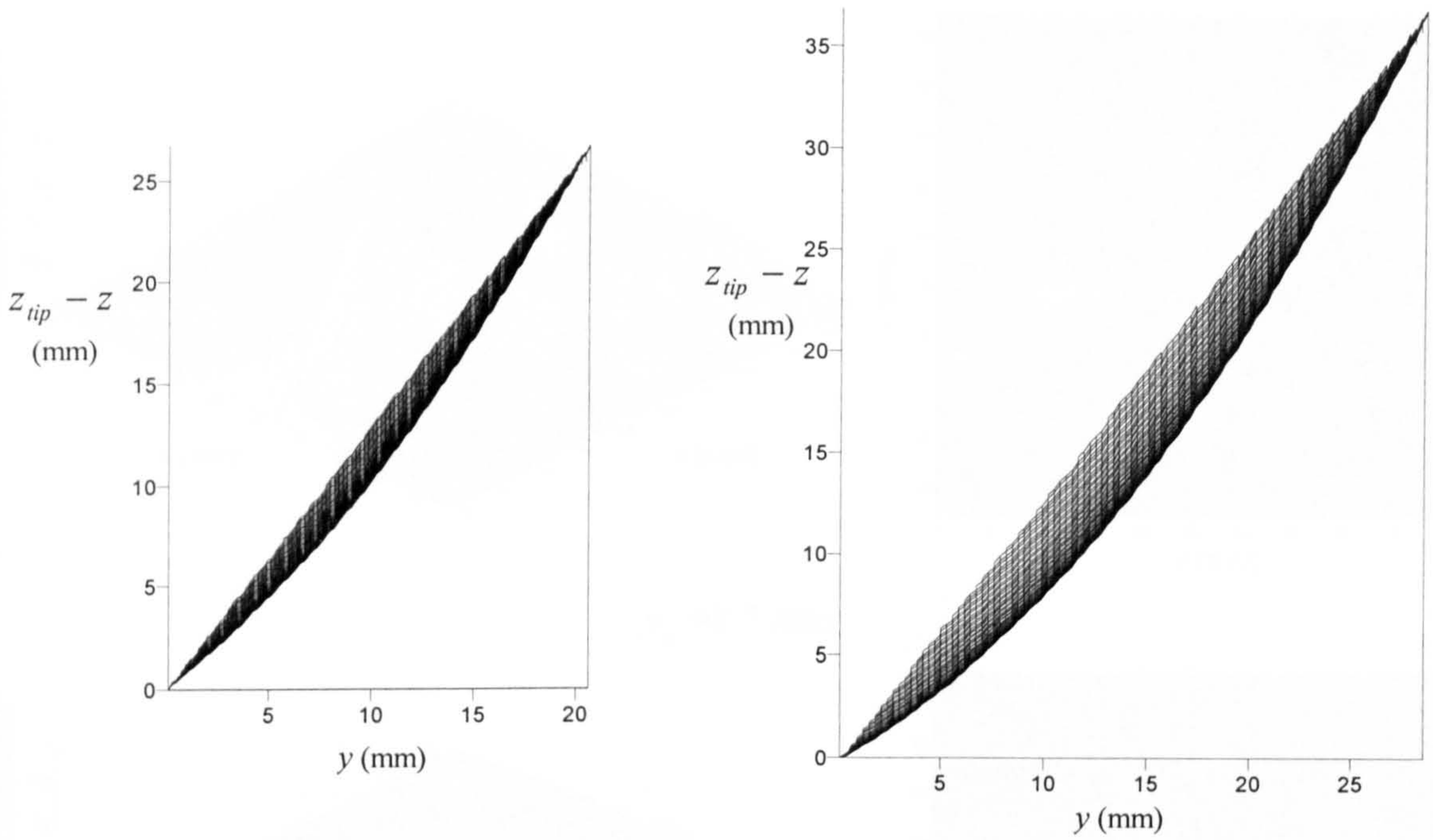

Smaller mirror: $d_{mirror} = 20.6$mm

Larger mirror: $d_{mirror} = 28.6$mm

Figure 6.15: The cross section of the larger and smaller mirrors

The effect of altering the location of the focal point (i.e. in changing the focal length and hence curvature of the parabolic mirror) has also been investigated. The predicted pressure fields from four simulated mirrors can be compared with that from the experimental device. In each case, d_{mirror}, d_{source} and z_{off} are as before, and again the origin of the *u*, *v*, *w*, coordinate system has been fixed for all of the mirrors at the location of the tip of the original device, so direct comparisons can be made. In Figure 6.17, the peak-to-peak pressure amplitude field from mirrors with three different focal points are shown, y_f is at 8.7, 12.7, and 16.7mm, with the value of z_f fixed at 29.5mm. The middle y_f value is that of the mirror used earlier, and the value of z_f are the same throughout.

It can be seen from Figure 6.16 that the effect of increasing y_f is to enlarge the focal point in both width and length, as the shorter focal length has a tighter focus as would be expected. Figure 6.17, shows the cross section of the mirrors with a value of y_f = 8.7 and 16.7 mm, through the x = 0 plane, these can be compared to that of the experimental device given in Figure 6.9. It can be seen that the effect of a decreasing value of y_f is that the mirror becomes more concave.

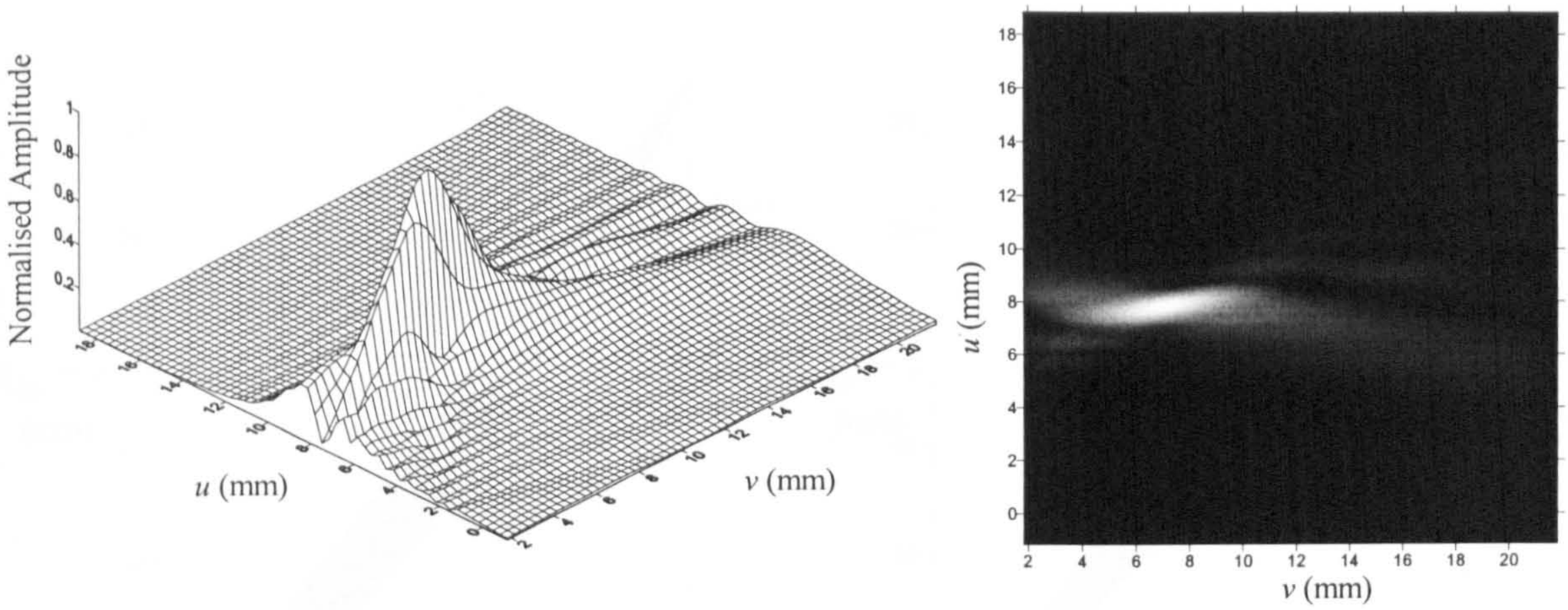

y_f =8.7 mm

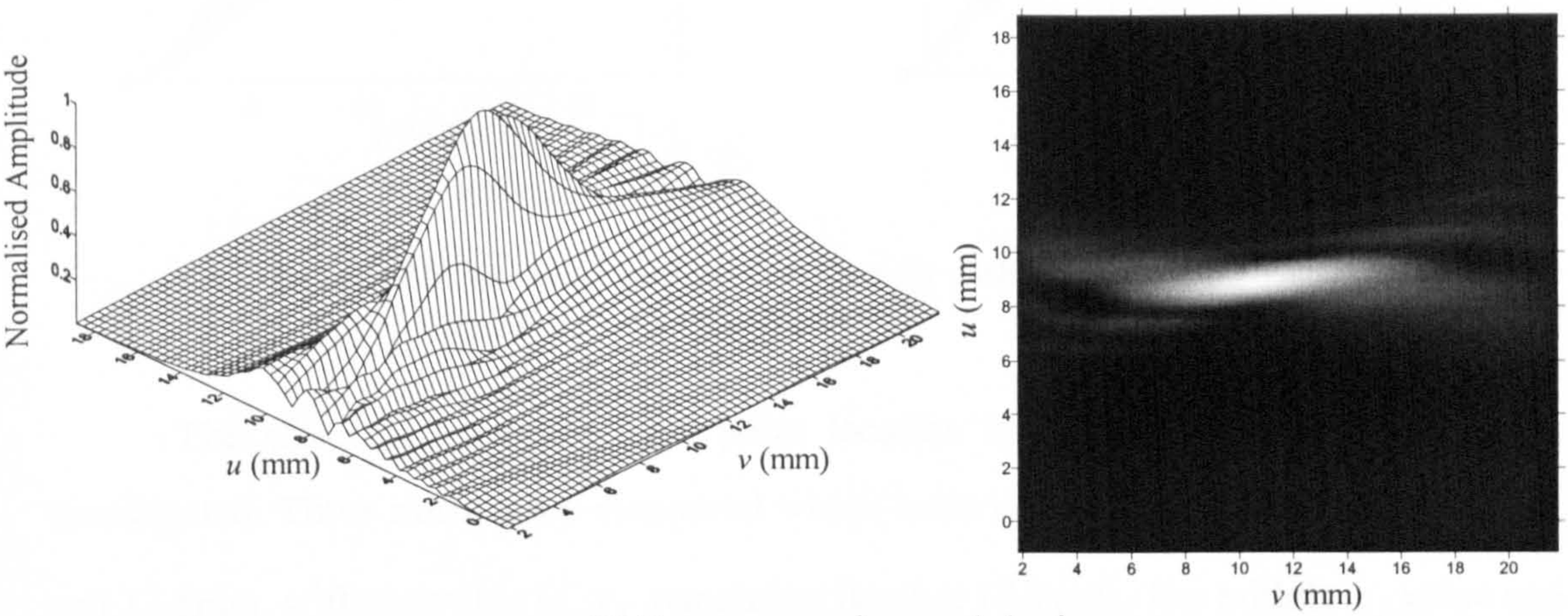

y_f =12.7 mm, experimental device

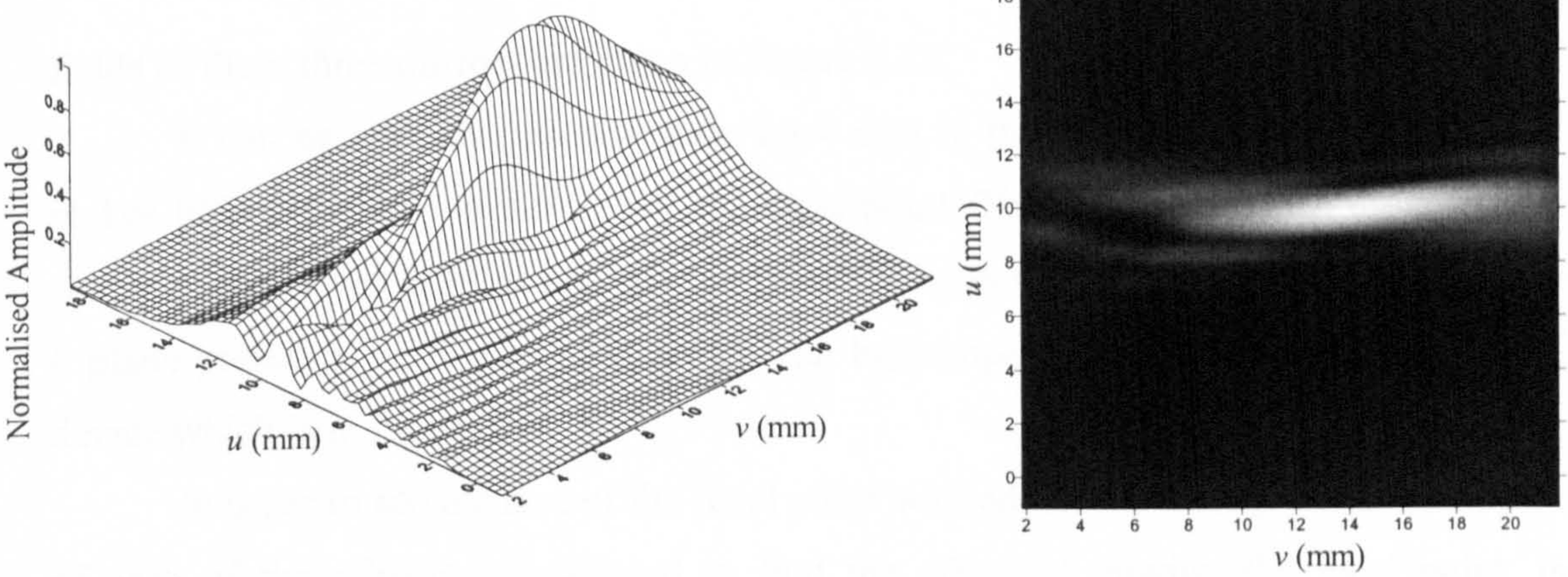

y_f =16.7 mm

Figure 6.16: A comparison of the predicted pressure field from three mirrors with focal points located at different y_f values, displayed as wireframe and image plots

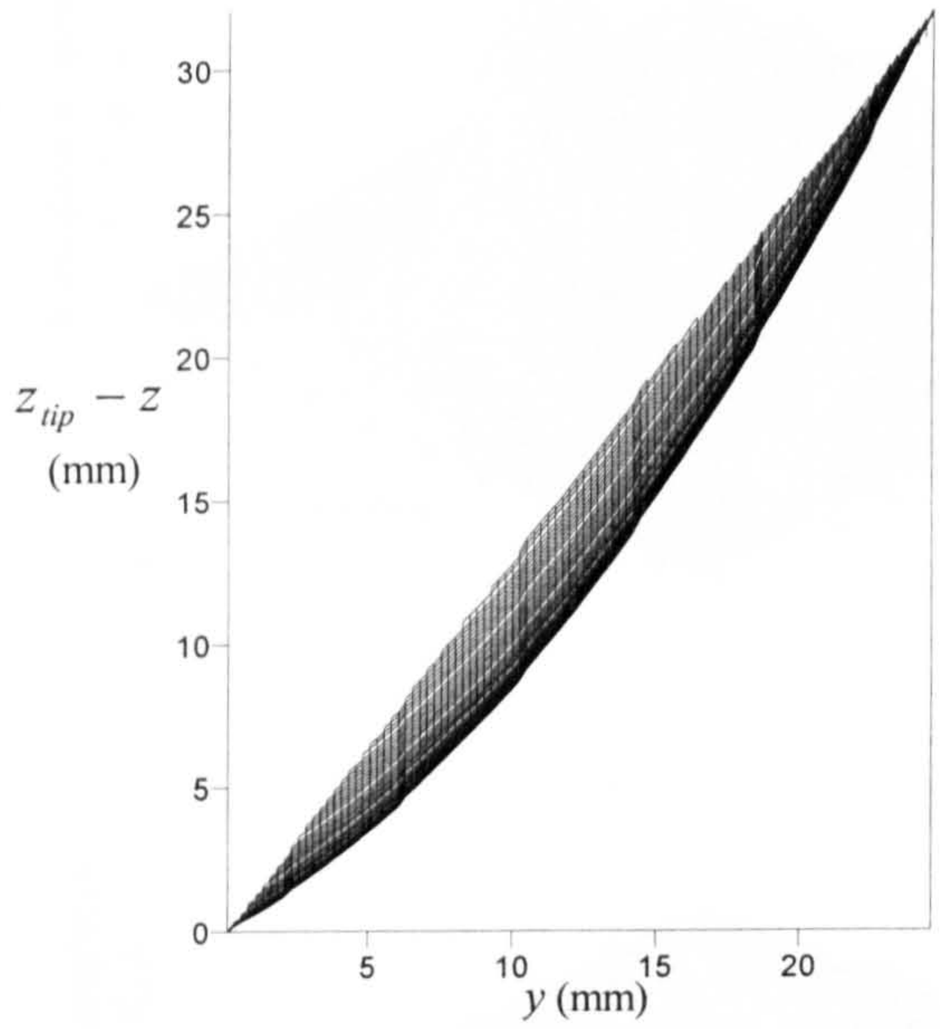

y_f =8.7 mm

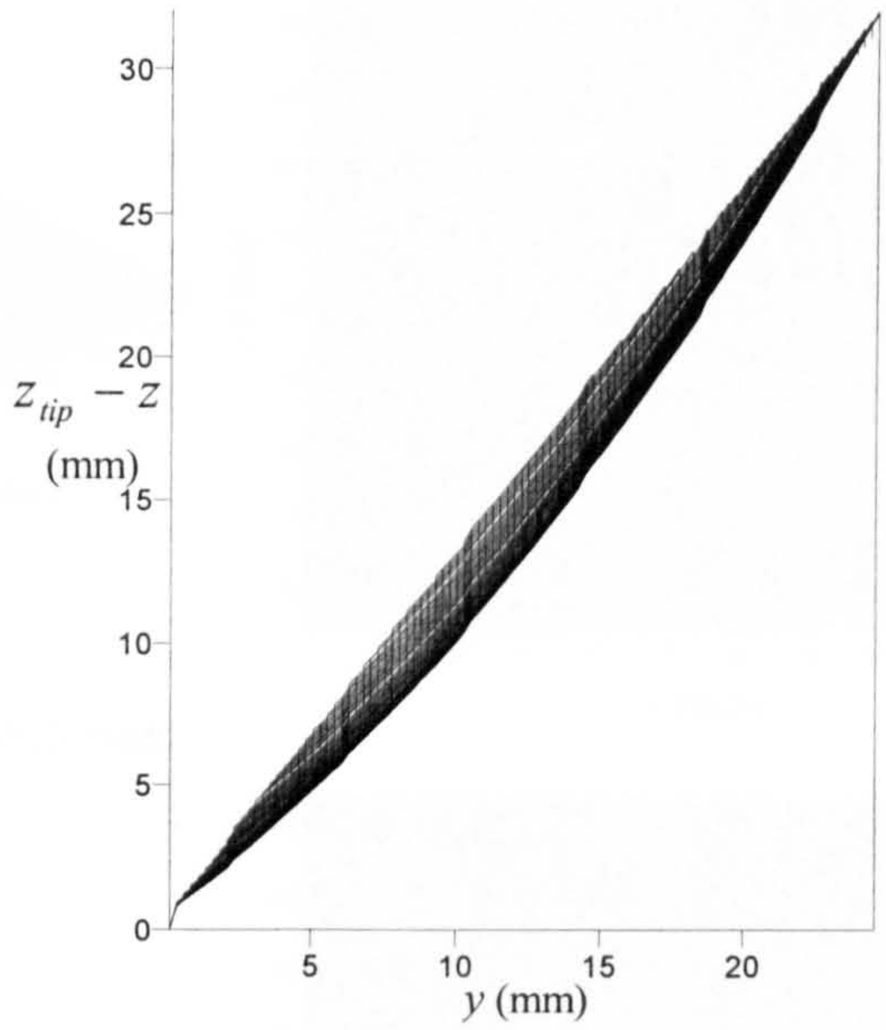

y_f =16.7 mm

Figure 6.17: The cross section of two mirror with a different y_f value

The effect of a change focal point location in the z direction has also been investigated. Three mirrors are compared which have values of z_f equal to 25.5, 29.5, and 33.5mm, with the value of y_f remaining fixed at 12.7mm. The middle z_f value and the value of y_f are the same as that for the experimental device. The predicted pressure fields of these three mirrors are given in Figure 6.18.

It can be seen that an alteration by 4 mm in the z direction of the focal point makes little difference to the size of the focal point. The degree to which the mirror is concave also varies little, as can be seen from the cross section of each mirror in the x = 0 plane presented in Figure 6.19, which can be compared to that of the experimental device which is in Figure 6.9.

In order to see the size of the focal point with additional clarity, the contour plot of each of the mirrors investigated to find the effect of moving the focal point, is presented in Figure 6.20. The outer contour line is at 50% of the maximum, so indicating the size of the full width half maximum (FWHM), and the inner one at 95% to locate the focal point.

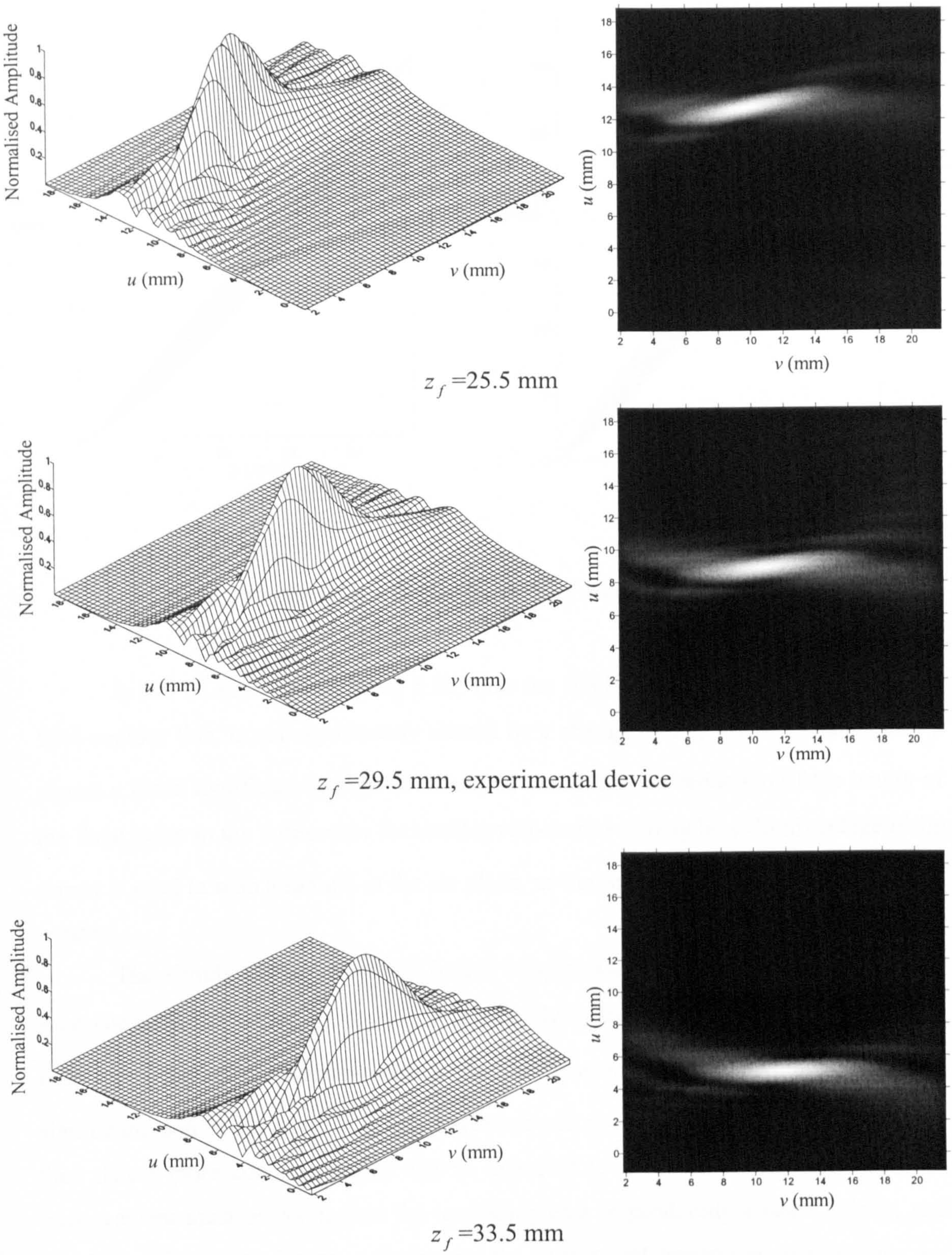

z_f =25.5 mm

z_f =29.5 mm, experimental device

z_f =33.5 mm

Figure 6.18: A comparison of the predicted pressure field from three mirrors with focal points located at different z_f values, displayed as wireframe and image plots

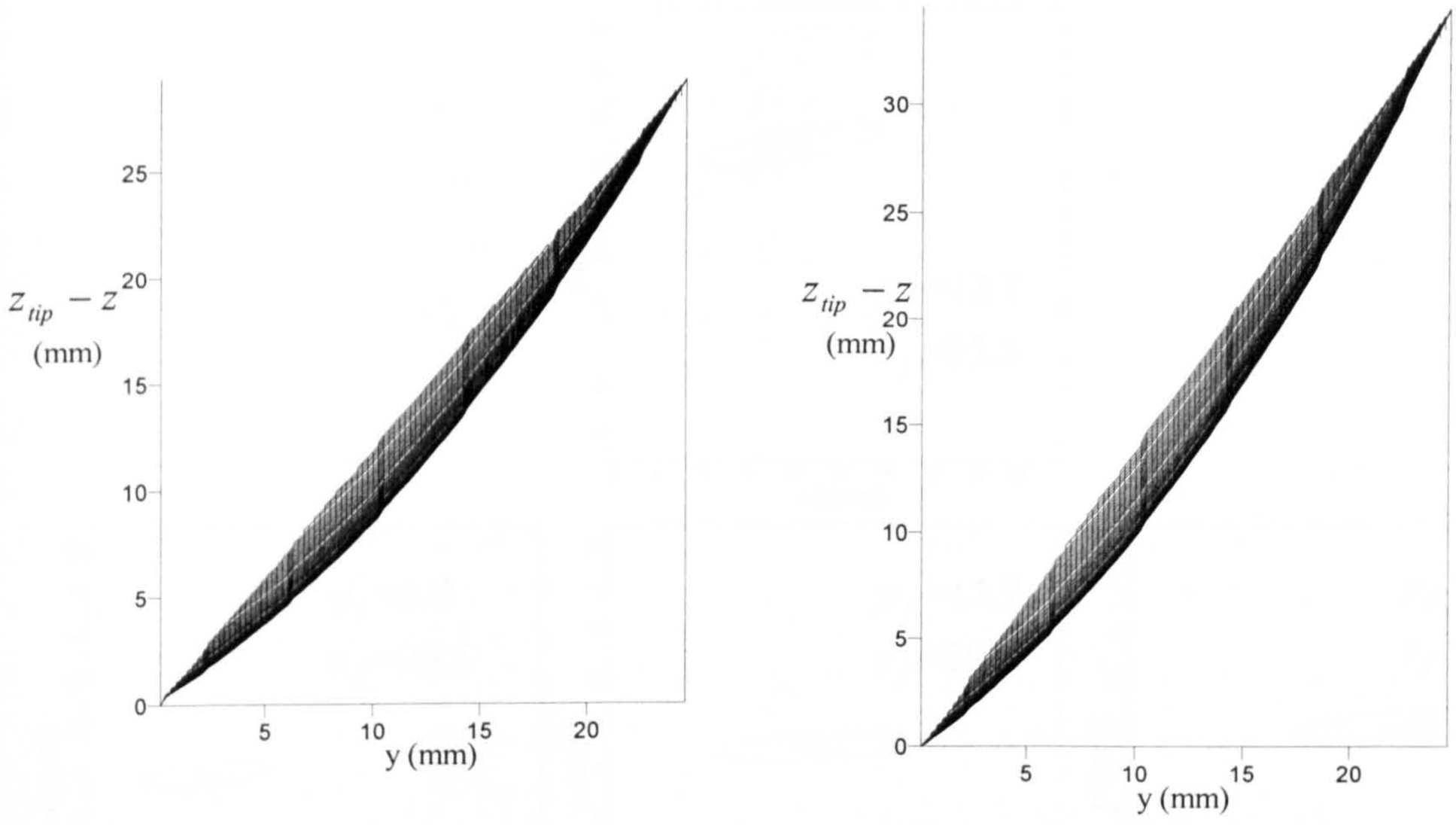

z_f =25.5mm z_f =33.5mm

Figure 6.19: The cross section of two mirrors with a different z_f value

It can be seen from Figure 6.20, that the FWHM, corresponding to the outer 50% contour line, is not significantly altered by a change in z_f, whilst a change in y_f causes a more significant change. It should be noted that the reduction of the length of the focal point in the *y* direction for smaller values of y_f, may be a disadvantage if the mirror is used to scan a sample in the *uw* plane, as the accuracy of alignment required is greater.

The simulation results given in this chapter show that the focal point can be sharpened, by decreasing y_f or more dramatically by increasing the mirror diameter. In both cases the mirror becomes more concave. The effect of changing z_f was not significant, and in this case the mirror curvature was not greatly changed. It would seem than that a more concave mirror can be expected to give a better focal point. This improvement must be set against the increasing cost of producing a larger mirror, and the difficulties of producing a casing for the mirror and transducer, which does not impede usage when y_f is reduced.

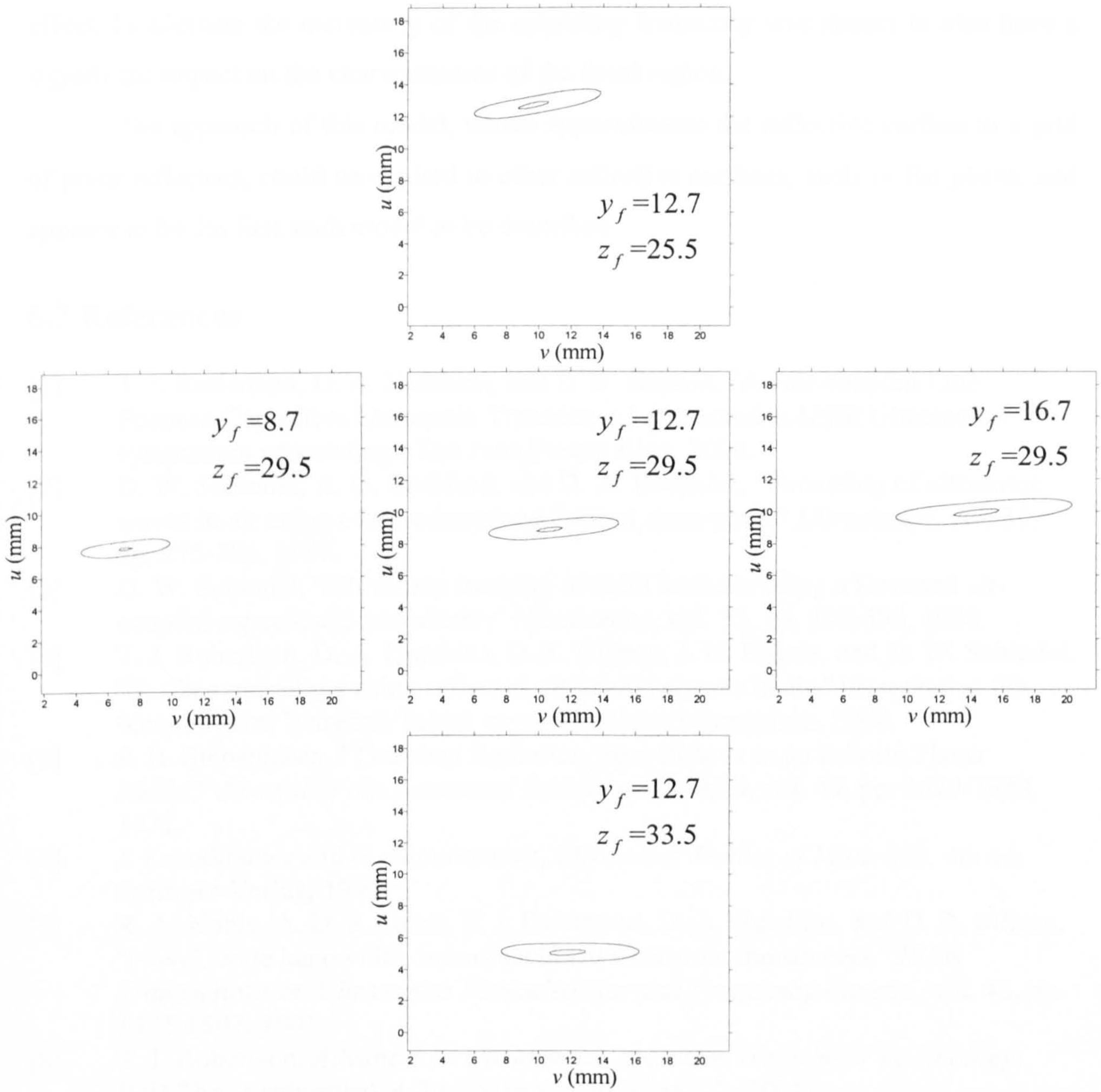

Figure 6.20: Contour plots of the focal point for five mirrors defined by different focal points

6.6 Conclusions

A model has been produced which predicts the emerging pressure field from a parabolic mirror. A comparison of the predicted and experimental results, show a good correlation.

The model has been used to investigate the effect on the focal point size of altering different mirror geometries. It was found that improvements can be made, by moving the focal point, and increasing the mirror diameter was found to have a large

effect. In addition the increasing of the operating frequency was shown to also have a significant impact on the characteristics of the focal region.

The approach of this model, which approximates the reflective surface to a grid of point reflectors, could be applied to other reflective surfaces, such as flat plates, and appears to be the first such model to be described.

6.7 References

[1] T. J. Robertson, D. A. Hutchins, and D. R. Billson, "An air-coupled Line Focused Capacitive Ultrasonic Transducer," presented at IEEE Ultrasonics symposium proceedings, San Juan,Puerto Rico, 2000.

[2] D. W. Schindel, A. G. Bashford, and D. A. Hutchins, "Focussing of ultrasonic waves in air using a micromachined Fresnel zone-plate," *Ultrasonics*, vol. 35, pp. 275-285, 1997.

[3] D. W. Schindel, "Ultrasonic imaging of solid surfaces using a focussed air-coupled capacitance transducer," *Ultrasonics*, vol. 35, pp. 587-594, 1998.

[4] T. J. Robertson, D. A. Hutchins, D. R. Billson, J. H. Rakels, and D. W. Schindel, "Surface metrology using reflected ultrasonic signals in air," presented at 6th biennial joint Warwick/Tokyo nanotechnology symposium, 2000.

[5] P. R. Stepanishen, "Transient Radiation from Pistons in an Infinite Planar Baffle," *Journal of the Acoustical Society of America*, vol. 49, pp. 1629-1638, 1971.

[6] J. Krautkrämer and H. Krautkrämer, *Ultrasonic Testing of Materials*, 4th ed: Springer-Verlag, 1990.

[7] R. A. Noble, A. D. R. Jones, T. J. Robertson, D. A. Hutchins, and D. R. Billson, "Novel, wide bandwidth, micromachined ultrasonic transducers," *IEEE Transactions on Ultrasonics Ferroelectrics and Frequency Control*, vol. 48, pp. 1495-1507, 2001.

[8] T. J. Robertson, *Advances in Ultrasonic Capacitive Transducer Technology*: PhD Thesis submitted at the University of Warwick, 2001.

Chapter 7: Imaging with ultrasonic capacitive arrays

7.1 Introduction

In Chapter 4 the design and manufacture of capacitive ultrasonic arrays for use in air-coupled work was described. These arrays were tested as phased sources and shown to correlate well with the theory, developed in Chapter 3. In this Chapter similar devices will be used as receivers in order to produce images. This will be done in three different ways: through-transmission using a large planar source, using a combined phased source and receiver, and finally using signal processing techniques (SAFT (Synthetic Aperture Focussing Technique) and ellipse crossing).

7.2 Cross Coupling

In order to use an array as a receiver, it is first necessary to establish that each element acts independently. A large source, with a diameter of 50 mm, was thus positioned at an angle to a line array, and a waveform was recorded from each element in turn. The large source was driven by a Panametrics PR5055, which outputed a short voltage pulse. This drive signal resulted in a broadband signal, centred at approximately 500 kHz, to be emitted from the polymer-membrane capacitive source. The experimental apparatus used is shown in Figure 7.1. It can be seen that only one wire connected the array to the Cooknell charge amplifier, as in this experiment the waveform was recorded from one element at a time. The array used was a 16 element line array with each element measuring 1.1 mm × 10 mm on a pitch of 1.45 mm. The polymer membrane was held in place using a brass front plate with a chamfered rectangular aperture measuring 36 mm × 10 mm. The source was positioned at an angle of approximately 45° to the receiver array.

The signal received on each element is displayed in Figure 7.2. It can be seen that each element received a signal at a different time, as would be expected from the differences in path lengths. It can also be seen that there is a second feature, the delay of this was shorter for element 1 than for element 16. This indicates that a reflection was probably present.

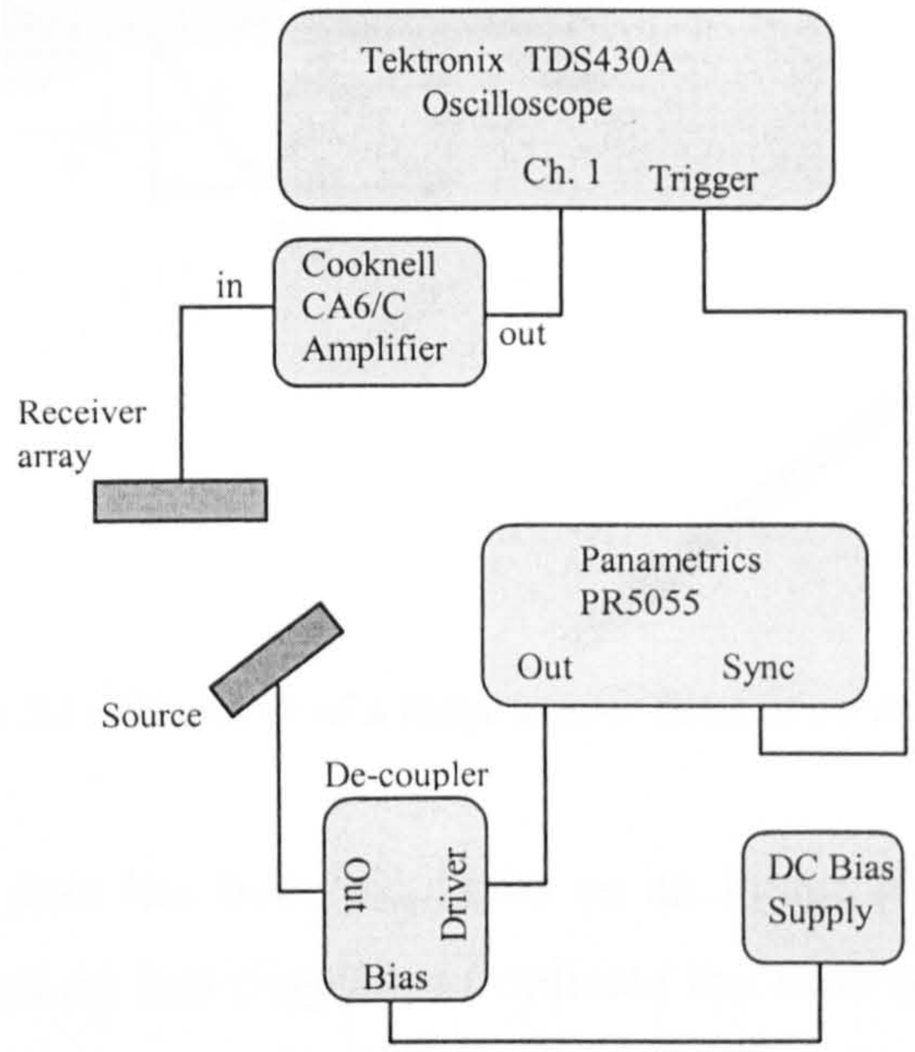

Figure 7.1: Experimental apparatus used to establish that each element acts independently

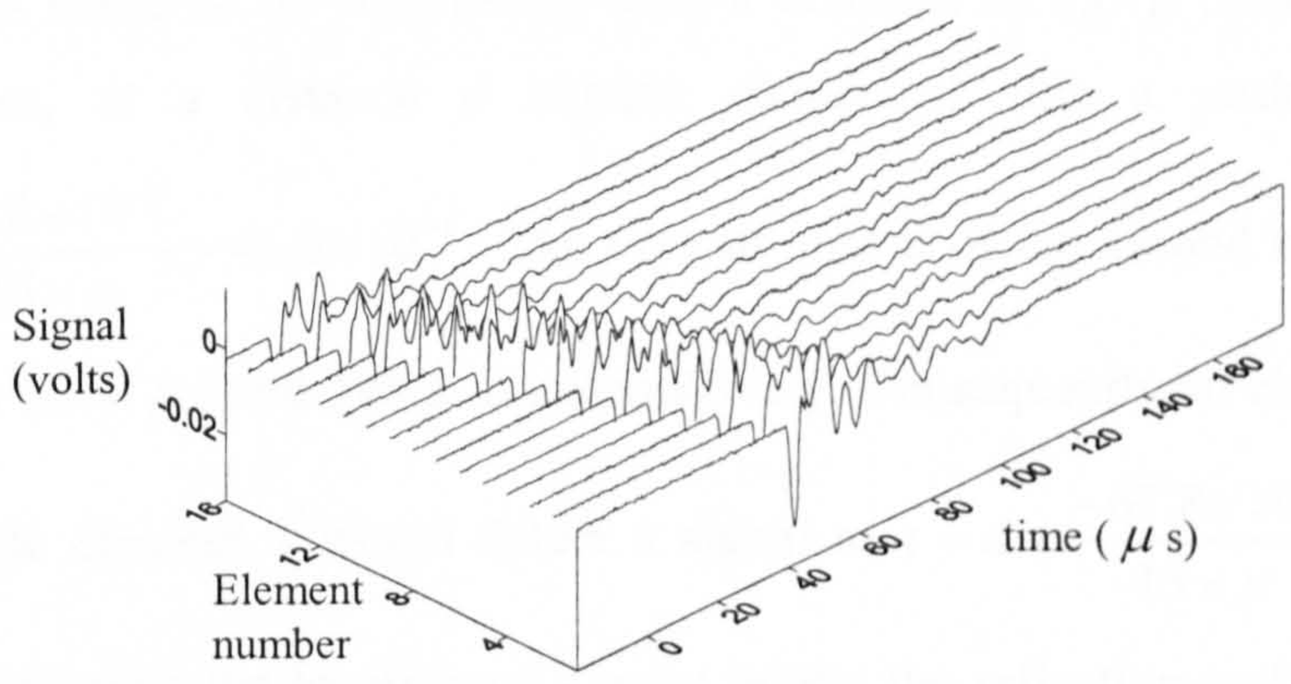

Figure 7.2: The received waveform from each element, numbered from 1 to 16

Figure 7.3 shows a diagram of the set up, showing the relevant distances required to analyse the source of the echo. The relative arrival times of the main peaks at elements 1 and 16 are 41.8 μs and –5.0 μs respectively, a difference of 46.8 μs. The distance between the centres of these two elements is $15 \times p$, where p is the pitch, or 21.75 mm. Consequently the angle of the source relative to the receiver, α, can be found by considering length b. Firstly using geometry, $b = 15 \times p \times \sin(\alpha)$, and secondly using the difference in time of flight to calculate the difference in path length, $b = 46.8 \times 10^{-6} \times c$, where c is the speed of sound in air (343ms^{-1}). Consequently $\alpha = 47.6°$, which agrees well with the intended 45°.

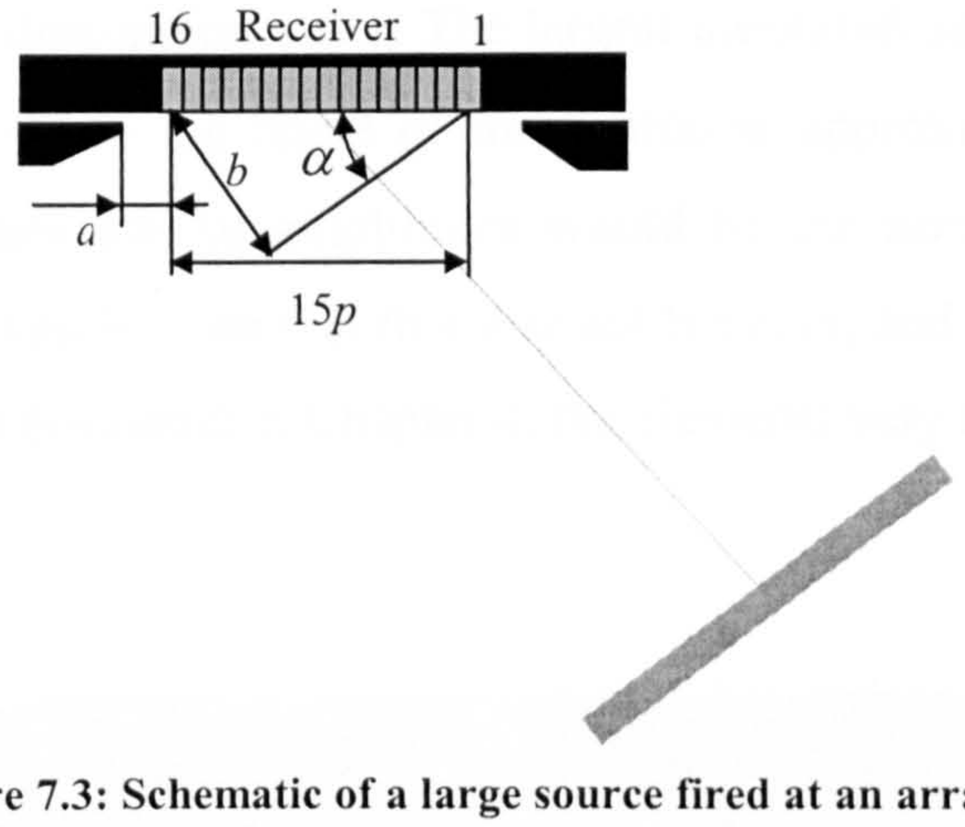

Figure 7.3: Schematic of a large source fired at an array receiver

The received signal data has been displayed as an image plot in Figure 7.4. Straight lines have been drawn on this diagram to indicate the time of arrival of both the main pulse and the reflection. These lines have been extended so that they meet at time t_1, a distance d from element 1. In order to find t_1 and d_1, firstly the line connecting the main peaks needs to be considered, over a distance of $15\times p$ these differ in time by $46.8\,\mu$s, so, at a distance d outside element 1 this a peak would occur at $t = d\times\frac{46.8\times10^{-6}}{15\times p}+41.8\times10^{-6}$. The time of arrival of the second ripple at elements 1 and 16 are 80.3 μs and 148.1 μs respectively. Consequently an element at a distance of d outside element 1 would detect a signal at $t = d\times\frac{-67.8\times10^{-6}}{15\times p}+80.3\times10^{-6}$. In order to determine the location of a point where the reflection and main signal would occur at the same time, and hence be the point of reflection, these two simultaneous equations need to be solved. This can be done to give a time of $t_1 = 58.2$ μs, and $d_1 =$ 7.3 mm. The distance a as labelled in Figure 7.3, is $\frac{36-15.p}{2}$ mm, as the aperture is 36 mm wide which equates to a = 7.1 mm. Consequently, it was concluded that the reflection causing the secondary ripple occurs at the edge of the aperture of the brass plate used to secure the membrane in place.

The peak-to-peak amplitude measured by each element is given in Figure 7.5. In the first case this amplitude was taken from the data set presented above, in the second the array was rotated 180° around the axis, so that element 16 was the most distant. For ease of comparison the second set of measured amplitudes has be displayed from

elements 16 to 1 in descending order. The largest measured amplitude has been used to normalise the data. With the angle of the source at approximately 45°, it would be expected that the two sets of amplitudes would be the same, if each element were equally sensitive. It can be seen that this was not the case, and as with using the array as a source, which was discussed in Chapter 4, the elements vary in sensitivity.

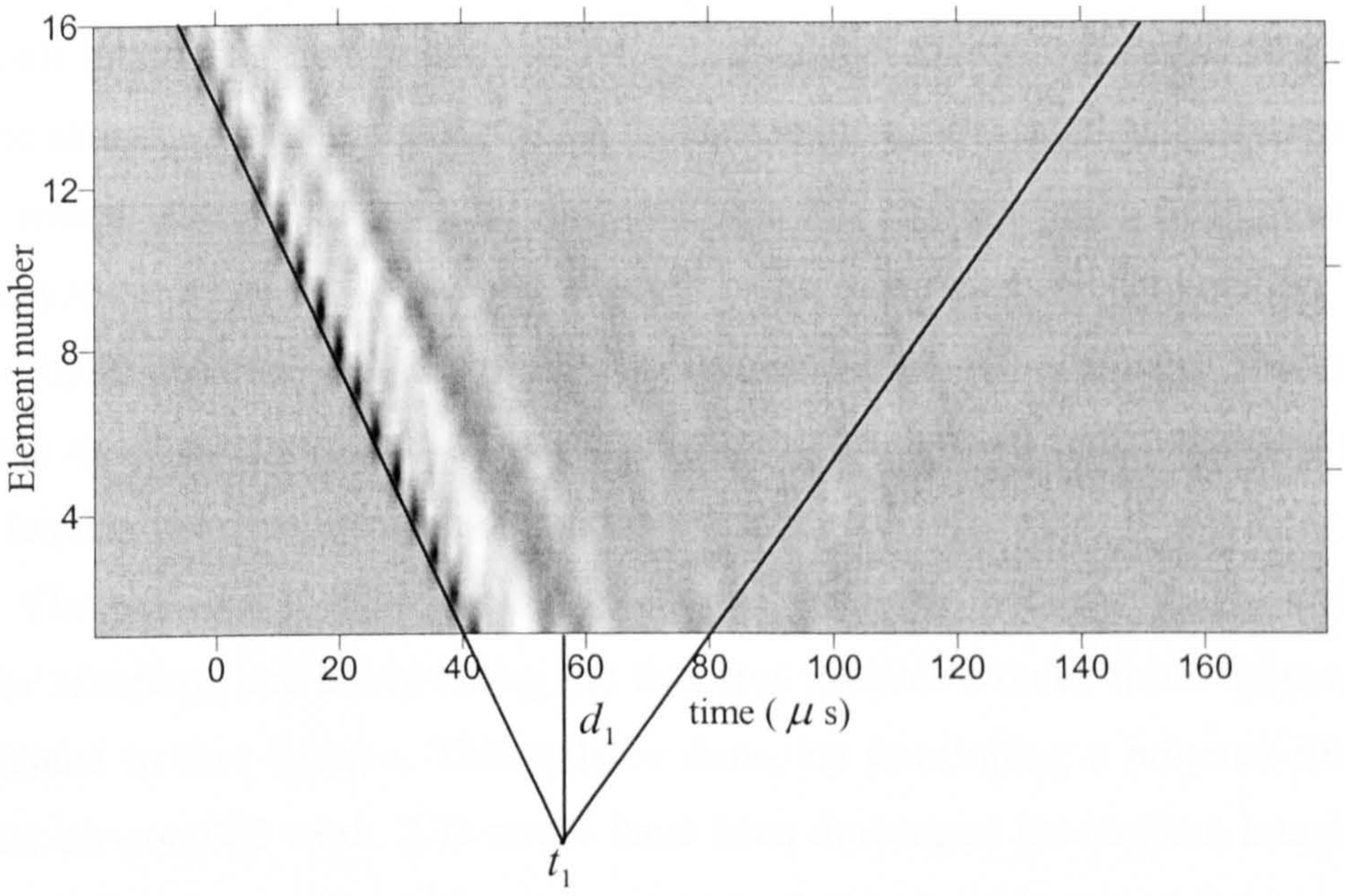

Figure 7.4: Analysing the origin of the secondary waveform

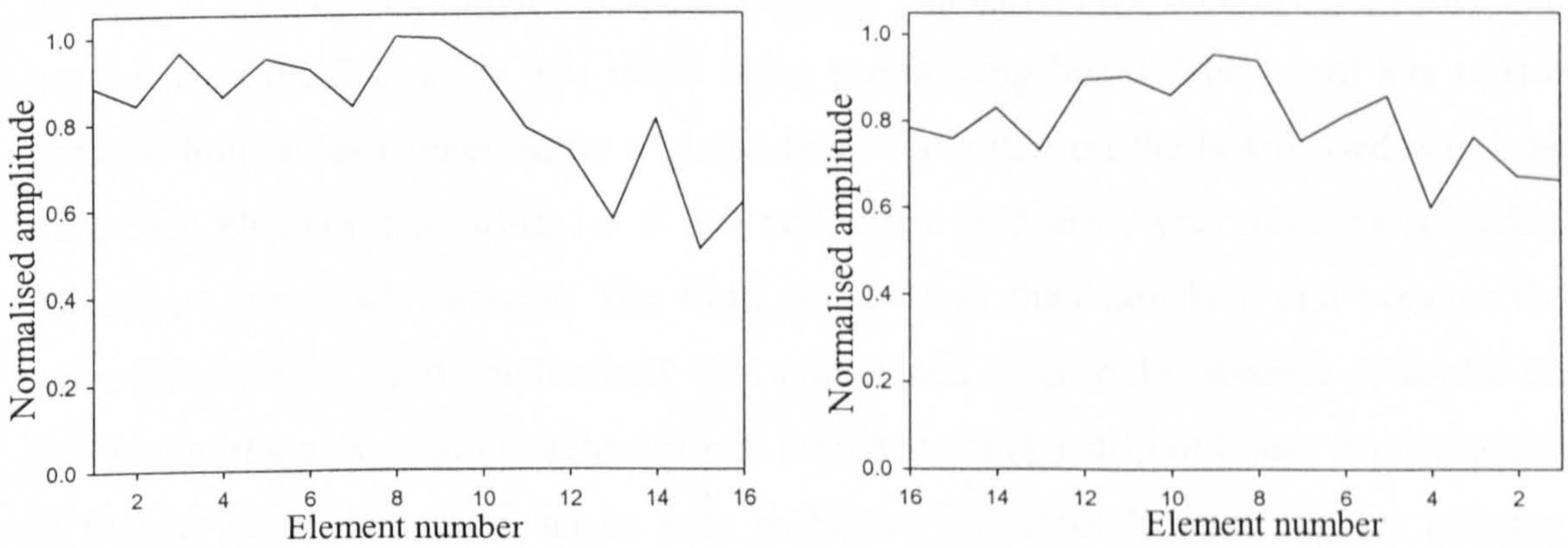

Figure 7.5: The peak-to-peak amplitude measured by each element, (i) for the case described above, and (ii) when the array is rotated about the axis by 180°

In all other array work presented in this thesis, the brass plate has not been used to position the membrane in order to minimise the problem of unwanted reflections, and

to simplify construction. It can, however, be concluded from this experiment that each element acts independently. Consequently capacitive arrays manufactured in this manner can be used for imaging.

7.3 Through-thickness imaging of solids using a 2-D array receiver

In Chapter 6, a through-thickness image was presented of a defect in a composite plate. This was achieved by scanning the source and receiver transducers over the sample. A disadvantage of this method is the time it requires. A system already exists which allows imaging through the use of an immersion technique termed acoustography. Here, a large piezoelectric source is used in conjunction with an acousto-optic detector, and the result is a near-real-time visual image. This technique has been used to investigate fatigue-after-impact damage in composites, by applying cyclic loading to an impact damaged sample [1, 2].

The possibility of producing air-coupled through-thickness images without the need for scanning, and hence taking the first step towards a much faster system, will be investigated in this Section. This will be done, by developing a polymer-filmed 2-D array for air-coupled work. 2-D arrays have been developed for medical imaging using both piezoelectric and capacitive micromachined elements; however little air-coupled work has been carried out [3, 4].

In this section the manufacture of a 2-D array will be described. This array will be used to produce a through-thickness image of a defect within a composite plate. The backplate of the 2-D array was made using prototyping board. The board has square pads on both sides connected by a plated hole. The pitch on the board used was 2.54 mm, each element measuring 1.9 × 1.9 mm. An 8 × 8 array was made by soldering connectors onto each element. The front surface was then polished, and because the holes were plated good conductivity was maintained despite the absence of solder on the front surface. An earth attachment was prepared using a strip of brass. A photograph of the device at this stage can be seen in Figure 7.6. Prior to attaching the polymer membrane the unused pads were connected together and to the earth by a coating of conductive paint. The membrane was then attached to the earthed part of the backplate again using conductive paint.

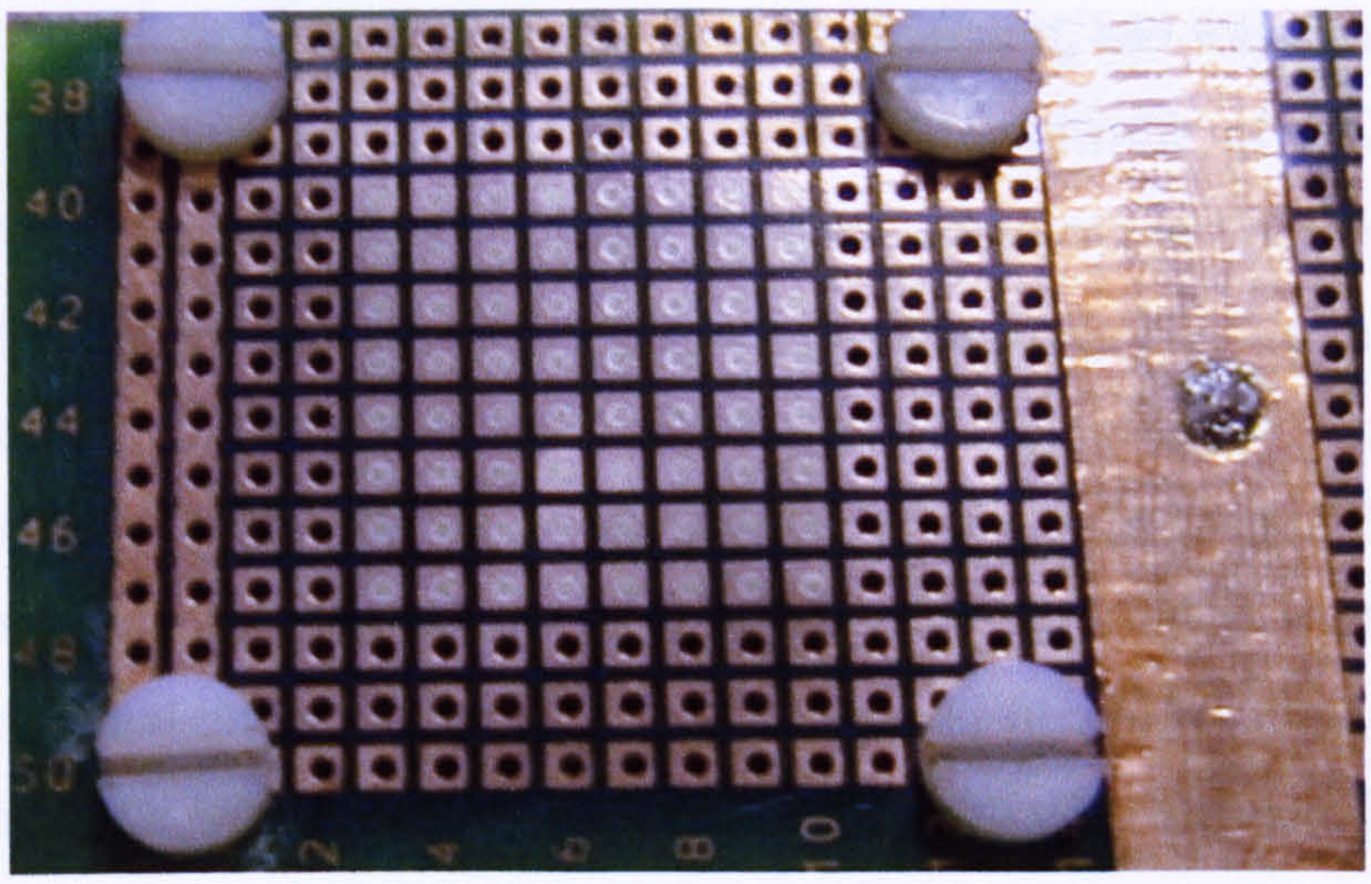

Figure 7.6: The backplate of a 2-D array

For the purpose of measuring waveforms from each element, a 9-way plug was used. The centre pin was connected to the Cooknell charge amplifier, and the surrounding 8 were earthed to reduce electrical noise. The apparatus used to take a Through-thickness image of a defect within a composite plate is shown in Figure 7.7. The composite plate used was the same as that scanned using the device focussed by a parabolic mirror, which has been presented in Chapter 6, Figure 6.12, it has a known defect of 25 mm square.

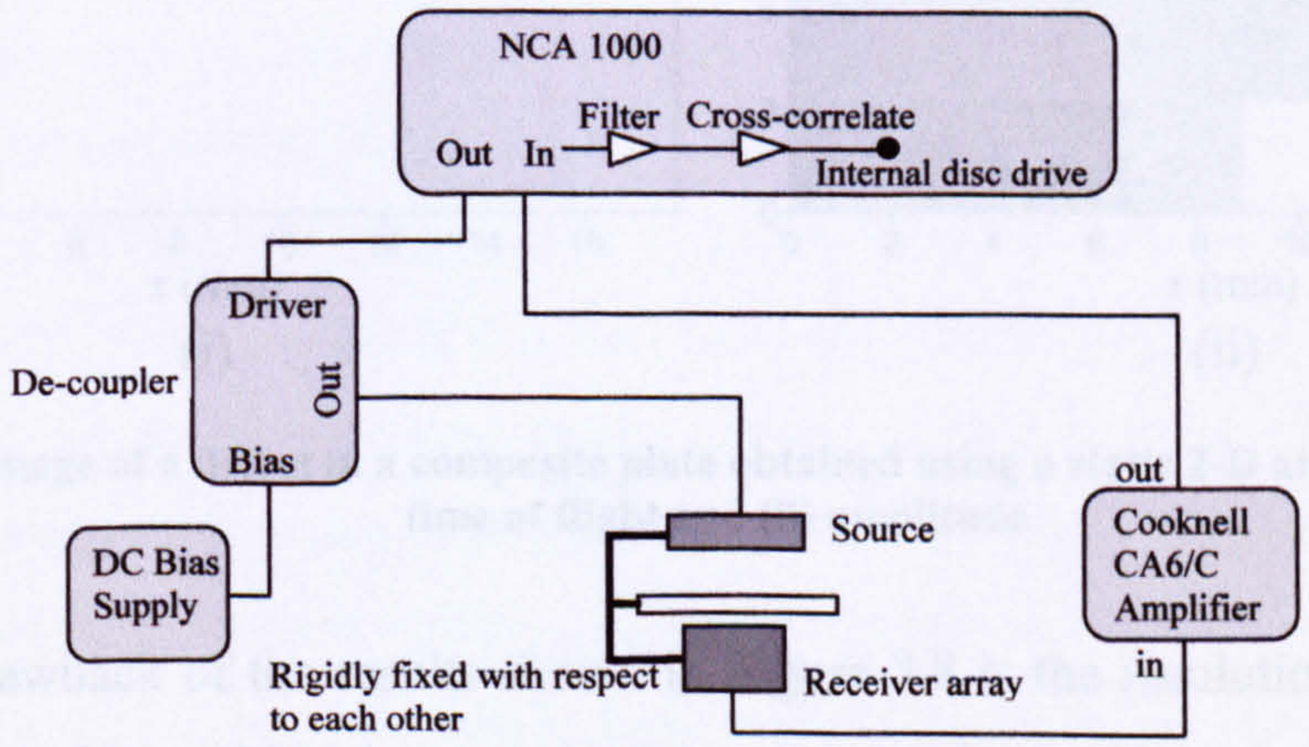

Figure 7.7: The apparatus used to create a through-thickness image using a 2-D array

It can be seen from Figure 7.7 that both the large source, sample and array remained static. The source was positioned at a distance of 20 mm from the sample, and the array at 10 mm, the composite plate was arranged so that a part of the defect covered

one corner of the array. The source had a diameter of 50 mm, and was driven by a chirp drive signal, with a centre frequency of 500 kHz, a bandwidth of 500 kHz, and a duration of 1000 μs. After amplification, the received signal was filtered and cross-correlated within the NCA 1000, and the result for each element recorded on disk.

The results of this experiment are shown in Figure 7.8. Two images are presented. The first Figure 7.8 (i) is the absolute difference in the time of flight from the average, where it can be seen that there is a defect covering a corner of the array as expected. The second image (Figure 7.8 (ii)) used the maximum amplitude of the same data. It is clear that a better image was obtained using the time of flight than using the maximum amplitude data. This was because when receiving the same pressure waveform each element can be expected to register a different amplitude, as was seen in Figure 7.5. It would be possible, in future work, to correct for this.

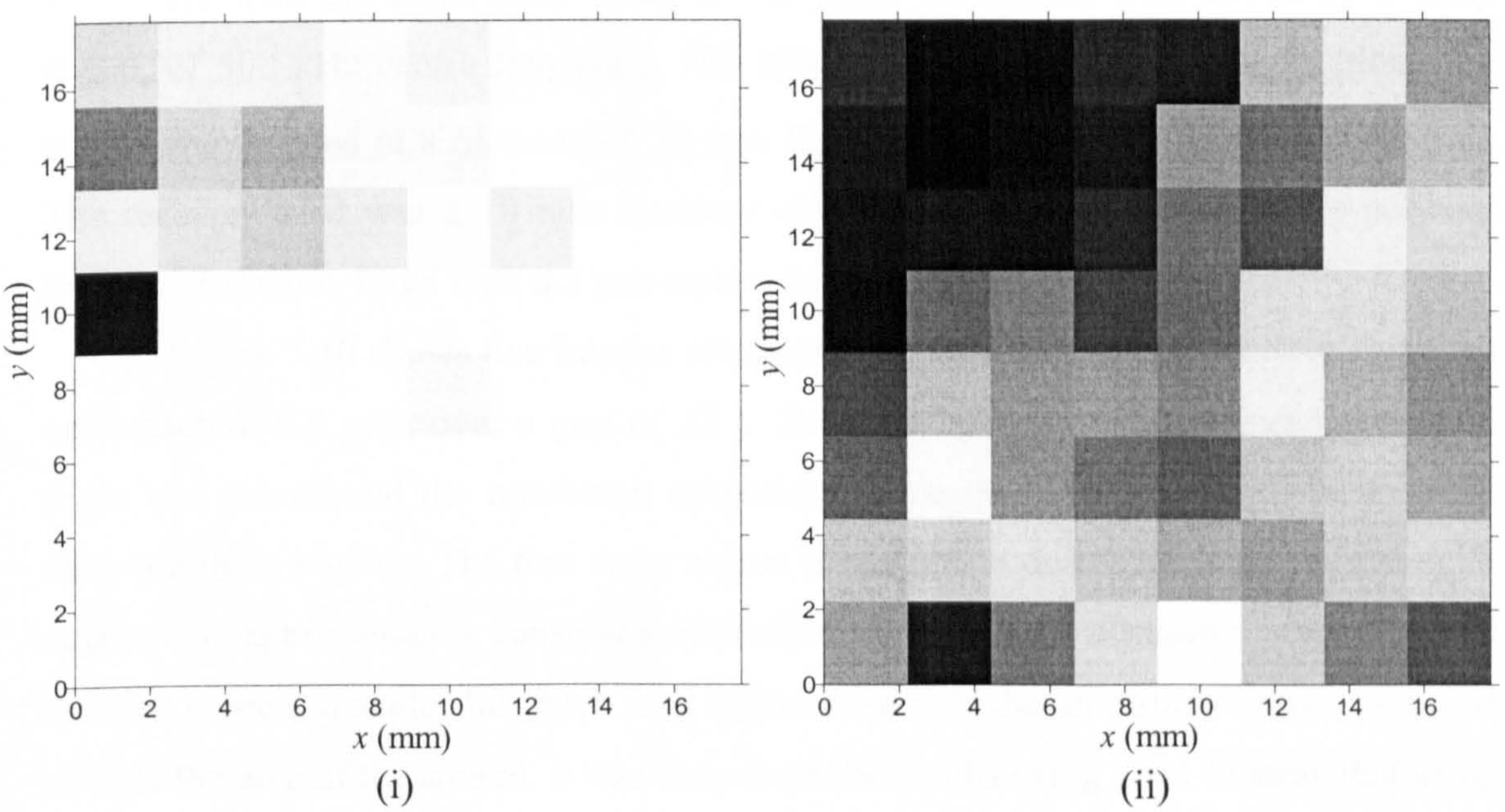

Figure 7.8: Image of a defect in a composite plate obtained using a static 2-D array, taken using (i) time of flight and (ii) amplitude

A drawback of the results shown in Figure 7.8 is the resolution and area of the scan, although this could be improved using an array of more elements and multiplexing between elements. To simulate what would be possible using a larger array of smaller elements, two scans have been performed. In each of these scans a small square receiver has been stepped at a constant pitch to simulate at each step an individual element in an array. The large source, of 50 mm diameter, remained static as shown in Figure 7.9.

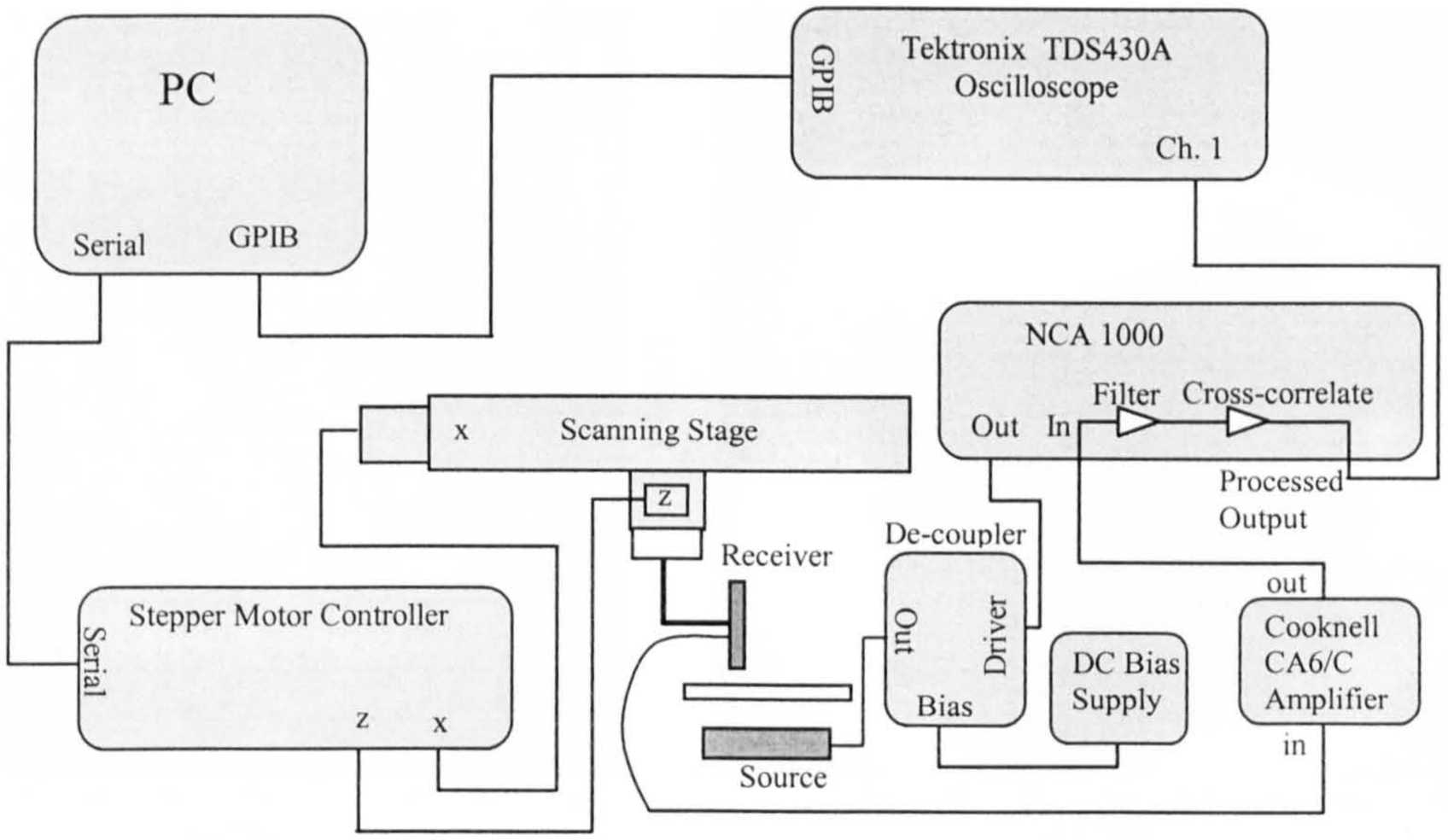

Figure 7.9: Simulating a larger 2-D array by stepping a small receiver

As with the experiment using a 2-D array the source was driven by a chirp signal, of 500 kHz centre frequency, 500 kHz bandwidth and 1000 μs duration. The source was located at a distance of 20 mm from the plate and the receiver at 10 mm. The receiver used was a 10 mm diameter circular micromachined backplate polymer membrane device, fitted with a 2 mm square paper aperture.

Figure 7.10 shows two images produced when a 2 mm square receiver is moved on a pitch of 2.2 mm, over a grid of 23 $\times$ 23 points. The first image uses the time of flight and the second the maximum amplitude. It can be seen from both images that there are three regions. The first inner region is the square defect, with an outer circular region with approximately constant amplitude representing the ultrasonic beam from the circular source, outside this there is a region in which the amplitude drops, as it lies outside the area of the source. It was seen from the results using the 2-D array that using the maximum amplitude produced unclear images, as each element differs in sensitivity, so it is the image of the time of flight, which may be reproducible using a multiplexed 2-D array, which could remain static, unless the element sensitivity can be corrected for.

Figure 7.11 shows the results from a similar experiment using a 1 mm square receiver, stepped on a pitch of 1.5 mm, over a grid of 41 $\times$ 41 points. Even with a receiver of this size it can be seen that enough signal is received to produce a good image of the plate defect, and a clear outline of the source.

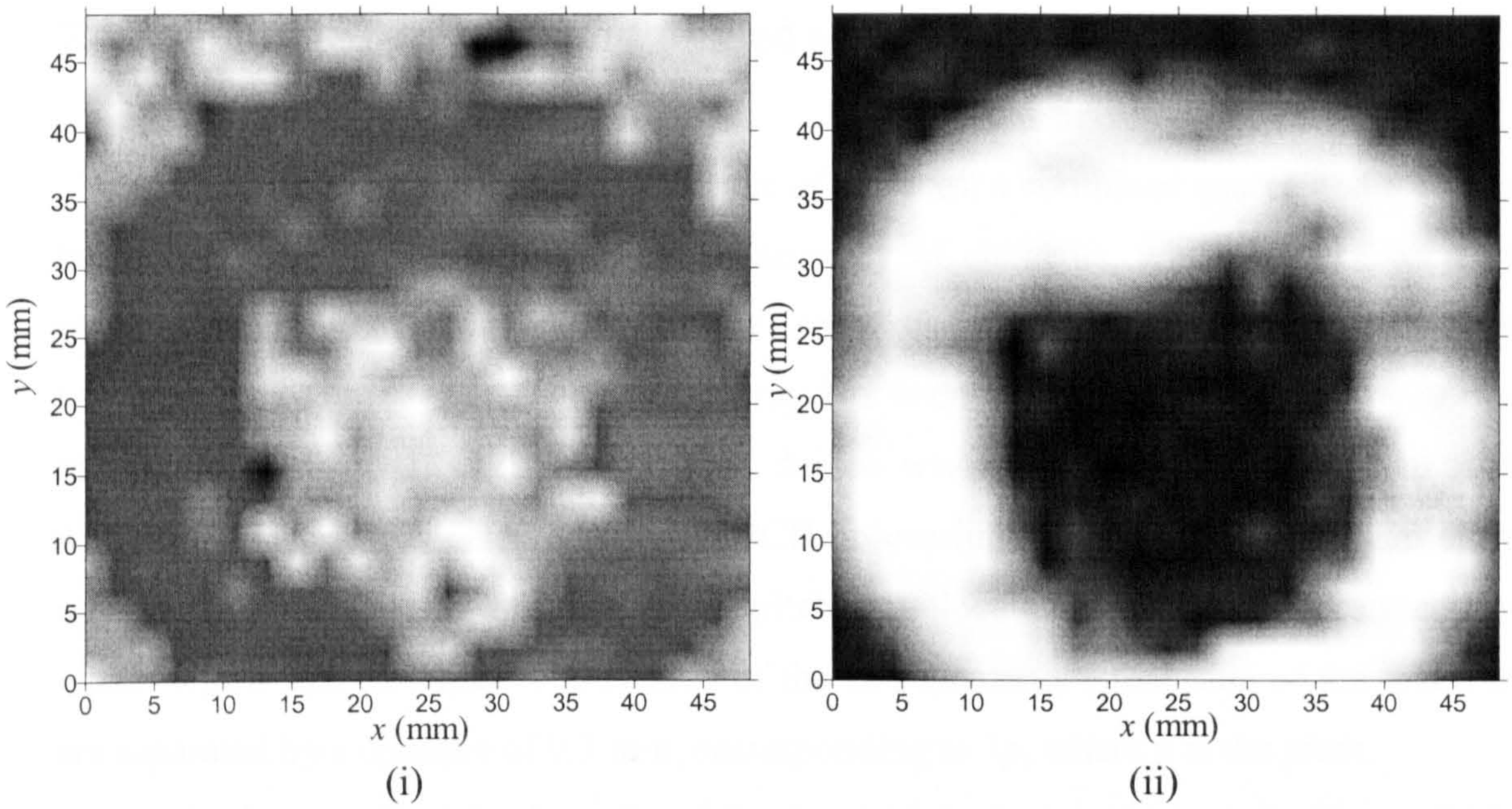

Figure 7.10: A 25 mm square defect imaged using a simulated 2-D array, of 23× 23 elements each measuring 2 mm square on a pitch of 2.2 mm, taken using (i) time of flight and (ii) the maximum amplitude using a tight time window

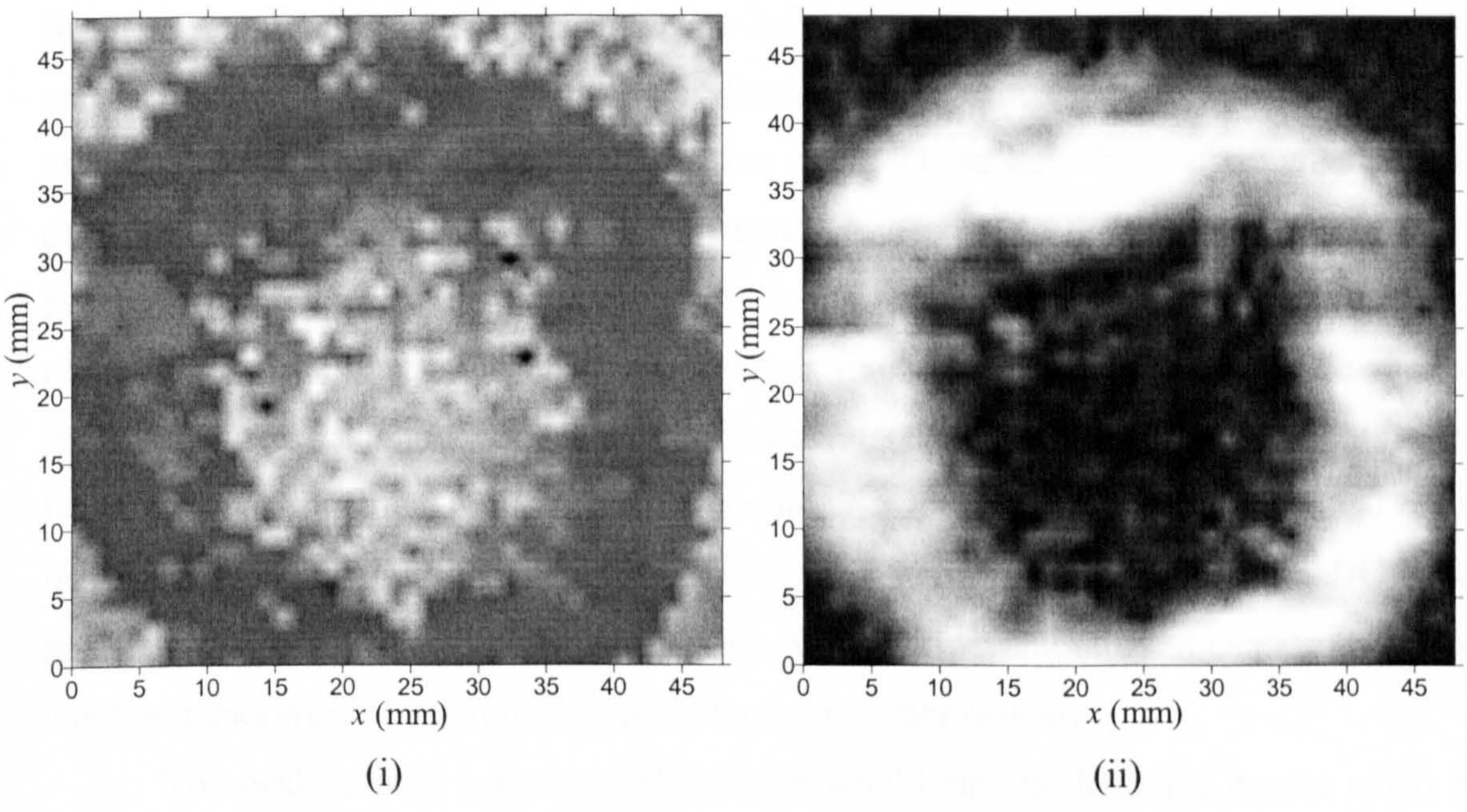

Figure 7.11: A 25 mm square defect imaged using a simulated 2-D array, of 41× 41 elements each measuring 1 mm square on a pitch of 1.5 mm, taken using (i) time of flight and (ii) the maximum amplitude using a tight time window

This work demonstrates the possibility of producing a system in which an image can be produced whilst both source and receiver remain static. With the use of a fast multiplexer, it may be possible to use such a system to create images much faster than can be achieved by scanning.

7.4 A combined receiver and phased source array for surface imaging

In order to produce focussed images of surfaces, a combined source and receiver board has been designed. The source is an array of elements, which will be used to create a focal point using phasing. At the centre of the array there is a wider element which acts as the receiver. The source array has been used to focus on axis, with the receiver detecting reflected signals. This device was made in a similar way to that described for arrays in Chapter 4, using PCB processing. An array of 16 element each measuring 1 mm in width on a 1.3 mm pitch, was located either side of the receiver which was 5 mm in width. The centres of the two elements either side of the receiver are separated by a distance of 9.1 mm, corresponding to $7p$, where p is the pitch.

A photograph and schematic of the finished device can be seen in Figure 7.12. Prior to applying the polymer membrane, the length of the elements and receiver is dictated by the location of two strips of clear insulating tape separated by 10 mm. Separate membranes were used for the two halves of the source and the receiver, as this was found to lower electrical pick-up. Each of the membranes for the arrays was attached in three locations using conductive paint. These have been numbered on the photograph, numbers 1 and 5 provide an earth connection to the membranes from the board, whilst 2, 4, 6 and 8 are located on the insulating tape, and serve just to secure the membranes. The central receiver membrane was fixed in two places (3 and 7), number 3 provided an earth connection, which was separate to that of the source, as this was found to lower electrical pick-up, whilst number 7 is located on the insulating tape. The membranes appear wrinkled in places, however above the active areas the DC bias applied to both source elements and receiver, pulls it down smoothly. It can also be seen that the tracks were covered in insulating tape, for safety reasons.

The peak-to-peak pressure field, which would emerge from the source when 8 elements either side of the receiver are focussed on axis at a distance of 25 mm from the device, has been modelled. This has been done using the procedure described in Chapter 3. This procedure requires a constant pitch between elements, which is possible by modelling a continuous array of 22 elements, and using apodisation such that the centre 6 of which emit no signal. A plot of the resulting predicted field is shown in Figure 7.13, where it can be seen that the signals from both sides of the array converge to cause

a focal point at the desired location. The emergent waveform used in the simulation for each element is a broadband signal ($K = 5$) centred at 500 kHz.

(i)

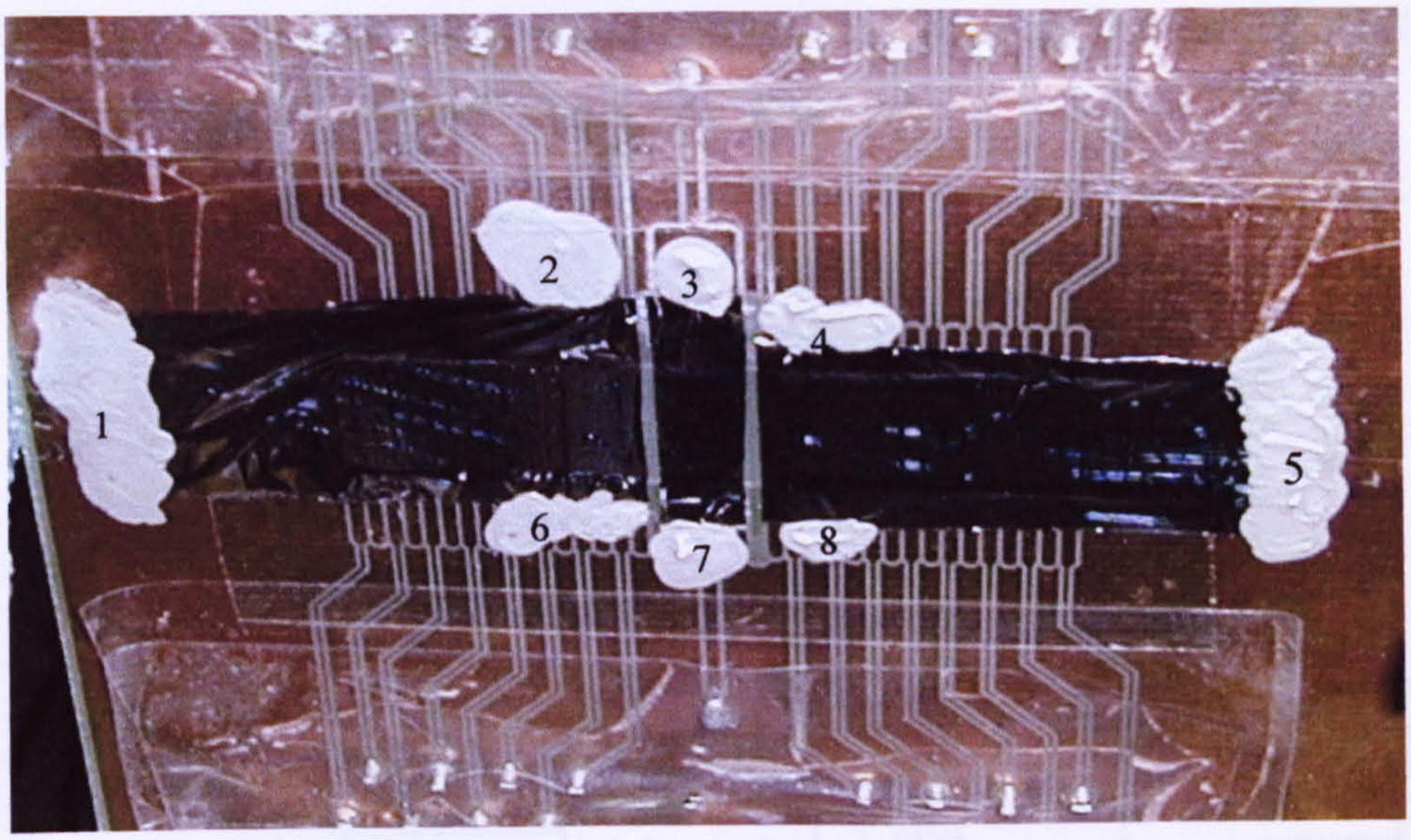

(ii)

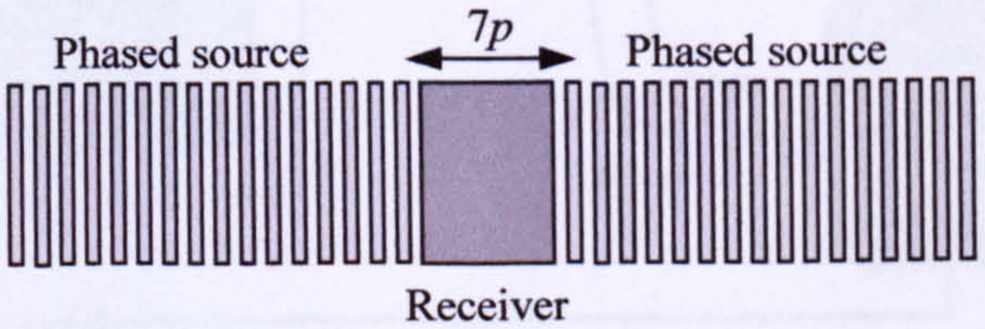

Figure 7.12: A (i) photograph and (ii) schematic of a combined phased source and receiver transducer

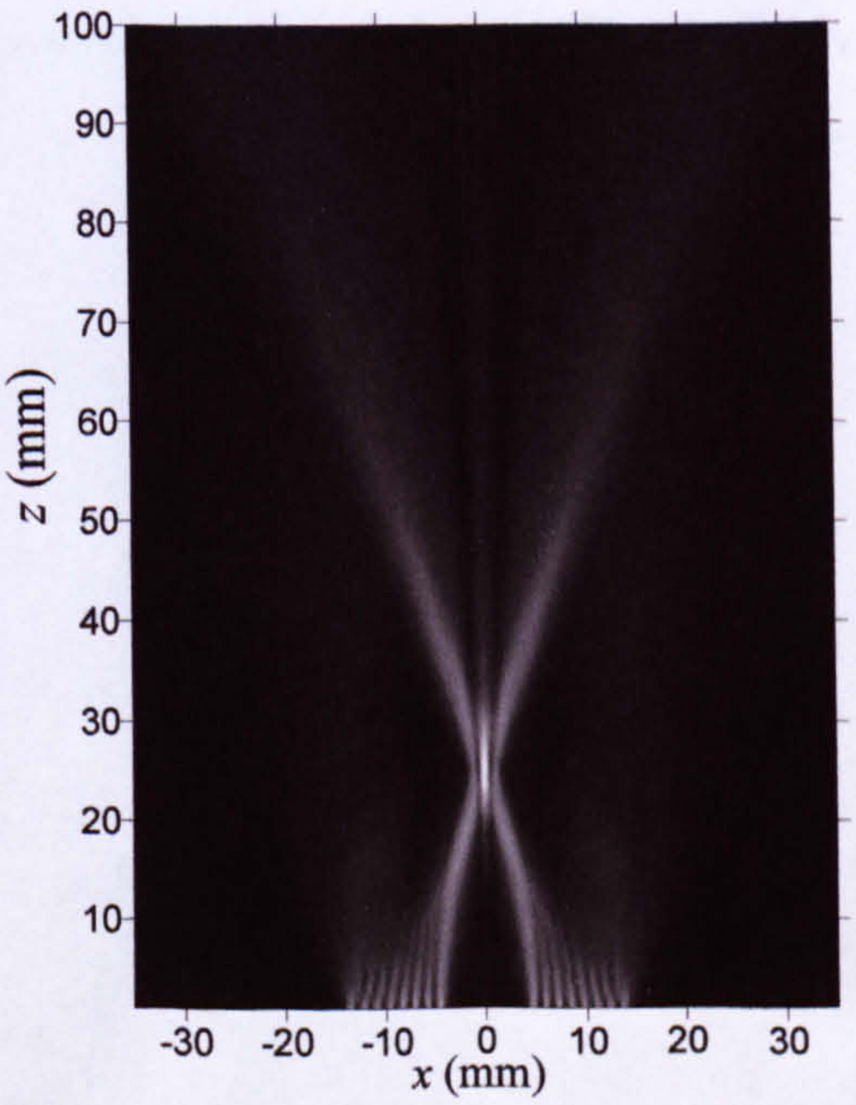

Figure 7.13: A simulation of the pressure field emerging from the split source

In order to investigate the performance of this device, 16 elements, that is eight either side of the receiver, were driven with phasing applied to cause on-axis focussing at $z = 25$ mm. A line scan of the emergent pressure field was performed using a 0.5 mm square micromachined receiver. The line scan was at a constant distance of $z = 25$ mm. This was done using the apparatus shown in Figure 7.14.

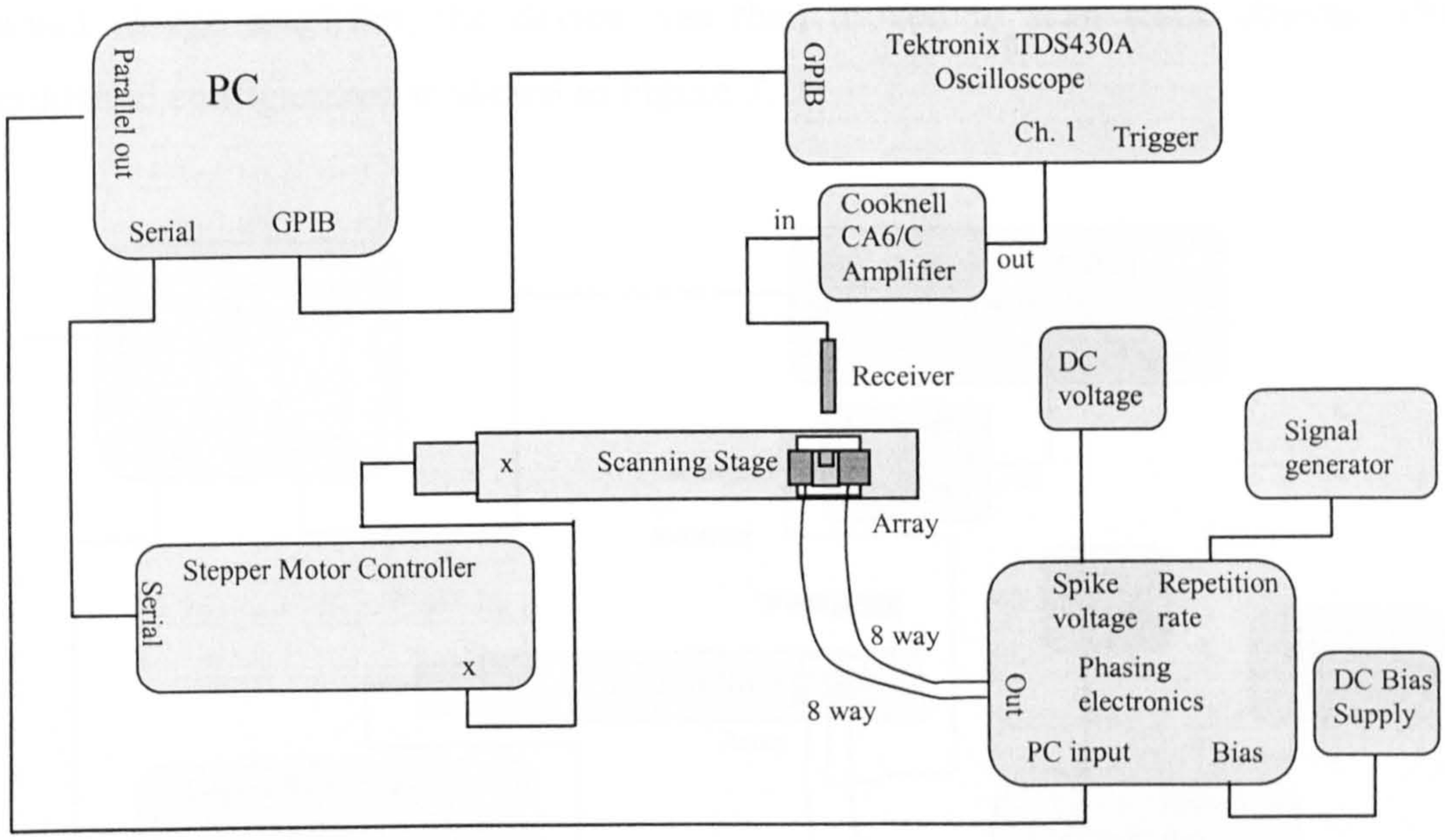

Figure 7.14: Apparatus used to line scan the phased source

The result of the line scan is shown in Figure 7.15, along with a theoretical prediction.

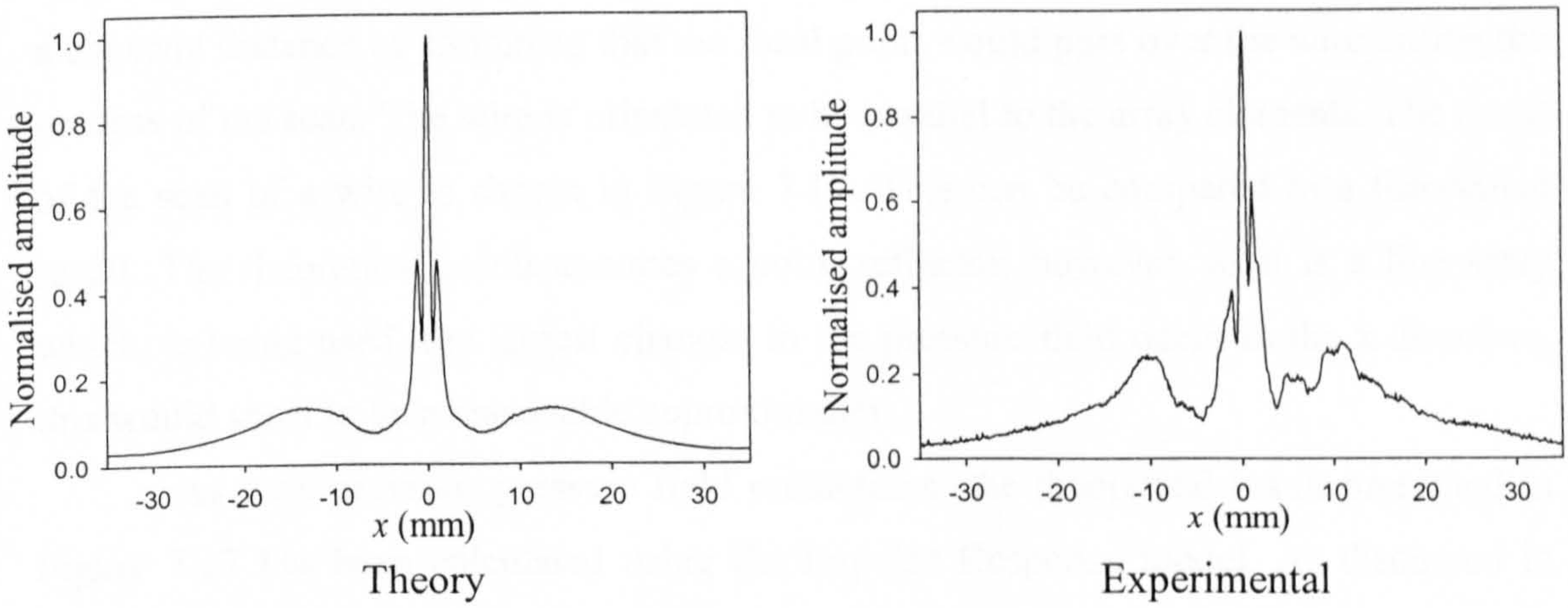

Figure 7.15: A theoretical and experimental line scan through the focal point of the phased source

It can be seen from the line scan in Figure 7.15, that the main grating lobe was greater in amplitude on one side, and this was due to a difference in performance of the two separate membranes used on the source. It can be seen that the focal width appeared to be larger in the experimental measurements than in the theoretical result, and this is probably due to a slight misalignment.

In order to measure reflected signals, the central receiver was connected to the Cooknell charge amplifier, the device was then moved to scan static objects. This experimental configuration is shown in Figure 7.16.

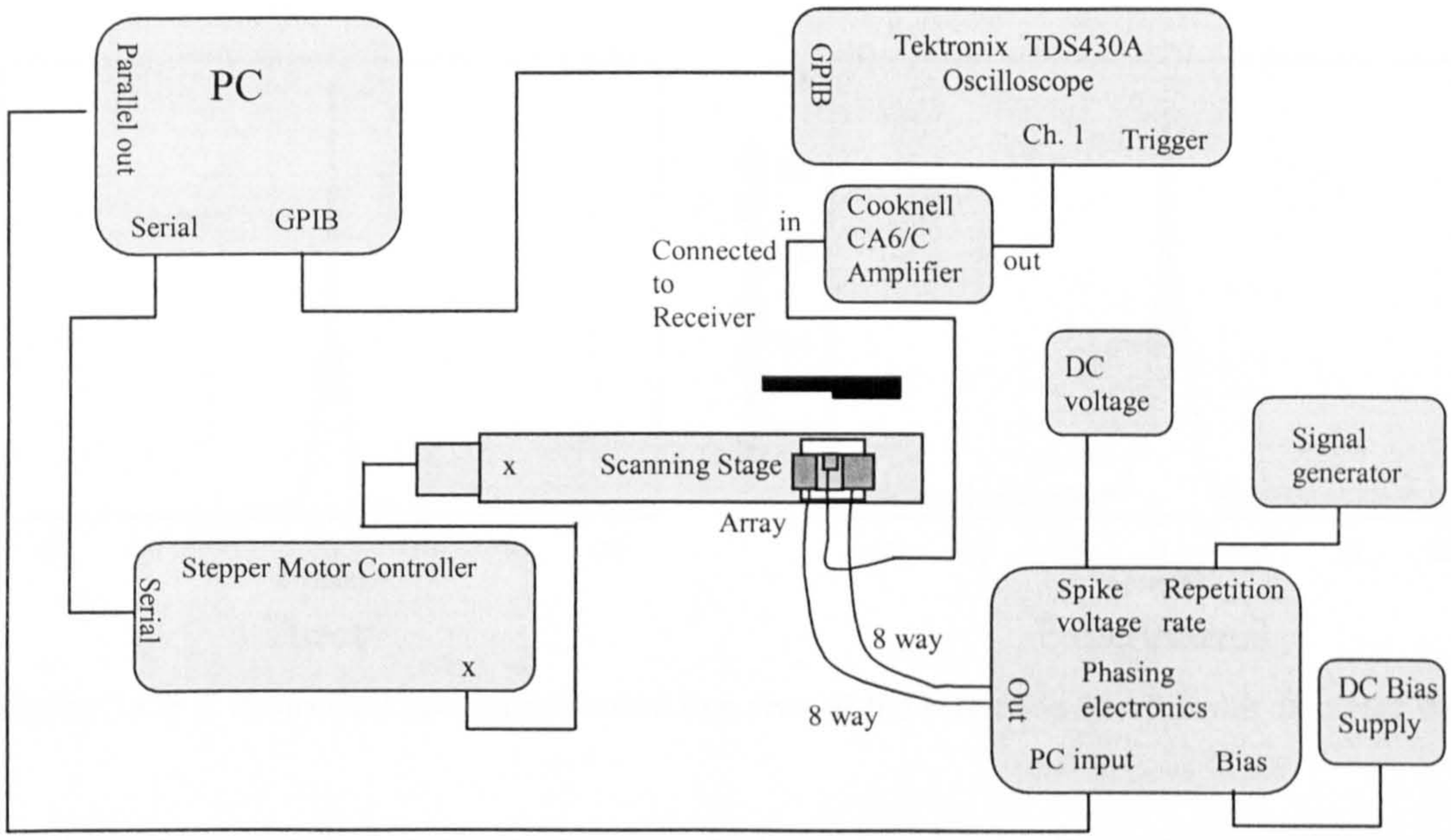

Figure 7.16: Experimental apparatus used for scanning reflecting surfaces

A scan has been performed of a wire of 0.5 mm diameter. This was performed at a constant distance of 25 mm so that the focal point would pass over the wire during the process of the scan. The wire is orientated to be parallel to the array elements. The result of the scan of a wire is shown in Figure 7.17. This can be compared to a theoretical result. The theoretical result assumes a point reflector, however, as it is a line array which, is being used, the largest changes in the pressure field occur in the x direction, this would seem to be a reasonable approximation.

As with previous pressure field predictions, the theoretical result presented in Figure 7.17 has been calculated using the Impulse Response model. As discussed in Chapter 1, this uses the principle that if the field can be found when the planar piston source is driven by a Dirac delta function, then the pressure field can be found for any

other drive waveform by a convolution process. At any given field point the result of an impulse drive applied to the source is termed the impulse response, this can be found geometrically. Each point on the surface of the piston will arrive at a given time dictated by the distance it is from the field point. Hence, at a given moment in time, t, the area of the piston from which a signal can arrive at a field point is the intersection of a sphere centred on the field point of radius $R = tc$, with the piston surface. The impulse response is proportional to this area divided by the distance travelled, to allow for the pressure amplitude from a point source being related to $1/R$.

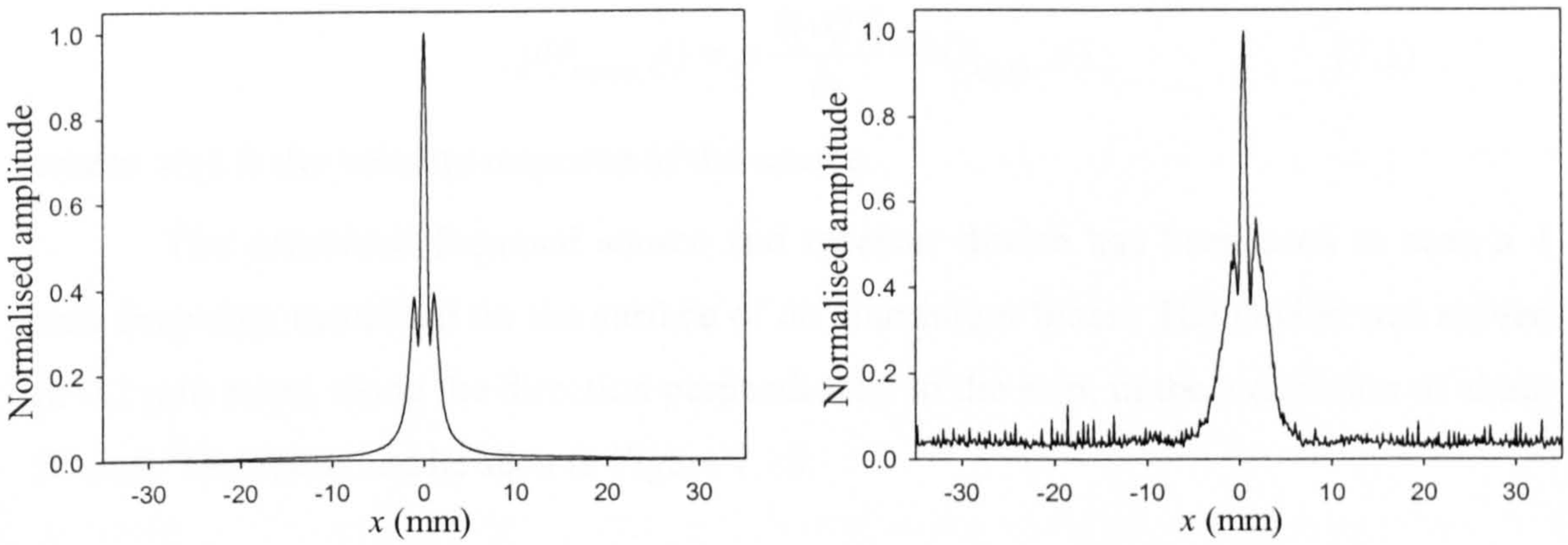

Theory Experimental

Figure 7.17: A theoretical and experimental line scan of the reflection of a 0.5 mm diameter wire

For the case when a planar receiver is considered, which measures the pressure wave emitted from a point source, the scenario is the same. The area of the receiver which will receive a signal at a given time, t, will be the same intersection of a sphere radius $R = tc$, with the piston surface, and again this must be divided by R, to allow for the pressure amplitude drop with $1/R$.

A convolution is utilised as part of the process to change the result from an impulse response to a pressure waveform. This is because any drive waveform applied to the source can be built up from a series of sequential Dirac delta functions. If the case of receiver measuring the signal from a source reflected by a point is considered. Then the impulse response arriving at the point reflector can be found using the method described above, resulting in $h_{source}(\bar{r}_{source}, t)$, where $\bar{r}_{source}$ locates the point with respect to the source. This is then reflected and measured by the receiver. The impulse response from a Dirac delta emerging from the point reflector arriving at the receiver,

$h_{receiver}(\bar{r}_{receiver},t)$, (where $\bar{r}_{receiver}$ locates the point with respect to the receiver) can be found as above. The total impulse response of the system can then be found by convolving the two together, as the emergent impulse response from the point reflector can be built up from a series of Dirac delta functions in exactly the same way as is performed for a drive waveform. So $h_{system}(\bar{r}_{system},t) = h_{source}(\bar{r}_{source},t) * h_{receiver}(\bar{r}_{receiver},t)$, where $\bar{r}_{system}$ locates the reflecting point with respect to the source and receiver, with the source and receiver fixed in relation to each other. Hence in the same way as done in Chapter 1, for the pressure waveform arriving at a point from a planar source, the pressure can be found using,

$$p(\bar{r}_{system},t) = \rho \frac{\partial[v(t)]}{\partial t} * h(\bar{r}_{system},t) \qquad (7.1)$$

where $v(t)$ is the velocity response of the source.

The combined focussed source and receiver device has been used to scan a 1 mm deep step machined on the surface of an aluminium block. The device was moved in 0.1 mm steps, along the direction perpendicular to the step, in the z direction of about 25 mm. The result can be seen in Figure 7.18.

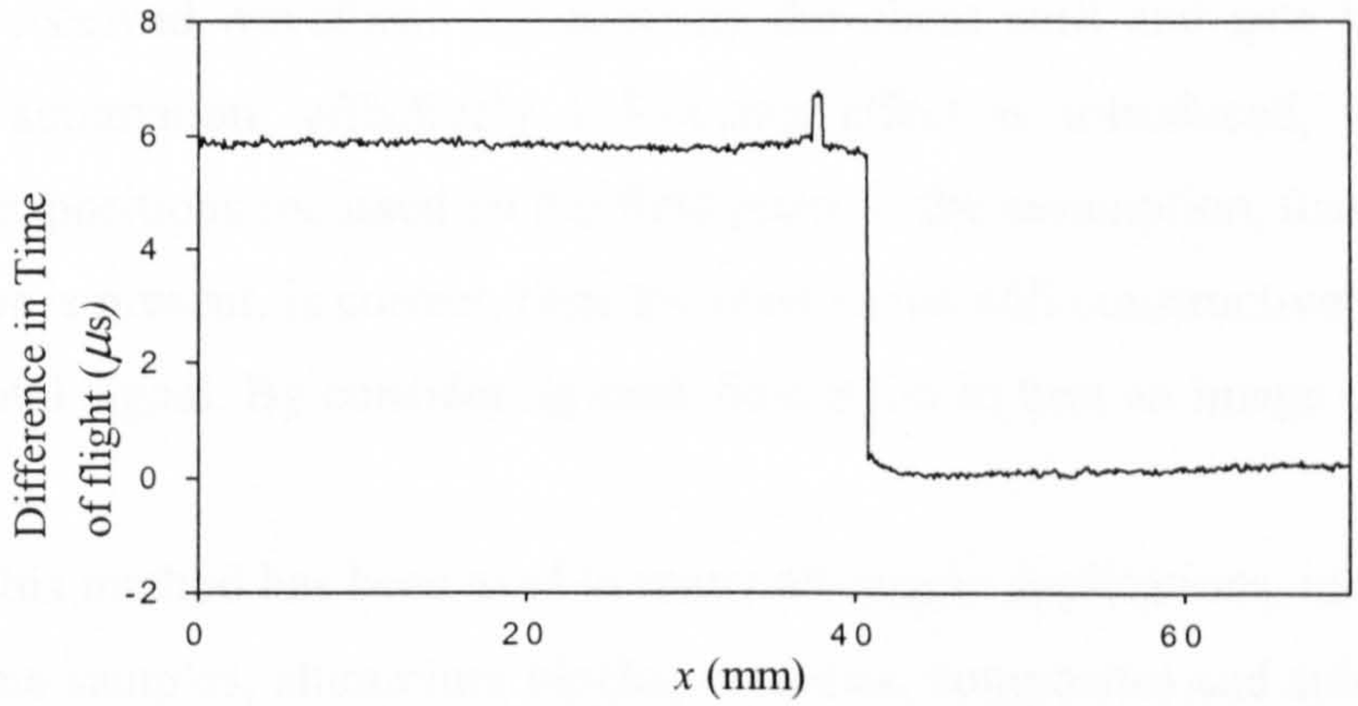

Figure 7.18: A line scan of a 1 mm step in a aluminium sample

The y-axis is labelled in μ s, as the time of flight has been measured, the step is measured as a shift in the time of flight by 5.9 μ s. The speed of sound in air is 343 ms^{-1}, so this time difference corresponds to distance of 2.02 mm. This is as expected as the reflection of the sample means that the path length varies by twice the step size. It can be seen from Figure 7.18, that the step occurs over a very short distance, in fact from one data point to the next. There is an unexpected rise in the time of flight, by 0.6 μ s, at

38.8 mm, a distance of 1.8 mm from the step, lasting for a distance of 0.7 mm. From the data collected this appears to occur as two waveforms interfere, one of these waveforms is presumably a reflection from the step.

7.5 Synthetic aperture focussing technique and ellipse crossing for volumetric imaging in air

The synthetic aperture focussing technique (SAFT) algorithm is an imaging technique which has been used in a broad range of applications, such as radar, geophysical exploration, radio astronomy, and ultrasonic testing [5]. The SAFT algorithm allows a simulation to be made of a large aperture focussed device by the use of small devices, which are scanned over an area. The algorithm achieves a better image resolution than the raw data measured by the small device [6].

The data is processed by assuming that at a point in the field there is an object, which would cause a reflection, either a flaw in a solid sample, or a surface. The path length that has been travelled is calculated from the source to the assumed field point and back to the receiver. This path length is used to calculate a phase shift and time gate for each received waveform. By applying the phase shift and gate to each waveform prior to summation, effectively a focusing effect is introduced, with the multiple transducer positions focussed on the field point. If the assumption, that at this field point a reflector is present, is correct, then the waveforms will constructively interfere to give a large total signal. By considering each field point in turn an image can be built up [7, 8].

This method has been used in many ultrasonic applications, including the testing of concrete samples, aluminium blocks, pipelines, composites and subsurface defects in a non-contact manner using laser systems [7-12].

In the work described in this Section rather than scanning the receiver, an array of elements will be used, and the SAFT method will be used to find surface profiles using air-coupled ultrasound.

Figure 7.19 shows how the path length for a given pixel can be calculated, in this case a pitch catch method is used, with the position of the source being parallel to the receiver positions. Two different field points are illustrated, labelled P_1 and P_2, the paths are shown to two receivers labelled A and B.

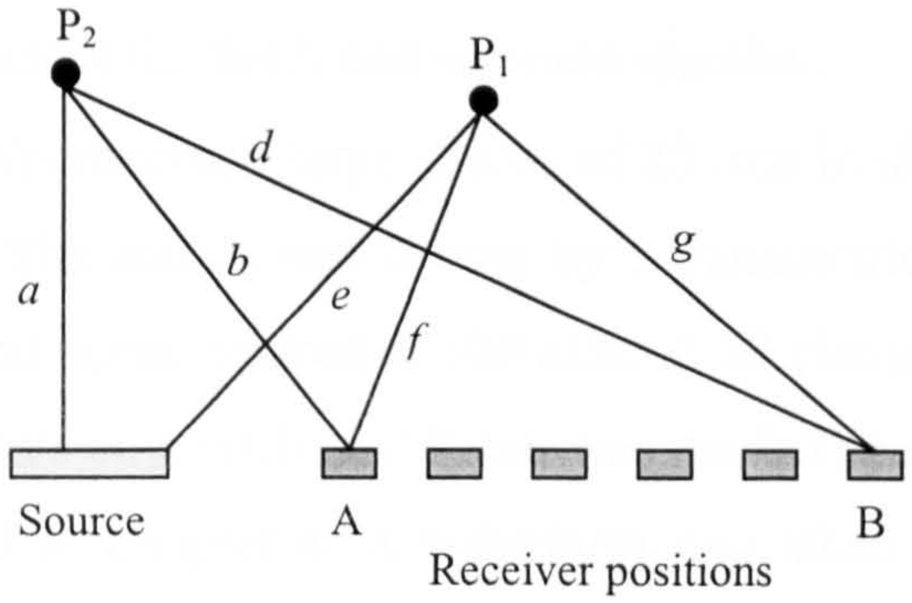

Figure 7.19: The paths travelled between source and receiver via a field point

It can be seen from Figure 7.19, that the path from the source to P_2; *a*, is measured normally to the source; and to P_1 the distance is *e*, measured from the nearest edge of the source. From P_2 the distance to receiver position A is labelled *b*, and the position B is labelled *d*. Similarly from P_1 to receiver position A is *f*, and position B is *g*. In order to calculate the phase and gate to apply to the waveforms from each receiver position the total path lengths must be found, if it is assumed that the gate width is t_{gate} long. In the case of field point P_1, the data to be extracted from the waveform measured at receiver position A occurs between times $\frac{e+f}{c}$ and $\frac{e+f}{c}+t_{gate}$, whilst for position B the time bracket is between $\frac{e+g}{c}$ and $\frac{e+g}{c}+t_{gate}$, where *c* is the speed of sound in air. So a phased shifted gate has been applied to the signals, these are then summed for all the receiver positions. The path lengths can be used in a similar manner for point P_2 and all other field points, until an image is built up. This has been done by writing series of Matlab programs, (as can be seen in Appendix B.8).

The ellipse crossing method uses the time of flight to each receiver, rather than the whole waveform. The pathlength travelled is the distance from the source to the reflecting point and from the reflecting point to the receiver. This being the case, when the path length is known, and it is found by the time of flight multiplied by the speed of sound in air, the possible location of the defect will lie on an ellipse. If the ellipse for each receiver is found, then the location of the defect is at the crossing points. This has also been implemented as a Matlab program, (see Appendix B.8). The program considers each receiver in turn, for a given *x* value, the *z* value of the field point is increased until the total pathlength for that point exceeds the pathlength for that receiver. When this occurs the preceeding *x*, *z* field point is assigned a value of 1, this is

repeated for each x value, and then in turn for each receiver. In this way a series of ellipses are plotted across the field, and summed together.

In the first experiment, a large source of 25 mm in diameter, was located at 90° to a receiver array. The source was driven by a Panametrics PR5055, resulting in an output of a broadband signal centred at 500 kHz. A 32 element array of elements of 0.4 mm × 10 mm elements on a pitch of 0.7 mm was used. The array was made in the same manner as described in Chapter 4. A waveform was taken from each element on the array in turn, prior to displacing it by a distance of $32 \times p$, where p is the pitch, and recording a further 32 waveforms. In this way a 64 element array was simulated. The object under examination was a bar of a diameter of 3 mm. The experimental apparatus is shown in Figure 7.20.

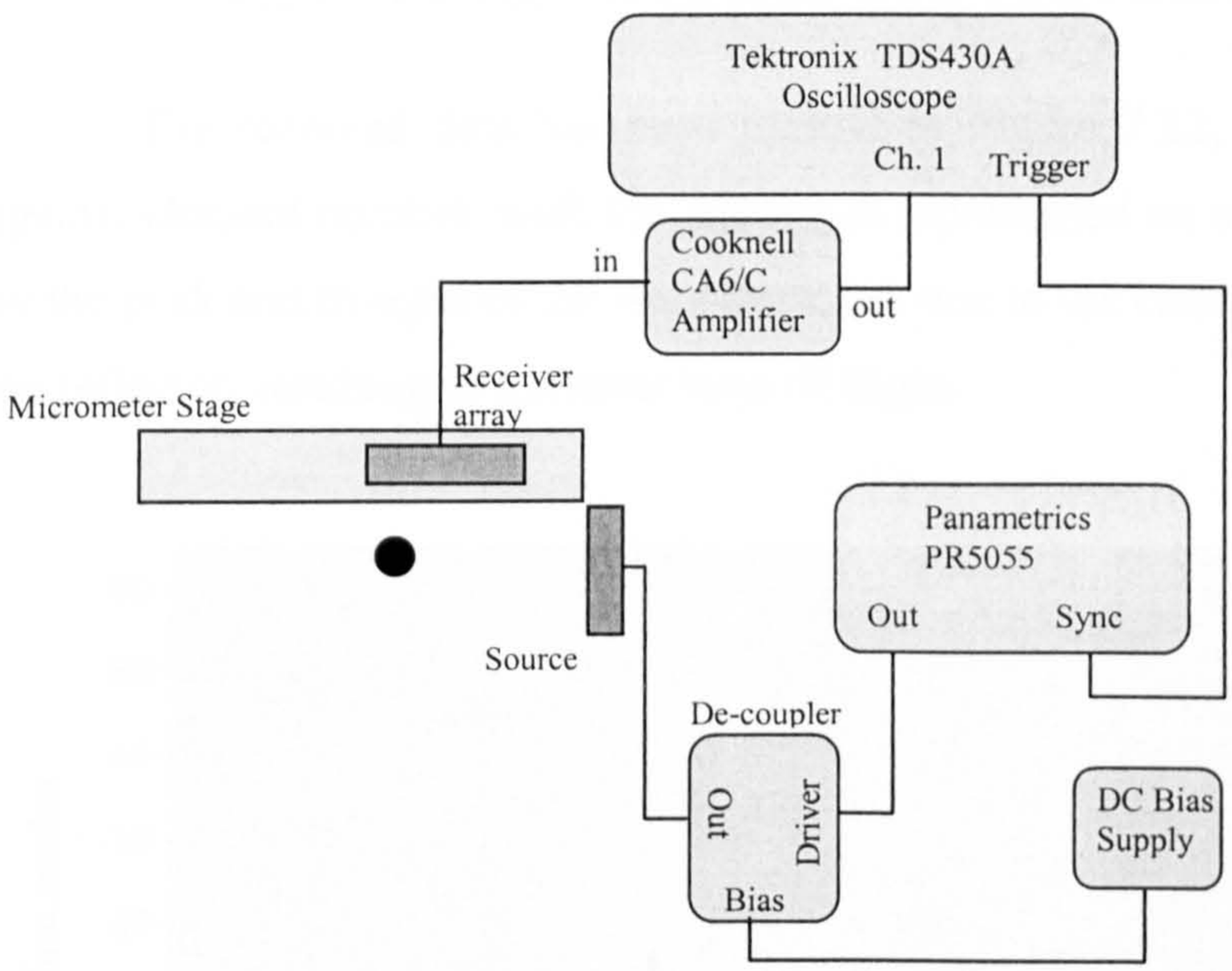

Figure 7.20: Experimental apparatus used to image a 3 mm bar

Figure 7.21 shows the resulting image of a 3 mm bar found using an array of 64 elements and a source positioned at 90° to the receiver. Two images have been found, one by SAFT and the other using the ellipse crossing method, in both cases the location and size of the reflector has been indicated. It can be seen that the ellipse crossing method has produced a tighter image, the crossing ellipses can be clearly seen.

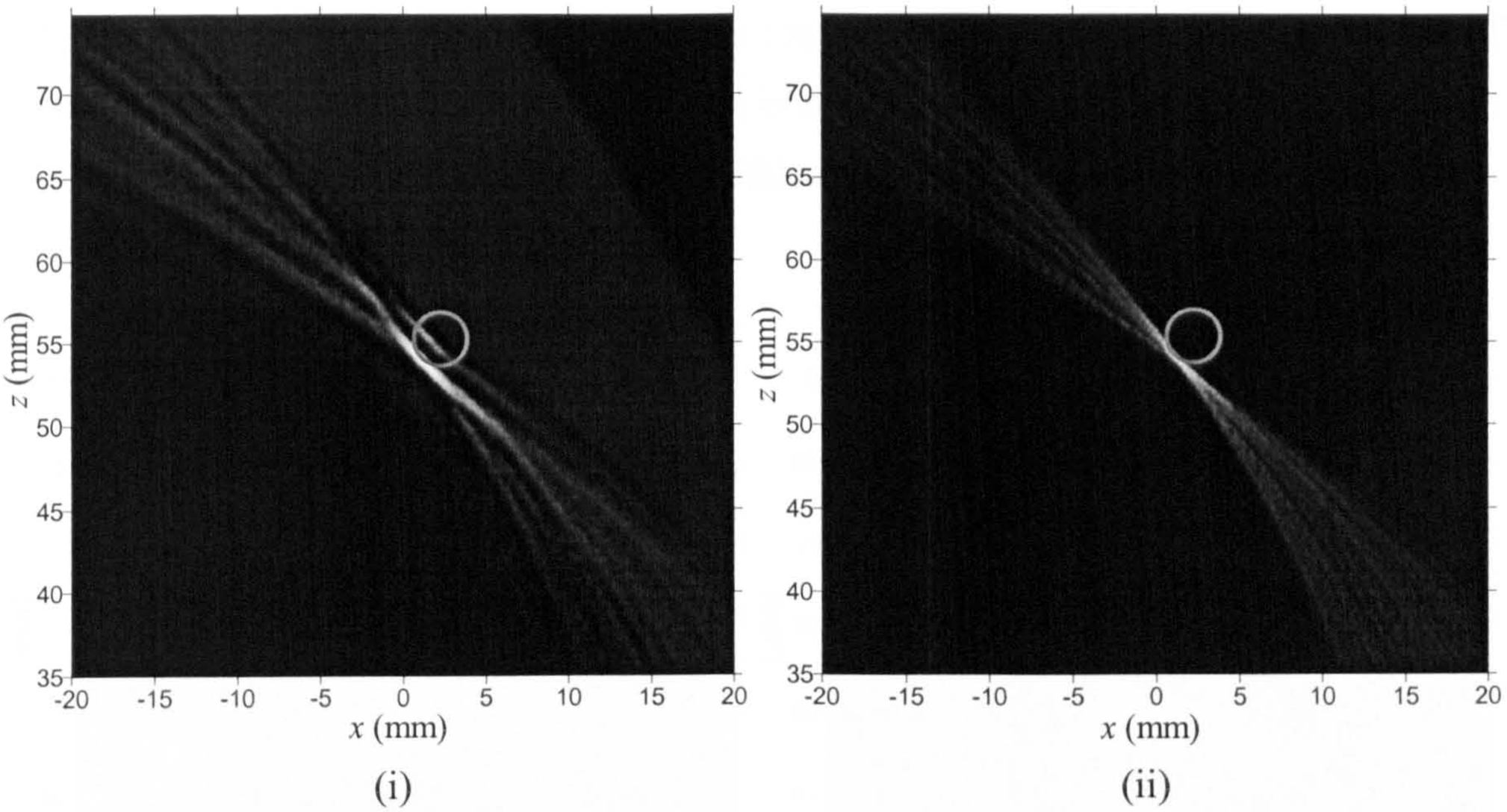

Figure 7.21: An image of a 3 mm bar using a source located at 90° to the receiver array, using both a (i) SAFT and (ii) ellipse crossing method using a broadband drive signal

The received data has been plotted in Figure 7.22, as an image plot of time against element number, with the amplitude represented on a greyscale. The arc formed by the peak and troughs of the waveform, are due to the central elements being closer to the reflector, resulting in a shorter time of flight.

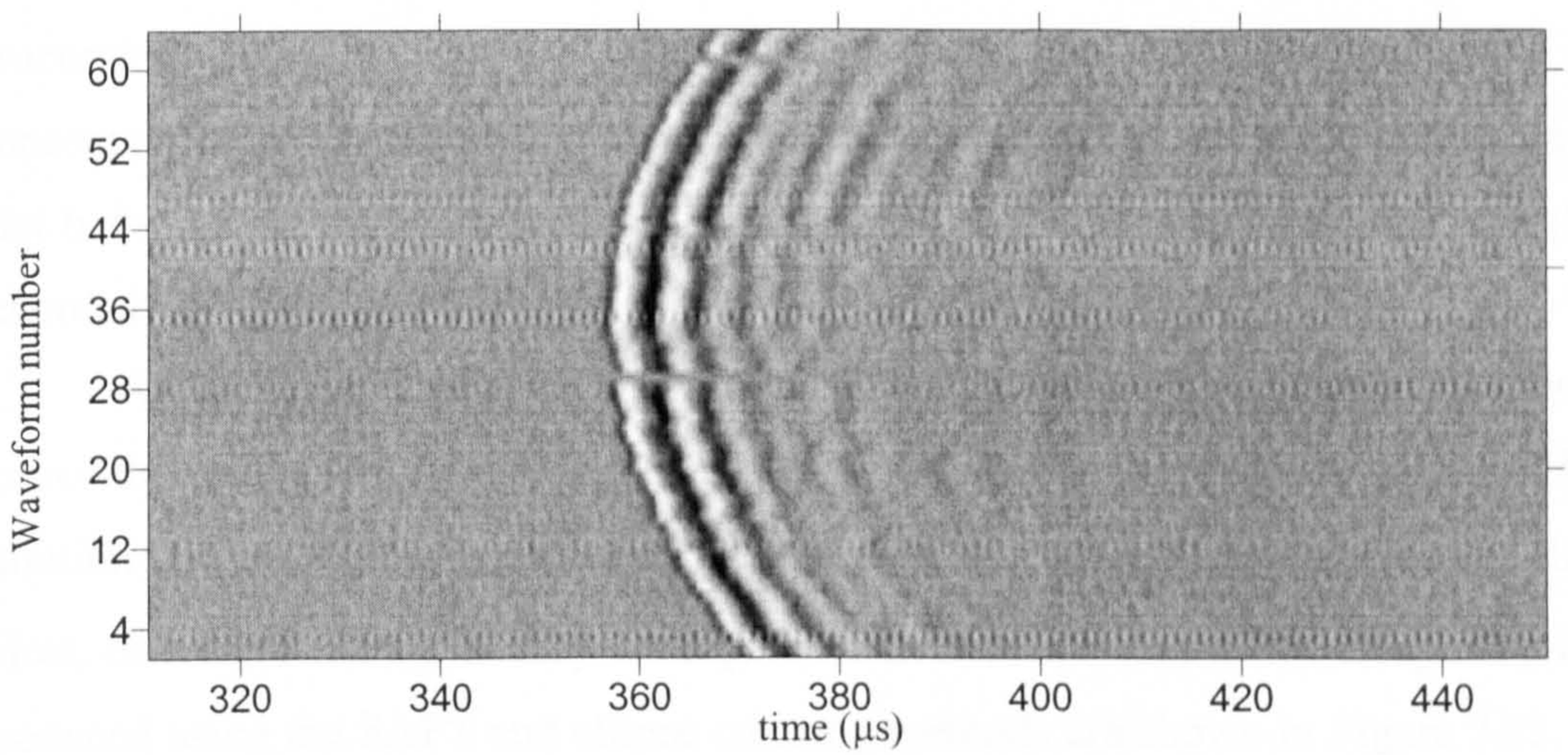

Figure 7.22: The waveforms reflected by a 3 mm diameter bar, when a source at 90° to the receiver array is used with a broadband drive signal

The experiment was repeated with the source driven by a NCA1000 chirp generator. The chirp signal used was of a bandwidth of 500 kHz centred at 500 kHz, and a duration of 600 μ s. The received waveform from each element was filtered and cross-correlated. The results are shown in Figure 7.23, where again it can be seen that a

tighter image is obtained using the ellipse crossing method. Due to the high degree of accuracy in finding the time of flight of the cross-correlated chirp method, it can be seen that the ellipse crossing image is tighter in this case than for the broadband signal case.

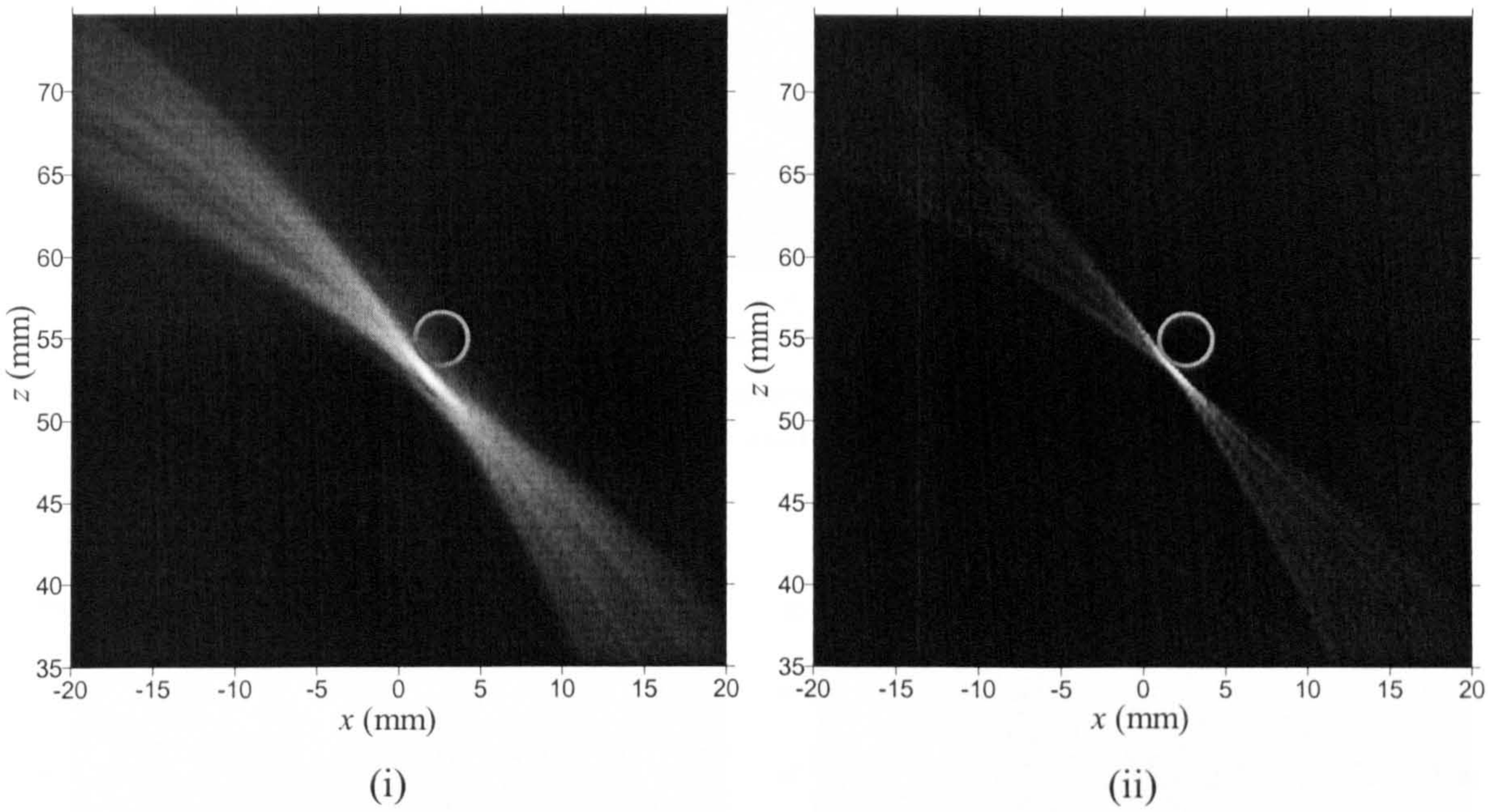

Figure 7.23: An image of a 3 mm bar using a source located at 90° to the receiver array, using both a (i) SAFT and (ii) ellipse crossing method using with a chirp drive signal

The recorded data is shown in Figure 7.24. The output from the signal processing performed by the NCA1000, is a positive value for each time point, consequently when no signal is present the value is zero, resulting in a large area of the plot being black. It can be seen that in both this and the previous case that one element recorded no signal, and consequently breaks were seen in the arcs.

A third experiment was performed using the same arrangement, again with the source driven by a chirp signal of bandwidth of 500 kHz, centred around 500 kHz, and duration 600 μ s. In this experiment the 3 mm bar was replaced by two 0.5 mm diameter wires, orientated such that they were parallel to each element of the array. The images produced using the SAFT and ellipse crossing methods are shown in Figure 7.23. Again it can be seen that a tighter image was obtained using the ellipse crossing method.

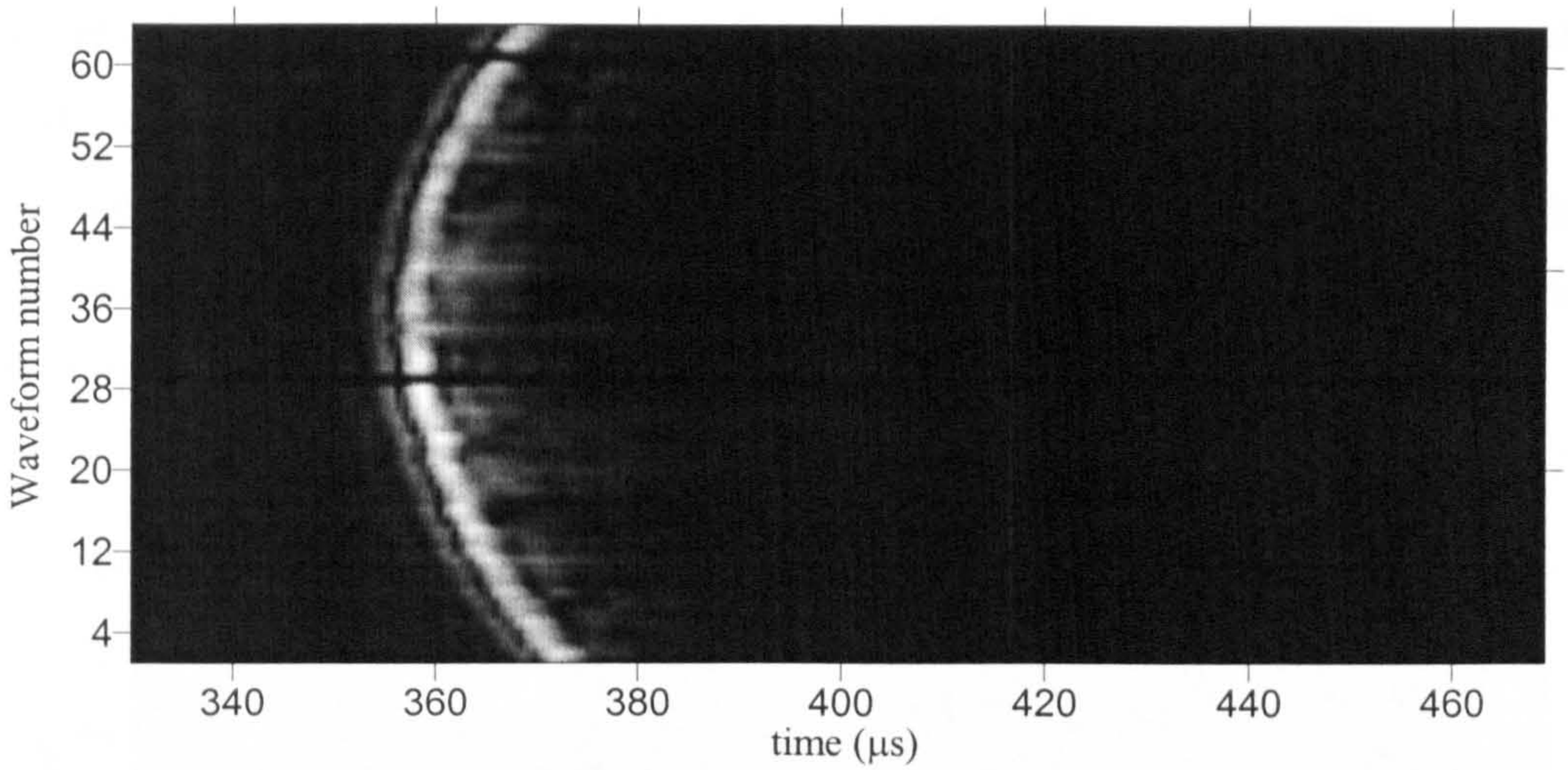

Figure 7.24: The cross-correlated waveforms reflected by a 3 mm diameter bar, when a source at 90° to the receiver array is used with a chirp drive signal

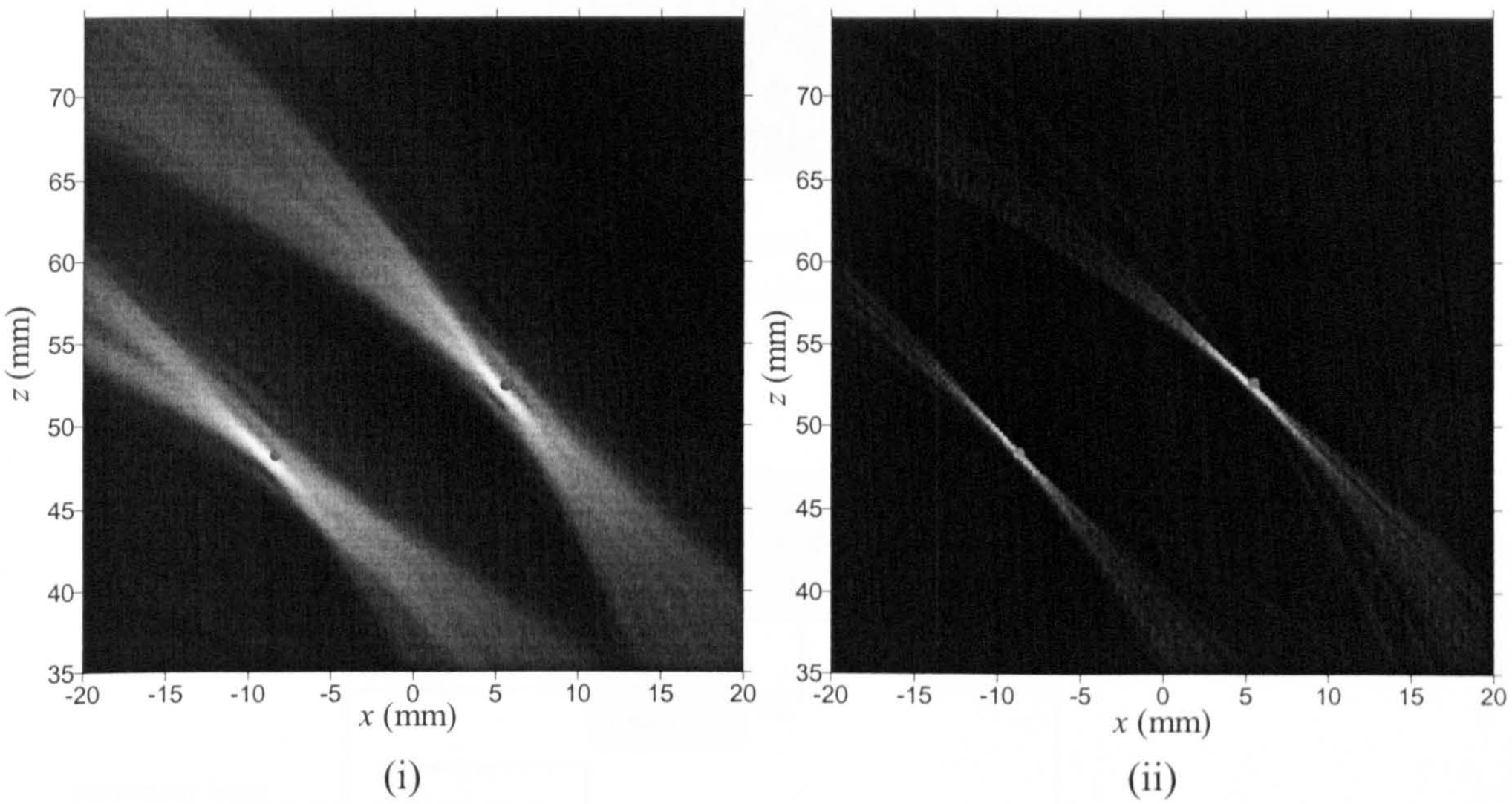

Figure 7.25: An image of two wires using a source located at 90° to the receiver array, using both a (i) SAFT and (ii) ellipse crossing method using with a chirp drive signal

The recorded data for the experiment involving two wires is shown in Figure 7.26.

In each of the sets of images presented, the object has been located accurately, however it appears greatly elongated in the direction of the arcs. This is because the arcs cross at small angles with respect to each other, by moving the source and repeatedly recording data a better image could be reconstructed.

The combined source and receiver, described in Section 7.4, has been used for imaging using the SAFT and ellipse crossing methods. However in this case, the inner, larger element is used as the source, and the two arrays on either side used as the

receivers. The board was positioned in front of a 3 mm diameter bar. The inner element was driven using the Panametrics PR5055, and a waveform was recorded of each of the 16 elements on either side. The device was then moved on the micrometer stage by a distance of 5 mm, and the process was repeated. The experimental arrangement is shown in Figure 7.27.

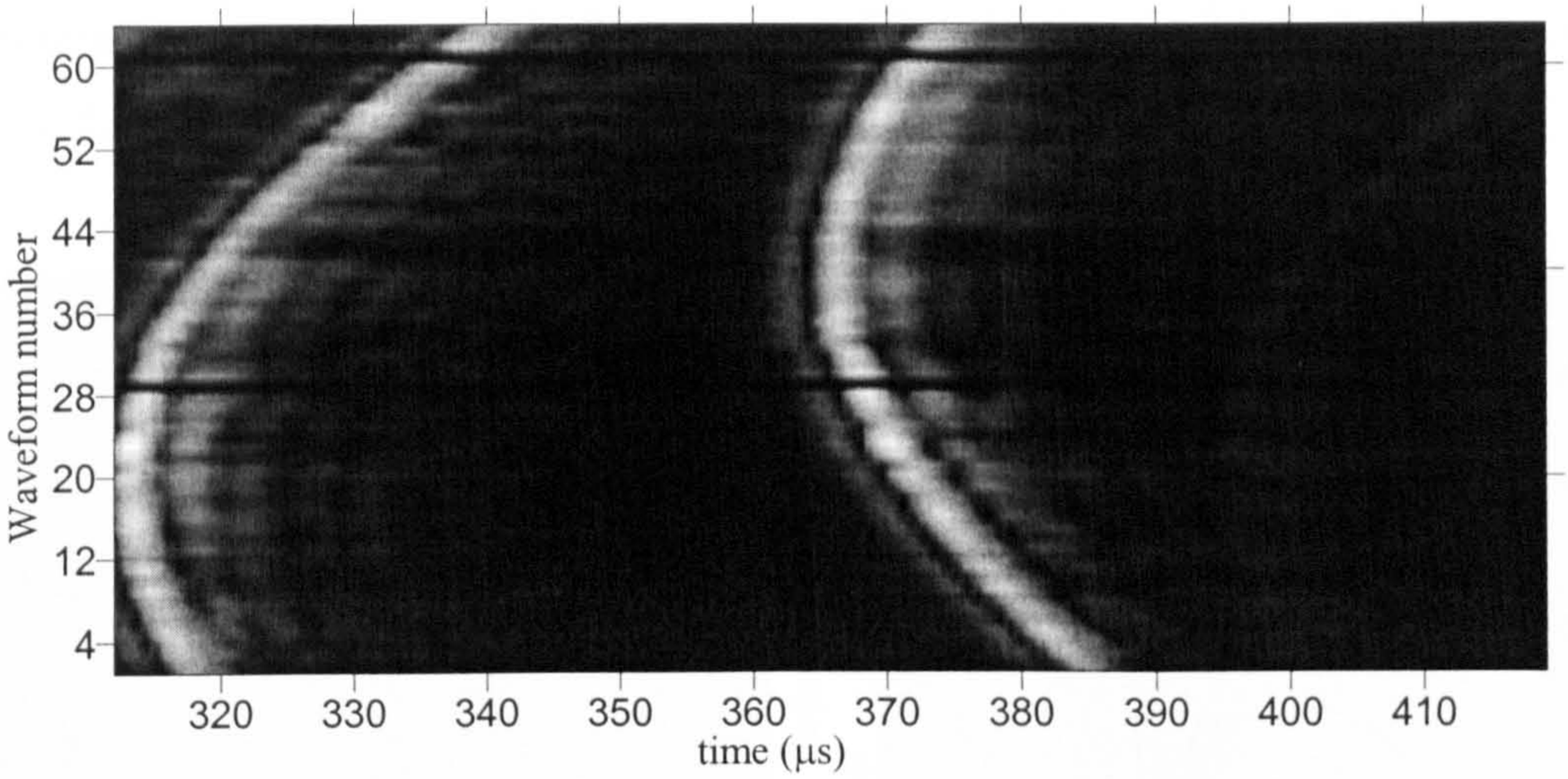

Figure 7.26: The cross-correlated waveforms reflected by two wires, when a source at 90° to the receiver array is used with a chirp drive signal

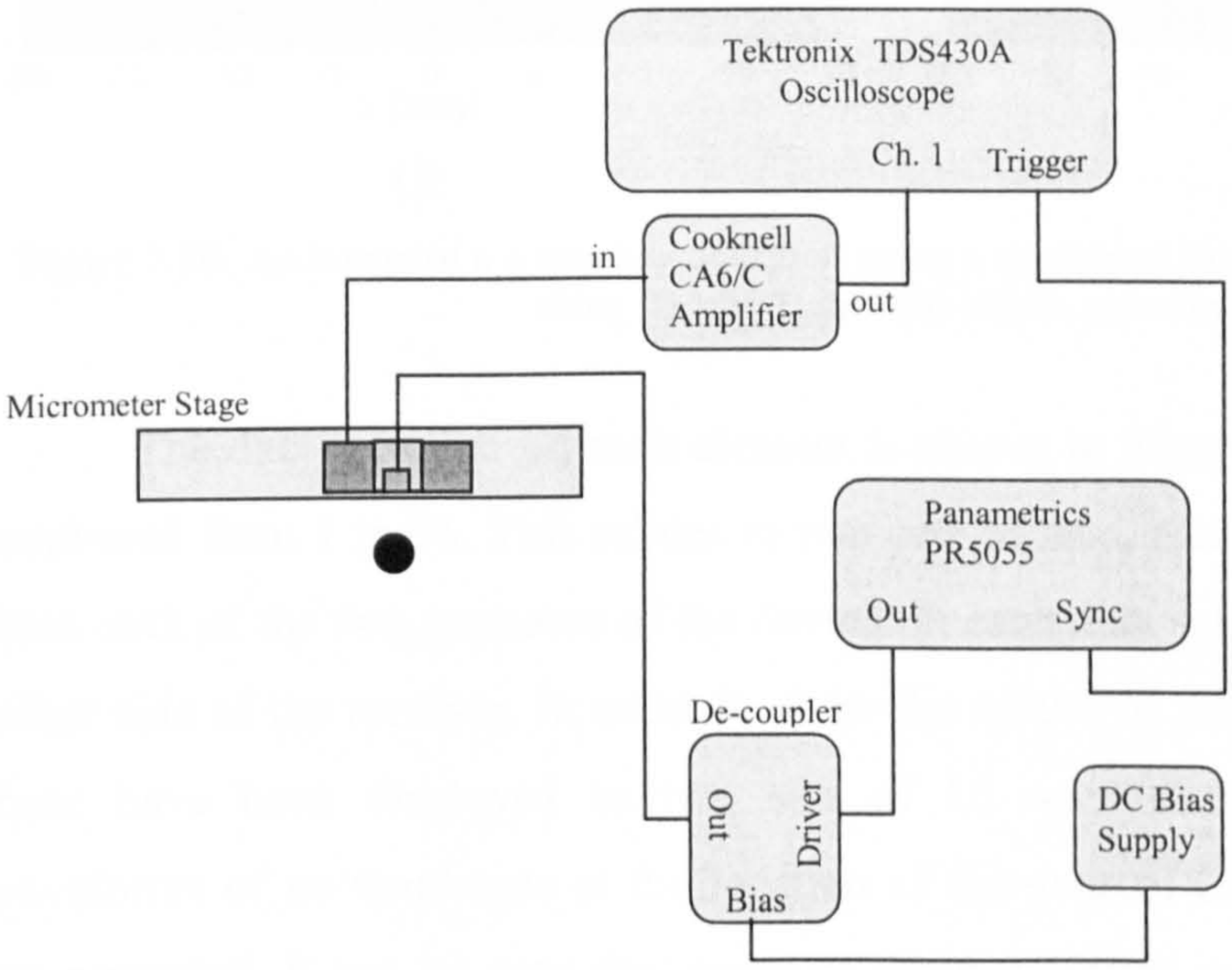

Figure 7.27: Experimental apparatus used to image a 3 mm bar using a combined source and receiver device

Figure 7.28 shows the resulting images obtained using the (i) SAFT and (ii) ellipse crossing methods. It can be seen that with this orientation of source with respect

to receiver, the arcs in the images cross at a larger angle and hence a more defined image is achieved. It can also be seen that the SAFT image is much better than the ellipse crossing image, this is due to a lower signal to noise ratio in this case than in previous examples. The ellipse crossing method relies on accurately finding the time of flight, with a low signal to noise ratio this is made more difficult, resulting in a poorer image. In both cases a better image can be built up by moving the device to more positions, hence reflecting off different parts of the object, a multiplexing system would enable this to be done quickly.

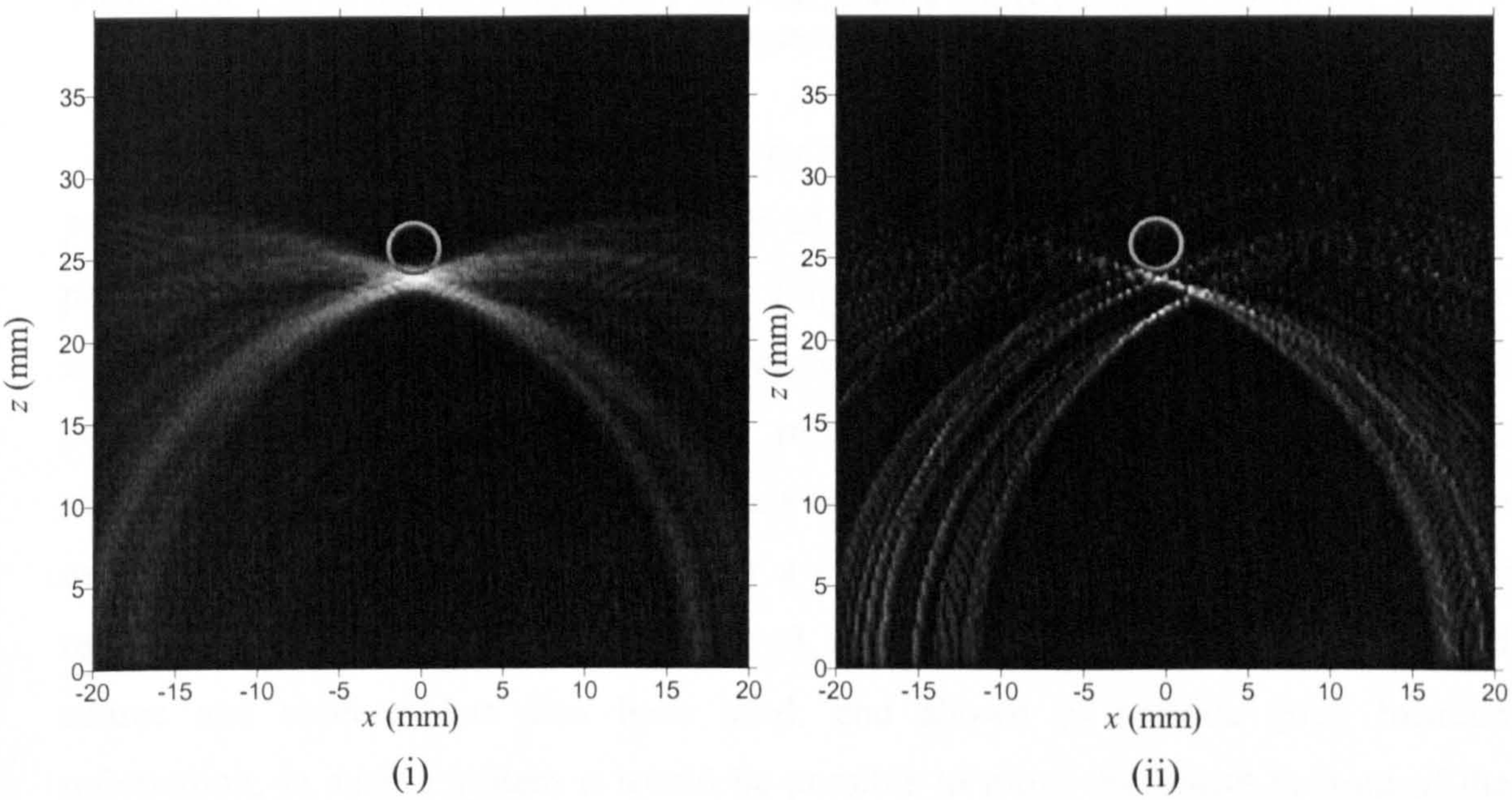

Figure 7.28: An image of a 3 mm bar obtained using a combined source and receiver transducer, using (i) SAFT, and (ii) ellipse crossing

The data recorded on each element is shown in Figure 7.29. The waveforms are numbered from 1 to 76. This relates to two sets of data, each of 38 waveforms, one set from each of the two positions of the device. In each data set 32 elements were used, 16 either side of the receiver, in order to show the nature of the arc of the peak amplitude these have been displayed as two sets of 16 waveforms separated by 6 sets of waveforms of no amplitude at the location of the source. Consequently 72 waveforms are presented. It can be seen that some of the waveforms are very noisy, it is in these cases that the maximum amplitude is not due to the ultrasonic waveform but due to noise. Hence the resultant calculation of the time of flight does not relate to the path length.

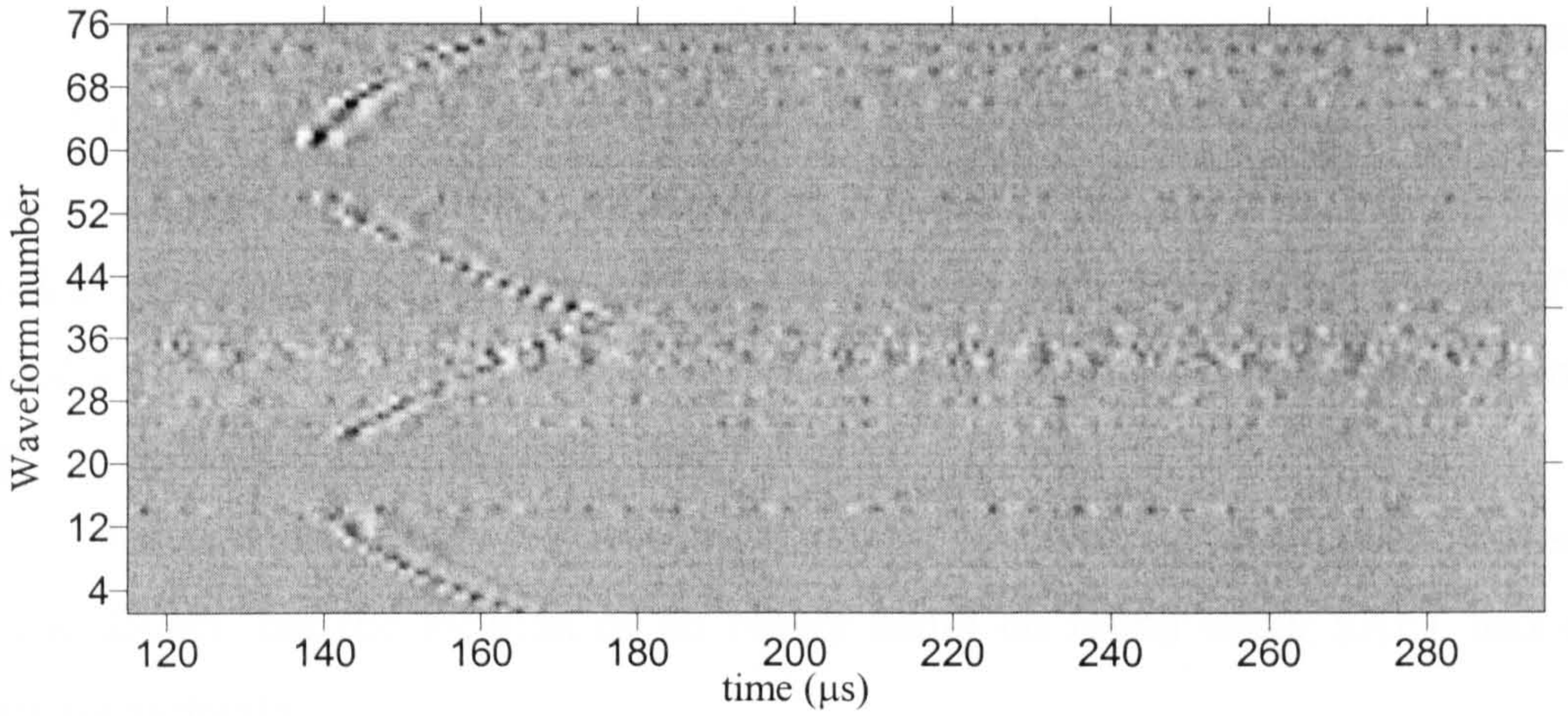

Figure 7.29: The waveforms reflected by a 3mm bar, when a source parallel to the receiver array is used with a broadband drive signal

It will be seen in the above that, by using an array as a receiver, it has been possible to accurately locate objects using an air-coupled ultrasonic system. Two data processing methods were used, SAFT and ellipse crossing, it has been seen that for low signal to noise ratio systems SAFT provides better results. This type of imaging is often performed using multiple source and receiver locations, which requires many movements of each transducer. Here the use of an array has been shown to be possible as a receiver. This makes it possible for a system to be used in which the receiver remains fixed, and only the source is moved, resulting in a faster system. A combined source and receiver has also been used, and shown to provide good location information, in such a system it would be possible to move the object in front of the device, and in doing so image it, using a multiplexing system on the receiver arrays.

7.6 Conclusions

In this Chapter, ultrasonic capacitive arrays have been used in a variety of ways to produce images. Initially it was shown that each element of an array acts independently as a receiver, this was done by receiving the signal emitted by a large source located at an angle to the receiver.

A 2-D array was used to image a composite sample using through transmission. In this experiment, a large source was driven by a chirp signal, with both the source, receiver and sample remaining static. The results that could be expected from a larger and finer array were also shown by moving a small receiver in a plane parallel to the sample.

A combined source and receiver device was also constructed. It was used as a phased array source, split into two parts with a receiver at the centre. The source was scanned using a small receiver and shown to behave in a manner which agrees well with predicted theoretical results. The device was used to scan a fine wire, the result of which agreed well with a theory developed for this system. This device was shown to image a step in a metal surface with good result.

Arrays have also been used as receivers of reflected signals in several scenarios. It was shown that the location of an object could be found using SAFT and ellipse crossing methods.

The work described in this chapter could be extended to create better imaging systems. With a larger 2-D array and the use of multiplexing between elements, a fast imaging system of subsurface defects could be developed. Multiplexing circuitry would also allow more data to be taken for SAFT and ellipse crossing processing, which would result in a better image. With the possibility of modelling the combined source and receiver device confirmed, a new system could be fabricated in such a way as to produce a sharper focal point. If an array of annuli were to be used, then a point focus, as opposed to a line focus achievable with a line array, would be possible allowing the 2-D scanning of a surface. In addition the modelling method for a source and receiver system described could be used for other configurations. It may be useful to simulated the field from a focussed transducer, such as the parabolic mirror described in Chapter 6, when used for pulse echo work. This would be possible by combining the field prediction work of Chapter 6 with the source and receiver method developed here. In such a system h_{source} would equal $h_{receiver}$.

7.7 References

[1] A. S. Chen, D. P. Almond, and B. Harris, "Impact damage growth in composites under fatigue conditions monitored by acoustography," *International Journal of Fatigue*, vol. 2002, pp. 257-261, 2002.

[2] A. S. Chen, D. P. Almond, and B. Harris, "In situ monitoring in real tiem of fatigue-induced damage growth in composite materials by acoustography," *Composites Science and Technology*, vol. 61, pp. 2437-2443, 2001.

[3] M. Akhnak, O. Martinez, L. G. Ullate, and F. Montero de Espinosa, "64 Elements two-dimensional piezoelectric array for 3-D imaging," *Ultrasonics*, vol. 40, pp. 139-143, 2002.

[4] J. Johnson, O. Oralkan, U. Demirci, S. Ergun, M. Karaman, and B. T. Khuri-Yakub, "Medical imaging using capacitive micromachined ultrasonic transducer arrays," *Ultrasonics*, vol. 40, pp. 471-476, 2002.

[5] S. R. Doctor, T. E. Hall, and L. D. Reid, "SAFT- the evolution of a signal processing technology for ultrasonic testing," *NDT International*, vol. 19, pp. 163-167, 1986.

[6] Y. Ozaki, H. Sumitani, T. Tomoda, and M. Tanaka, "A New System for Real-Time Synthetic Aperture Ultrasonic Imaging," *Ieee Transactions on Ultrasonics Ferroelectrics and Frequency Control*, vol. 35, pp. 828-838, 1988.

[7] J. A. Johnson and B. A. Barna, "The Effects of Surface Mapping Corrections with Synthetic-Aperture Focussing Techniques on Ultrasonic Imaging," *IEEE Transactions on Sonics and Ultrasonics*, vol. 30, pp. 283-294, 1983.

[8] M. S. Hughes, D. K. Hsu, F. Margetan, R. B. Thompson, S. R. Ghorayeb, D. K. Holger, L. W. Zachary, and D. O. Thompson, "Application of SAFT on Composites," in *Review of Progress in Quantative Nondestructive Evaluation*, vol. 11, D. E. Chimenti, Ed. New York: Plenum Press, 1992, pp. 1413-1419.

[9] B. Koehler, G. Hentges, and W. Mueller, "Improvement of ultrasonic testing of concrete by combining signal conditioning, scanning laser vibrometer and space averaging techniques," *NDT&E International*, vol. 31, pp. 281-287, 1998.

[10] D. Levesque, A. Blouin, C. Neron, and J.-P. Monchalin, "Performance of laser-ultrasonic F-SAFT imaging," *Ultrasonics*, vol. 40, pp. 1057-1063, 2002.

[11] M. Krause, F. Mielentz, B. Milman, W. Mueller, V. Schmitz, and H. Wiggenhauser, "Ultrasonic imaging of concrete members using anarray system," *NDT&E International*, vol. 34, pp. 403-408, 2001.

[12] V. Schmitz, S. Chakhlov, and W. Mueller, "Experiences with synthetic aperture focussing techniques in the field," *Ultrasonics*, vol. 38, pp. 731-738, 2000.

Chapter 8: Conclusions and further work

8.1 General conclusions

This work described in this thesis has been on the subject of ultrasonic air-coupled polymer-membrane arrays. Much of the work has been on modelling pressure fields, which has been achieved by using the Impulse Response model, in novel ways.

Chapter 1 described the basic properties of sound, such as Snell's law, attenuation, impedance mismatching at an interface and diffraction, which are required in further work in this thesis. Particular attention was paid to diffraction, and two existing models for the field patterns of a single source were described, these were the Farfield Approximation and Impulse Response methods.

Chapter 2 gave a literature review of air-coupled technology. The different types of capacitance transducers were described, in both operation and construction. The advantages of air-coupled broadband transducers were described, namely that they are capable of producing high-resolution images without causing damage to the sample.

In Chapter 3, the Impulse Response model was extended in order to model phased arrays; this was done using a translation in space and time for each element in the array. This model was used to investigate some of the geometrical factors, which determine the focussing performance of an array. To do this a model involving idealised sources was used, this allowed the interference patterns to be studied. In addition, the effect of the directivity of the individual elements was discussed. The conclusions were that a lower element width with respect to frequency increases the merging of individual elements pressure fields, leading to more effective focussing, and that the number of elements has a large effect on the interference field. An increased number of elements, or more specifically a larger overall array width, was shown to lead to a better interference field. In order to combine these two factors, a large number of small elements are required. In practice, the number of channels is limited, and hence, this will lead to a degree of compromise.

In Chapter 4, the construction of polymer-membrane capacitive ultrasonic arrays was described. A simple and effective manufacturing technique was developed using PCB technology. These arrays were used in conjunction with some existing phasing circuitry to produce focussed and beam-steered pressure field plots. These field plots

were compared to those predicted using the simulation developed in the previous Chapter, with good correlation. In addition the FWHM of the focal point of the phased arrays was investigated for a variety of applied phasing. It was found that the width and location of the focal point are closely related. Again this was compared to theory, and the correlation was good.

Chapters 3 and 4 together provide the first comprehensive treatment of arrays used in air, in that an accurate model has been produced which agrees well with experimental measurements throughout the radiated fields. An extensive literature search has demonstrated that, in the particular case of the nearfield response and the details in and around the focus, little has been previously published in any medium. It is thus thought that this work will be of interest to other groups, in areas such as medical imaging, and underwater acoustics.

Chapter 5 describes the development of a new model; this model allows predictions to be made of the pressure field of rectangular transducers, as measured by finite sized receiver. Previously this has only been possible for two circular transducers aligned coaxially. This development was made, by approaching the Impulse Response model in a novel way, which allowed an integration to be performed over the area of the receiver. The model was validated by comparing results with a different approach, which involves treating the receiver as a series of point receivers. As the number of points were increased this approximate method gave results which tended towards the integration method. In addition the integration technique was shown to be much quicker. Further validation of the model was presented by comparing theoretical predictions to experimental results. These results showed good correlation. The model was used to determine the required size of receiver to measure the pressure field of the linear array, used in the previous Chapter, such that the effect on the measured field is negligible.

The results of Chapter 5 represent a major contribution to the subject of diffraction and the accurate measurement of transducer fields. There does not appear to be any other model published which can predict the effect of a finite size receiver on the full radiated field from a rectangular source. It is thought that this approach will be of wide interest, and particularly to those researchers specialising in transducer calibration.

Chapter 6 described a model, which has been developed to predict the pressure field from a circular transducer, which is focussed by a parabolic mirror. Again this is based on the Impulse Response method. The mirror was approximated to an array of

point reflectors, and the differences in the pathlength from the transducer to each field point via each point on the mirror surface was used to apply a suitable phase. A comparison of the predicted and experimental results, show a good correlation. In addition the model was used to investigate the effect of different mirror geometries on the focussing behaviour of the device. It was found that improvements can be made, by moving the focal point, and increasing the mirror diameter. In addition, increasing of the operating frequency was shown to have a large effect. The approach used in this model could be applied to other reflective surfaces, such as flat plates.

Again, an extensive literature search failed to find previous references where the full diffraction field from a plane piston could be treated mathematically after reflection from a curved mirror. It is likely that this will also be of interest to groups working in acoustical imaging.

The topic of Chapter 7, was the imaging of a solid object using air-coupled ultrasonic arrays. This was done in three different ways. Firstly a combined source and receiver array was used to scan a step in a sample, with good results. The device was shown to behave according to theory as a source, and a combined source and receiver. This involved the development of a model for such a pitch catch system. Secondly a through transmission image of a defect in a composite plate was obtained using a large source and a 2-D receiver array. The result obtained with this system shows excellent potential for future systems, which would allow much faster scanning as the physical movement of the transducer would be replaced by a fast multiplexing system. In addition a linear array was used for object location using two post-processing techniques, namely SAFT and ellipse crossing. The results from ellipse crossing were tighter than SAFT for high signal to noise ratios, with the reverse being true for comparatively smaller signals.

8.2 Further work

It is felt that the work presented in this thesis has increased the existing knowledge in the subject of air-coupled arrays, and pressure field modelling. It is hoped that it will prove useful in the development of future ultrasonic systems. However, the work could be extended in several ways.

The phased array model, which was developed in Chapter 3, could be used to predict fields in medical imaging and immersion acoustics. The finite size receiver model, developed in Chapter 5, could be applied to immersion systems, and the effect of finite size receivers considered, especially for high frequency medical imaging systems. This would also benefit from extending the model to consider a circular source and receiver, although the results would be expected to follow the same general trends, but with a more complicated theoretical solution.·

The model developed in Chapter 6, for the circular planar source focussed by a parabolic mirror could be used to produce optimised focussing systems for operation in air or water.

The work on imaging using arrays, presented in Chapter 7 could be extended by fabricating a multiplexer for rapid through-transmission air-coupled imaging. This would lead eventually to a real-time ultrasonic imaging system for use in air.

Publications

To date the publications arising from the work presented in this thesis are:

T. J. Robertson, A. Neild, D.A. Hutchins, J. S. McIntosh, D. R. Billson, R. A. Noble, R. R. Davies, and L. Koker, "Radiated fields of rectangular air-coupled micromachined transducers," presented at the IEEE International Ultrasonics Symposium, Atlanta, Oct 2001.

A. Neild, D.A. Hutchins, T. J. Robertson, and D. W. Schindel, "Theoretical modelling of a planar piston field focussed by reflection," presented at the IEEE International Ultrasonics Symposium, Munich, Oct 2002.

Appendix A: Phasing for 2-D array beam-steering

In Chapter 3 the phasing which will cause a line array to beam-steer was calculated. It was stated that the wavefronts from each element at the time that the last element is driven should form a straight line (Figure 3.2). As an extension to this, when a 2-D array is beam-steered, the wavefronts will form a flat plane. The steering angle will be defined as α in the x direction and β in the y direction. The centre of the element under consideration, (element N, M), lies at point x^{n}_{centre}, y^{m}_{centre} as given in equations 3.1 and 3.4. This allows the problem to be represented as in Figure A.1, where the centre of the element is labelled B.

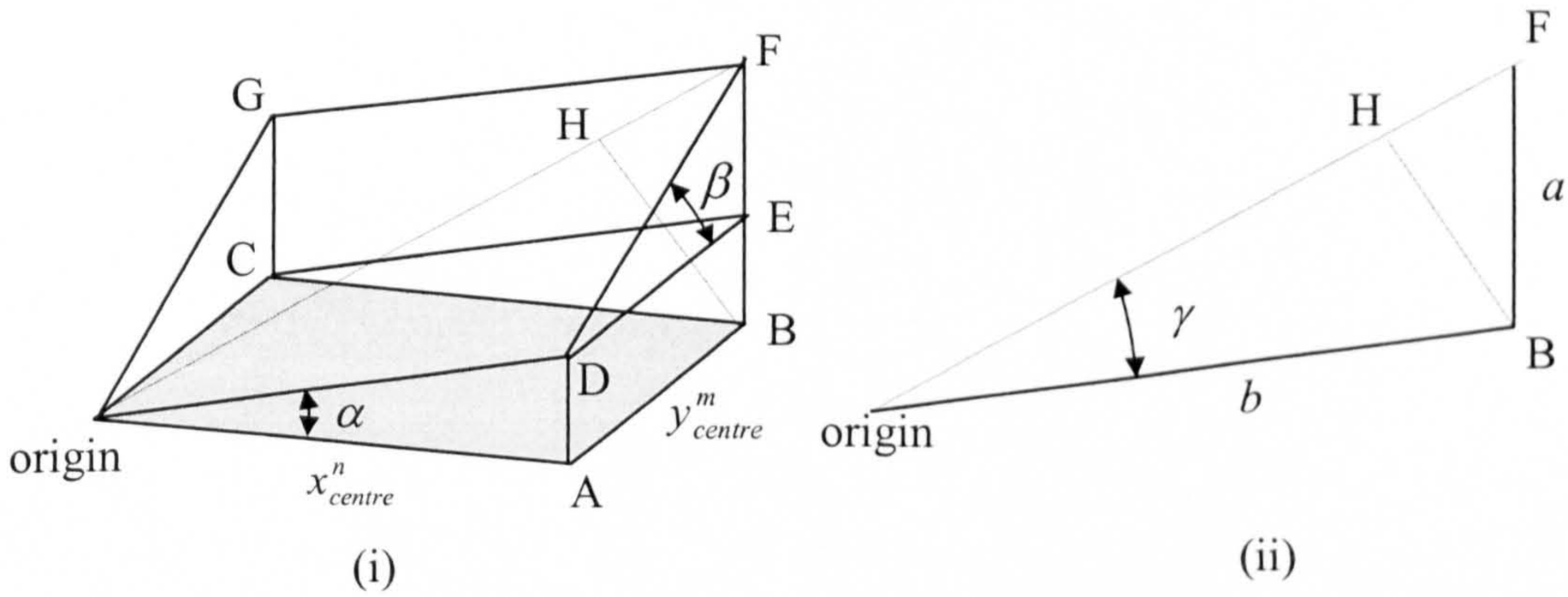

Figure A.1: The geometry of 2-D array beam-steering

The wavefronts will lie in the plane in Figure A.1 (i) passing through the points DFG and the origin. The path difference for a point at x^{n}_{centre}, y^{m}_{centre} (relating to the centre of element N, M) with reference to the origin is the length labelled BH, which meets the plane passing through points DFG and the origin perpendicularly as shown in Figure A.1 (i). Figure A.1 (ii) shows the right-angled triangle passing through BF and the origin, line BH meeting the line from the origin to point F at 90°. It is first necessary to find the length BF, termed a, it can be seen from Figure A.1 (i), that this is given by

$$a = x^{n}_{centre}.\tan(\alpha) + y^{m}_{centre}.\tan(\beta). \qquad (A.1)$$

The distance from the origin to point B, labelled b, is given by

$$b = \sqrt{x_{centre}^{n\ 2} + y_{centre}^{m\ 2}} \,. \tag{A.2}$$

Consequently, the angle γ can be found as

$$\gamma = \tan^{-1}\left(\frac{x_{centre}^{n}.\tan(\alpha) + y_{centre}^{m}.\tan(\beta)}{\sqrt{x_{centre}^{n\ 2} + y_{centre}^{m\ 2}}} \right). \tag{A.3}$$

The path difference, the length B to H, can now be found as,

$$pl_{bs}^{n,m} = \sqrt{x_{centre}^{n\ 2} + y_{centre}^{m\ 2}}.\sin\left\{ \tan^{-1}\left(\frac{x_{centre}^{n}.\tan(\alpha) + y_{centre}^{m}.\tan(\beta)}{\sqrt{x_{centre}^{n\ 2} + y_{centre}^{m\ 2}}} \right) \right\}. \tag{A.4}$$

This allows the phase difference to be calculated in the same way as for the 2-D array focussing case, using equation 3.6.

Appendix B: Matlab programs

B.1 Pressure field model of an array

Withheld for commercial reasons

Subroutine: impulseftspc

```
%Function returns impulse response, at position x,y,z
%for a rectangular transducer of size width by length
%at position 0,0,0.  Impulse response calculation from
%" Diffraction impulse response of rectangular transducers"
%J. Luis, S. Emeterio, L.G. Ullate J. Acoust. Soc. Am Vol. 92,
%No. 2, Pt. 1., 1992

%Difference to impulse: not 1:2000, but minrelevantT:Td
% Hence ftsp: few time steps possible
% takes average for case 4 very effective (but if need alterations for
higher x values must try _apc2
function out=impulseftspc(width, length, x, y, z, tmax, tstep,
tstart,c)

A=width/2;
B=length/2;
%reserve array memory
d=zeros(1,4);
alpha=zeros(1,4);
Ts=zeros(1,2);

d(1)=x-A;
d(2)=y-B;
d(3)=x+A;
d(4)=y+B;

Ta=(sqrt(d(1)^2+d(2)^2+z^2)/c);
Tb=(sqrt(d(2)^2+d(3)^2+z^2)/c);
Tc=(sqrt(d(1)^2+d(4)^2+z^2)/c);
Td=(sqrt(d(3)^2+d(4)^2+z^2)/c);
ivp=zeros(1,ceil((Td-tstart)/tstep+1));
h=zeros(1,ceil((Td-tstart)/tstep+1));
Tm=min(Tb,Tc);
TM=max(Tb,Tc);
T0=z/c;
%define geometrrical regions
if (x>=A & y>=B)
        region=1;
elseif (x<=A & y>=B)
   region=2;
elseif (x>=A & y<=B)
   region=3;
elseif (x<=A & y<=B)
   region=4;
end

for i=1:2
  Ts(i)=(sqrt(d(i)^2+z^2)/c);
```

```
end

switch region
case 1

      for T=ceil(((Ta)-tstart)/tstep+1):ceil((Td-tstart)/tstep+1)
      t=(T-1)*tstep+tstart+eps;
      sigma=sqrt(c^2*t^2-z^2)+eps;

      for i=1:4
               a(i)=asin(d(i)/sigma);
               end
            if(Ta<=t & t<=Tm)
             ivp(T)=pi/2-a(1)-a(2);
             elseif(Tm<=t & t<=TM & Tb<=Tc)
              ivp(T)=-a(1)+a(3);
             elseif(Tm<=t & t<=TM & Tc<=Tb)
              ivp(T)=-a(2)+a(4);
             elseif(TM<=t & t<=Td)
            ivp(T)=-pi/2+a(3)+a(4);
              end
       end
case 2
      for T=ceil(((Ts(2))-tstart)/tstep+1):ceil((Td-tstart)/tstep+1)
      t=(T-1)*tstep+tstart+eps;
      sigma=sqrt(c^2*t^2-z^2)+eps;
                     for i=1:4
                     a(i)=asin(d(i)/sigma);
                     end
                     ab(4)=sign(d(4))*asin(min((abs(d(4))/sigma),1));
                    if (0<t & t<Ta)
                              if (Ts(2)<t)
                         ivp(T)=pi-(2*a(2));
                              end
                    elseif(Ta<=t & t<=Tm)
                           ivp(T)=pi/2-a(1)-a(2);
                    elseif(Tm<=t & t<=TM & Tb<=Tc)
                           ivp(T)=-pi-a(1)+a(3)+2*ab(4);
                    elseif(TM<=t & t<=Td)
                          ivp(T)=-pi/2+a(3)+a(4);
                    end
          end
  case 3
    %tstart=Ts(1)+eps-50e-7;
        for T=round(((Ts(1))-tstart)/tstep+1):ceil((Td-
tstart)/tstep+1)
        t=(T-1)*tstep+tstart;
        sigma=sqrt(c^2*t^2-z^2)+eps;
         %cse=3
        if (0<t & t<Ta)
                     if (Ts(1) < t)

ivp(T)=2*(sign(d(3))*asin(min((abs(d(3))/sigma),1)))-
2*(asin(d(1)/sigma));
                       % Tzone=1
                    end
              elseif(Ta<=t & t<=Tm)
                       ivp(T)=-pi/2-(asin(d(1)/sigma))-
(asin(d(2)/sigma))+2*(sign(d(3))*asin(min((abs(d(3))/sigma),1)));
                    %Tzone=2
```

```
            elseif(Tm<=t & t<=TM & Tb<=Tc)
                    ivp(T)=-asin(d(1)/sigma)+asin(d(3)/sigma);
                %Tzone=3
            elseif(Tm<=t & t<=TM & Tc<=Tb)
               ivp(T)=-pi-
asin(d(2)/sigma)+2*(sign(d(3))*asin(min((abs(d(3))/sigma),1)))+asin(d(
4)/sigma);
                 %Tzone=4
            elseif(TM<=t & t<=Td)
                    ivp(T)=-pi/2+asin(d(3)/sigma)+asin(d(4)/sigma);
                %      Tzone=5
                  end
        end
case 4
        ivph=zeros(1,ceil((Td-tstart)/tstep+1));
         ivpl=zeros(1,ceil((Td-tstart)/tstep+1));
%tstart
        for T=round(((T0)-tstart)/tstep+1):ceil((Td-tstart)/tstep+1)
             t=(T-1)*tstep+tstart+eps;
             % cse=4

        sigma=sqrt(c^2*t^2-z^2)+eps;
        if (0<t & t<Ta)
                  if (T0<t)
                       ivph(T)=-2*pi-
2*(sign(d(1))*asin(min((abs(d(1))/sigma),1)))-
2*(sign(d(2))*asin(min((abs(d(2))/sigma),1)))+2*(sign(d(3))*asin(min((
abs(d(3))/sigma),1)))+2*(sign(d(4))*asin(min((abs(d(4))/sigma),1)));
                   %Tzone=1
                   end
            elseif(Ta<=t & t<=Tm)
                        ivph(T)=-((3*pi)/2)-asin(d(1)/sigma)-
asin(d(2)/sigma)+2*(sign(d(3))*asin(min((abs(d(3))/sigma),1)))+2*(sign
(d(4))*asin(min((abs(d(4))/sigma),1)));
                        %Tzone=2
            elseif(Tm<=t & t<=TM & Tb<=Tc)
                      ivph(T)=-pi-
asin(d(1)/sigma)+asin(d(3)/sigma)+2*(sign(d(4))*asin(min((abs(d(4))/si
gma),1)));
                     %Tzone=3
            elseif(Tm<=t & t<=TM & Tc<=Tb)
                        ivph(T)=-pi-
asin(d(2)/sigma)+2*(sign(d(3))*asin(min((abs(d(3))/sigma),1)))+asin(d(
4)/sigma);
                     %  Tzone=4
            elseif(TM<=t & t<=Td)
                       ivph(T)=-pi/2+asin(d(3)/sigma)+asin(d(4)/sigma);
                  %Tzone=5
                  end
                       for T=round(((T0)-tstart)/tstep+1):ceil((Td-
tstart)/tstep+1)
                t=(T-1)*tstep+tstart;
                % cse=4
           sigma=sqrt(c^2*t^2-z^2)+eps;
           if (0<t & t<Ta)
                    if (T0<t)
                         ivpl(T)=-2*pi-
2*(sign(d(1))*asin(min((abs(d(1))/sigma),1)))-
2*(sign(d(2))*asin(min((abs(d(2))/sigma),1)))+2*(sign(d(3))*asin(min((
abs(d(3))/sigma),1)))+2*(sign(d(4))*asin(min((abs(d(4))/sigma),1)));
```

```
                    %Tzone=1
                    end
              elseif(Ta<=t & t<=Tm)
                     ivpl(T)=-((3*pi)/2)-asin(d(1)/sigma)-
asin(d(2)/sigma)+2*(sign(d(3))*asin(min((abs(d(3))/sigma),1)))+2*(sign
(d(4))*asin(min((abs(d(4))/sigma),1)));
                     %Tzone=2
            elseif(Tm<=t & t<=TM & Tb<=Tc)
                     ivpl(T)=-pi-
asin(d(1)/sigma)+asin(d(3)/sigma)+2*(sign(d(4))*asin(min((abs(d(4))/si
gma),1)));
                   %Tzone=3
            elseif(Tm<=t & t<=TM & Tc<=Tb)
                     ivpl(T)=-pi-
asin(d(2)/sigma)+2*(sign(d(3))*asin(min((abs(d(3))/sigma),1)))+asin(d(
4)/sigma);
                    %  Tzone=4
            elseif(TM<=t & t<=Td)
                      ivpl(T)=-pi/2+asin(d(3)/sigma)+asin(d(4)/sigma);
                   %Tzone=5
               end
               end
               for T=round(((T0)-tstart)/tstep+1):ceil((Td-
tstart)/tstep+1)
                ivp(T)=(ivph(T)+ivpl(T))/2;
                end
   end
   h=ivp./(2*pi/c)
out=h;
```

B.2 Interference fields

Withheld for commercial reasons

B.3 Comparative interference fields

Withheld for commercial reasons

B.4 Half pressure fields

```
%add on to end of program listed in Appendix B.1
nxmax=16;
xfac=2;
sfx=zeros(1,nxmax);
for nx=1:nxmax
   sfx(nx)=(-(nxmax+1)+2*nx)*xfac;
end
[a,b]=size(ampp);
hamp=zeros(a,b);
for bnu=1:a
   for vug=1:b
      if ampp(bnu,vug)>0.5*ampp(bnu,(b+1)/2)
         hamp(bnu,vug)=1;
      end
   end
```

```
end
elem=zeros(a,nxmax);
bestposs=zeros(a,b-((max(sfx))*2));
for i=1:b-((max(sfx))*2)
   i
   for n=1:nxmax
      elem(:,n)=hamp(:,i+max(sfx)+sfx(n));
   end
   bestposs(:,i)=sum(elem,2);
end
```

B.5 Full width half maximum

```
width=[];
maxi=[];
for col=3%1:5%2:16
    col
    datcol=data(:,col);
int=[];
int=interp(datcol,10);
ve=[];
for a=1:610
    if int(a)<max(int)/2
        ve(a)=0;
    else
        ve(a)=1;
    end
end
di=[];
di=find(ve==1);
wid=0;
wid=max(di)-min(di);
width(col)=wid/10*.15;%.275/2; %mm
maxi(col)=1000*max(int);
end
```

B.6 Finite receiver program

Withheld for commercial reasons

B.7 Parabolic mirror model

```
%calculates the field from a reflective focussing mirror, by dividing
it up into pts,
%and treating them as point sources.
%Must define the mirror we have
%firstly known values
kzoff=3e-3;
kztip=34.9e-3;
%dia of mirror
kdia=24.6e-3;
kdrilldia=0e-3;
%dia of transducer
tdia=22e-3;
%about scan plane
%Then calc values
```

```
cvoff=1.5e-3;  %see page r19
guoff=-1.5e-3;       %guess
ang=atan(10.5/38);
%from notes which accompany mirror
kyfd=12.7e-3;
kzfd=29.5e-3;
%design constants to define mirror
% diameter of source
dia=kdia;
%dist from membrane to near tip of mirror
zoff=kzoff;
%focalpoint measured in z from source face
zfd=kzfd;
%focal point measured in y direction from lowest edge of source
yfd=kyfd;

pl=zoff+sqrt((zfd-zoff)^2+(yfd+dia)^2);
%ztip is z calc at y=0,that is xmid at 0
ztip=(pl^2-zfd^2-yfd^2)/2/(pl-zfd);

c=340

%scanned field parameters
%angle of plane to z
hyp=sqrt(10.5^2+38^2);
%size of plane "across" mirror
usize=20e-3;
%size of field away from field
vsize=20e-3;
%no. of points across
uno=61;
%no. of points away
vno=61;
%dist from tip of mirror
uoff=guoff;
voff=cvoff;

%step sizee
ustep=usize/(uno-1);
vstep=vsize/(vno-1);

% mm between points across source face (each point is of same area)
xp=.06e-3*2;
yp=.06e-3*2;
%no. of points can be even or odd
yno=round(dia/yp);
%maxphuse occurs at max u, min v
zscan=38/hyp*(uno-1)*ustep;
yscan=10.5/hyp*(uno-1)*ustep;
%maxphuse+maxlongesth shouldn't be much bigger than 1000, in timing
run 1150,
%takes one sec per simple mirror pt loop
delta_t=((sqrt(dia^2+zoff^2)-zoff)+(sqrt((yscan+dia)^2+(ztip-zscan-
zoff)^2)))/c/991;
%make delta_t 2 sig fig
mult=delta_t;
for mu=1:20
if mult<10
   mult=mult*10;
elseif mult>=10
   break
```

```
end
end
ro=round(mult);
delta_t=ro*10^(-mu+1);
%!!!
```

```
            H((V-1)*uno+U,1:phuse+longesth-cut)=H((V-
1)*uno+U,1:phuse+longesth-cut)+2*hfac;
          end
       end
end
end
Q=H;


%undo wrap
for j=1:uno*vno
htemp=0;
htemp=H(j,:);
aa=htemp(1);
bb=htemp(Hlength);
ind=0;
if aa==0
   ind=find(htemp);
   cc=min(ind);
   dd=max(ind);
   length=dd-cc+1;
   H(j,1:length)=htemp(cc:dd);
   H(j,length+1:Hlength)=zeros(1,Hlength-length);
elseif aa~=0 & bb~=0
   ind=find(htemp==0);
   cc=min(ind);
   dd=max(ind);
   H(j,1:Hlength-dd)=htemp(dd+1:Hlength);
   H(j,Hlength-dd+1:Hlength-dd+cc-1)=htemp(1:cc-1);
   H(j,Hlength-dd+cc:Hlength)=zeros(1,dd-cc+1);
end
end

%now convolve each line
density=1.2
%Constant for wave equation
K=0.2%3.7%3.2%as with mm plots %0.437
%Frequency of excitation
f=500000
Tmax=2000;

%calc v(t) and dv(t)/dt
V=zeros(1,Tmax);
v=zeros(1,Tmax);
tm=zeros(1,Tmax);
for T=1:Tmax
   t=(T-1)*delta_t;
   tm(T)=t;
   thta=2*pi*f*t;
   V(T)=3*c*t^2*exp(-K*f*t)*cos(thta)-c*t^3*K*f*exp(-K*f*t)*cos(thta)-
2*c*t^3*exp(-K*f*t)*sin(thta)*pi*f;
   v(T)=c*t^3*exp(-K*f*t)*cos(thta);
   %V(T)=-cos(2*pi*f*t);
end
in=find(V);
sta=min(in);
sto=max(in);

ampp=zeros(uno,vno);
l=0;
n=1;
```

```
for k=1:uno*vno
   l=l+1;
   hh=0;
   hconv=0;
   if l==uno+1
      l=l-uno;
      n=n+1
   end
   hh=H(k,:);
   indi=find(hh);
   start=min(indi);
   stop=max(indi);
   hconv=conv(hh(start:stop),V(sta:sto));
   ampp(l,n)=max(hconv)-min(hconv);
end

toc
```

Subroutine: cirimpftsp

```
%Function returns impulse response, at position x,y,z
%for a circular transducer of specific dia
%at position 0,0,0.  Impulse response calculation from
%Lockwood and Willette 1973 Jasa vol5s no3 p735 to p741
%Difference to impulse: not 1:2000, but minrelevantT:Td
% Hence ftsp: fewest time steps possible
function out=cirimpftsp(dia, x, y, z, tmax, tstep, tstart)

c=340;
%reserve array memory
d=zeros(1,4);
alpha=zeros(1,4);
Ts=zeros(1,2);
ivp=zeros(1,tmax);
h=zeros(1,tmax);
rho=sqrt(x^2+y^2);
Ta=(z/c);
Tb=(1/c)*(sqrt(z^2+(rho-dia/2)^2));
Tc=(1/c)*(sqrt(z^2+(rho+dia/2)^2));

%define geometrrical regions
if (rho<=dia/2)
        region=1;
elseif (rho>dia/2)
         region=2;
end

switch region
case 1

      for T=ceil(((Ta)-tstart)/tstep+1):ceil((Tc-tstart)/tstep+1)
      t=(T-1)*tstep+tstart+eps;

            if(Ta<t & t<=Tb)
             ivp(T)=1;
            elseif(Tb<t & t<=Tc)
             ivp(T)=(1/pi)*acos((c^2*t^2-z^2+rho^2-
(dia/2)^2)/(2*rho*(sqrt(c^2*t^2-z^2))));
             end
       end
```

```
 case 2
      for T=ceil(((Tb)-tstart)/tstep+1):floor((Tc-tstart)/tstep+1)

      t=(T-1)*tstep+tstart+eps;

                    ivp(T)=(1/pi)*acos((c^2*t^2-z^2+rho^2-
(dia/2)^2)/(2*rho*(sqrt(c^2*t^2-z^2))));


        end
   end
   h=ivp.*c;
   out=h;
```

B.8 SAFT and ellipse crossing programs

B.8.1 Main program

```
%SAFT software
%data needed for program, SI units
%source location
sourcex=[-67.95e-3,0];
sourcez=[47.7e-3,10];
%angle of source wrt array (in degrees)
ang=90;
%s0urce size
sourcedia=24e-3;
%array dimensions
pitch=.7e-3;
elementwidth=.4064e-3;
%speed of sound in medium
c=343;
%First run this master program then whichever of the other sub
programs required,
%each of which will input and output a file of the same name, so only
the variables
%need changing.
%load TimeData.txt;%datafilename;
%load R0.txt;%datafilename;
%load R1.txt;%datafilename;   %add more if more than two transmiters
%load R0;%datafilename;
%load R0;%datafilename;
%r0=R0;
%r1=R1;
%timedata=TimeData;
%number of transmitters
nooftrans=1;%2;
%data=r0;%[r0;r1];%datafilename;
r0=data;
[noofele,noofpts]=size(r0);
A=1;
B=noofpts;
initialtime=datao(1,1)%timedata(1);
delta_t=datao(2,1)-datao(1,1);%timedata(2);
tlength=noofpts;

alpha=ang/180*pi;
%ROUTINE:
```

```
%Stage 1
   %resample
   %Interpolates between time points or elements
         %interpolate
%Stage 2
   %levelshift
   %alligns data amplitude
%Stage 3
   %rastallign
   %Removes data differences
%Stage 4
   %time base filter
         %tfilter
%Stage 5
   %Window
   %A
      %Manual time base windowing using plot
      %with care not to lose part of the signal, this could be done on
the scope
         %manualtwindow
         %windowcorrect
      %B
      %If em pickup at start of signel cut of first with manualtwindow
      %Automatic time base windowing, by finding waveform max
         %autotwindow
         %autotwindowcorrect
%Stage 6
   %Alter Data
   %Takes appodization and some other factors into account
%Stage 7
   %Calc Image
   %Uses focussing of beamsteered subarrays to find and plot an image
         %calcimage
%Stage 8
   %Output to surfer
         %surferfileout
```

B.8.2 Filtering

```
%filters in the time domain for each transmitter/element combination
tic
sampling_freq=1/delta_t;
nyq=sampling_freq/2;
norder=2;
% bandpass fiter
% lower freq in khz
lfreq=100;
% higher freq in khz
hfreq=600;%2500;
wn=[lfreq*1000 hfreq*1000]/nyq;
for tr=1:nooftrans
   for el=1:noofele
      xx=data((tr-1)*noofele+el,:);
 [bb,aa]=butter(norder,wn);
yy=filter(bb,aa,xx);
      data((tr-1)*noofele+el,:)=yy;
   end
end
toc
```

B.8.3 Time windowing

```
%Windows data in time frame, assuming no large em pick up at start

%Finds min and max in waveform then puts window round it proportional
in
%length to the time difference at which thes occur
%INPUT VALUES
%proportion of time window to time difference between min and max,
should be >2
tprop=3;
%initialise to 0
loc=zeros(nooftrans*noofele,2);
%loop through transmitters
for tr=1:nooftrans
   %loop through elements
   for el=1:noofele
      %find size and locaton of max
      [smax,lmax]=max(data((tr-1)*noofele+el,1:tlength));
      %find size and locaton of min
      [smin,lmin]=min(data((tr-1)*noofele+el,1:tlength));
      %array of location for each element
      loc((tr-1)*noofele+el,1:2)=[lmax,lmin];
   end
end
%assume whichever of max and min occur first will occur first for all
%elements and transmitters
%loc(29,2)=700;
if lmax>lmin
   %min first
   firstpeak=1;
elseif lmax<lmin
   %max first
   firstpeak=2;
end
%find location of first max and last min, or reverse
if firstpeak==1
   firstn=min(loc(:,2));
   lastn=max(loc(:,1));
elseif firstpeak==2
   firstn=min(loc(:,1));
   lastn=max(loc(:,2));
end
firstneed=max(firstn-(lastn-firstn)*(tprop-1)/2,0);
lastneed=min(lastn+(lastn-firstn)*(tprop-1)/2,tlength);
%find new overall time window to include all wave forms
toverall=lastneed-firstneed+1;
datanew=zeros(nooftrans*noofele,toverall);
gg=1
ff=0
%loop through transmitters
for tr=1:nooftrans
   %loop through elements
   for el=1:noofele
      %finds the length of window for element/transmitter combination
      locallength=min(tlength,abs(loc((tr-1)*noofele+el,1)-loc((tr-
1)*noofele+el,2))*tprop);
      %find the first and last point needed
      if firstpeak==1
      beforef=max(1,loc((tr-1)*noofele+el,2)-(tprop-1)/2*locallength);
      afterl=min(tlength,loc((tr-1)*noofele+el,1)+(tprop-
1)/2*locallength);
```

```
      elseif firstpeak==2
      beforef=max(1,loc((tr-1)*noofele+el,1)-(tprop-1)/2*locallength);
      afterl=min(tlength,loc((tr-1)*noofele+el,2)+(tprop-
1)/2*locallength);
   end
   ff=ff+1
      %finds the first and last value in window
       firstvalu=data((tr-1)*noofele+el,1);
       lastvalu=data((tr-1)*noofele+el,tlength);
       %new data file
       datanew((tr-1)*noofele+el,beforef-firstneed+1:afterl-
firstneed+1)=data((tr-1)*noofele+el,beforef:afterl);
       if beforef~=firstneed
          datanew((tr-1)*noofele+el,1:max(1,beforef-firstneed))=0;
       end
       if afterl~=lastneed
          datanew((tr-1)*noofele+el,afterl-firstneed+2:toverall)=0;
       end
     end
  end
data=datanew;
[nothing,tlength]=size(datanew);
initialtime=initialtime+(firstneed-1)*delta_t;
```

B.8.4 SAFT image calculation

```
%INPUT DATA
%size of subarray in number of elements;
subsize=1;
%offset of subarray in terms of no of elements
offsetsub=1;
%step and noof points, and start point of field,
zstep=.25e-3;
zmax=160;
xmax=161;
xstep=.25e-3;
zstart=0e-3;
%always centered on center of array except if xstart not=0
xstart=[-2.5e-3,2.5e-3];
%%%%%%%%%%%%%%%%%%%%%%%%%%%%%%%%%%%%%%%%%%%%%%%%%%%%%%%%%%%%
%number of subarrays
subs=floor((noofele-subsize+offsetsub)/offsetsub);
%arrays
wave=zeros(subsize,1);
wavesub=zeros(subs,1);
sourceimage=zeros(xmax,zmax);
endimage=zeros(xmax,zmax);

%loop through transmitters
for tr=1:nooftrans
   %loop over area of image
   for Z=1:zmax
      z=zstart+(Z-1)*zstep;
      Z
      for X=1:xmax
         x=xstart(tr)+(X-1-(xmax-1)/2)*xstep;
         xd(X)=x;
         %min distance wave must travel from source to pixel
            %firstly redefine coordinates wrt source- u,w
            u=cos(alpha(tr))*(x-sourcex(tr))-sin(alpha(tr))*(z-
sourcez(tr));
```

```
            w=sin(alpha(tr))*(x-sourcex(tr))+cos(alpha(tr))*(z-
sourcez(tr));
         if u<-sourcedia(tr)/2
            sourced=sqrt((u+sourcedia(tr)/2)^2+w^2);
         elseif -sourcedia(tr)/2<=u & u<=sourcedia(tr)/2 % source
perpendicular to rec
            %Then in front of source ie plane wave
            sourced=abs(w);
         elseif u>sourcedia(tr)/2
            sourced=sqrt((u-sourcedia(tr)/2)^2+w^2);
         end
         check(X,Z)=sourced;
         %loop through subarrays
         for sub=1:subs
            %find center of subarray
            subcenter=-.5*((noofele-
1)*pitch+elementwidth)+offsetsub*(sub-1)*pitch+((subsize-
1)*pitch+elementwidth)/2;
            %angle from center of subarray to pixel
            ang=atan((x-subcenter)/z);
            %distance to center of subarray from pixel
            subd=sqrt((x-subcenter)^2+z^2);
            di(X,sub)=subd;
            %total dist from source to sub array center via pixel in
time
            tptstart=(sourced+subd)/c;
            fgh(X,sub)=tptstart;
            %loop for each element in subarray
            for subele=1:subsize
               %beamsteer time difference in t points
               bsdiff=((subele-1)*pitch-(subsize-
1)*pitch/2)*sin(ang)/(c*delta_t);
               %element number
               ele=(sub-1)*offsetsub+subele;
               %start point of interest in time points
               firsttpt=1+round((tptstart-initialtime)/delta_t-
bsdiff);
               ftptlist(sub)=firsttpt;
               if firsttpt<=0
                  wave(subele)=0;
               elseif firsttpt>=1 & firsttpt<=tlength
                  wave(subele)=abs(data(ele+(tr-1)*noofele,firsttpt));
               elseif firsttpt>tlength
                  wave(subele)=0;
               end
            end
            if subsize==1
               wavesub(sub,:)=wave;
            else
               wavesub(sub,:)=sum(wave);
            end
         end
         sourceimage(X,Z)=sum(wavesub);
      end
   end
   endimage=endimage+sourceimage;
   if tr==1
      res1=sourceimage;
   elseif tr==2
      res2=sourceimage;
   elseif tr==3
```

```
      res3=sourceimage;
   end

end
toc
```

B.8.5 Ellipse crossing image calculation

```
%"elipse crossing" method, using time of flight, here use time to
first peak
%for use after autowindow
tic
%element location
for no=1:noofele
   xele(no)=(no-.5-noofele/2)*pitch;
end
%spatial area
%step and no. of points, and start point of field,
zstep=.25e-3;
zmax=160;
xmax=161;
xstep=.25e-3;
zstart=35e-3;
%always centered on center of array except if xstart not=0
xstart=0;
%no of elements between those in the pair considered
eloff=2;
firstpeak=1
%is min or max first?
if firstpeak==1   %min first
   loccol=2;
elseif firstpeak==2   %min first
   loccol=1;
end
loccol=1;
field=zeros(xmax,zmax);
elipsecross=zeros(xmax,zmax);
fieldam=zeros(xmax,zmax);
elipsecrossam=zeros(xmax,zmax);
test=[];
test2=[];
%loop through transmitters
for tr=1:nooftrans
   %loop through each pair of adjacent elements
   for gr=1:noofele-3
      gr
         toff=loc((tr-1)*noofele+gr,loccol);
         toff2=loc((tr-1)*noofele+gr+eloff,loccol);
         fac=(toff*delta_t+initialtime)/(delta_t);
         fac2=(toff2*delta_t+initialtime)/(delta_t);
      %loop over area of image
      for Z=1:zmax

      z=zstart+(Z-1)*zstep;
      for X=1:xmax
         x=xstart(tr)+(X-1-(xmax-1)/2)*xstep;
         %min distance wave must travel from source to pixel
            %firstly redefine coordinates wrt source- u,w
            u=cos(alpha(tr))*(x-sourcex(tr))-sin(alpha(tr))*(z-
sourcez(tr));
```

```
            w=sin(alpha(tr))*(x-sourcex(tr))+cos(alpha(tr))*(z-
sourcez(tr));
          if u<-sourcedia(tr)/2
             sourced=sqrt((u+sourcedia(tr)/2)^2+w^2);
          elseif -sourcedia(tr)/2<=u & u<=sourcedia(tr)/2 % source
perpendicular to rec
             %Then in front of source ie plane wave
             sourced=abs(w);
          elseif u>sourcedia(tr)/2
             sourced=sqrt((u-sourcedia(tr)/2)^2+w^2);
          end
          %check(X,Z)=sourced;
          line1=0;
            line2=0;
            am1=0;
            am2=0;
            %min distance wave must travel from pixel to element
            noone=sqrt((x-xele(gr))^2+z^2);
          notwo=sqrt((x-xele(gr+eloff))^2+z^2);
            tptone=(noone+sourced)/c/delta_t;
            tpttwo=(notwo+sourced)/c/delta_t;
            diff1=tptone-fac;
            diff2=tpttwo-fac2;
            if X>1 & diff1*diff1p<=0
                line1=1;
                am1=max(data((tr-1)*noofele+gr,:))-min(data((tr-
1)*noofele+gr,:));
            end
            if X>1 & diff2*diff2p<=0
                line2=1;
                am2=max(data((tr-1)*noofele+gr+eloff,:))-min(data((tr-
1)*noofele+gr+3,:));
             end
             diff1p=diff1;
             diff2p=diff2;
             field(X,Z)=line1*line2+field(X,Z);
                fieldam(X,Z)=am1*am2+fieldam(X,Z);
            gf(X,Z)=(toff2*delta_t+initialtime)/(delta_t);
             fg(X,Z)=round((notwo+sourced)/(c*delta_t));
             test(X,Z)=line1;
             test2(X,Z)=line2;
             elipsecross(X,Z)=line1+line2+elipsecross(X,Z);
             elipsecrossam(X,Z)=am1+am2+elipsecrossam(X,Z);
        end
    end
end
if tr==1
   r1=elipsecross;
elseif tr==2
   r2=elipsecross-r1;
elseif tr==3
   r3=elipsecross-r2;
elseif tr==4
   r4=elipsecross-r3;
end
end
 toc
```

Appendix C: Equipment specifications

C.1 Panametrics 5055PR

Pulser	
Maximum pulse amplitude	-250 V into 50 Ω
Minimum rise time	10 ns
Pulse energy	18 – 110 μJ (four settings)
Damping range	10 – 250 Ω
Pulse repetition rate	100 – 2000 Hz
Receiver	
Voltage gain	40 dB or 60 dB
Input impedance	500 Ω
Output impedance	50 Ω
Bandwidth	10 kHz – 10 MHz
Noise levels	50 μV peak-to-peak referred to the input

C.2 Second wave NCA1000 Chirp generator

Dynamic range	>140 dB
Frequency range	100 kHz – 5 MHz
Time resolution (in air)	± 1 ns
Time resolution (through sample at max dynamic range)	± 25 ns
Pulse repetition frequency	>20 Hz
Maximum output voltage	400 V peak-to-peak

C.3 Cooknell CA6/C charge amplifier

Input impedance	100 Ω above 10 kHz
Sensitivity	250 mV/pC
Series noise voltage generator	0.6 nV/Hz
Parallel noise voltage generator	4×10^{-14} A/Hz
Bandwidth	<10 kHz - >10 MHz
Maximum output level	1 V rms into 50 Ω

C.4 Scanning Stage

Two Thomson linear stages, driven by synchronous stepper motors

Motor steps per revolution	400
Motor steps per mm	80
Maximum stroke	526 mm
Accuracy	0.023 mm per 300 mm travel
Repeatability	0.005 mm

Appendix D: Calculation of Finite receiver model integrals

In the calculation of a model, which predicts the pressure waveform received by a rectangular finite receiver from a rectangular source, three integrals were performed; they are listed along with the solutions as equations 5.15, 5.16 and 5.17. In this appendix the workings will be shown.

D.1 Integral A

The integration that needs to be performed is

$$A = C_b.C_d.\int_{u_1^{lower}}^{u_1^{upper}} \sin^{-1}(u_1/r)du_1. \tag{D.1}$$

Firstly using the substitution $a = \sin^{-1}(u_1/r)$, then $u_1 = r.\sin(a)$ and $du_1 = r\cos(a).da$, hence

$$A = C_b.C_d.\int_{u_1^{lower}}^{u_1^{upper}} a.r.\cos(a)da\,. \tag{D.2}$$

Then using integration by parts, with $u(a) = a.r$, and $\frac{dv(a)}{da} = \cos(a)$, so that $\frac{du(a)}{da} = r$ and $v(a) = \sin(a)$ gives

$$A = C_b.C_d.\left\{[a.r.\sin(a)]_{u_1^{lower}}^{u_1^{upper}} - r.\int_{u_1^{lower}}^{u_1^{upper}} \sin(a)da\right\}. \tag{D.3}$$

The integration term can be easily solved, to give

$$A = C_b.C_d.[a.r.\sin(a) + r.\cos(a)]_{u_1^{lower}}^{u_1^{upper}}. \tag{D.4}$$

By reversing the substitution, this gives

$$A = C_b.C_d.\left[u_1.\sin^{-1}(u_1/r) + \sqrt{r^2 - u_1^2}\right]_{u_1^{lower}}^{u_1^{upper}}, \tag{D.5}$$

as given as the solution in equation 5.18.

D.2 Integral B

The integration that needs to be performed is

$$B = C_b.C_c.\int_{u_1^{lower}}^{u_1^{upper}} \sqrt{r^2 - u_1^2}.\sin^{-1}(u_1/r)du_1. \tag{D.6}$$

The first step is to use the substitution $\theta = \sin^{-1}(u_1/r)$, then $u_1 = r.\sin(\theta)$ and $du_1 = r\cos(\theta).d\theta$, so that

$$\begin{aligned} B &= C_b.C_c.\int_{u_1^{lower}}^{u_1^{upper}} \sqrt{r^2 - r^2.\sin^2(\theta)}.\theta.r.\cos(\theta)d\theta \\ &= C_b.C_c.\int_{u_1^{lower}}^{u_1^{upper}} \theta.r^2.\cos^2(\theta)d\theta \end{aligned} \quad (D.7)$$

Using integration by parts, such that $u(\theta) = r^2\theta$, and $\frac{dv(\theta)}{d\theta} = \cos^2(\theta)$, so that $\frac{du(\theta)}{d\theta} = r^2$ and $v = \frac{\theta}{2} + \frac{\sin(2\theta)}{4}$, then

$$B = C_b.C_c.\left\{\left[r^2\theta.\left(\frac{\theta}{2} + \frac{\sin(2\theta)}{4}\right)\right]_{u_1^{lower}}^{u_1^{upper}} - \frac{r^2}{4}.\int_{u_1^{lower}}^{u_1^{upper}} 2\theta + \sin(2\theta)d\theta\right\}. \quad (D.8)$$

The integration term can be found giving

$$B = C_b.C_c.\frac{r^2}{8}.\left[2\theta^2 + 2\theta.\sin(2\theta) + \cos(2\theta)\right]_{u_1^{lower}}^{u_1^{upper}}. \quad (D.9)$$

By reverting the substitution performed earlier and using $\cos(2\theta) = 1 - 2\sin^2(\theta)$, this gives

$$B = C_b.C_c.\frac{r^2}{8}.\left[2\left(\sin^{-1}(u_1/r)\right)^2 + 4\sin^{-1}(u_1/r).\frac{u_1}{r}.\sqrt{1 - \frac{u_1^2}{r^2}} + 1 - 2.\left(\frac{u_1}{r}\right)^2\right]_{u_1^{lower}}^{u_1^{upper}}. \quad (D.10)$$

Which can be simplified to give the result stated in equation 5.19, that

$$B = C_b.C_c.\left[\frac{r^2}{4}.\left(\sin^{-1}(u_1/r)\right)^2 + \frac{u_1}{2}.\sin^{-1}(u_1/r).\sqrt{r^2 - u_1^2} + \frac{r^2}{8} - \frac{u_1^2}{4}\right]_{u_1^{lower}}^{u_1^{upper}}. \quad (D.11)$$

D.3 Integral C

The integration that needs to be performed is

$$C = C_a.\int_{u_1^{lower}}^{u_1^{upper}} C_c\sqrt{r^2 - u_1^2} + C_d du_1. \quad (D.12)$$

By using the substitution $\theta = \cos^{-1}(u_1/r)$, then $u_1 = r.\cos(\theta)$ and $du_1 = -r\sin(\theta).d\theta$, so that

$$C = C_a.\left(\int_{u_1^{lower}}^{u_1^{upper}} - C_c.r^2.\sin^2(\theta)d\theta + \int_{u_1^{lower}}^{u_1^{upper}} C_d du_1\right). \quad (D.13)$$

By using $\sin^2(\theta) = \frac{1-\cos(2\theta)}{2}$, the integral can be performed to give

$$C = C_a.\left(C_c.\frac{r^2}{2}\left[\frac{\sin(2\theta)}{2} - \theta\right]_{u_1^{lower}}^{u_1^{upper}} + \left[C_d.u_1\right]_{u_1^{lower}}^{u_1^{upper}} \right). \qquad \text{(D.14)}$$

By reversing the substitution, and using $\sin(2\theta) = 2\cos(\theta).\sqrt{1-\cos^2(\theta)}$ this becomes the answer given in equation 5.20, that is

$$C = C_a.\left[C_c\left\{\frac{u_1}{2}.\sqrt{r^2-u_1^2} - \frac{r^2}{2}.\cos^{-1}(u_1/r)\right\} + C_d.u_1 \right]_{u_1^{lower}}^{u_1^{upper}}. \qquad \text{(D.15)}$$